Modeling Drilled Shafts in MSE Block Walls

By:

Matthew Pierson

Submitted to the graduate degree program in Civil Engineering and Graduate Faculty of the University of Kansas in partial fulfillment of the requirements for the degree of Doctor of Philosophy in Civil Engineering

Chairperson: _____
Dr. Robert L. Parsons

Committee Members: _____
Dr. Jie Han

_____
Dr. Anil Misra

_____
Dr. Michael H. Taylor

_____
Dr. C. Bryan Young

Date defended: _____

The Thesis Committee for Matthew Pierson Certifies that
this is the approved Version of the following thesis:

Modeling Drilled Shafts in MSE Block Walls

Chairperson: _____
Dr. Robert L. Parsons

Date approved: _____

Table of Contents

Table of Contents (cont).

List of Figures:

List of Figures Continued:

List of Figures Continued:

List of Figures Continued:

List of Figures Continued:

List of Figures Continued:

List of Tables:

ACKNOWLEDGEMENTS

The Kansas Department of Transportation was critical to the success of this study. Without the support of people from the KDOT administration, maintenance, and geotechnical engineering units none of this would be possible. Tensar International Corporation was very supportive of the project and contributed materials and support to the study. Applied Foundation Testing and Dan Brown and associates completed the load testing and post analysis with exceptional professionalism. The University of Kansas department of Civil Environmental and Architectural Engineering also provided invaluable support for this project.

ABSTRACT

Mechanically stabilized earth (MSE) technology is recognized for its efficiency for constructing earth retention structures. In some cases structural foundations must pass through the reinforced fill due to the required footprint of the reinforced zone behind the facing. Limited information about the interaction between the structure and the MSE mass has been published, making efficient design difficult. It is very costly to construct and test all possible geometries or applications; therefore numerical modeling must be used to supplement physical data.

This thesis contains a discussion of the analysis of physical test data and numerical modeling of an MSE test wall containing foundation elements. The test wall consists of an MSE wall with cast-in-place shafts contained within and solely supported by the reinforced fill. The finite difference numerical modeling program FLAC3D was used for analysis. A parametric study was conducted to determine how the various constituents of the physical wall as well as wall height affect wall – shaft behavior. Geogrid properties, particularly stiffness, were found to have the greatest influence on behavior. Wall height has a large influence on capacity at shaft movement of more than 2 inches. Analyses of the modeling results were then used to create design recommendations for MSE walls with foundation elements.

CHAPTER ONE

Introduction

The use of mechanically stabilized earth (MSE) technology has become widely accepted as an economical construction technique. The term MSE can be used to describe a reinforced slope or a retaining wall. As the MSE technology has become more accepted, its uses have expanded from its initial purposes. One example of this is an MSE wall that supports a structure subjected to a significant lateral load. Past practice has called for a deep foundation, often a concrete shaft, which passes through the reinforced mass. There is no accepted technique for developing lateral load / response characteristics for the shaft and MSE wall for this situation. As a result the design method is simplified by assuming there is no lateral resistance provided by the MSE structure. This means, for design purposes, all lateral load is assumed to be carried by the foundation of the drilled shaft. This in turn requires a significant socket foundation for the shaft and potentially larger shaft diameter and more reinforcing steel. A significant cost and time savings could be had if the drilled shaft foundation below grade could be eliminated and the entire lateral load carried by the MSE structure (Figure 1).

The Kansas Department of Transportation (KDOT) partnered with The University of Kansas (KU), Applied Foundation Testing (AFT), and Tensar International Corporation to construct and test an MSE wall – shaft system. This system consisted of a twenty foot tall MSE wall with eight concrete shafts contained within and solely

supported by the MSE mass. After testing was completed the performance of these shafts was reported in (Pierson, 2008).

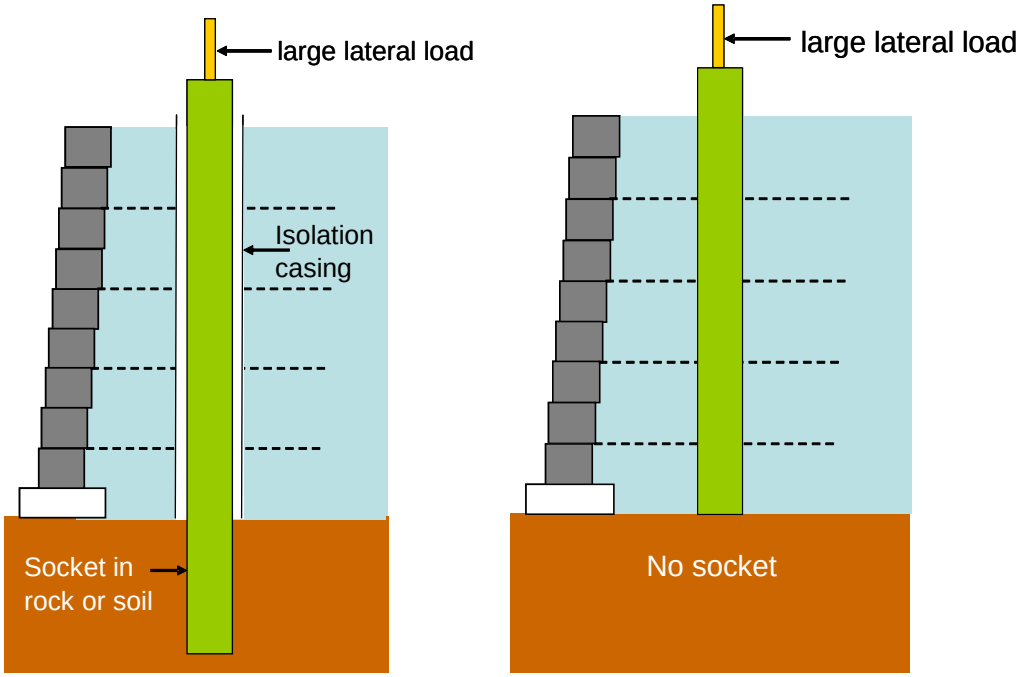

Figure 1.1 Schematic of current practice and of experimental program.

This dissertation describes the extension of this work through advanced three dimensional finite difference modeling using FLAC 3D (Itasca 2006). Modeling permits the evaluation of an essentially infinite number of wall / shaft configurations. Once the model was calibrated using existing data from field testing, properties in the model were changed such as backfill friction angle, wall height, and shaft spacing. These new models were then evaluated to determine an appropriate design method.

The following chapters describe the current state of the practice, background information about the methods used in the analysis, construction and testing of the field test, analysis of field test data, a detailed description of FLAC 3D as it relates to this problem, modeling calibration, modeling results, and conclusions and recommendations.

CHAPTER TWO

Literature Review

2.1 Physical Testing

Other than material directly related to this project, there is little published guidance for designing laterally loaded shafts supported within an MSE Wall. However there are complete design procedures for each item individually (Section 2.1.1, 2.1.2, and 2.1.3). These will be reviewed, as well as two other research projects that examined the use of MSE Walls to support bridge abutments (Section 2.1.4). Much of section 2.1.1 through 2.1.4 was presented in Pierson 2008. This will then be followed by selected results from physical testing of laterally loaded shafts contained within and solely supported by an MSE wall (Section 2.1.5).

2.1.1 MSE Wall Design (FHWA)

An MSE wall uses inclusions that are placed within a soil mass to help distribute tensile loads and prevent soil failure. One type of MSE structure not discussed here, Reinforced Soil Slopes (RSS), incorporates planar reinforcing elements in constructed earth-sloped structures with face inclinations of less than 70 degrees (FHWA, 1997). MSE Walls use the same planar reinforcing and typically require a facing to retain the soil within the structure. "Some common facings include precast concrete panels, dry cast modular blocks, metal sheets and plates, gabions, welded wire mesh, shotcrete, wood lagging and panels, and wrapped sheets of geosynthetics" (FHWA, 1997). Most MSE systems use either a galvanized or epoxy coated steel reinforcement, or synthetic reinforcement like high density polyethylene (HDPE),

polypropylene, or polyester yarn. The wall system used for the field project is developed by Tensar International (See Figure 2.1). It utilizes dry cast modular blocks and HDPE reinforcement.

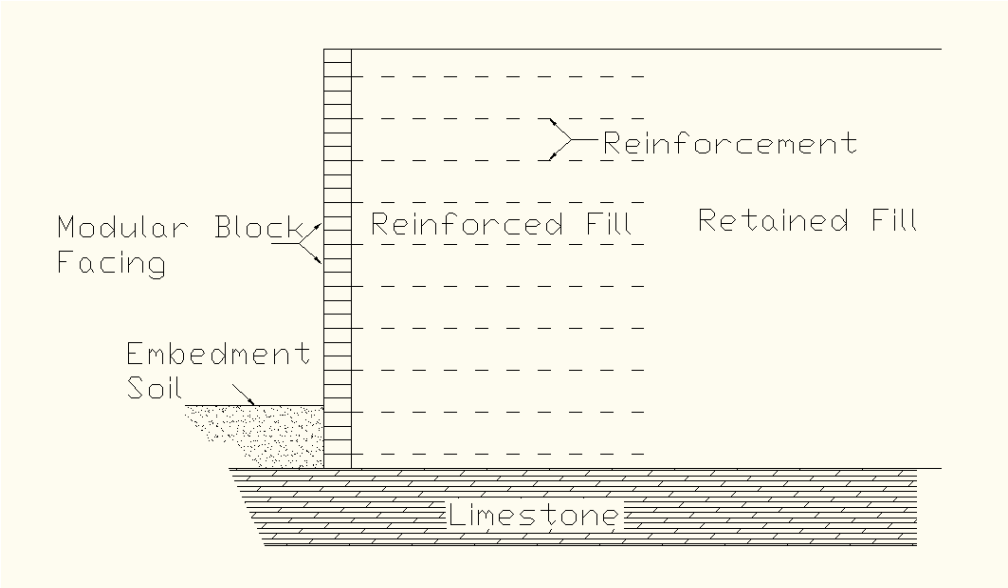

Figure 2.1 Cross-section of typical MSE block wall.

According to FHWA (FHWA, 1997), branches and other different types of reinforcement have been used for at least 1,000 years. Beginning in the early 1960s, reinforced soils began to be used in engineering by the French architect and engineer Henri Vidal who developed Reinforced Earth™. In 1972 the first wall to use this technology in the United States was built in California.

Some of the advantages of the MSE structure over a conventional concrete gravity retaining wall system reported by the FHWA include:

- Simple and rapid construction procedures that do not require large construction equipment.
- Experienced craftsmen with special skills for construction are not required.
- Less site preparation then other alternatives is required.

- Less space in front of the structure for construction operations is needed.
- A rigid, unyielding foundation is not required because MSE structures are tolerant of deformations.
- Cost effectiveness.
- The technically feasible to heights in excess of 25 meters.

When designing an MSE Wall structure there are several different failure modes that must be checked. Design should consist of checking these modes of failure using one or more of the following; working stress analysis, limit equilibrium analysis, and deformation evaluations (FHWA). The first potential mode of failure is external stability. This involves treating the entire reinforced mass as an internally stable block and checking conventional failure modes typical for gravity wall systems. Possible failure mechanisms include, sliding, overturning, bearing capacity, and deep seated stability. Internal stability pertains to the reinforced soil mass. The reinforcement has two failure types, elongation or breakage and reinforcement pullout. Bulging is a possibility consisting of local failure of the facing. This could be a problem if the reinforcement locations are not spaced closely enough to prevent the lateral movement of individual blocks. The step by step internal design process is as follows: (FHWA, 1997)

- Select a reinforcement type
- Determine the location of the critical failure surface.
- Select a reinforcement spacing compatible with the facing connections and to prevent bulging.
- Calculate the maximum tensile force at each reinforcement level, static and dynamic and compare with the allowable load.

- Calculate the maximum tensile force at the connection to the facing and compare with the allowable load.
- Calculate the pullout capacity at each reinforcement level and compare with the allowable load.

Some additional issues may need to be addressed in design depending on the situation. Traffic barriers are designed to take impact forces. Drainage should be considered as well as the corrosion resistance of metal reinforcement. Utilities may need to pass through the reinforced soil mass. Differential settlement with cast-in-place structures must be considered. Surcharges as a result of road construction can increase demand placed on the reinforcement. Rapid drawdown conditions may need to be considered if tide or river fluctuations are possible. Obstructions in the reinforced soil zone, such as drainage inlets, must also be considered.

2.1.2 Design of Laterally Loaded Shafts

When horizontal loads are being designed for drilled shafts, the most common method for analysis is the p-y curve method. "This involves modeling the soil-structure interaction as a nonlinear beam on elastic foundation. The model assumes that the soil is continuous, isotropic, and an elastic medium. The drilled shaft is divided into equally spaced sections and the soil response is modeled by a series of closely spaced discrete springs called Winkler's springs" (Johnson, 2006). This model allows for the slope, moment, shear, soil reaction, and deflection to be found for all sections along the drilled shaft. The initial curves were found by doing full scale lateral load tests. The initial tests were performed in soft and stiff clay, sand, loess, and limestone. These lateral load tests are the most accurate, but also the most expensive way to find the soil structure p-y

response. There are programs that are available (LPILE) to predict p-y curves based on shaft geometry and soil conditions. Using engineering judgment it is possible to take the site materials and use computer programs to generate p-y curves without doing expensive lateral load testing. However, there are currently no models that will account for shafts supported by an MSE wall. One assumption made in each model is that soil is modeled as a homogeneous half space. For the MSE wall the soil is homogeneous but has discrete strips of reinforcement with different properties within it, and the mass is not a half space but rather slightly larger than a quarter space.

2.1.3 Design of Drilled Shafts Supporting Sound Walls

There are several design methods for drilled shafts used to support sound walls. Due to inconsistency between design methods and criteria used within design methods, a review of several design methods for laterally loaded drilled shafts was conducted by Yang et al. (2007). These methods were compared with load tests in both sand and cohesive material. The Brinch Hansen method (1961), Broms method (1964a and 1964b), Davidson et al. (1976), and Band and Shen (1989) were all compared with load tests to evaluate the ultimate lateral capacity of the drilled shafts. To evaluate serviceability requirements the NAVFAC DM-7, and COM624P or LPILE programs were compared to load test data at several different shaft deflections. The literature review concluded that the recommended deflection for serviceability and aesthetics was from 0.6 – 1.5 in. of shaft top movement. Additionally the recommended design approach was to estimate soil parameters using SPT correlations. Shaft length was estimated next using the Broms method with a factor of safety (FS) of 2. Finally serviceability is verified using COM624P (or LPILE). If the estimated deflection at the

design load is below the serviceability criteria then the shaft length is permissible. If serviceability controls then use COM624P to determine shaft length.

2.1.4 Topics Related to MSE Wall Interaction with Bridges

"There are two types of MSE abutments, true and mixed. In a true MSE abutment the bridge load is placed directly on the MSE structure (See Figure 2.2). To prevent overstressing the soil of a true abutment, the beam seat is sized so the centerline of the bearing is at least 3 feet behind the MSE wall face and the bearing pressure on the reinforced soil is no more then four kips per square foot…A mixed abutment has piles or shafts supporting the bridge seat (See Figure 2.3), with the MSE walls retaining the fill beneath and adjacent to the end of the bridge. In some cases a portion of the lateral load on the pile-supported seat is transmitted to the MSE fill. This load can be resisted by MSE reinforcements in the wall or by reinforcements extending from the back wall of the seat." (Anderson, 2005)

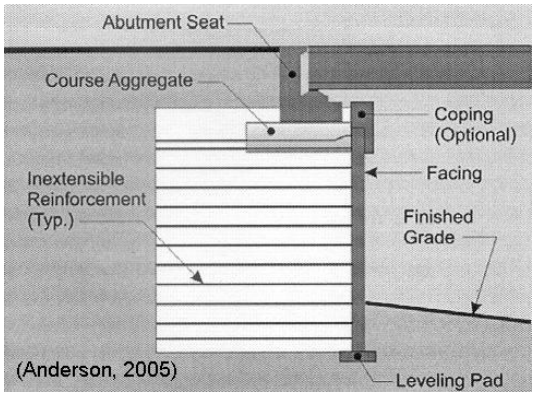

Figure 2.2 True MSE abutment.

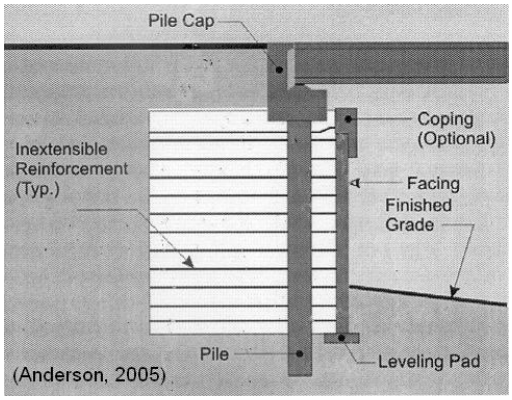

Figure 2.3 Mixed MSE abutment.

For FHWA funded projects the design should follow FHWA details on the use of integral abutments. There is no provision in the FHWA manual for shafts that are laterally supported within an MSE Wall.

Constructability tests were performed on piles driven through HDPE geogrid reinforced soil fill by Tensar International. A section of E-470 in Colorado contained several mixed abutment type bridges. It was found that driving piles as close as four feet from the facing caused no negative performance of the MSE structure. In addition to the pile driving investigation one of the shafts was laterally loaded using a D9 bulldozer. It was found that with three inches of pile movement only ¼" of facing movement occurred.

2.1.5 Lateral Loading of Facing and Retained Soil

Several tests were conducted to evaluate the lateral load behavior of foundation structures (shafts), such as those for electric poles, behind the reinforced zone as well as directly on top of the facing of a geosynthetic reinforced soil retaining wall with full height cast-in-place panels as the wall facing (Tamura, Y. et al., 1993 and Tateyama, M. et al., 1993). The results of these tests confirm significant lateral capacity of foundations associated with MSE structures (Figure 2.4 and 2.5). The highest capacity was found when the laterally loaded foundation was incorporated with the facing due to the very stiff nature of the tested wall facing (Figure 2.4). The facing was able to distribute the load to a wide area and the load was carried by the reinforcement. The tests with the laterally loaded shaft (2.3 ft diameter 8.2 ft length) located directly behind the reinforced zone indicate a higher strength than if the foundation was in level soil (Figure 2.5). This

is due to the confinement of the reinforcement and the tension membrane effect of the geogrid (Figure 2.6).

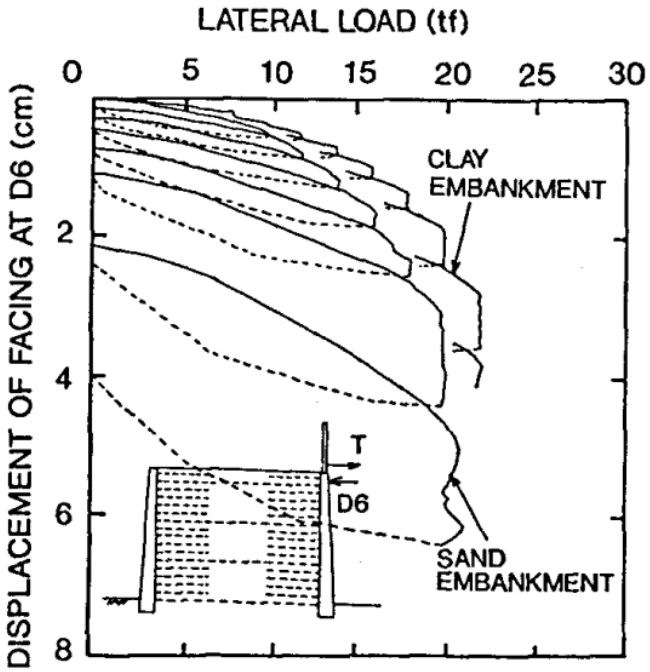

Figure 2.4 Lateral load response curves of the cast-in-place wall facing in sand and clay embankments (Yateyama, 1993).

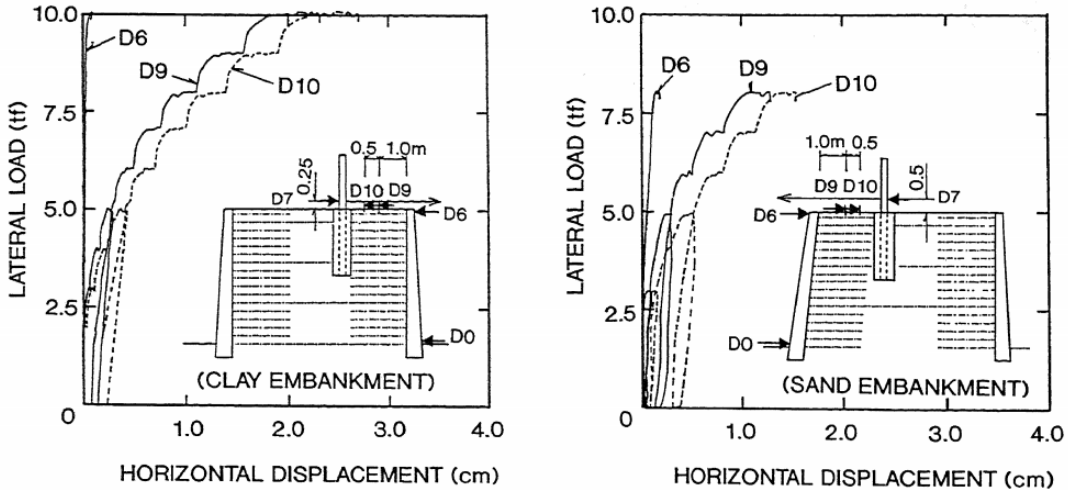

Figure 2.5 Lateral load response curves of shafts placed behind the reinforced zone in sand and clay embankments (Tamura, 1993).

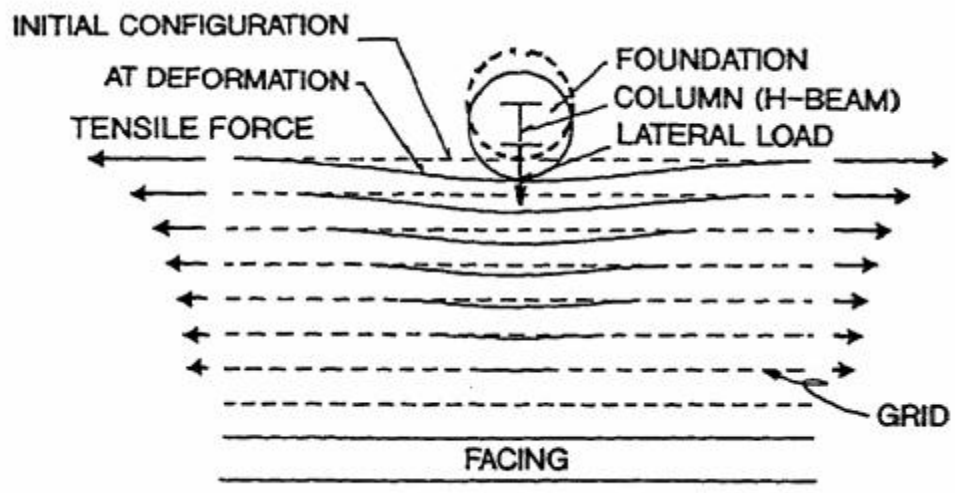

Figure 2.6 Schematic diagram illustrating the tensile behavior of the reinforcement parallel with the wall facing (Tamura, 1993).

2.1.6 Physical Test Results

In order to better understand the lateral load response characteristics of an MSE wall with cast-in-place shafts behind a modular block facing, the Kansas Department of Transportation partnered with The University of Kansas to develop a testing and analysis program of the system. This program consisted of full scale testing of the proposed system in six different configurations. Shafts were tested at four different distances from the back of the wall facing. Shafts were designated Shaft A, B, C, or D corresponding to the distance from the back of the wall facing to the center of the shaft (3, 6, 9, or 12 feet respectively) as seen in Figure 2.7. Additionally one shaft was constructed with the base at a shallower depth (Shaft B Short or BS) and three shafts were tested as a group (Shaft BG1, BG2, and BG3). Reaction shafts were anchored into the foundation limestone to counteract the resistance from the test shafts. These can be seen in Figure 2.7 as R1 through R5. Test sections were 15 feet in width. The next section contains a description of construction and instrumentation followed by testing and results. This information

was used for computer modeling of the system to expand on the results obtained from full scale testing. Additional analyses of test results beyond those published in Pierson 2008 were conducted as a part of this research and are presented in Chapter 3.

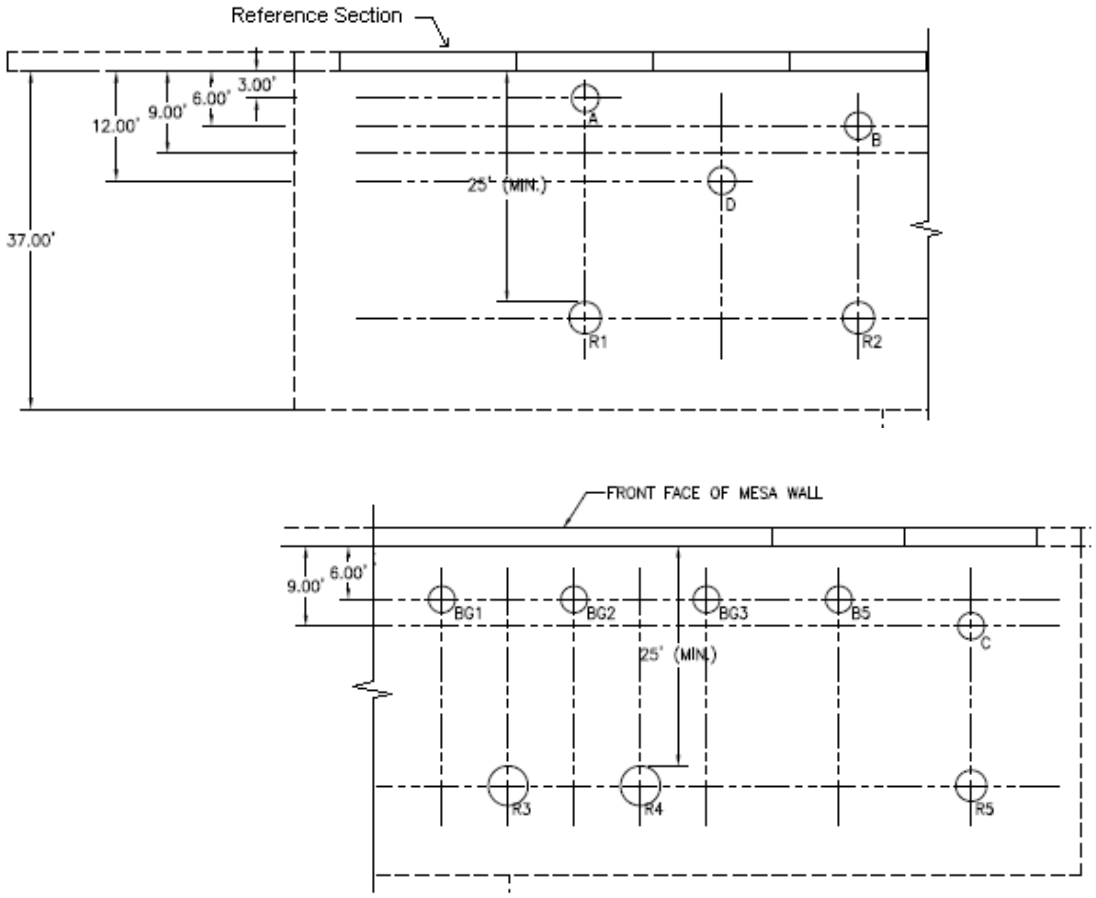

Figure 2.7 Plan view of MSE test wall and shafts (Tensar, 2007).

2.1.6.1 Construction and Instrumentation of Test Wall

This section describes the construction and instrumentation of the test wall as reported in Parsons et al. 2009b. The test site was located in Wyandotte County, Kansas, on the west side of the Kansas City metropolitan area (Figure 2.8). The soil was excavated to bedrock for a distance of 40ft behind the wall location to eliminate settlement and lateral pressures from the natural soils. The wall was designed and constructed in accordance with FHWA procedures (FHWA, 1997). Select design

drawings are shown in Figure 2.7, 2.8, and 2.9. At each shaft location a 36 in. diameter corrugated metal pipe (CMP) was placed to act as a form for the concrete and to prevent aggregate from entering the shaft area. The reinforcement layers consisted of uniaxial high density polyethylene geogrid with an ultimate tensile strength of 7,810 lb/ft for the lower reinforcement layers and an ultimate tensile strength of 4,800 lb/ft for the upper layers when tested in accordance with ASTM D 6637 (layers referred to as G1 and G2 in this paper). Reinforcement was spaced vertically every two feet of elevation. The lower four layers consisted of G1 and the upper six layers consisted of G2. The geogrid was cut to fit around the CMP as shown in Figure 2.11. Backfill material consisted of a clean crushed limestone rock whose specifications were established by KDOT as CA-5. The CA-5 used in the project had a peak friction angle of 51° based on large diameter triaxial cell testing for confining stresses within the range of the wall (5 – 20 psi). An eight inch low permeability cover was placed above the aggregate fill. Vertical slip joints were located in between test sections in an attempt to isolate the test sections from each other. For each slip joint the geogrid and facing blocks were cut such that forces could only be transmitted across the slip joint through aggregate interlock.

After the wall was constructed, the steel reinforcement cages were lowered into the CMP forms. The cages consisted of 12 evenly spaced #11 bars for longitudinal reinforcement and #5 hoops for transverse reinforcement spaced every six inches for the first three feet and every twelve inches for the remainder. High (9 in.) slump concrete was poured having an average compressive strength of 6,500 psi.

A) 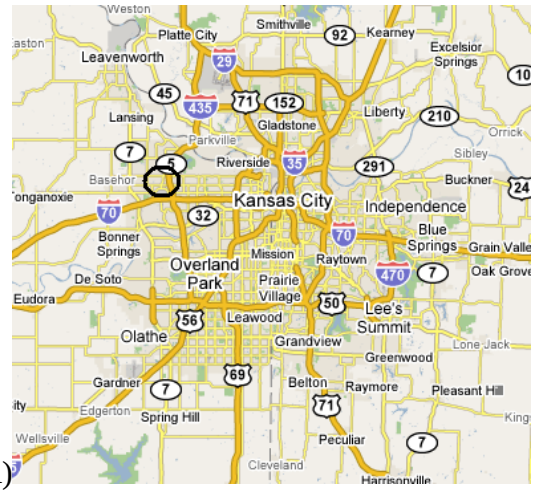

B) 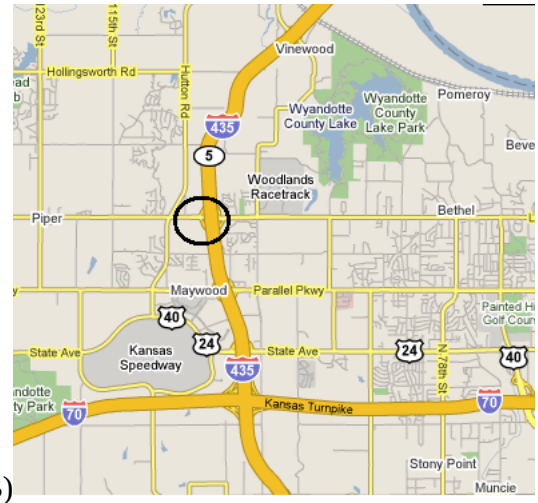

C) 

Figure 2.8 A) Regional map, B) Local map, C) Site map (Google 2008).

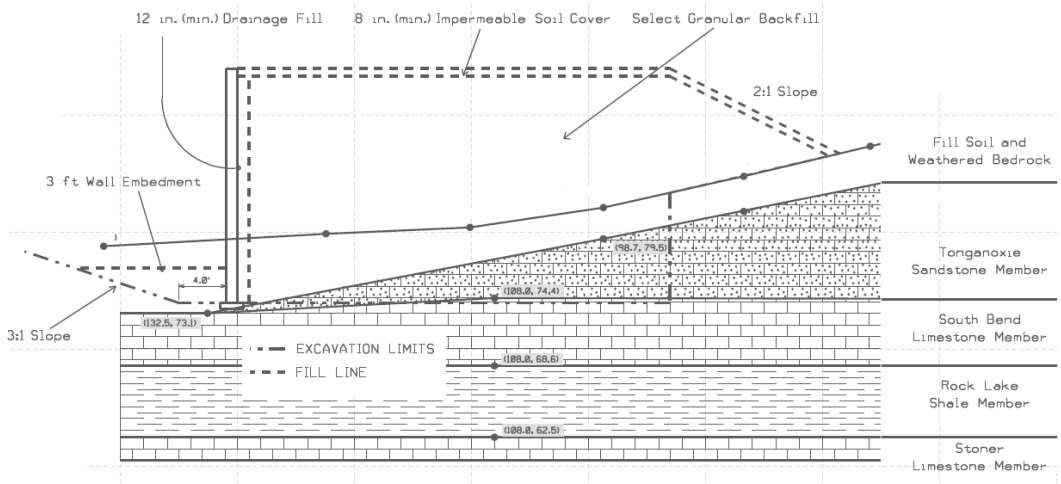

Figure 2.9 Proposed cross section of MSE wall and subsurface (Provided by KDOT).

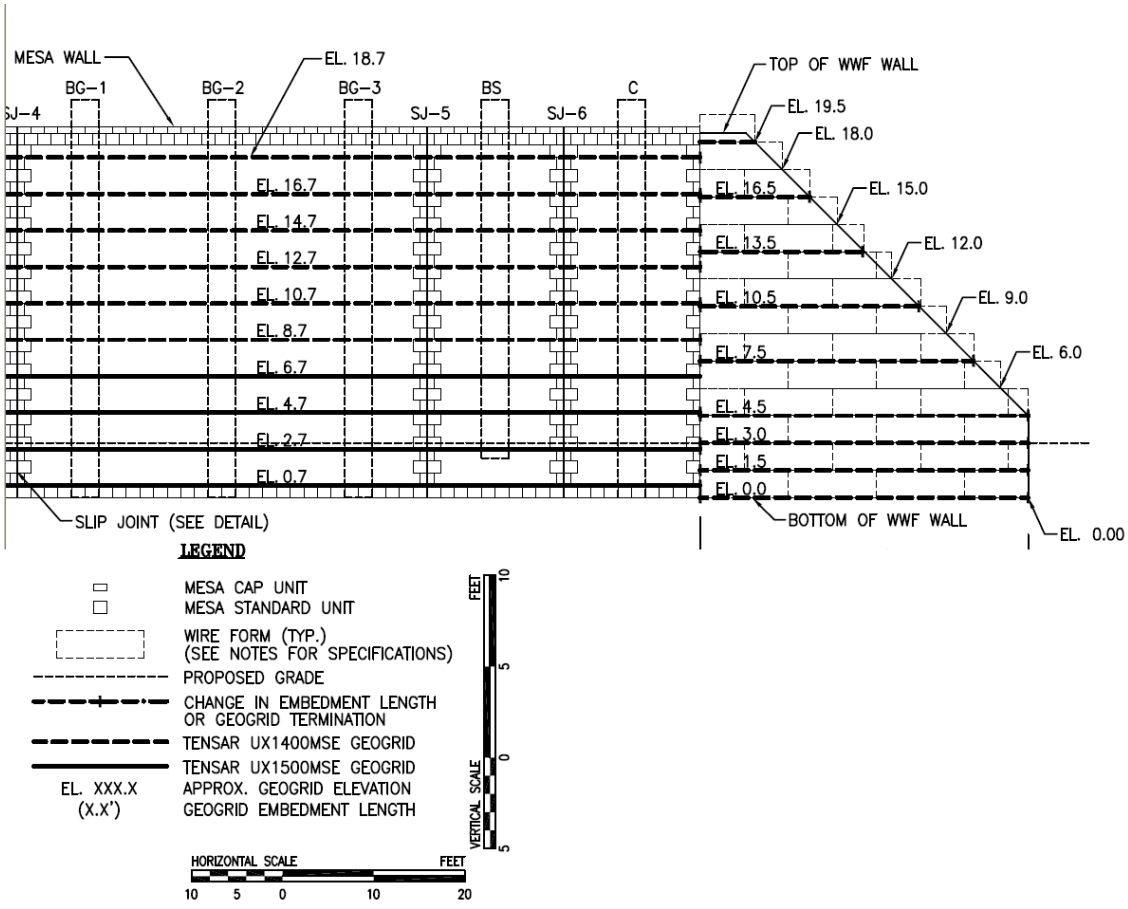

Figure 2.10 Wall facing layout (Provided by Tensar).

Figure 2.11 Cut geogrid around CMP metal forms.

Instrumentation consisted of three systems. Monitoring of the top of shaft was done using five LVDTs, a hydraulic pressure gage, and a load cell attached to a data acquisition system (Figure 2.12). Each test shaft and reaction shaft had two LVDTs attached and the hydraulic ram also had an LVDT to serve as a check of the shaft LVDTs. The hydraulic pressure gage served as a check for the load cell. Inclinometers were used as a second check of the LVDTs and to determine the magnitude of any of shaft bending. A second data acquisition system was used to monitor performance of the MSE wall using earth pressure cells and strain gages. Movements of tell tales installed within the fill and attached to the geogrid, as well as targets attached to the wall facing, were monitored using a digital camera and a photogrammetric process. Additional details on construction and instrumentation are located in Pierson et al. (2008 and 2009a).

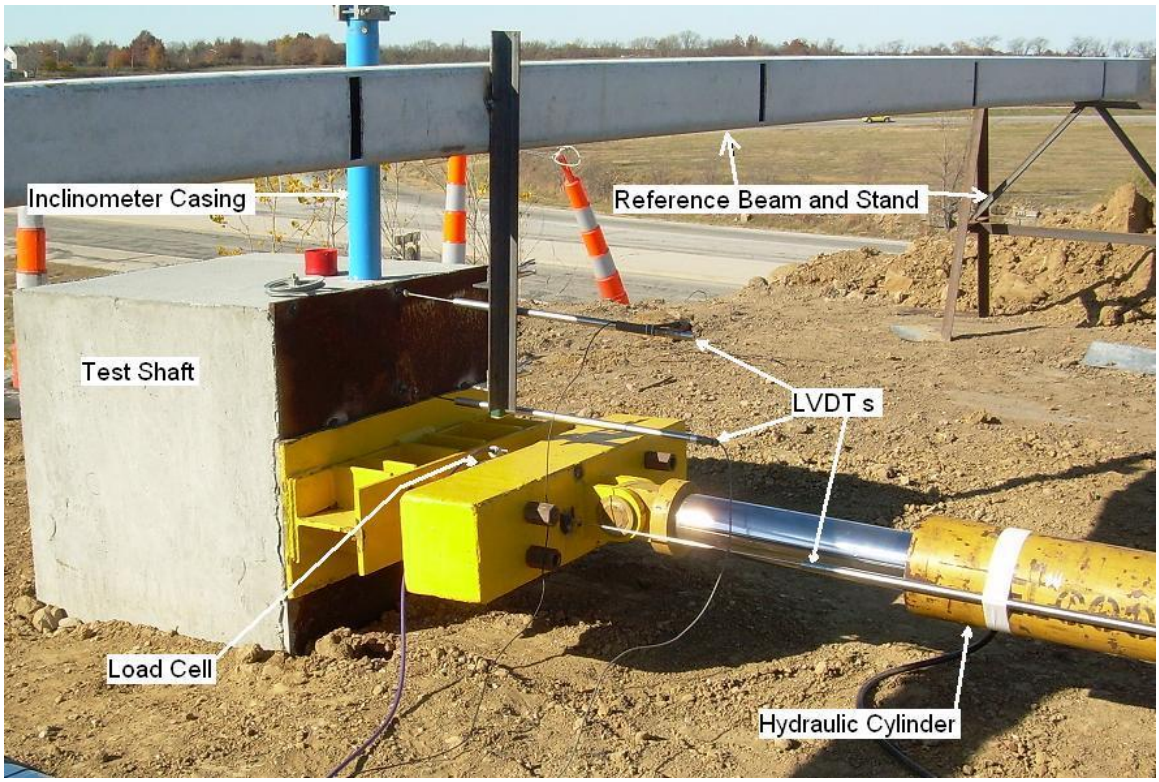

Figure 2.12 Typical test setup for single shafts.

2.1.6.2 Physical Testing and Results

Shaft Load Response

A schematic of shaft loading can be seen in Figure 2.13. Hydraulic fluid was pumped into the hydraulic cylinder until a specified deflection is reached and then movement is halted by closing the hydraulic valves (Figure 2.14). During the holding time the measured load at the shaft top decreased as the MSE – shaft system adjusted to the new loading conditions. Therefore three load values were reported corresponding to the initial peak load, load at 2.5 minutes after the peak load and the final load at the end of the holding period. This approach refined the data from Figure 2.14 to produce the load response curve in Figure 2.15 which is typical of all test results. Table 2.1 shows the tabulated results from all shaft testing. For additional information about initial physical results see Pierson et al. 2008.

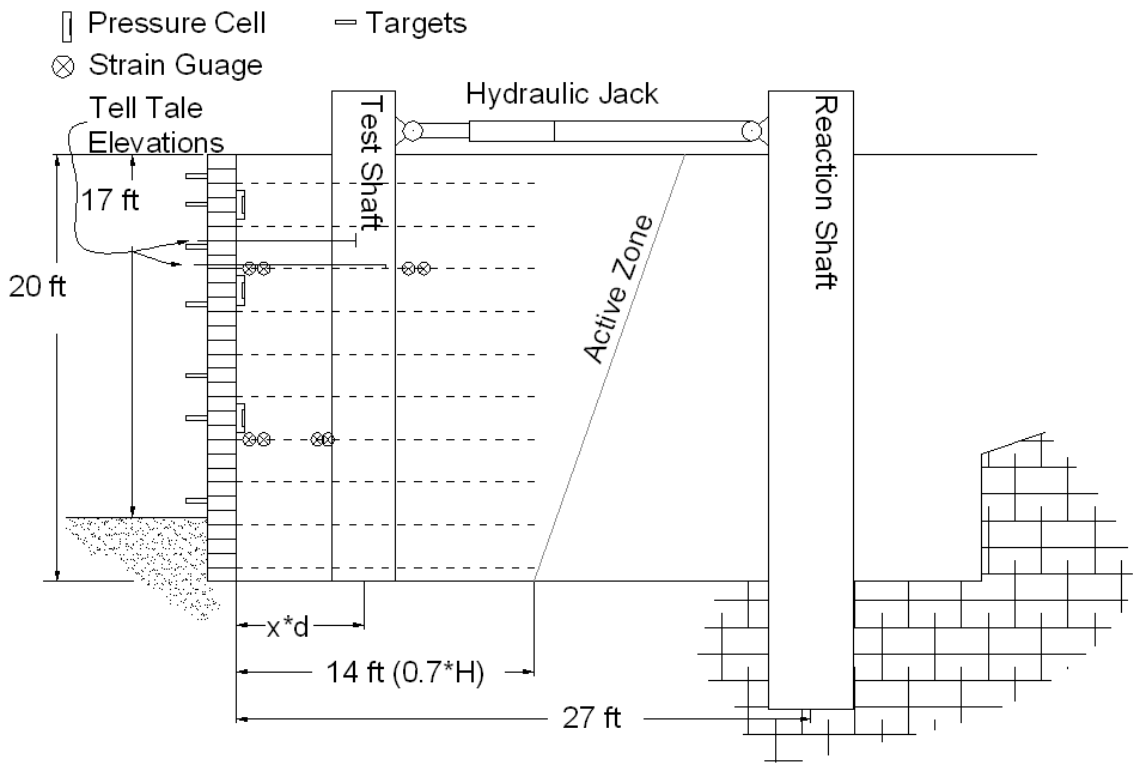

Figure 2.13 Typical cross section of MSE – shaft system with loading apparatus and instrumentation. d is the diameter of the shaft (3 ft) and x is 1, 2, 3, or 4 depending on test section.

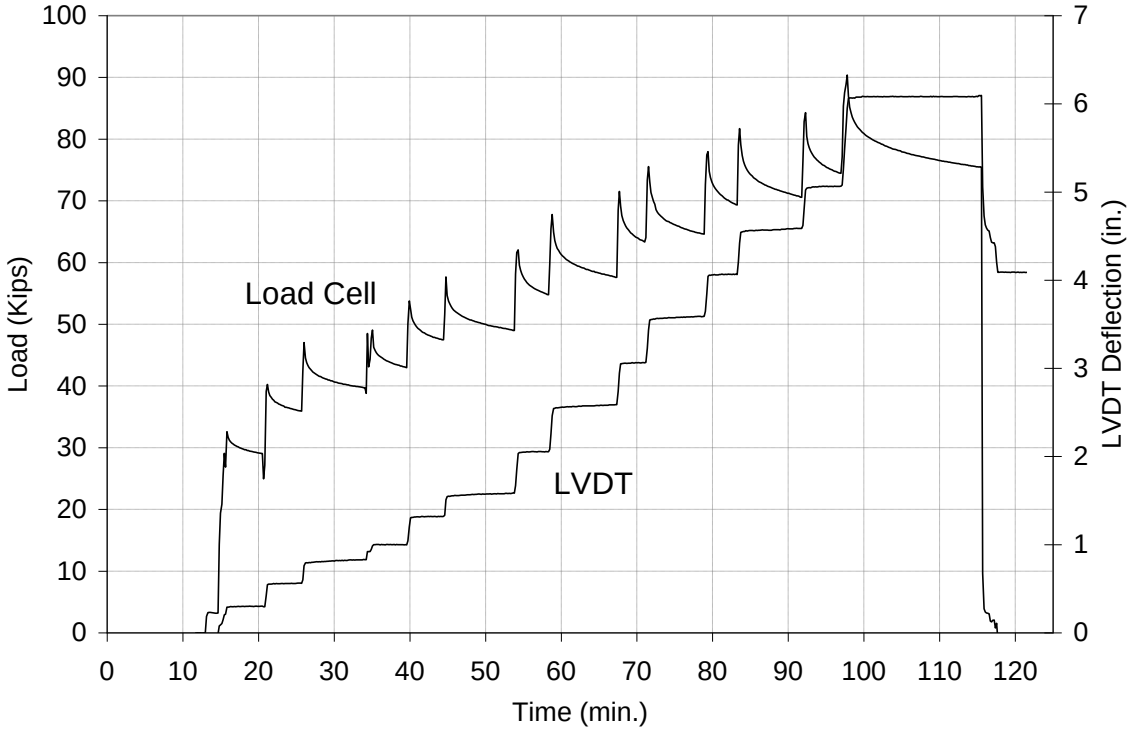

Figure 2.14 Shaft B load and deflection vs. time. Typical of all test results.

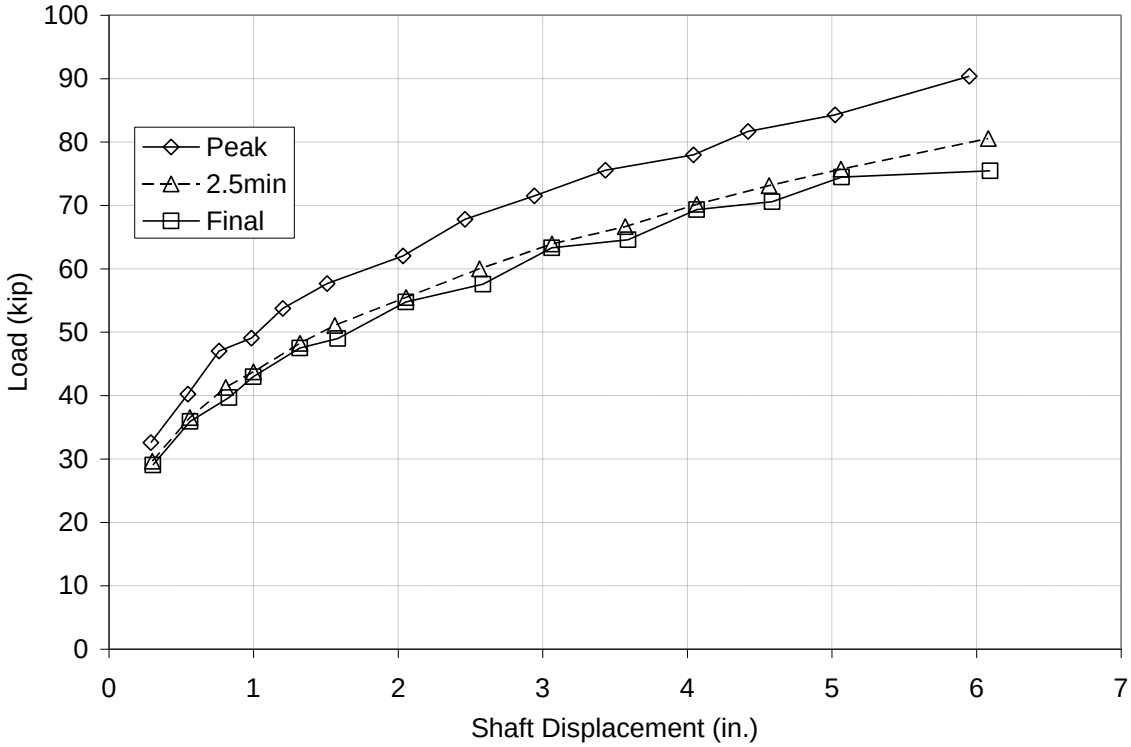

Figure 2.15 Shaft B peak, 2.5 minute, and final load vs. deflection.

Table 2.1 Load versus shaft displacement summary table.

Shaft	Dist. From Facing (in.)	Peak Load (kip)					
Displacement		0.5"	0.75"	1"	2"	4"	Ultimate
A	36	-	14	15	23	32	34
BS	72 (15' Length)	27	30	33	40	49	55
BG2	72 (15’ Spacing)	27	35	39	53	70	85
B	72	40	47	50	62	77	90
C	108	39	44	50	66	87	116
D	144	-	-	55	81	120	194
		Residual Load (kip)					
A	36	5.3	5.3	8	17	27	27
BS	72 (15' Length)	24	26	28	35	41	47
BG2	72 (15’ Spacing)	25	28	30	43	58	75
B	72	36	40	44	55	69	75
C	108	34	39	44	58	76	102
D	144	-	-	50	74	110	171

MSE Wall Response

Wall facing displacement was measured using the photogrammetric technique described in Pierson (2009a). Measurement points were located at an

elevation of 17.7 feet in a horizontal line on the wall facing and in a vertical line directly in front of the shaft (Figure 2.16). Results are presented as cross-sections or plan views with sequential movement shown corresponding to various shaft movement (Figure 2.17 and 2.18). Table 2.2 shows the tabulated results of load versus maximum wall facing displacement. Additional results are presented in Pierson et al. (2008, 2009b) and Parsons et al. (2009a).

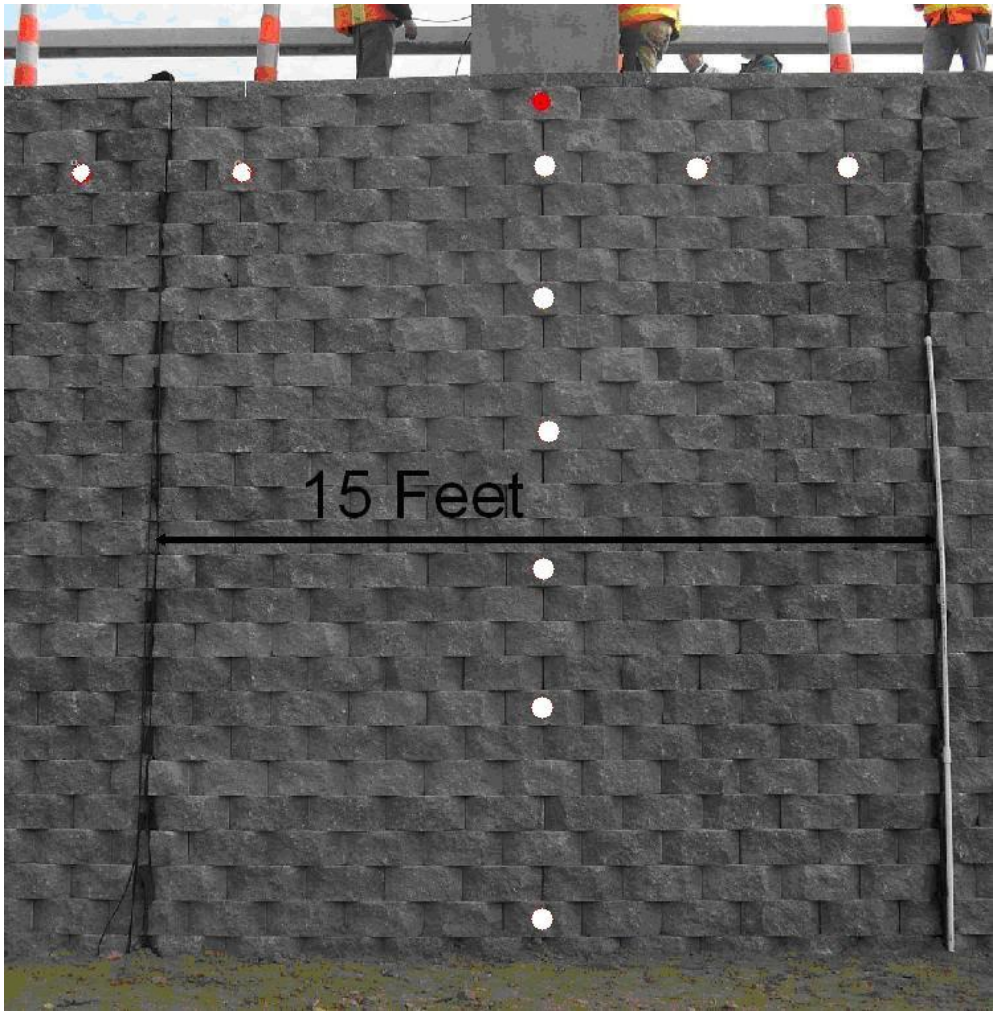

Figure 2.16 White dots indicate measurement location. The row of horizontal measurements is at an elevation of 17.7 ft. The test section width was 15 feet. The cut blocks at the edge of the test section are for the slip joint.

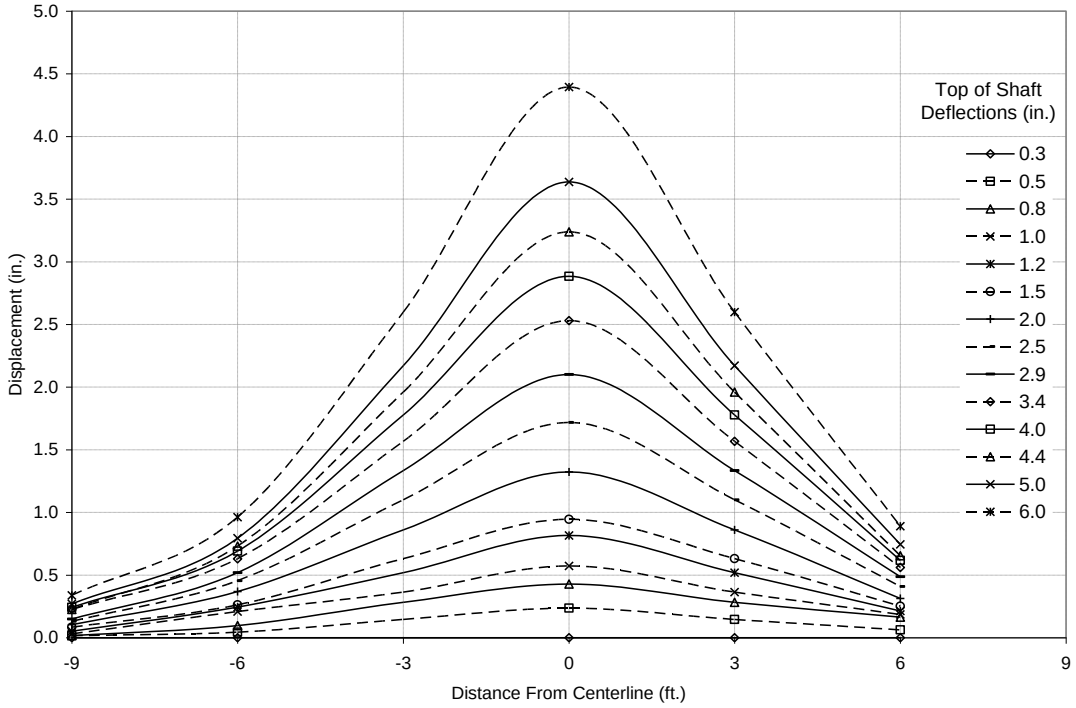

Figure 2.17 Plan view of wall facing displacement at elevation 17.7 ft. (Pierson et al. 2008).

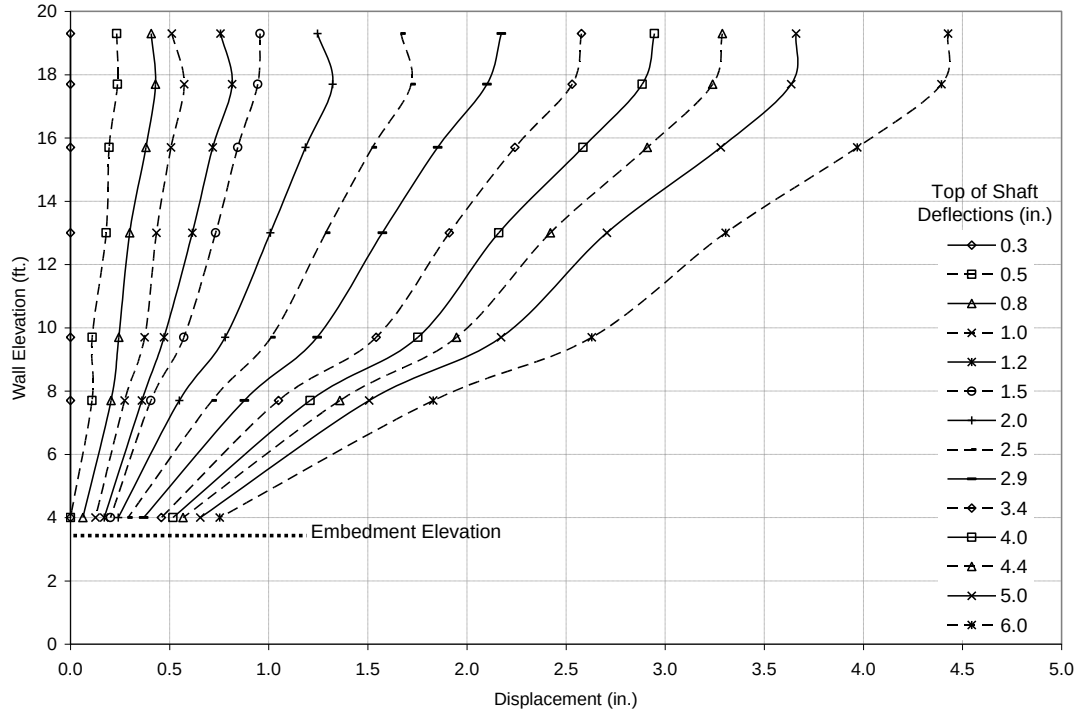

Figure 2.18 Cross-section of wall facing displacement in front of the shaft. (Pierson et al. 2008).

Table 2.2 Load versus maximum wall facing displacement summary table.

Shaft	Dist. From Facing (in.)	Peak Load (kip)					
Maximum Wall Deflection		0.5"	0.75"	1"	2"	4"	Ultimate
A	36	12	15	18	26	33	33
BG2	72 (15’ Spacing)	40	45	50	62	78	85
B	72	48	54	58	70	87	90
C	108	50	55	60	80	98	116
D	144	77	88	99	134	182	194
Shaft	Dist. From Facing (in.)	Residual Load (kip)					
A	36	8	10	15	22	-	27
BS	72 (15' Length)	24	29	31	37	46	47
BG2	72 (15’ Spacing)	34	37	41	43	41	46
B	72	43	48	50	61	75	76
C	108	43	49	52	69	90	102
D	144	78	82	90	122	166	171

2.2 Numerical Approaches

2.2.1 Introduction

Due to the limited published data available, a numerical modeling approach has been adopted to expand the understanding of the behavior of the MSE-Shaft system without the cost of additional field tests. The three dimensional aspect of the project causes the model to be quite complex compared to other published attempts at modeling MSE structures. As a result this will be the first numerical model known to model an MSE structure in 3 dimensions. Several published 2D modeling efforts will be presented here and then several aspects of each will be compared.

Several examples of numerical modeling to simulate the behavior of MSE walls were found. The Royal Military College of Canada has a very well instrumented series of full scale MSE block walls 11 feet in height which were monitored during construction and during surcharge loading. The results from those tests were used to calibrate the commercially available finite difference software FLAC (Itasca Consulting Group 2001). More information on this study can be found in Hatami and Bathurst (2005 and 2006),

Huang et al. (2009), and Karapurapu and Bathurst (1995). A case history of a failed retaining wall from Korea was modeled accounting for rainfall and agreed well with field data (Yoo, C. Jung, H 2006). In Japan the Public Works Research Institute (PWRI) constructed a well instrumented 20 ft tall MSE wall. These test results were then compared with results from a 2D model using different constitutive soil models (Ling, H. I., Liu, H., 2009; Ling, H. I., et al., 2000). A purely numerical study was conducted on a two tiered wall configuration by Yoo and Jeon in 2004. In this study the effect of wall offset and reinforcement length in the lower wall were evaluated.

Additional modeling research has been published, including modeling of an MSE wall along with other materials such as compressible foundation material or the structural elements of a mixed use bridge abutment. As a part of the I-15 National Test Bed, a 30 ft tall MSE wall over compressible material was instrumented during construction. The results were used to calibrate a commercially available finite element model called Plaxis (Bay et al. 2004, Budge et al. 2006). Another example of 2D numerical modeling was used during design of an expansion of Virginia Route 288 around Richmond. The design-build team chose to use tall MSE abutments rather than additional bridge spans saving an estimated $1 million in construction costs (Farouz et al. 2004). To evaluate the performance of MSE abutments the National Cooperative Highway Research Program (NCHRP) conducted the "NCHRP Experiment." In this experiment a 15 ft tall MSE wall was constructed and a localized load was applied at the top of the wall near the facing to simulate the "sill" which would support a bridge (Helwany et at. 2007). This research concluded that an MSE wall could effectively support a bridge and numerical modeling results agreed well with measured results.

2.2.2 Composite vs. Discrete

The wide range of approaches to numerical modeling can be divided into two categories. These range from a simplistic composite approach to a rigorous model using discrete components such as interfaces, structural elements, and advanced soil models. With increasing accuracy typically comes increased computing time and additional variables. The use of various approaches will be discussed and directly compared when possible.

A composite model groups together all of the properties of the soil, reinforcement, and facing. This is done to reduce computing time and simplify the problem. This simplified composite approach has been shown to compare well with a discrete approach (Shen et al. 1976). For MSE wall modeling a composite model would consist of a reinforced fill, retained fill, and any boundary conditions or foundation material.

With advances in modern computing power the discrete approach has taken over as the dominant method. A discrete model of an MSE structure would include separate elements and behavior for the soil, reinforcement, facing, and foundation. It may include interfaces at the base, sides and back of modular blocks, material boundaries, or structural elements. The discrete method will be used for this project.

2.2.3 Soil Model

Several soil models are appropriate for use in granular material and some are directly compared in 2D finite difference simulations. The two most popular soil models used in 2D simulations are the Duncan-Chang hyperbolic model (Duncan et al. 1980) and the linear elastic-plastic Mohr-Coulomb model. A comparison of the stress strain

behavior of both models and the triaxial data of the material used in the current study is shown in Figure 2.19.

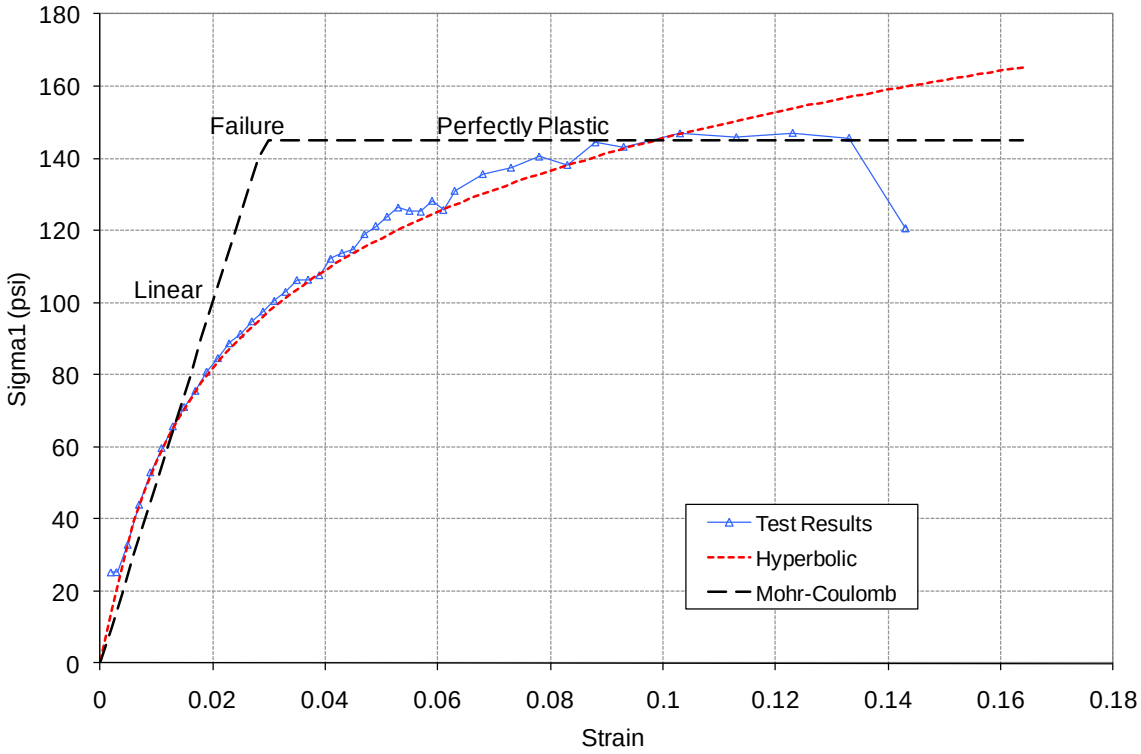

Figure 2.19 Comparison of triaxial test results with the Duncan-Chang and Mohr-Coulomb soil models.

In the Mohr-Coulomb model soil behaves as a linear elastic material below failure, and at the failure point transitions to a perfectly plastic material. Failure is determined from Coulomb failure criterion for frictional materials. The slope (stiffness of the material) of the linear elastic portion of the stress strain relationship is fixed for all confining stresses. Limitations of the Mohr-Coulomb model are that only the maximum and minimum confining pressures are considered and non-linear soil behavior, such as strain softening, is not captured (Huang et al. 2009).

The Duncan-Chang hyperbolic model is a nonlinear elastic soil model with a hyperbolic stress-strain function. During each computation cycle a new elastic tangent

modulus is calculated for each grid-point depending on stress and strain. Therefore this is a stress dependent model which gives different soil stiffness depending on confining stress. Limitations of the Duncan-Chang model are post peak strain softening is not captured, shear dilatancy is not considered, and failure of the soil is not modeled realistically (Huang et al., 2009).

Research by Huang et al. showed excellent agreement with test results for both the Duncan-Chang and Mohr-Coulomb models (Figure 2.20, 2.21). Ling and Liu 2009 demonstrated similar agreement with test results when comparing the Duncan-Chang and a generalized plasticity (Ling and Liu, 2003) soil model (Figure 2.22).

Additional factors can affect selection of a soil model. A commonly recognized limitation of the hyperbolic model is its inability to capture the plastic soil behavior at high stress levels, especially at failure (Ling and Liu, 2009). Also, the Duncan-Chang model was originally developed for modeling two dimensional problems. Duncan-Chang has been modified by Boscardin et al. (1989) to create a "true" tangent modulus. This was then expanded to three dimensions by Rodriguez-Roa (2000) and shown to be successful (Yang, 2010) but has not been widely demonstrated. Additionally, because the tangential modulus of the material must be calculated every cycle in the hyperbolic model it required additional computational time.

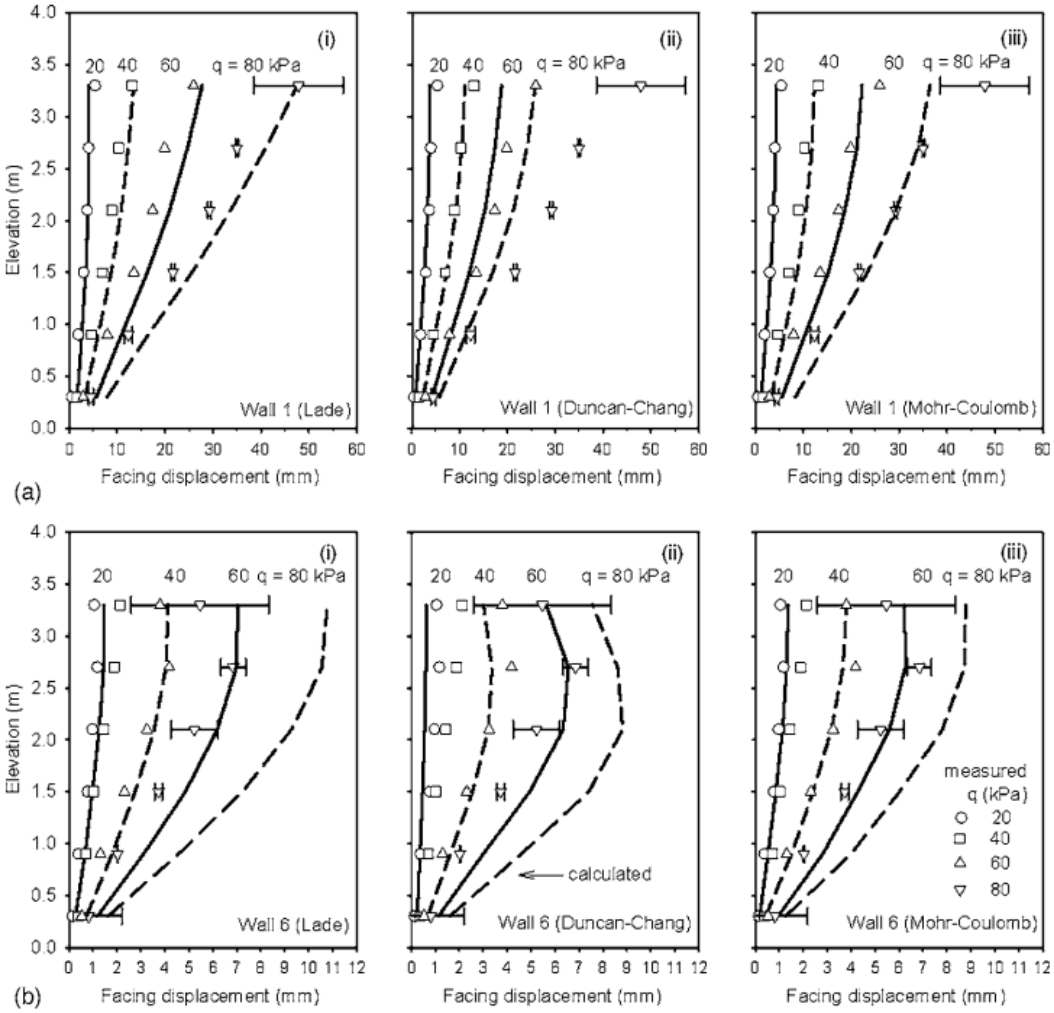

Figure 2.20 Measured and calculated post construction facing deformation (Huang et al. 2009).

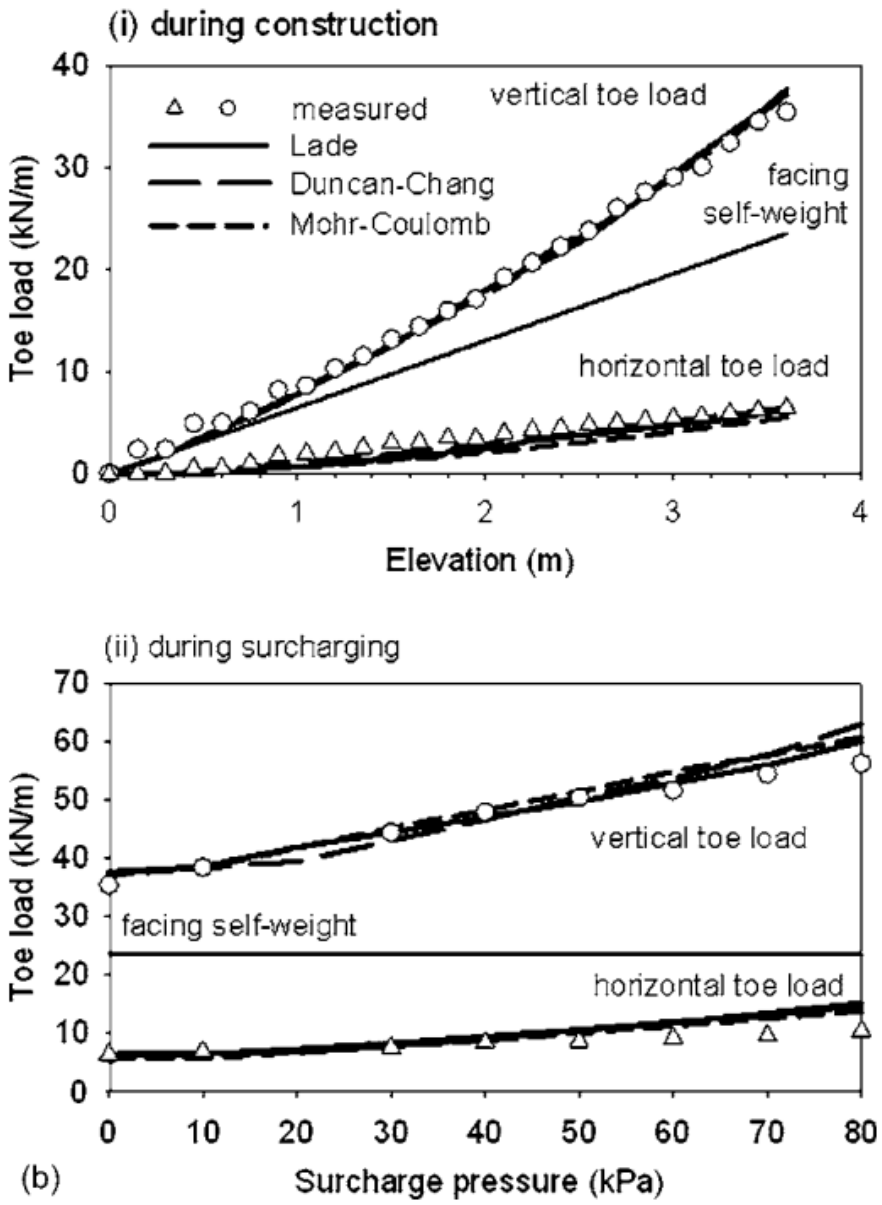

Figure 2.21 Measured and calculated vertical and horizontal loads at the toe or base of the wall facing (Huang et al. 2009).

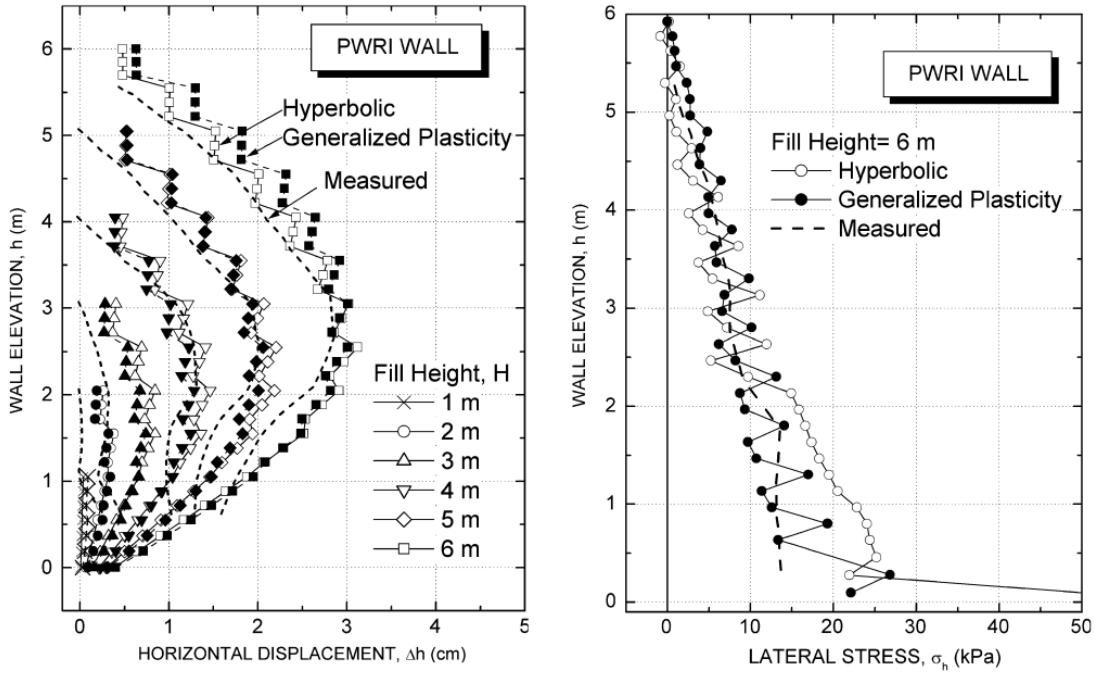

Figure 2.22 Comparison of horizontal displacement and lateral stress at the wall facing (Ling and Liu 2009).

2.2.4 Geosynthetic Model

The stress strain behavior of the geosynthetic reinforcement in the computer simulation is represented by an appropriate model. Possible models include linear elastic, nonlinear, and time dependant creep. Accepted practice for 2D models is to use a nonlinear hyperbolic stress strain model such as the one proposed by Ling and Liu (2009). Ling and Liu show agreement between model and experimental results (Figure 2.23). However, upon inspection it can be seen that a linear approximation is reasonable for the elastic portion of the stress strain curve, especially at lower strain values. The same pseudo-linear behavior has been found in the geogrid (UX1400) used on the current project (Figure 2.24).

Another material behavior of high density polyethylene (HDPE), which was used in the current study, is that its stiffness depends on the loading rate (personal communication with Dr. Jie Han). Some work has been done modeling the creep

function of geosynthetics (Lopes et al. 1994). This work compared a 2D numerical model using a constant stiffness and a variable stiffness with the measured performance of a reinforced soil slope (Figure 2.24). In some cases the fixed stiffness model matched the experimental model better than the creep model, but generally the creep model was more appropriate.

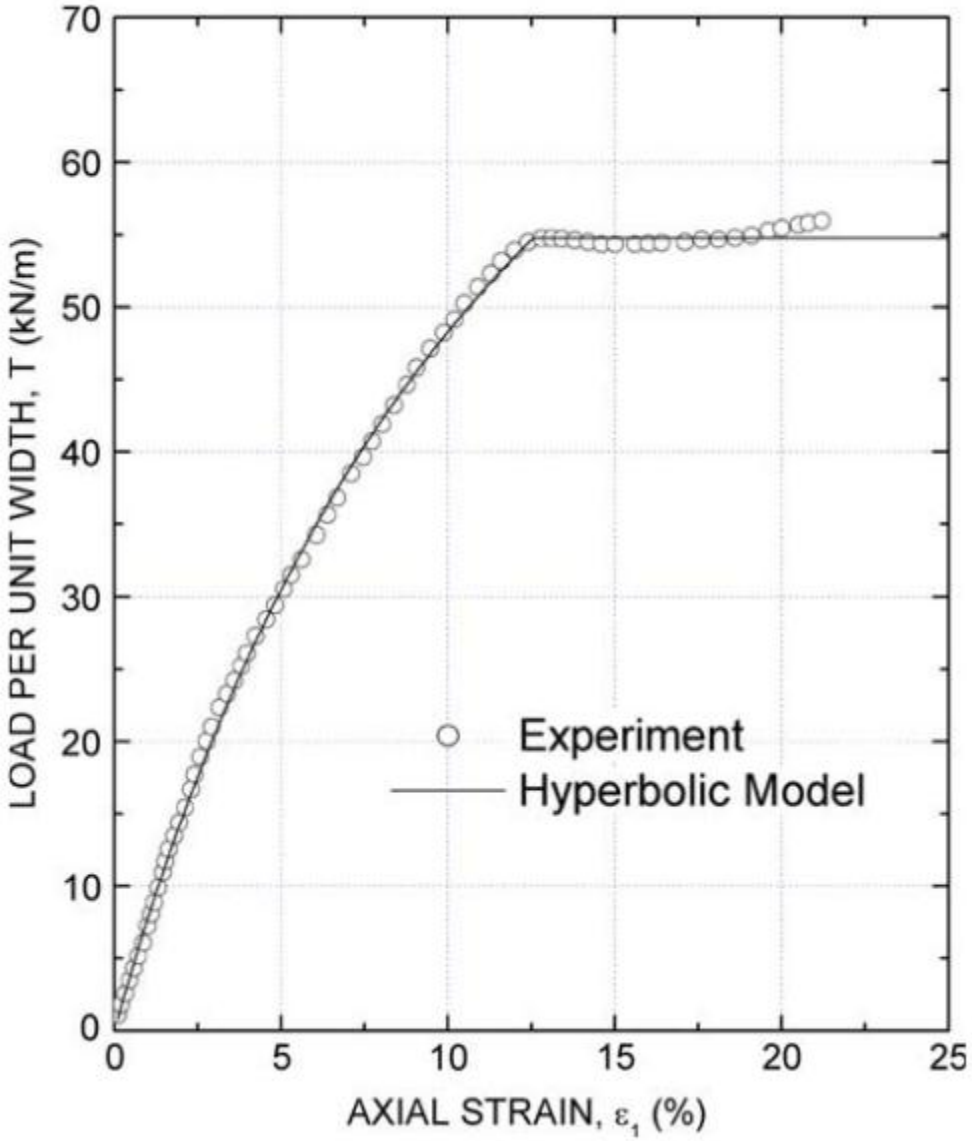

Figure 2.23 Comparison of geogrid experimental and model results after calibration (Ling and Liu 2009).

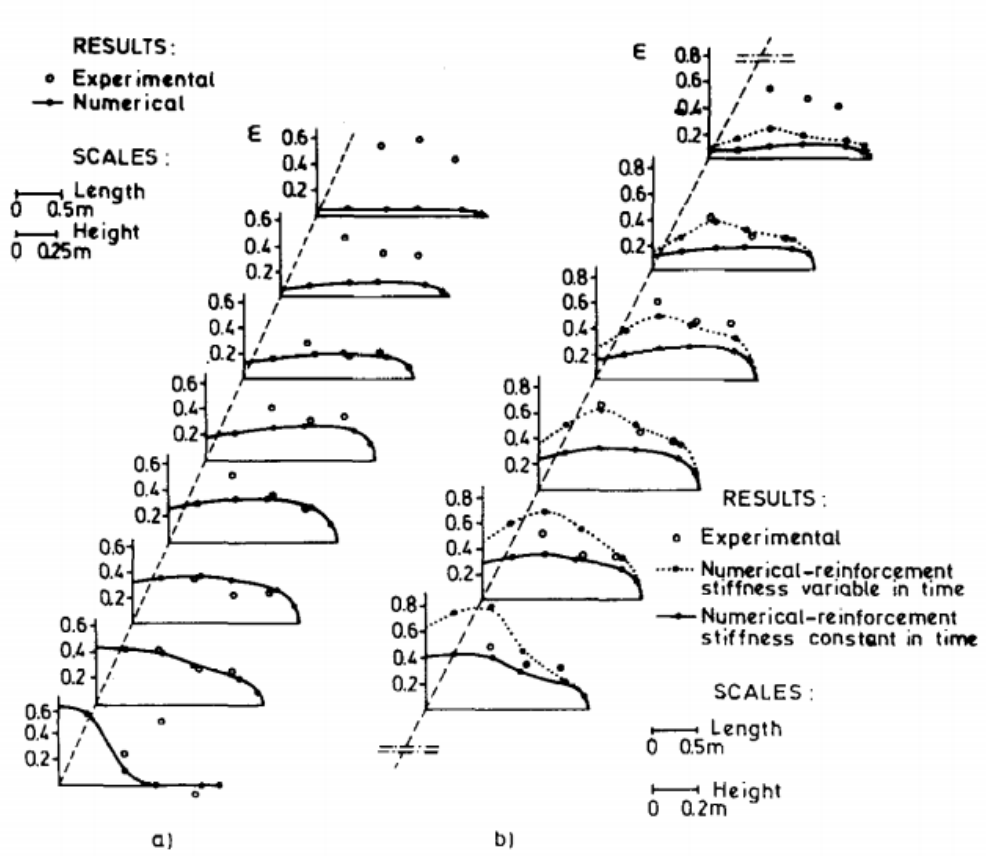

Figure 2.24 Experimental and numerical values: a) at the end of construction b) 4 weeks later (Lopes and Cardoso 1994).

2.2.5 Interface and Boundary Conditions

It is appropriate to place an interface to govern behavior at each location in the computer model where two materials interact. Also, boundary conditions exist at the edges of the model or where loads are placed. Use of the appropriate interface model and boundary conditions are crucial to accurate model behavior. Interface properties typically include normal and shear stiffness and often have a failure criterion. The stiffness maybe either fixed or variable (non-linear behavior).

In traditional 2D models the interaction of the geogrid and the soil is governed by an interface with linear elastic stiffness and Mohr-Coulomb failure criteria. The geogrid may be slaved to the soil if relative movement was not expected between the

reinforcement and the soil the geogrid. Hatami and Bathurst and others have slaved the geogrid to the soil in several models. This is due to the relatively small total displacements as well as post test inspection of exhumed geogrid sections. The accepted method for modeling other interfaces is using Mohr-Coulomb with a fixed stiffness and a friction angle to determine failure in shear.

Boundary conditions are used to govern the behavior of the model at the edges. When loading the boundaries it is possible to apply a velocity or a force to individual grid points. Applying a velocity is analogous to displacement control of a physical test and applying a force is analogous to load control. At other "non-loading" model edges two reasonable possibilities exist, either fixed stress or fixed displacement. Both represent reasonable conditions however it is suggested to place the boundaries of the model far enough away from areas of interest to prevent edge effects of the boundaries from impacting results from areas of primary interest.

2.2.6 Predictive Model of Physical Test

Numerical modeling of the physical testing described in section 2.1 began before field testing with a predictive model (Huang et al. 2010). The Huang model consisted of a continuous composite facing, discrete geogrid sheets, shaft, foundation, backfill soil, and embedment soil. The continuous composite facing was used to simplify the problem by eliminating the need to model the facing as individual blocks. After completion of physical testing the properties of the predictive model were changed to better capture the behavior of the system. The properties used in these two models can be found in Table 2.3.

Results from the predictive modeling and the post test modeling show the capability of the 3D numerical modeling technique to capture the overall response (Figures 2.25, 2.26, and 2.27). With the less advanced composite facing, strains measured in the geogrid as well as wall facing movement agree with the physical results.

Table 2.3 Material Properties Used for Predictive Model.

Material	Constitutive Model	Properties
Backfill Soil	Mohr-Coulomb	E = 835 ksf ν = 0.3 φ' = 34° c'=0 γ = 115 pcf
Retained Soil	Mohr-Coulomb	E = 418 ksf ν = 0.3 φ' = 30° c'=0 γ = 115 pcf
Grade Soil	Mohr-Coulomb	E = 418 ksf ν = 0.3 φ' = 30° c'=0 γ = 115 pcf
Foundation Soil	Elastic	E = 4,351 ksi ν = 0.3 γ = 115 pcf
Drilled Shaft	Elastic (Isotropic)	E = 4,351 ksi ν = 0.3 γ = 153 pcf
MSE Wall Facing	Elastic (Isotropic)	E = 43.5 ksi ν = 0.3 γ = 95 pcf
UX1	Elastic (Orthogonal)	J_{md} = 42.5 kip/ft J_{tr} = 4.25 kip/ft C_i = 0.8 ks = 0.11 ksi/in.
UX2	Elastic (Orthogonal)	J_{md} = 71 kip/ft J_{tr} = 7.1 kip/ft C_i = 0.8 ks = 0.19 ksi/in.
UX3	Elastic (Orthogonal)	J_{md} = 130 kip/ft J_{tr} = 13.0 kip/ft C_i = 0.8 ks = 0.35 ksi/in.
Interface Between Drilled Shaft and Backfill	Coulomb Sliding	φ' = 30° c'=0 γ = 115 pcf ks=0.06 kn=0.12

(Huang et al. 2010)

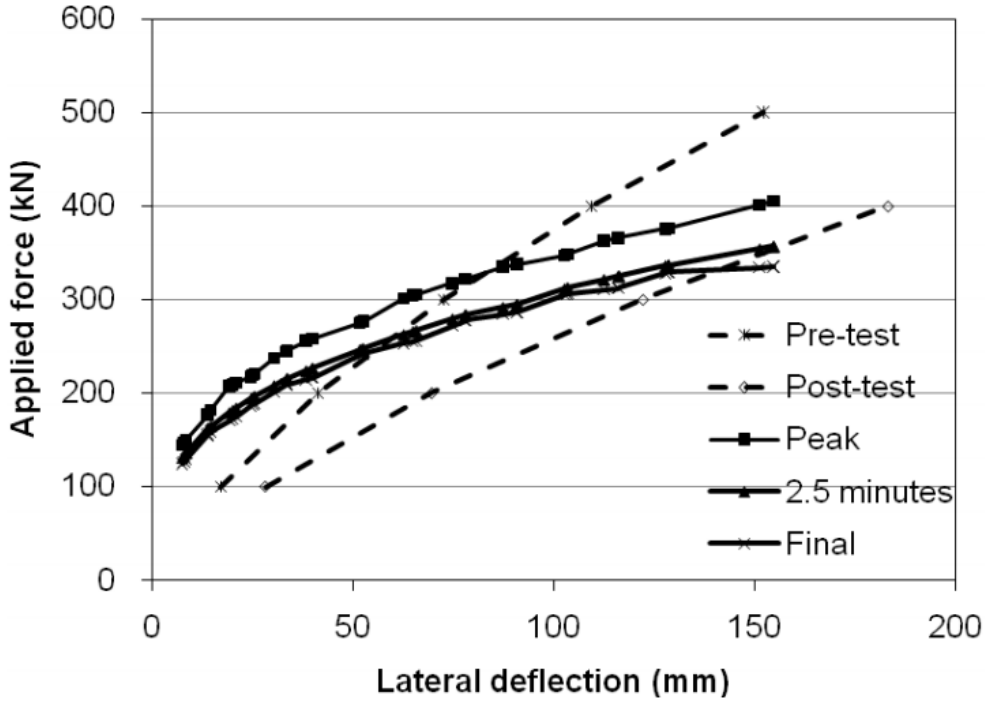

Figure 2.25 Load response curves of Shaft B and the pre and post test model results (Huang et al. 2010).

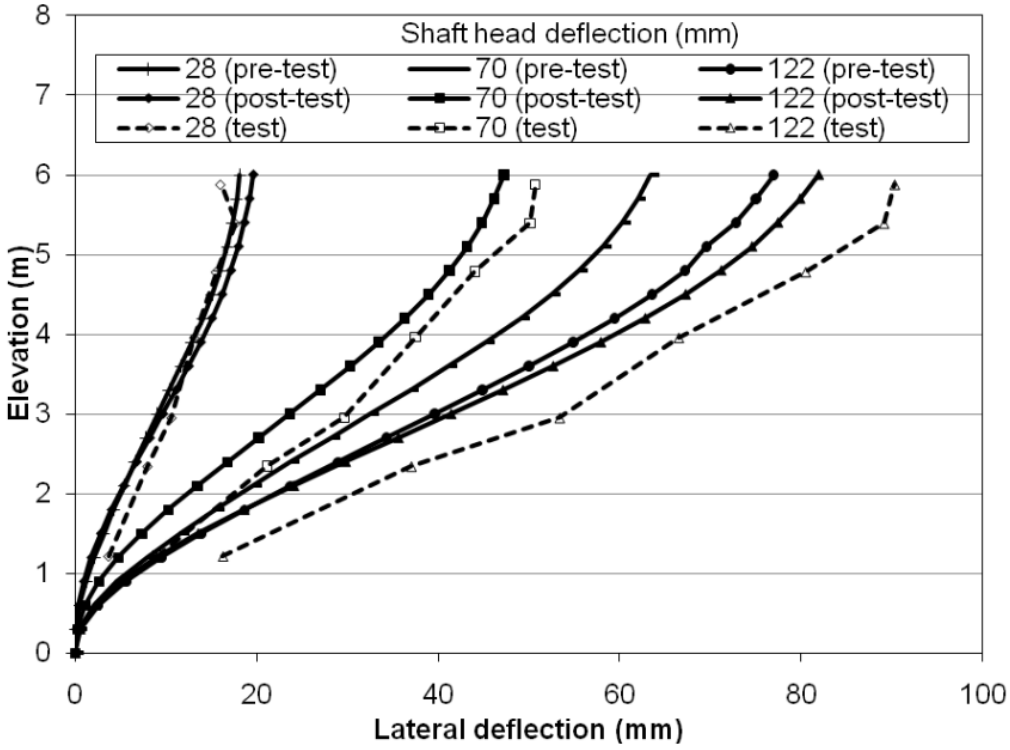

Figure 2.26 Wall facing displacement directly in front of Shaft B (Huang et al. 2010).

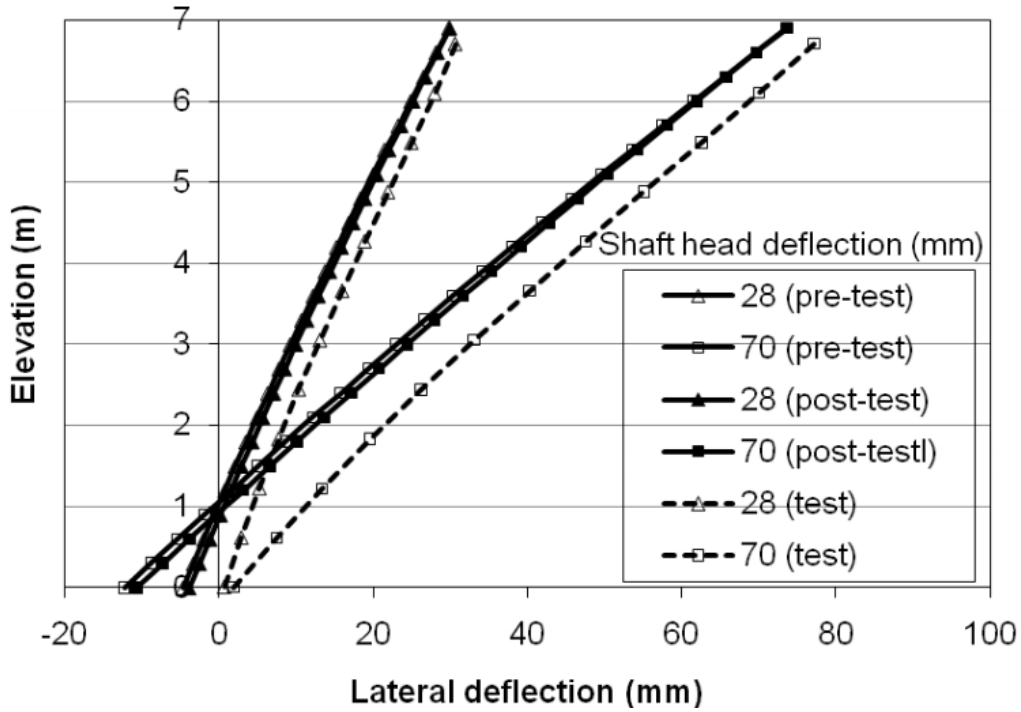

Figure 2.27 Shaft Displacement (Huang et al. 2010).

CHAPER THREE

Additional Analysis of Physical Test Results

Chapter three contains additional results from physical testing of the full scale wall facing, and results of additional material testing conducted after the summer of 2008.

3.1 Tell-Tales: Movement Within Fill

Lateral movement within the fill was measured with tell-tales attached to the geogrid or installed within the aggregate. The photogrammetric image analysis technique was used to gather the data during the test. Results from this information will be used to calibrate and verify the behavior of future numerical modeling.

Due to the design of the tell-tales, which utilize an inner and outer shaft, two measurements were taken. The inner movement measured represents the movement of only the location indicated. The movement of the outer shaft indicates the overall movement along the entire shaft from the location indicated to the wall facing. Therefore, the outer measurement is an indication of qualitative behavior only. All tell-tales attached to the geogrid were installed at elevation 14.7 ft. All tell-tales embedded within the fill are at elevation 16 ft. Figures 3.1, 3.2, and 3.3 show the location and movements of the tell-tales associated with Shaft A. Figures 3.4, 3.5, and 3.6 show the location and movements of the tell-tales associated with Shaft B. Figures 3.7 and 3.8 show the location and movements of the tell-tales associated with Shaft C. Figures 3.9, 3.10, and 3.11 show the location and movements of the tell-tales associated with Shaft D. Figures 3.12 and 3.13 show the location and movements of the tell-tales associated with

Shaft BS. Figures 3.11 and 3.12 show the location and movements of the tell-tales associated with group shafts.

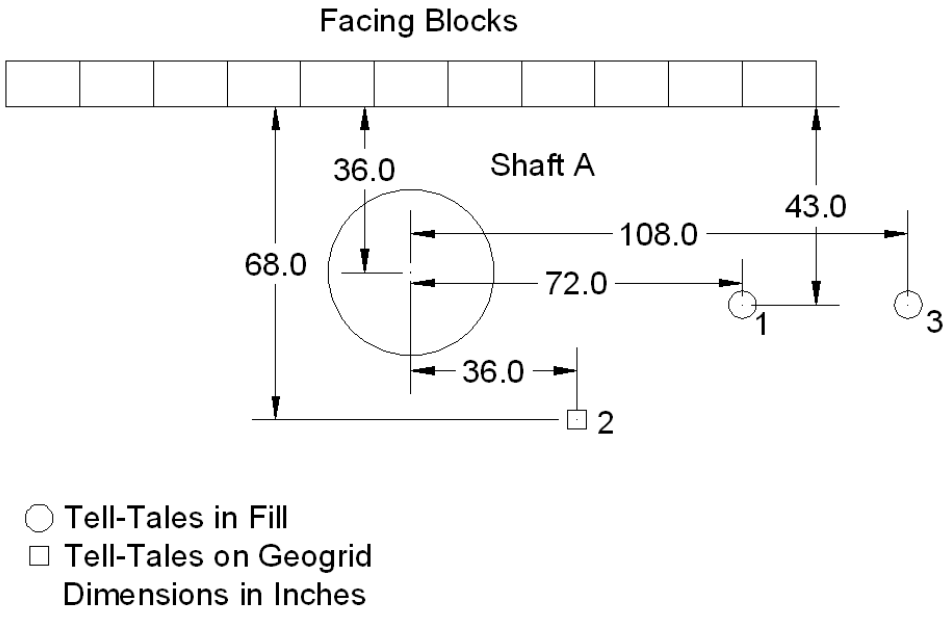

Figure 3.1 Location of tell-tales for Shaft A.

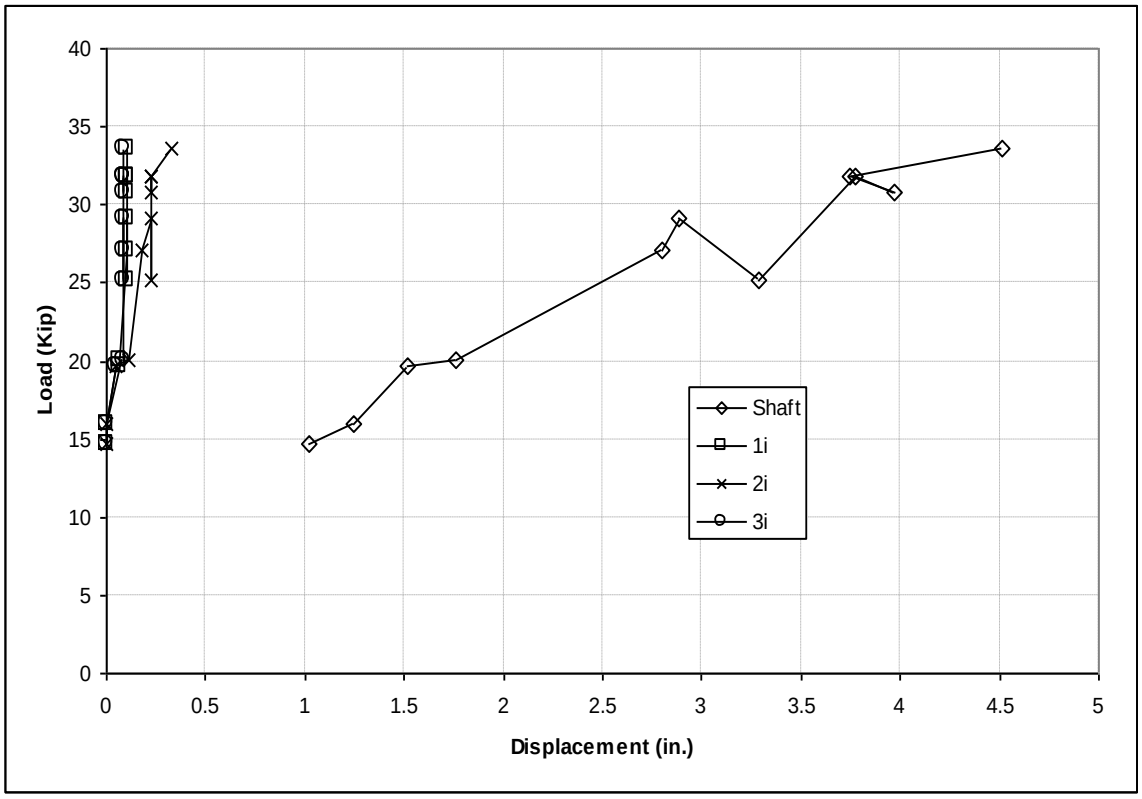

Figure 3.2 Displacement of inner tell-tales for Shaft A.

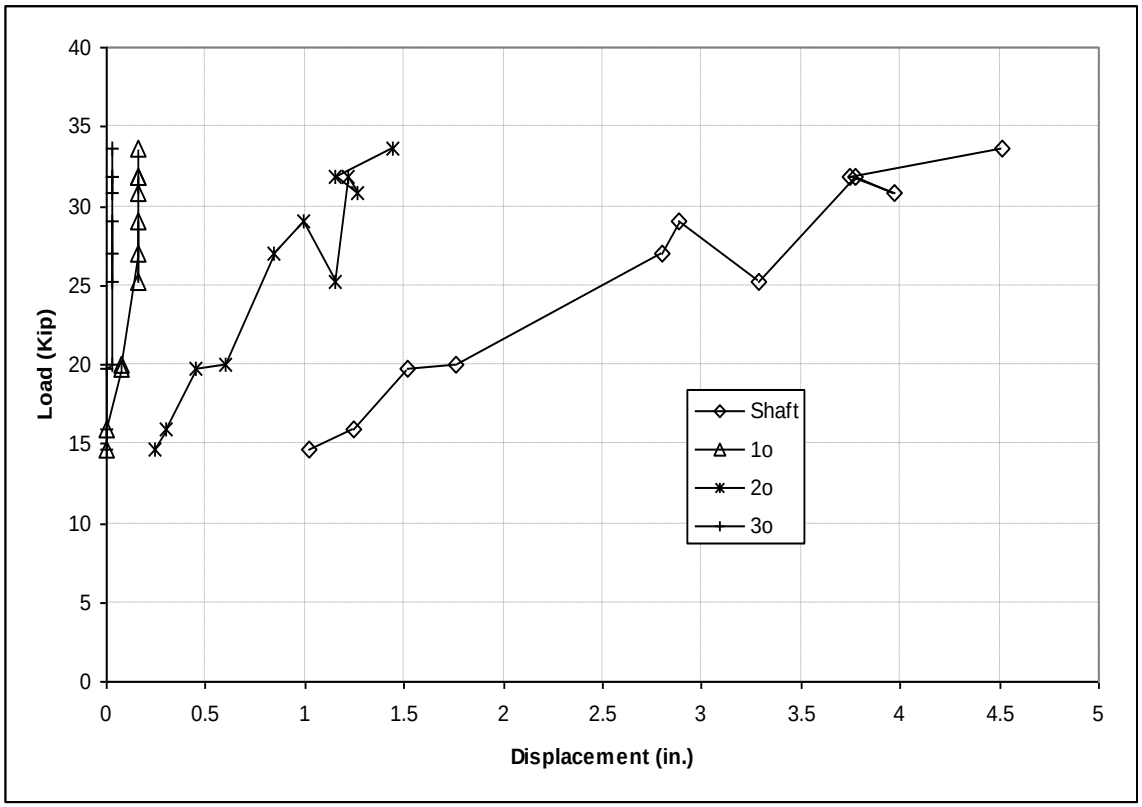

Figure 3.3 Displacement of outer tell-tales for Shaft A.

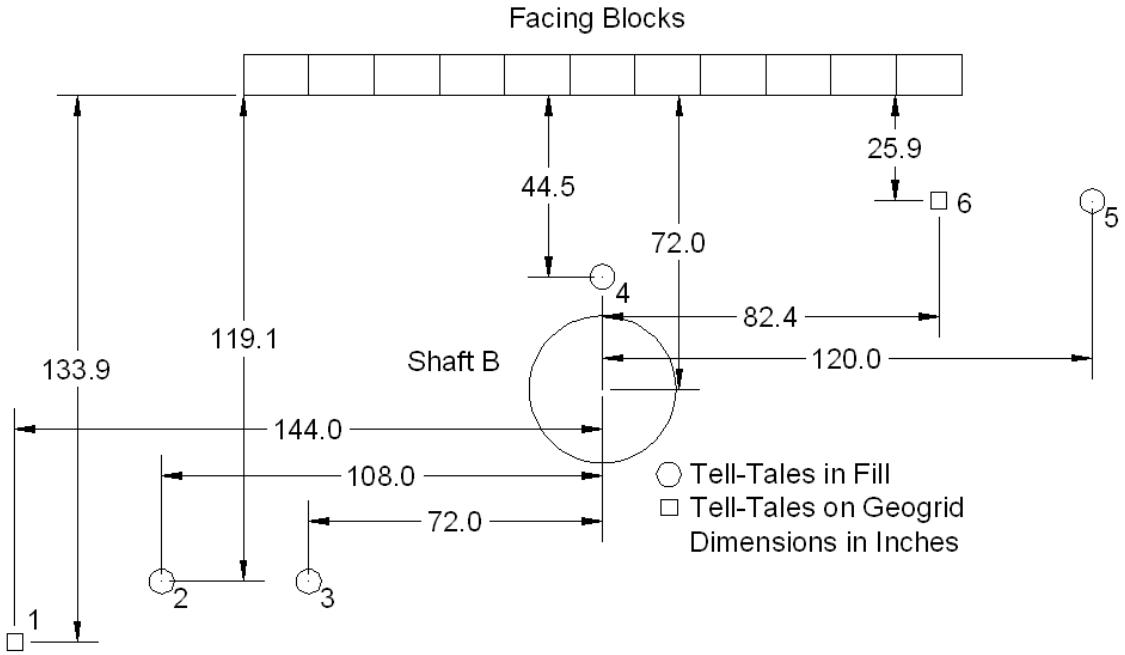

Figure 3.4 Location of tell-tales for Shaft B.

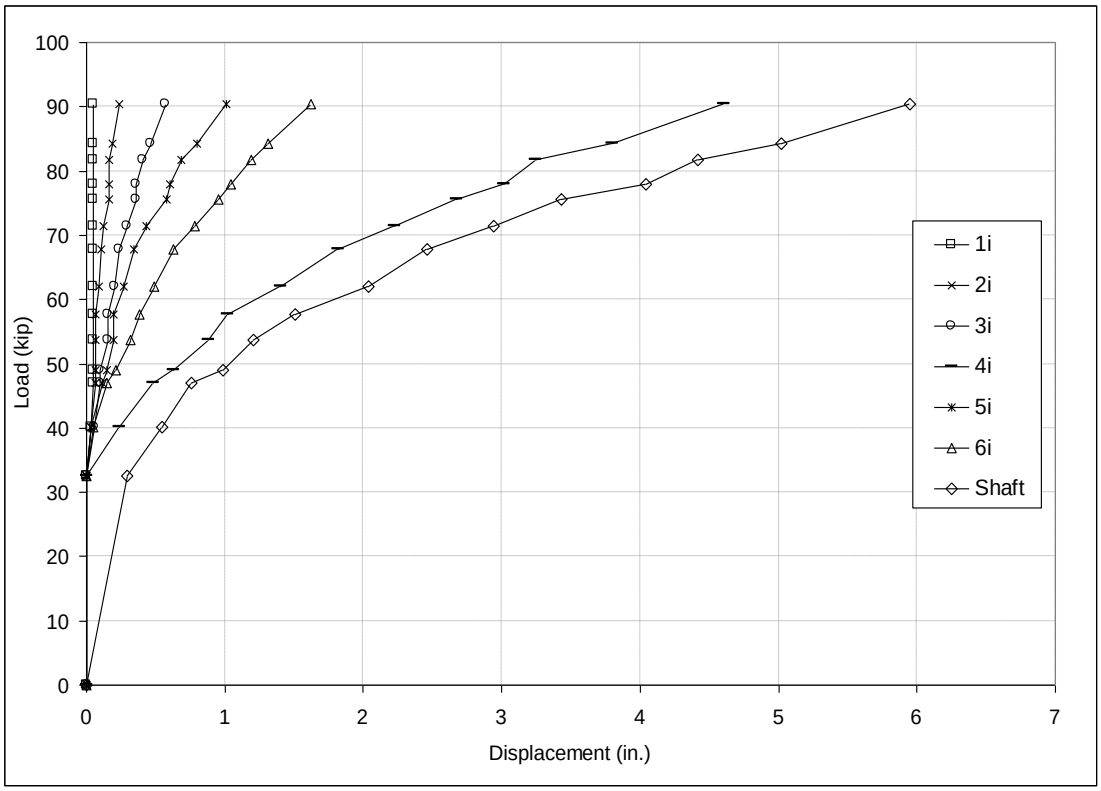

Figure 3.5 Displacement of inner tell-tales for Shaft B.

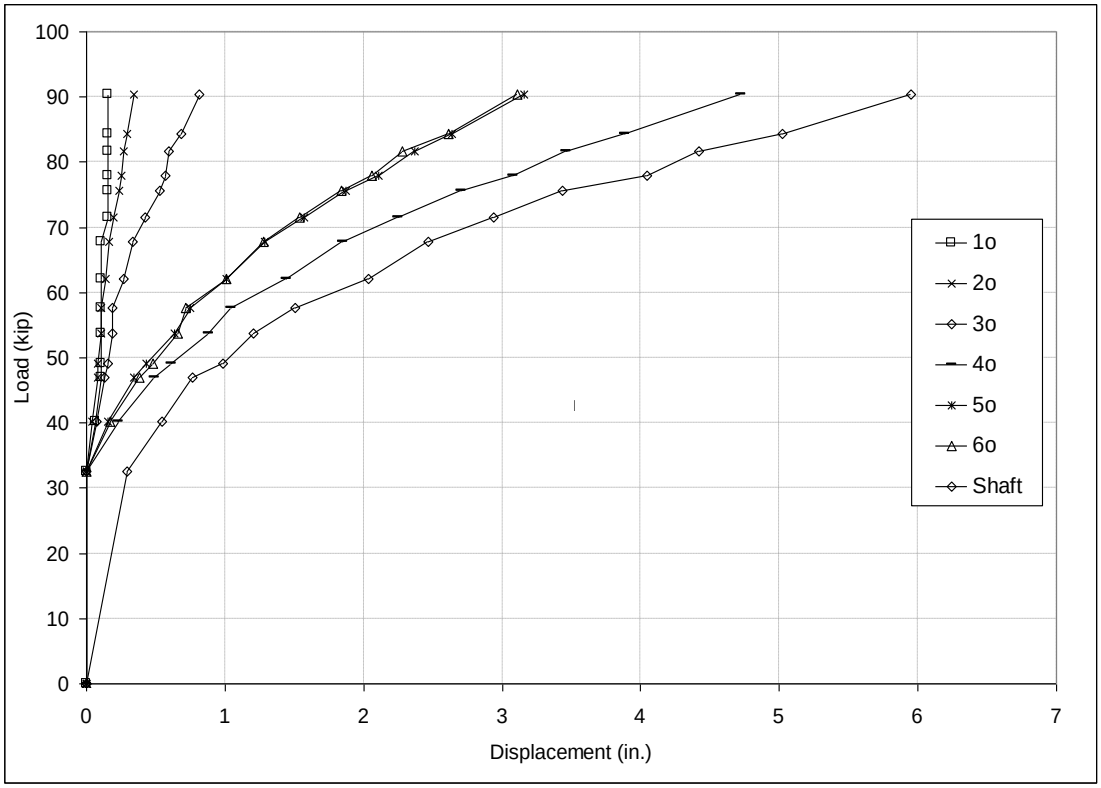

Figure 3.6 Displacement of outer tell-tales for Shaft B.

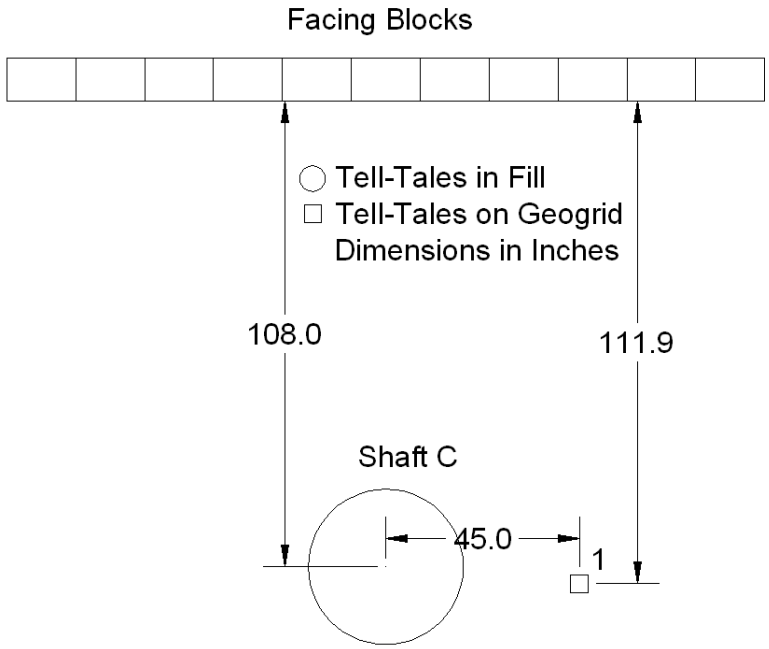

Figure 3.7 Location of tell-tales for Shaft C.

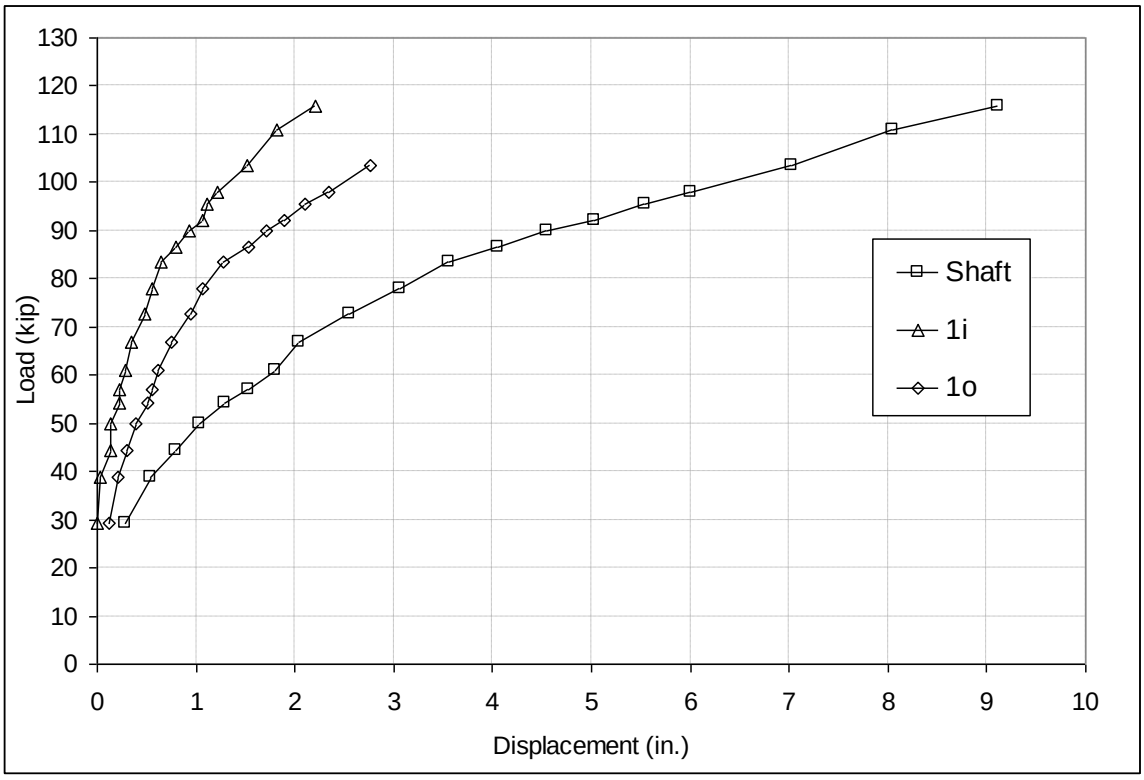

Figure 3.8 Displacement of tell-tales for Shaft C.

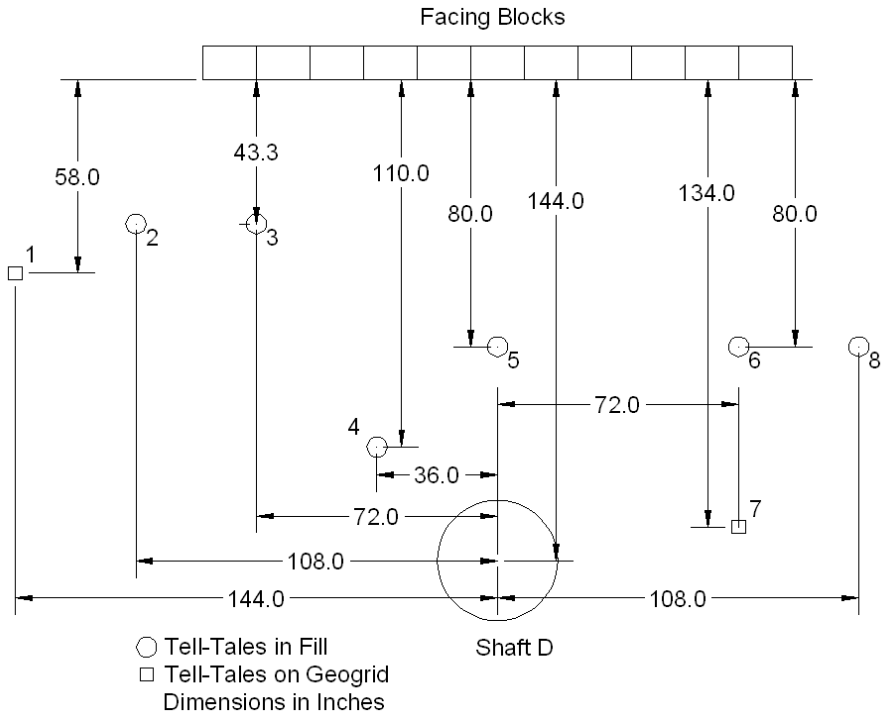

Figure 3.9 Location of tell-tales for Shaft D.

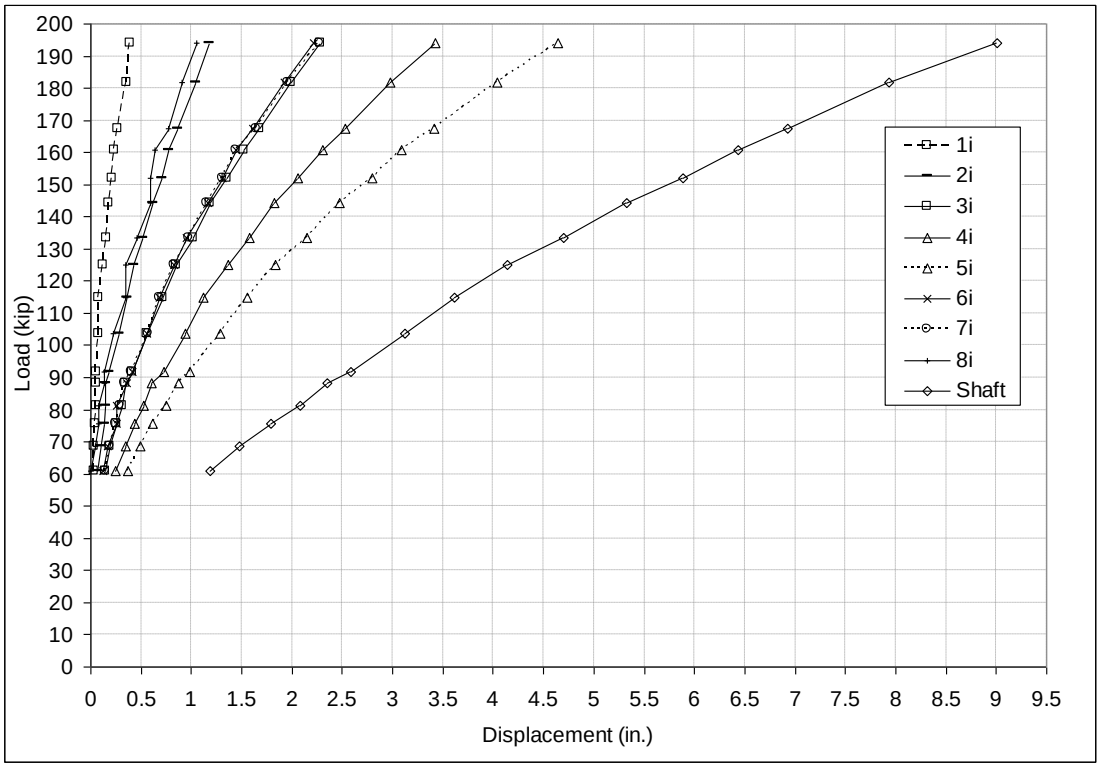

Figure 3.10 Displacement of inner tell-tales for Shaft D.

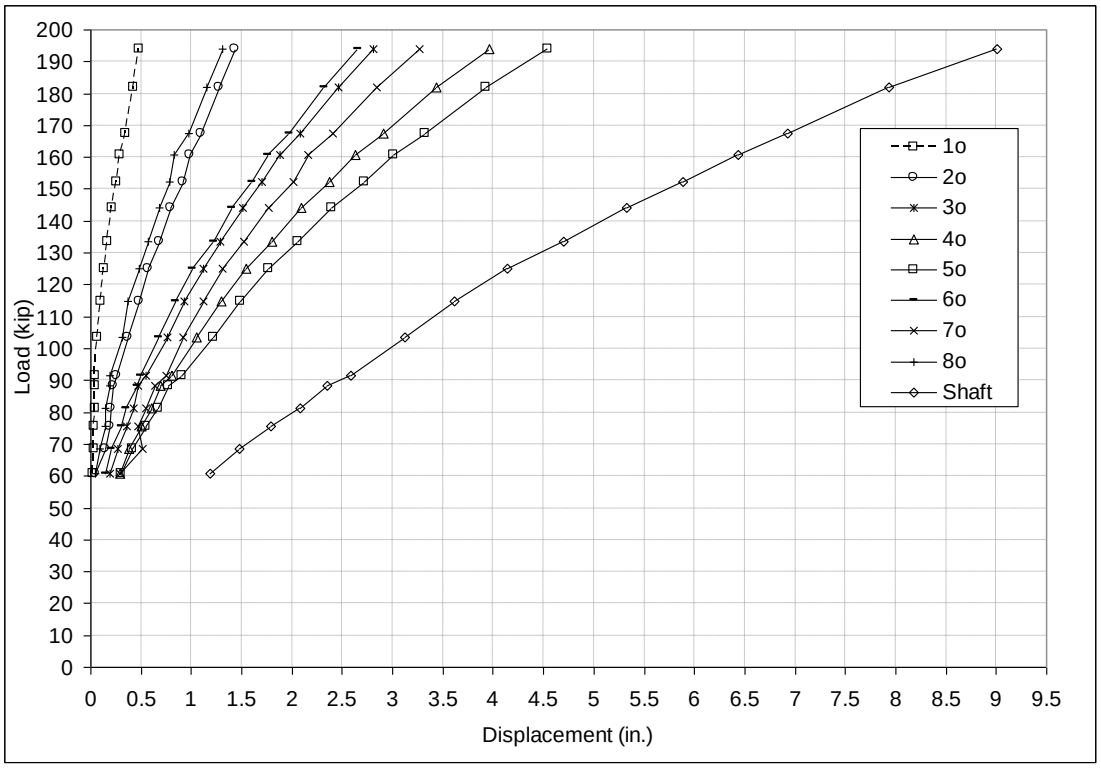

Figure 3.11 Displacement of outer tell-tales for Shaft D.

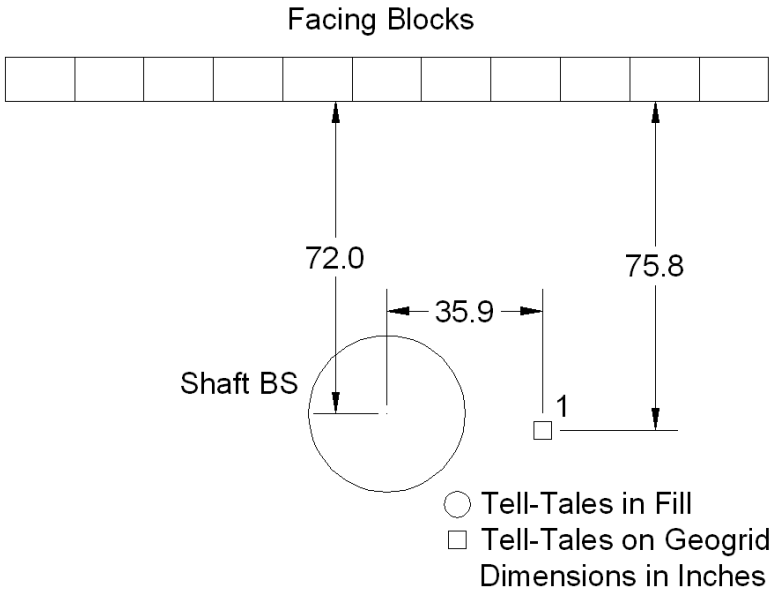

Figure 3.12 Location of tell-tales for Shaft BS.

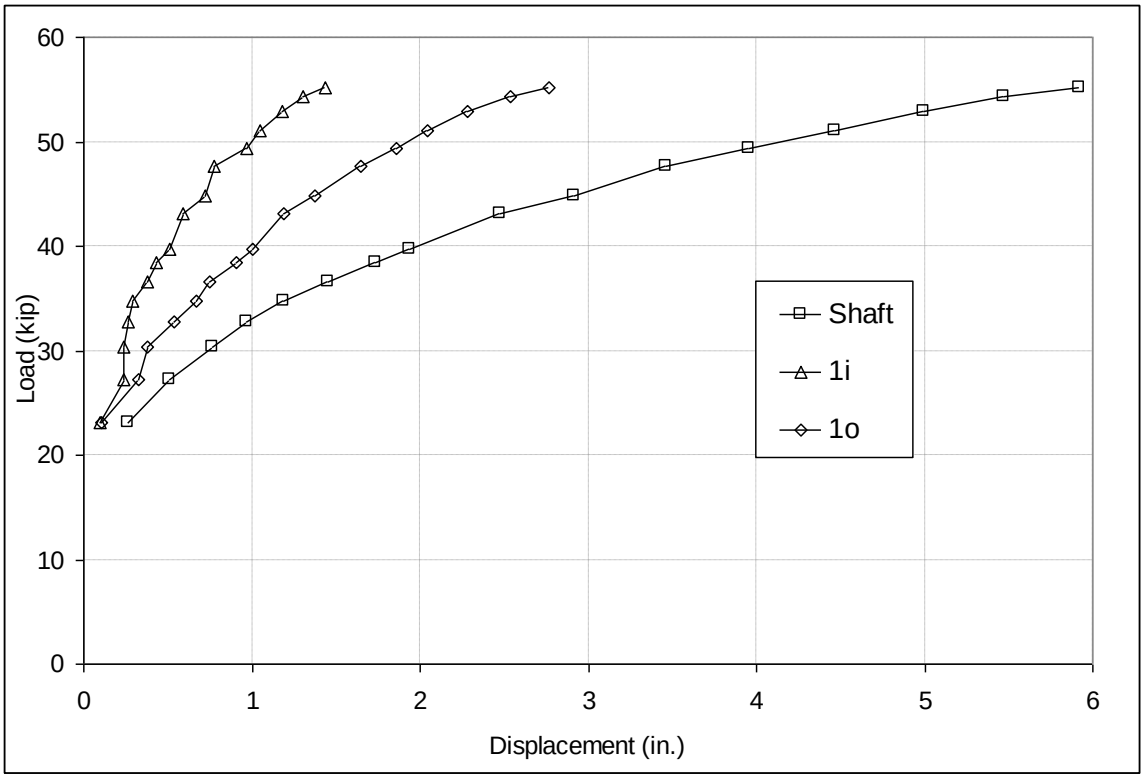

Figure 3.13 Displacement of tell-tales for Shaft BS.

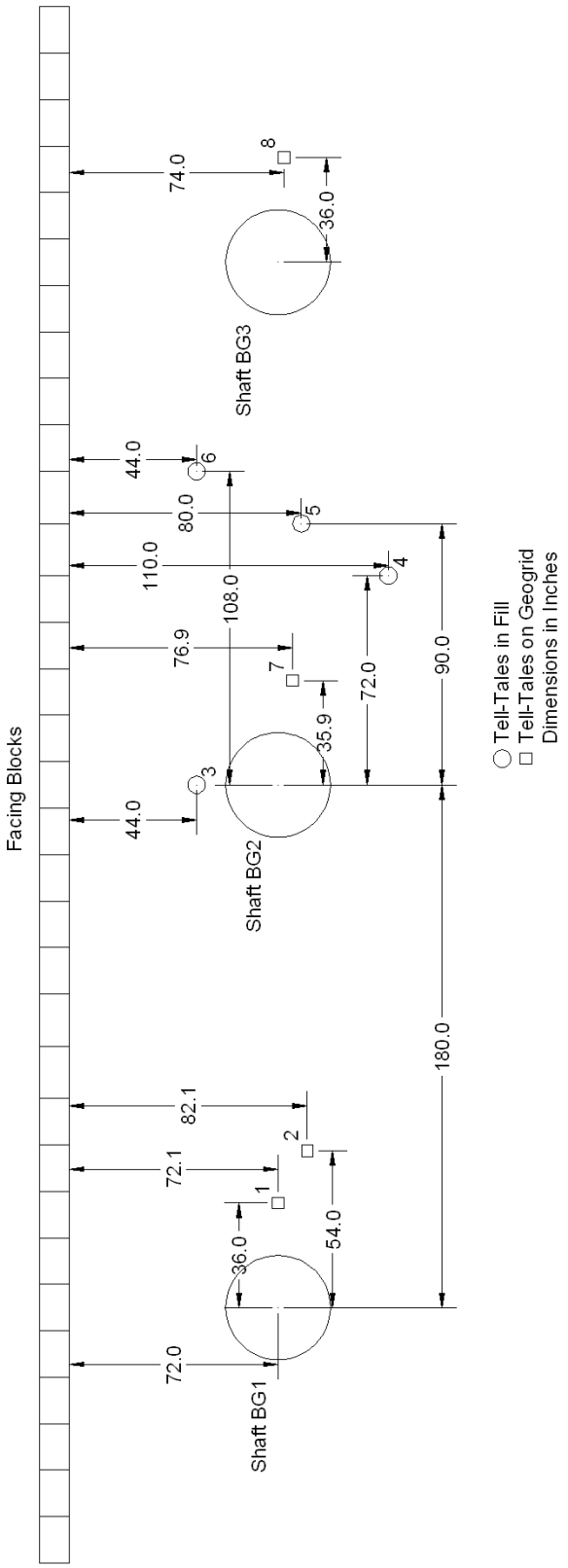

Figure 3.14 Location of tell-tales for the group shafts.

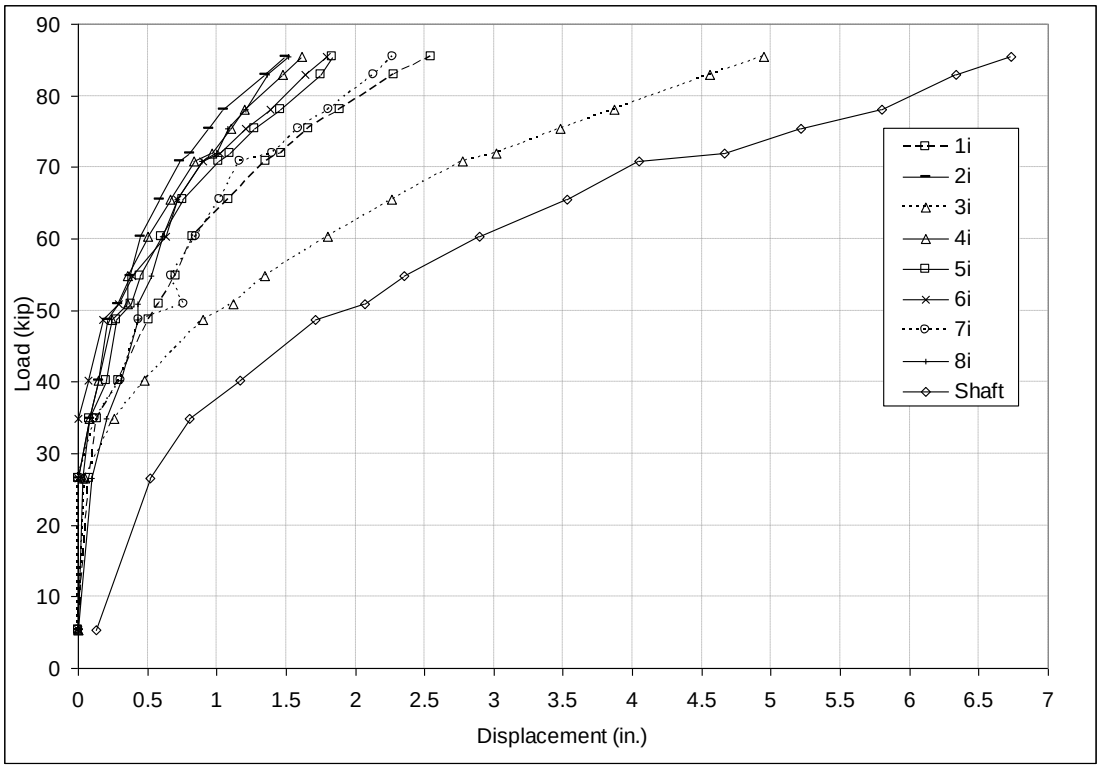

Figure 3.15 Displacement of inner tell-tales for Shaft BG.

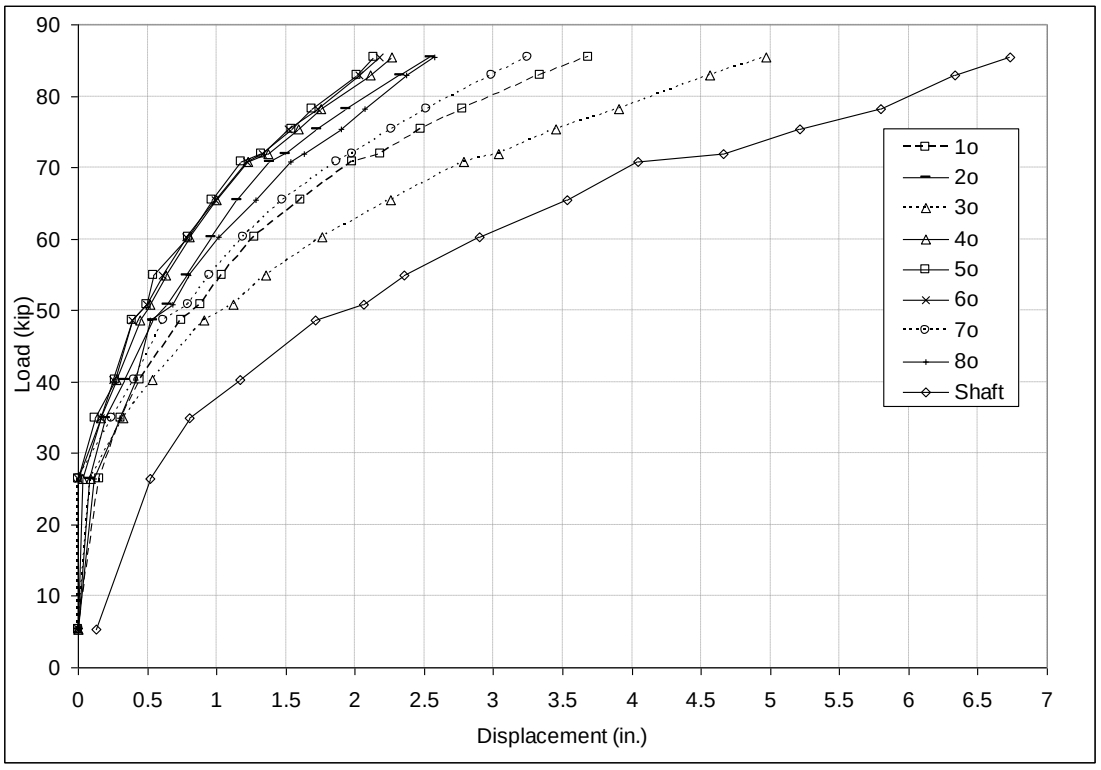

Figure 3.16 Displacement of outer tell-tales for Shaft BG.

3.2 Strain of Geogrid

An important aspect of the behavior of MSE systems is the load supported by the geogrid and the corresponding strain. During physical testing, described in Pierson et al. 2008, strains of the geogrid were measured at four points near the shafts at two separate elevations for Shafts A, B, BG1, and BG2. During construction, testing, and for several months after testing, strain in a control section was monitored. Strain of the geogrid in the control section was measured at six points in four different elevations. The results of each of these will be discussed in this sub section.

An 18 inch wide roll of geogrid was instrumented with strain gauges at specific locations on both the top and bottom side of the geogrid. Each gage was measured individually and the results from both the top and bottom gages were averaged for more accurate results. The instrumented roll of geogrid replaced the standard geogrid. It was placed either directly next to a shaft or within the control section. Kyowa 120 ohm strain gages were used and were bonded to the geogrid and encased in a protective material off site. After placement of the instrumented geogrid, small PVC pipe sections were used as an additional protection over the location. Three wire strain gage cable was then run from the gage through flexible tubing to a large PVC pipe which terminated at the data acquisition system. During testing the data acquisition system measured strain at twenty second increments. During the post test monitoring program strain and temperature were measured every one hour.

Initial modeling of the shaft - MSE wall system indicated additional testing of the geogrid material was required to determine the stress strain curve of the material. This testing will also be discussed in this subsection.

3.2.1 Strain Near Shafts During Testing

Strain measured in the geogrid near Shafts A, B, BG1, and BG2 during load testing is reported in this section. This information can be used to estimate the load carried by the geogrid, but will only be used to compare with results from the numerical model.

In the test sections strain was measured at 6.7 and 14.7 ft of elevation. Geogrid strain was measured at the first aperture and second bar at both elevations (Figure 3.17). The plan view of the strain gage locations for is shown in figures 3.18 and 3.19. The results from strain gages are plotted along with shaft displacement to assist in comparison and to establish a reference point for other types of data. The shape of the displacement plot is very similar to the shape of the strain gages plots (Figure 3.20). The strain gage results from Shaft A at elevation 6.7 and 14.7 feet are shown in Figures 3.20 and 3.21 respectively. The strain gages at elevation 6.7 feet measured very similar results in all of the strain gages. At elevation 14.7 feet the two gages nearest to the facing recorded the most strain. Strain of the geogrid recorded near Shaft B is shown in Figures 3.22 and 3.23. For Shaft B generally less strain was measured near the facing. However, the measured strain location furthest from the facing (location 4 and 8) was at the thicker bar section of the geogrid and recorded less than the measured strain at the aperture just nearer to the facing (location 3 and 7). Figures 3.24 and 3.25 show the strain measured in the geogrid near Shaft BG1 and Figures 3.26 and 3.27 show the strain measured near Shaft BG2. The three strain gages stopped responding during the group test. For this situation rather than averaging the strain of the gages above and below the geogrid the strain gage that stopped responding was ignored. During the test one strain gage at

locations 3 and 4 for BG1 and location 4 for BG2 stopped responding. Also location 7 for BG1 shows irregular readings. Strain measured near Shaft BG1 and BG2 agree well with each other and with Shaft B. This indicates the loss of a single strain gage at several locations did not severely affect the results at those locations.

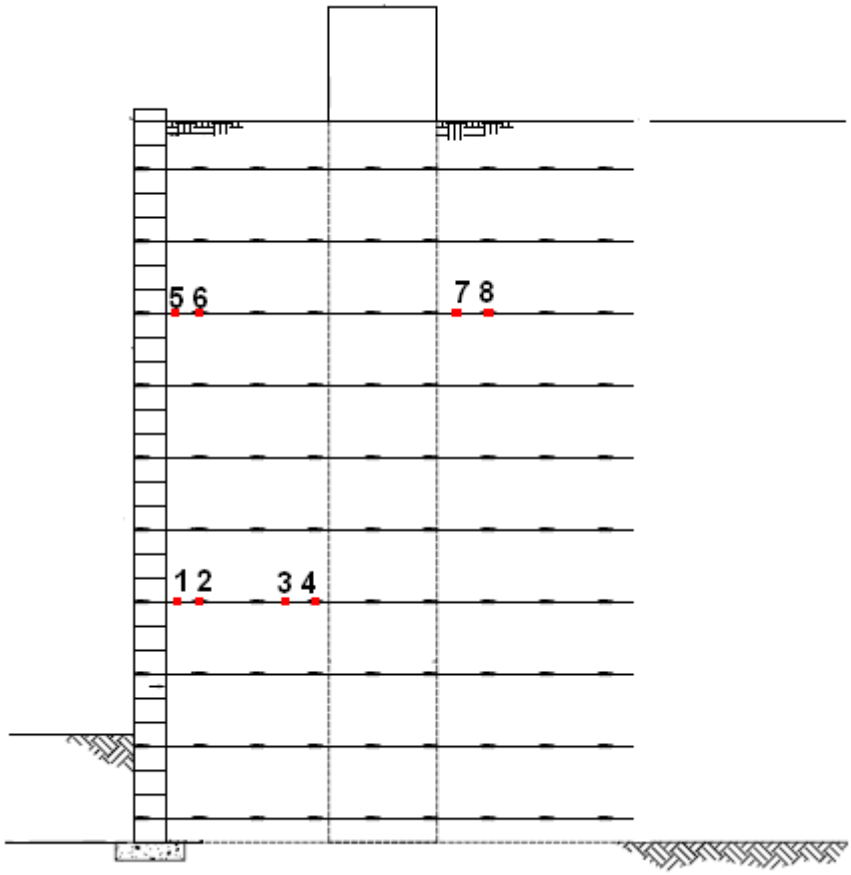

Figure 3.17 Cross section of system for Shaft B with strain gage identification numbers shown (placement of strain gages in all test sections are in the same location with respect to the facing).

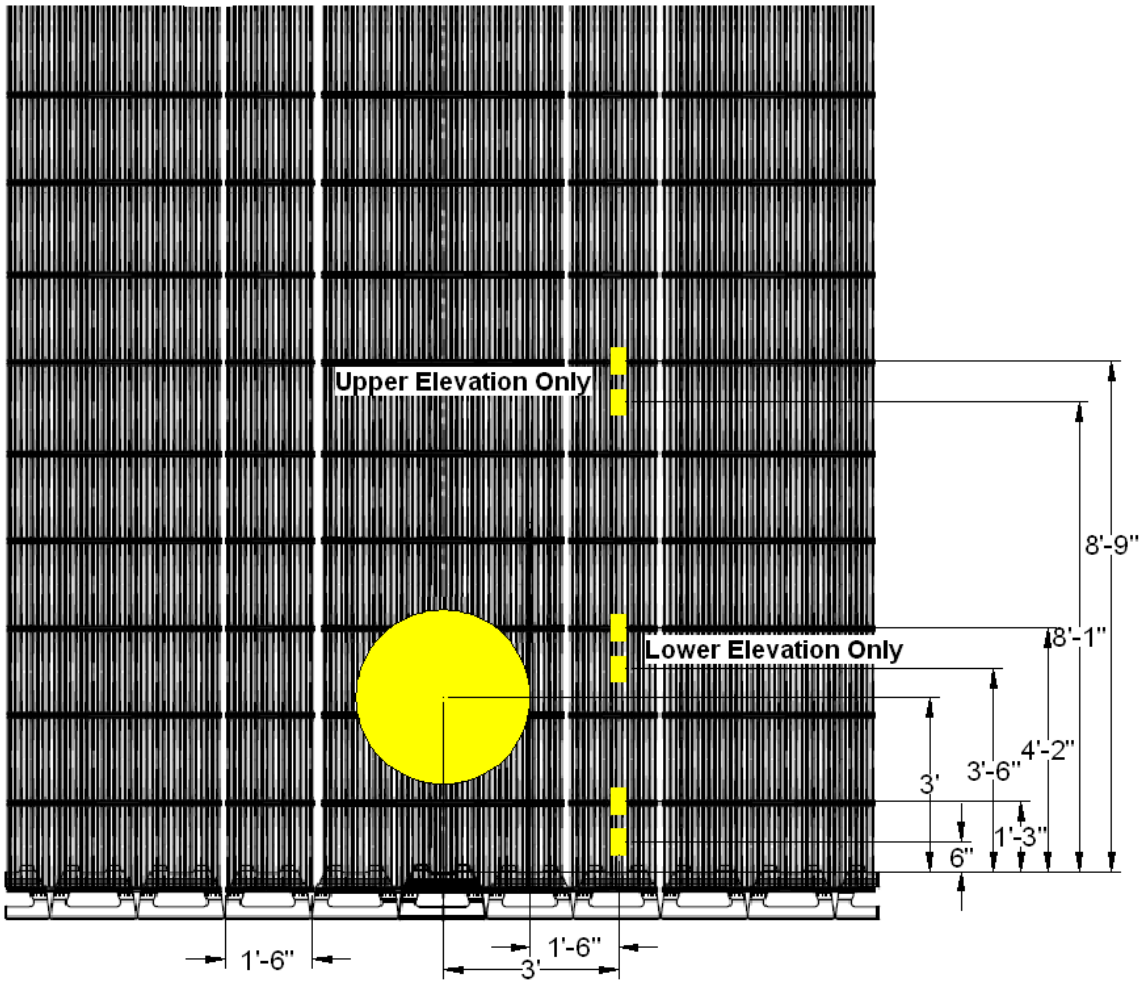

Figure 3.18 Plan view of strain gage locations for Shaft A. CMD bars are parallel to the wall facing.

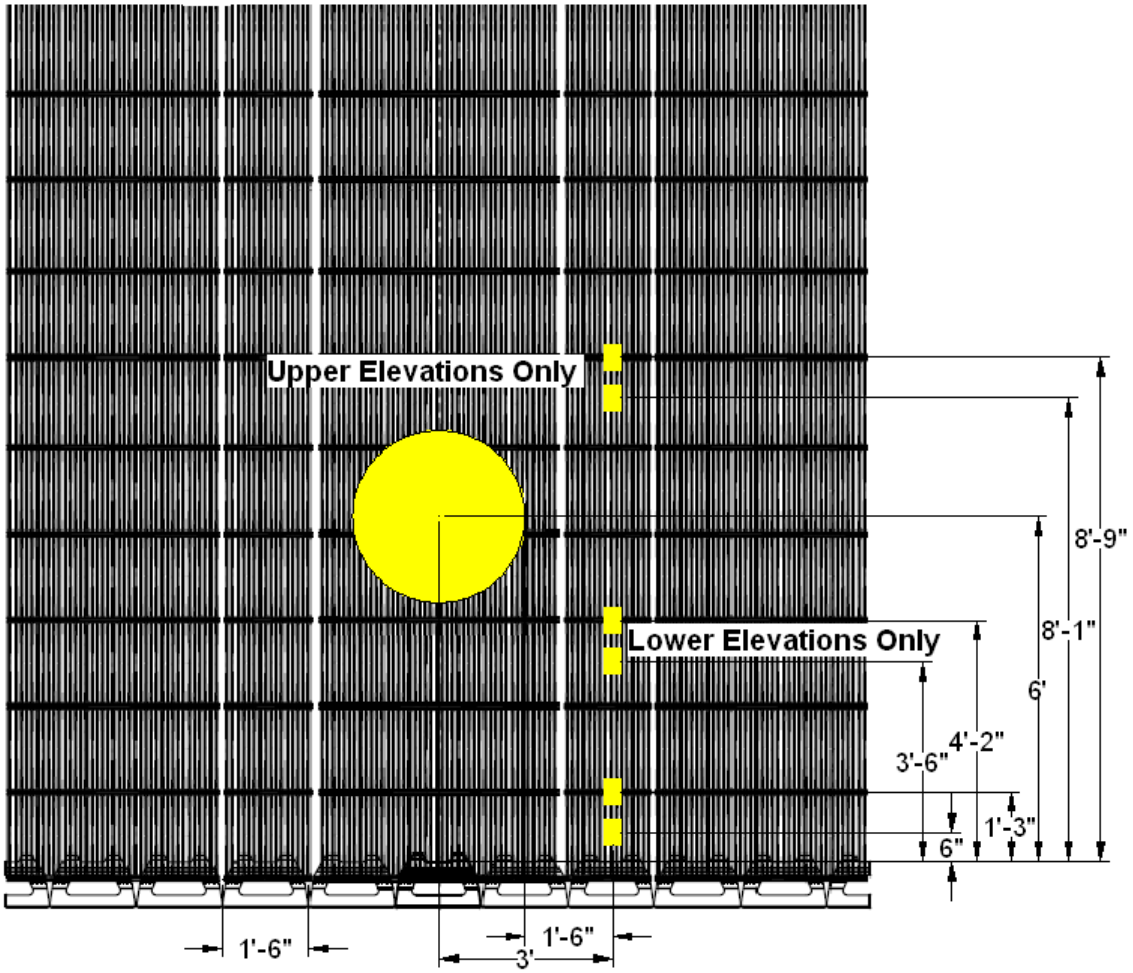

Figure 3.19 Plan view of strain gage locations for Shafts B, BG1, and BG2.

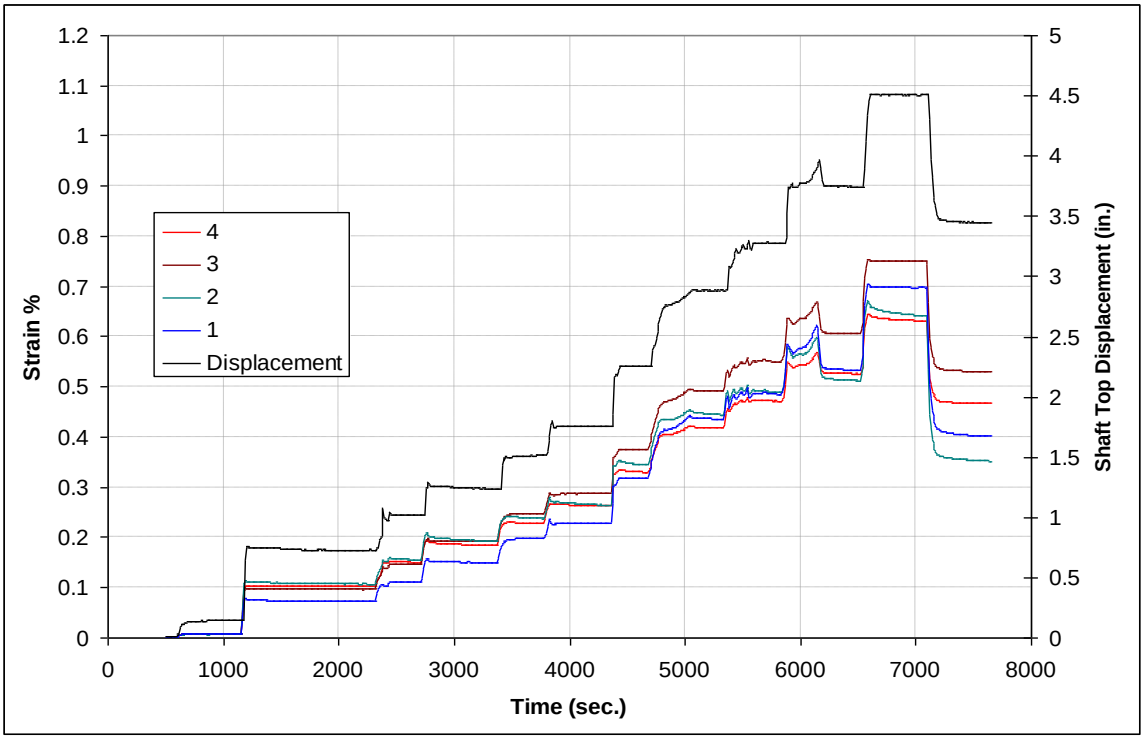

Figure 3.20 Strain measured at elevation 6.7 ft for Shaft A.

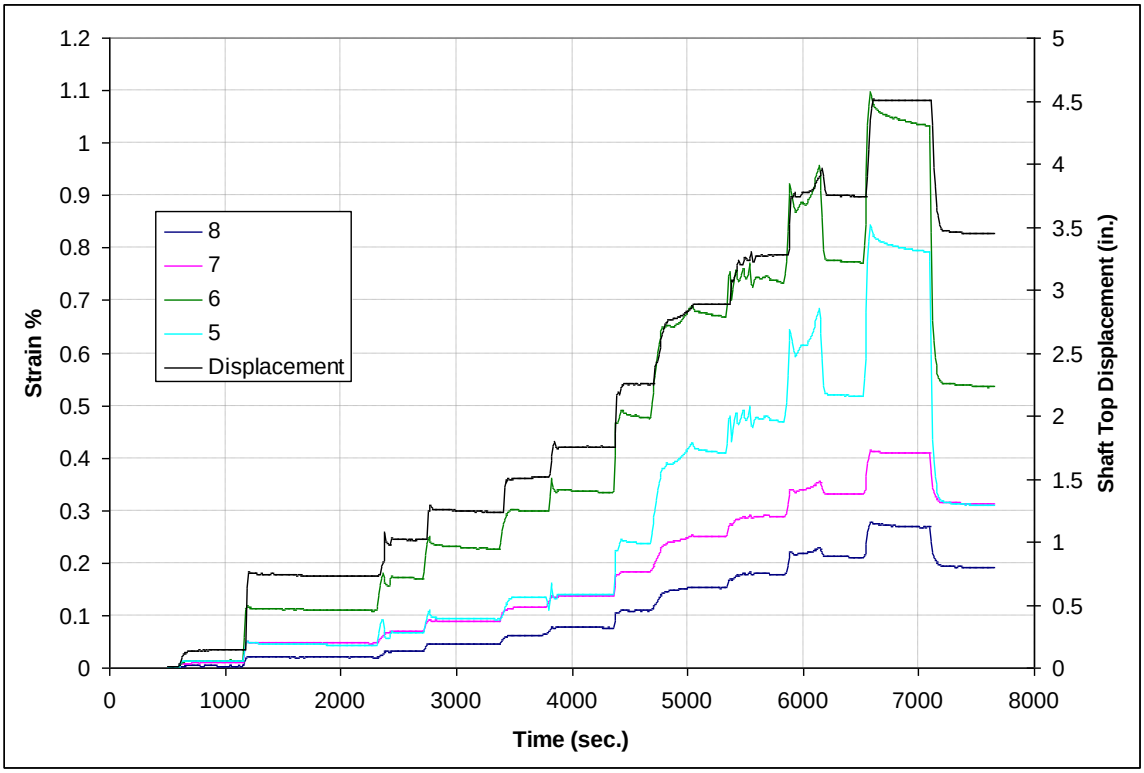

Figure 3.21 Strain measured at elevation 14.7 ft for Shaft A.

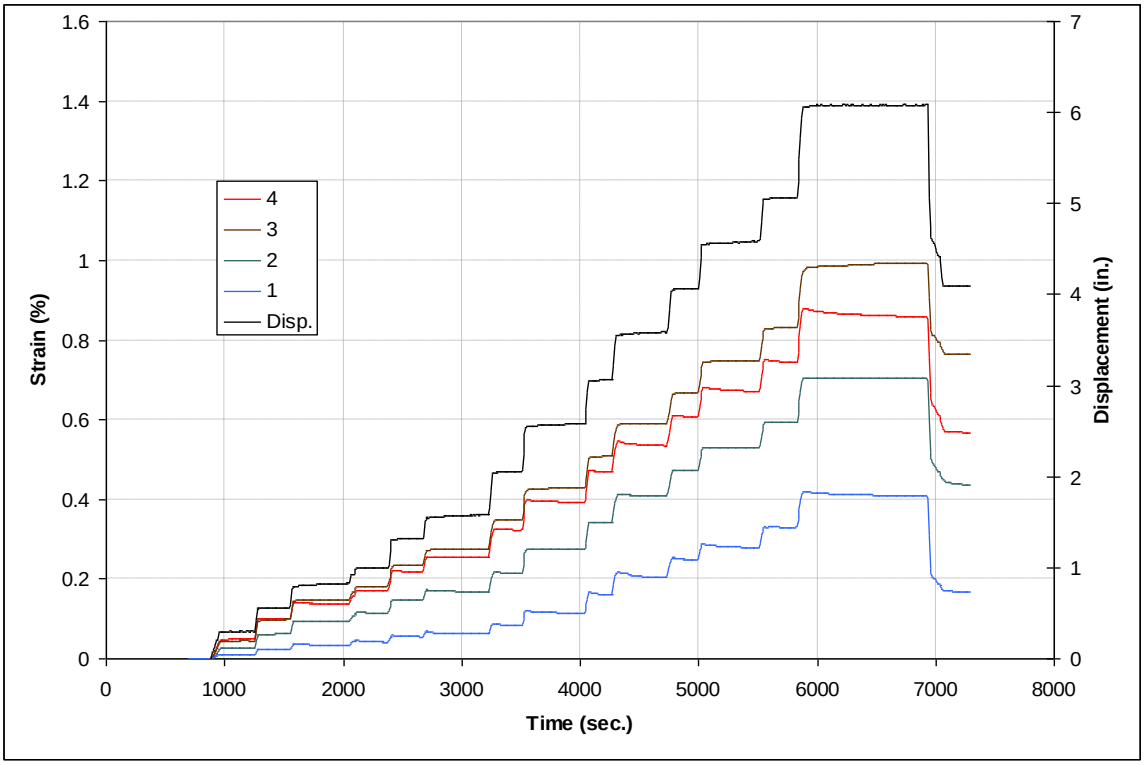

Figure 3.22 Strain measured at elevation 6.7 ft for Shaft B.

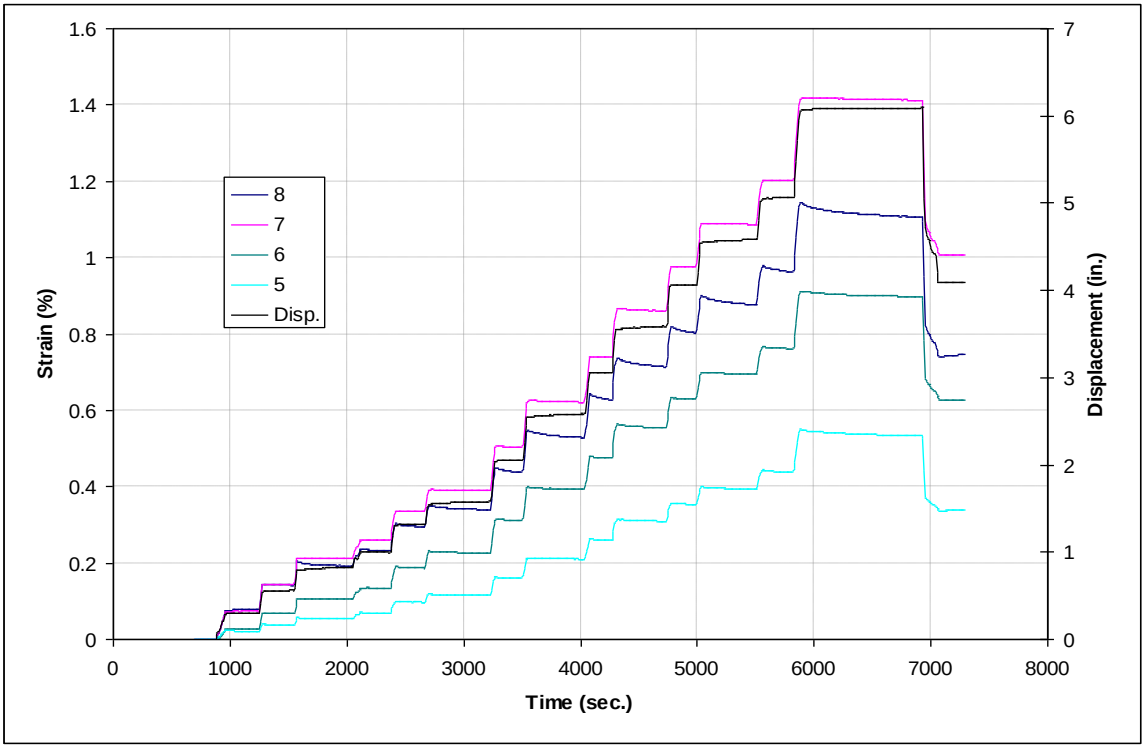

Figure 3.23 Strain measured at elevation 14.7 ft for Shaft B.

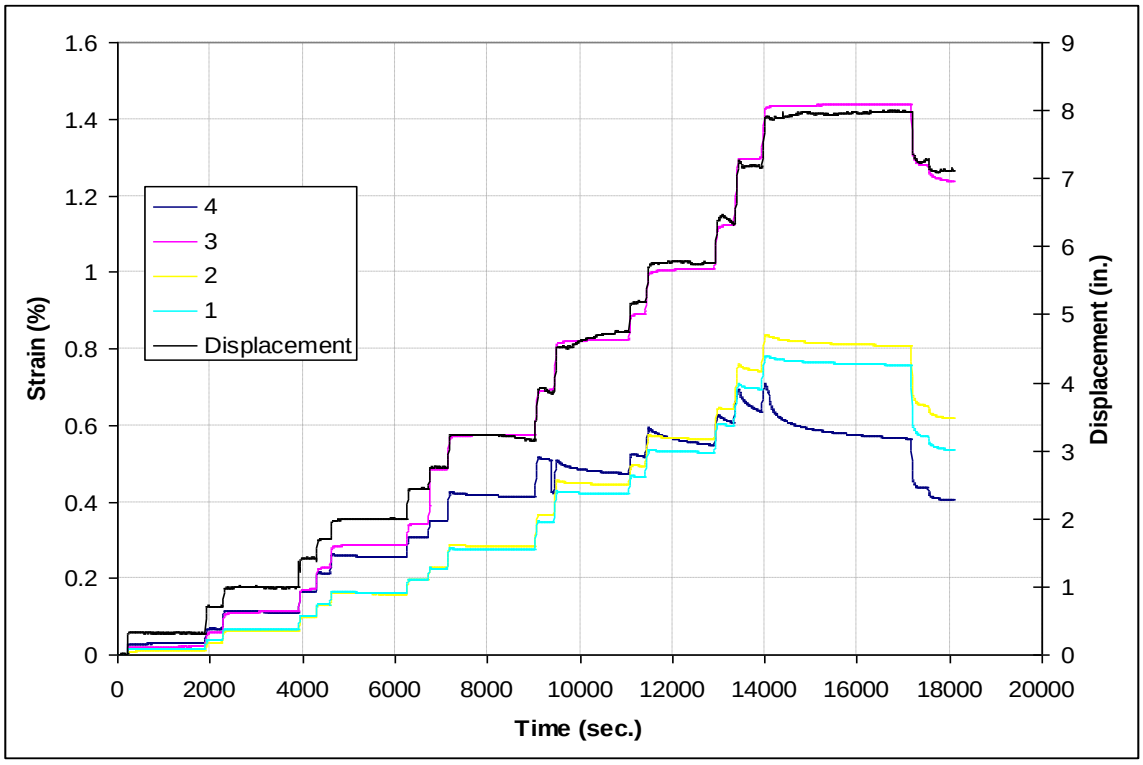

Figure 3.24 Strain measured at elevation 6.7 ft for Shaft BG1.

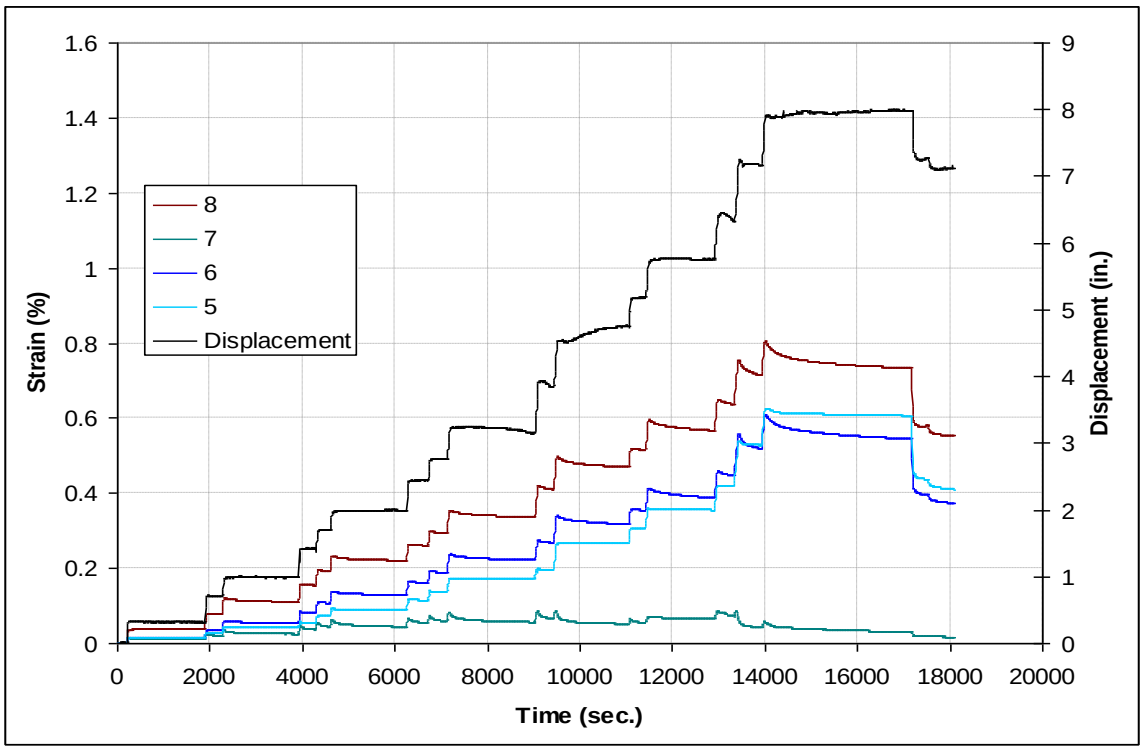

Figure 3.25 Strain measured at elevation 14.7 ft for Shaft BG1.

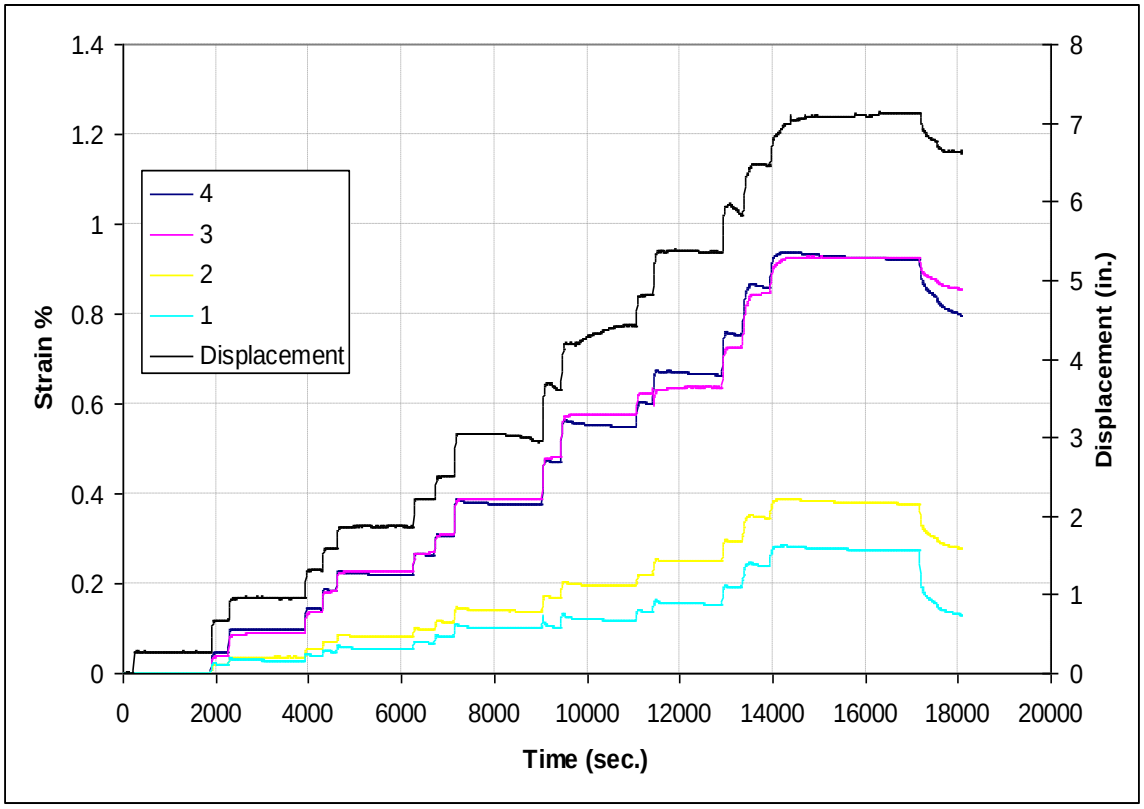

Figure 3.26 Strain measured at elevation 6.7 ft for Shaft BG2.

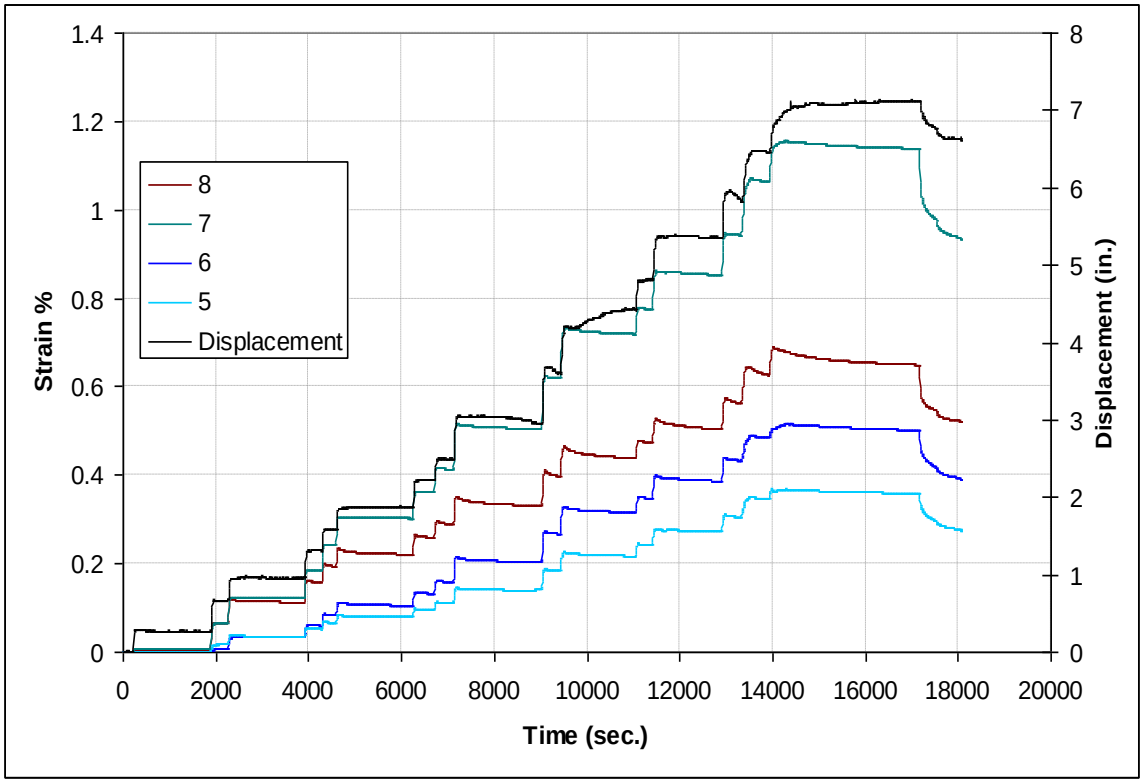

Figure 3.27 Strain measured at elevation 14.7 ft for Shaft BG2.

3.2.2 Strain Measured During First Winter

This section is an excerpt from Parsons et al. (2009b).

During construction (ends September 19th, 2007) a portable "Strain Indicator" box was used to measure each gage several times a week at generally the same time of day. This data is combined with hourly strain measurements or gages in the control section that began nearly a month before testing. Load testing was performed and one month after the load testing was complete hourly measurements of the gages in the control section were resumed (Figure 3.28). Figure 3.28 clearly shows the strains that developed during construction of the wall. Analysis of the control section yielded two trends among active strain gages, a sampling of which are reported in Figures 3.28 and 3.29. One group of strain gages followed temperature almost exactly while others showed little change over the time period studied. This difference may be the result of different localized stress levels in different elements of the grid. A closer analysis of the data collected during April of 2008 (Figure 3.29) shows the same two trends. Daily fluctuations were observed in both trends.

Several observations can be made based on the data in Figures 3.28 and 3.29. The early readings clearly reflect the strains that occurred during construction. The strains in the bottom of the fill were greater than those near the surface, and the maximum magnitude of the strains observed was less than 0.4 percent. After construction, both daily trends

and seasonal trends driven by temperature are visible in the strain data, but no significant permanent creep was observed.

When ambient temperature versus strain is plotted, the gages that correlate well with temperature yield a tight cluster of points (Figure 3.30) and the gages that do not correlate with temperature yielded a less distinct pattern, although an underlying trend of increasing strain with increasing temperature is still visible (Figure 3.31).

When strain at a particular temperature was isolated and then all strains at that temperature were plotted over time, little correlation could be found for either set of trends. Generally more change was found for gages that correlate well with temperature than gages that do not correlate well.

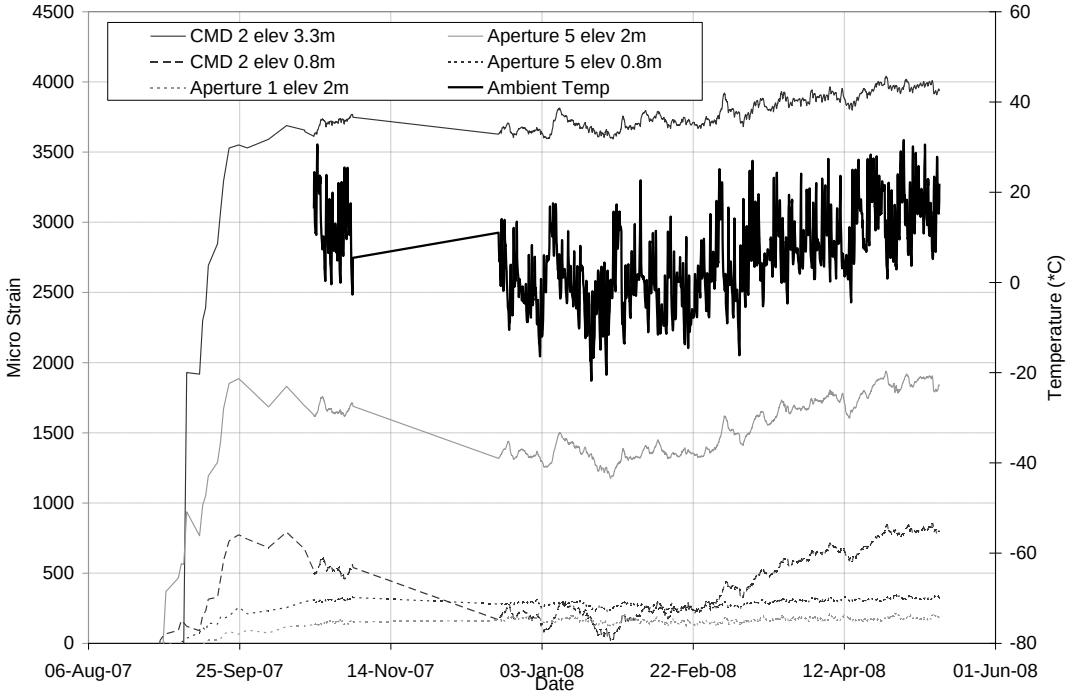

Figure 3.28 Shows temperature and all strain measurements over the period of study for three gages that correlate with ambient temperature and two that do not correlate.

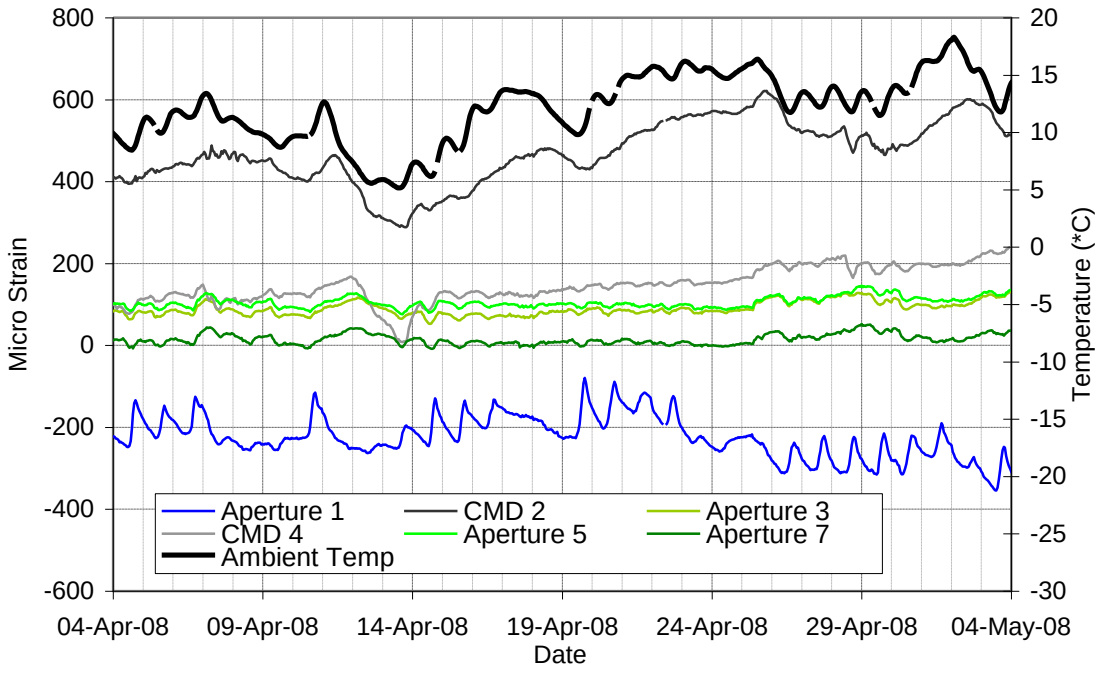

Figure 3.29 Shows temperature and all strain measurements at elevation 6.7 ft over a period of one month for four gages that correlate with ambient temperature and two that do not correlate.

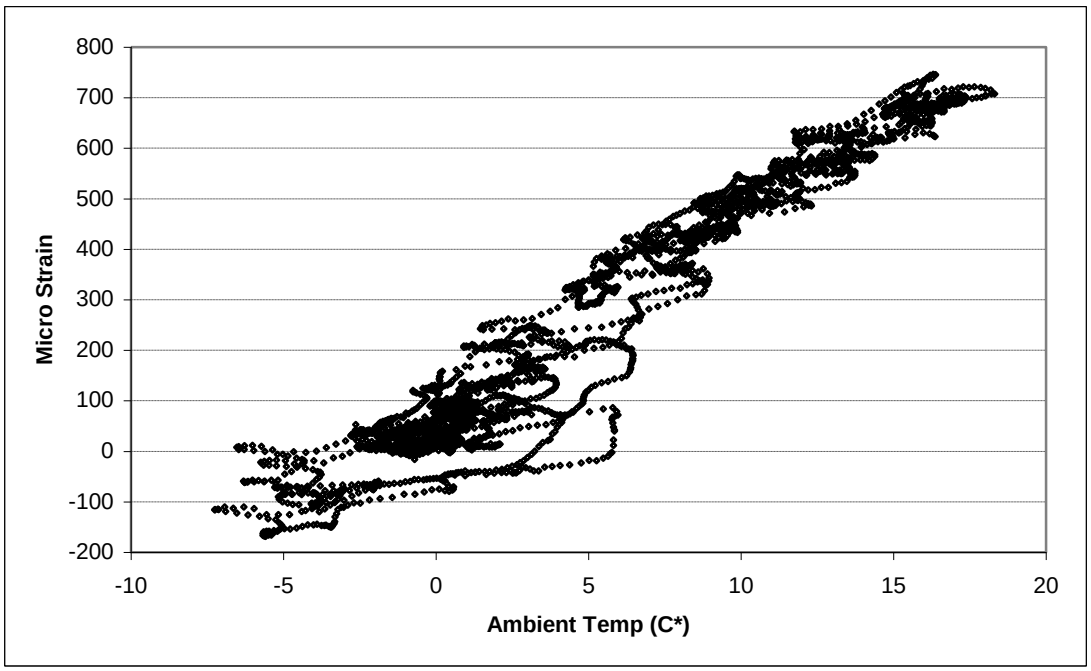

Figure 3.30 Data from strain gages that correlated well with ambient temperature.

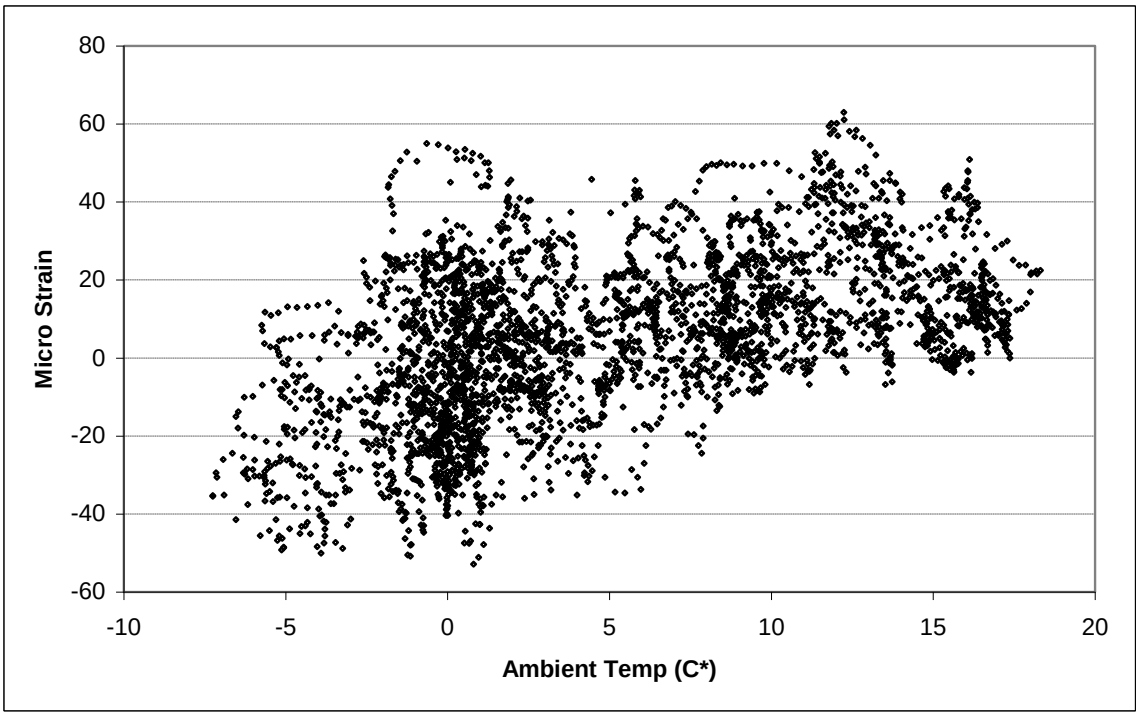

Figure 3.31 Weaker correlation for strain gages that did not correlate as well with ambient temperature.

3.2.3 Physical Testing of the Geogrid Material

Material properties of the HDPE uniaxial geogrid are provided by the manufacture in the strong direction, but not the weak direction. These properties only indicate the strength of the geogrid at 5% strain allowing for a linear stiffness to be applied to the material. The strength in the weak direction was understood to be $1/10^{th}$ the strength in the strong direction as a general rule (Personal communication with Dr. Jie Han). Initial model results indicated an increase of the geogrid stiffness would produce a better match with field and model results. To determine if an increase in stiffness would be justified the material was tested in the strong direction and the weak direction.

To test the geogrid in the strong direction a significant sample length was needed to prevent edge effects. This required the use of dead weight as the loading mechanism due to the required size of the loading frame that would be needed to accurately test the

sample hydraulically. The dead weight loading system is shown in Figure 3.32. Results from this test (Figure 3.33) show a higher initial stiffness than the value reported by the manufacturer, but a lower stiffness at the reported strain. The lower stiffness at higher strains could be caused by the slower rate of loading at The University of Kansas compared with the manufacturer. The testing done at KU should be considered conservative based on the loading rate.

To evaluate the strength in the weak direction a single CMD bar at a time was clamped in a hydraulic load frame and loaded at a constant rate of 100 lb/min. The results of three tests are shown in Figure 3.34. The results indicate that the appropriate stiffness in the weak direction is $1/10^{th}$ that of the stiffness in the strong direction reported by the manufacturer, and about $1/20^{th}$ that of the stiffness in the strong direction measured at KU.

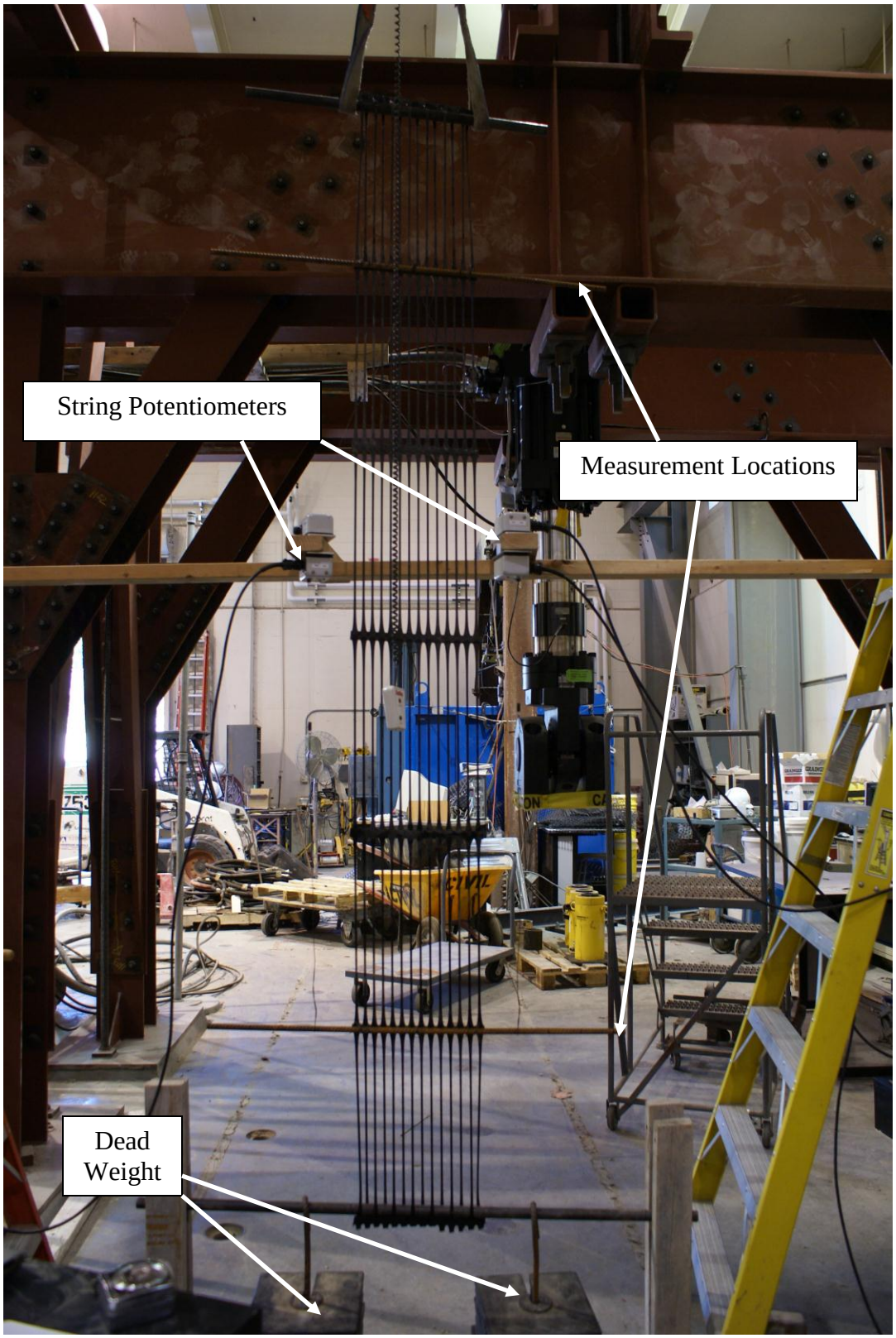

Figure 3.32 Image of dead weight loading system.

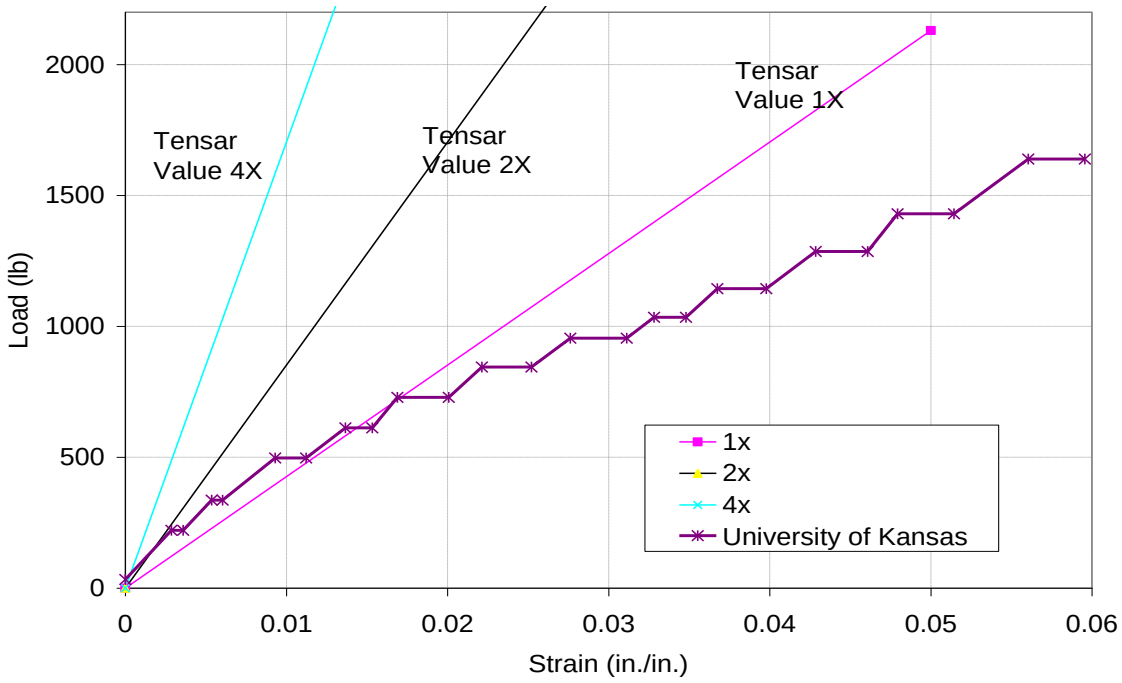

Figure 3.33 Load vs. strain curve for tested material in the strong direction compared with the values produced by the manufacturer.

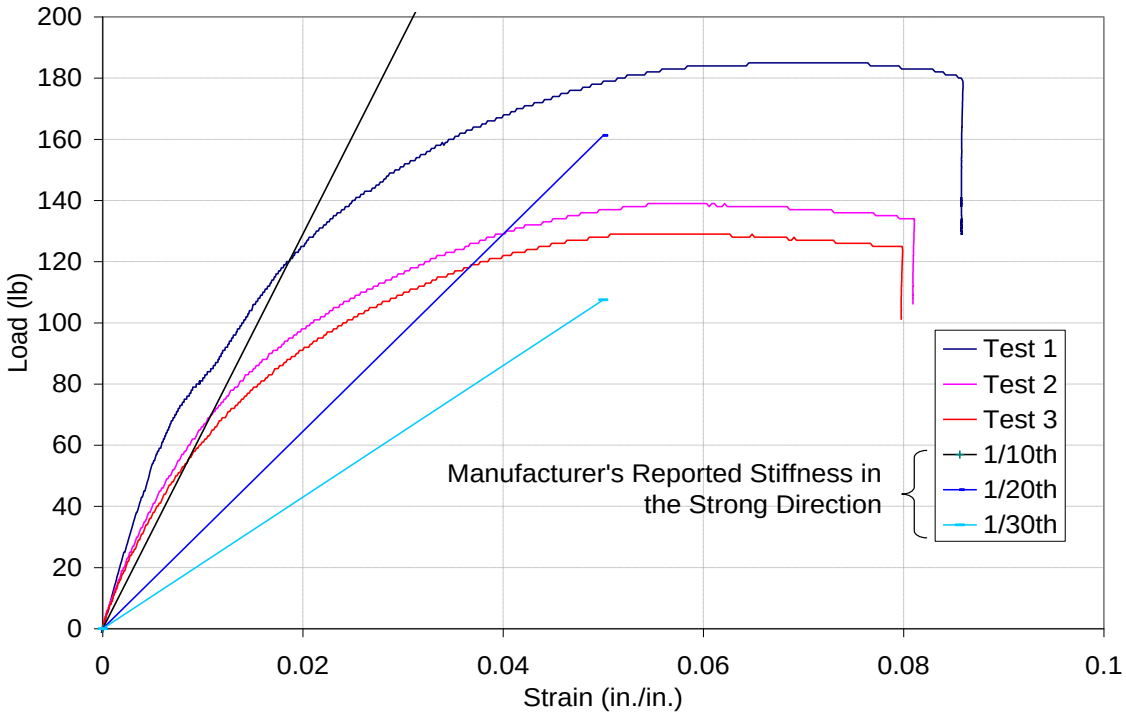

Figure 3.34 Load vs. strain curve for tested material in the weak direction compared with the values produced by the manufacturer.

3.3 Prediction of Load and Response

Section 2.1.6 describes the type of physical results reported in the original report to KDOT (Pierson et al. 2008). Based on the physical testing program, further analysis of this data was conducted to develop a design approach to predict the load and response of MSE wall – shaft systems with the same properties as those tested. Section 3.3 describes the design approach and its development. It contains excerpts from Pierson et al. 2010.

3.3.1 Prediction of Load and Response of Single Shafts

For this method only the peak load will be considered. From Table 2.1 a plot of peak load versus shaft distance from the back of the wall facing was developed (Figure 3.35). Trend lines and associated equations are shown connecting data points with equal shaft displacement. When designing for individual shaft capacity without site specific lateral load test information, capacities for shafts behind walls of similar geometry and backfill may be estimated from Table 2.1 or the trend lines or equations presented in Figure 3.35.

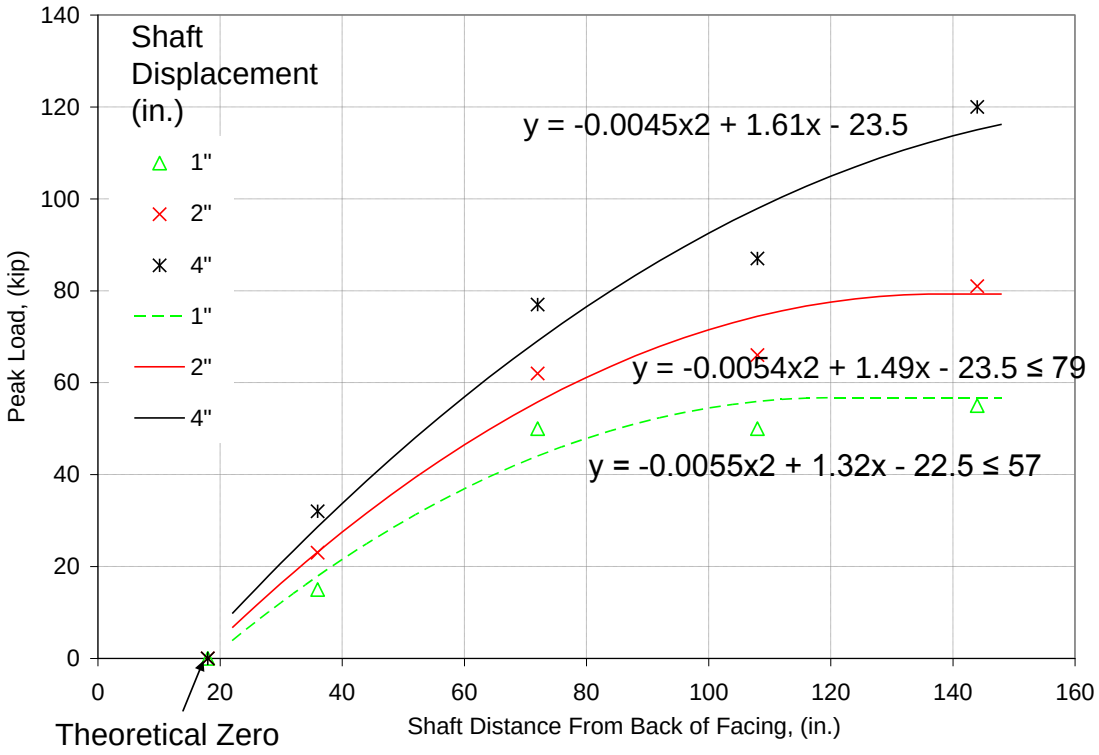

Figure 3.35 Distance from the center of the shaft to the back of the wall facing (D_w) vs peak load at three shaft deflections.

3.3.2 Influence Width of Individual Shafts

A reduction of strength due to a group behavior must be considered if shafts are to be spaced near each other. In addition to the reduction in shaft capacity due to a group effect shown in Table 2.1, a significant effect on wall deflection was also observed. This influence can be seen when the plan view of wall facing deflection for a single shaft is overlain by a group shaft with the same amount of shaft movement (Figure 3.36).

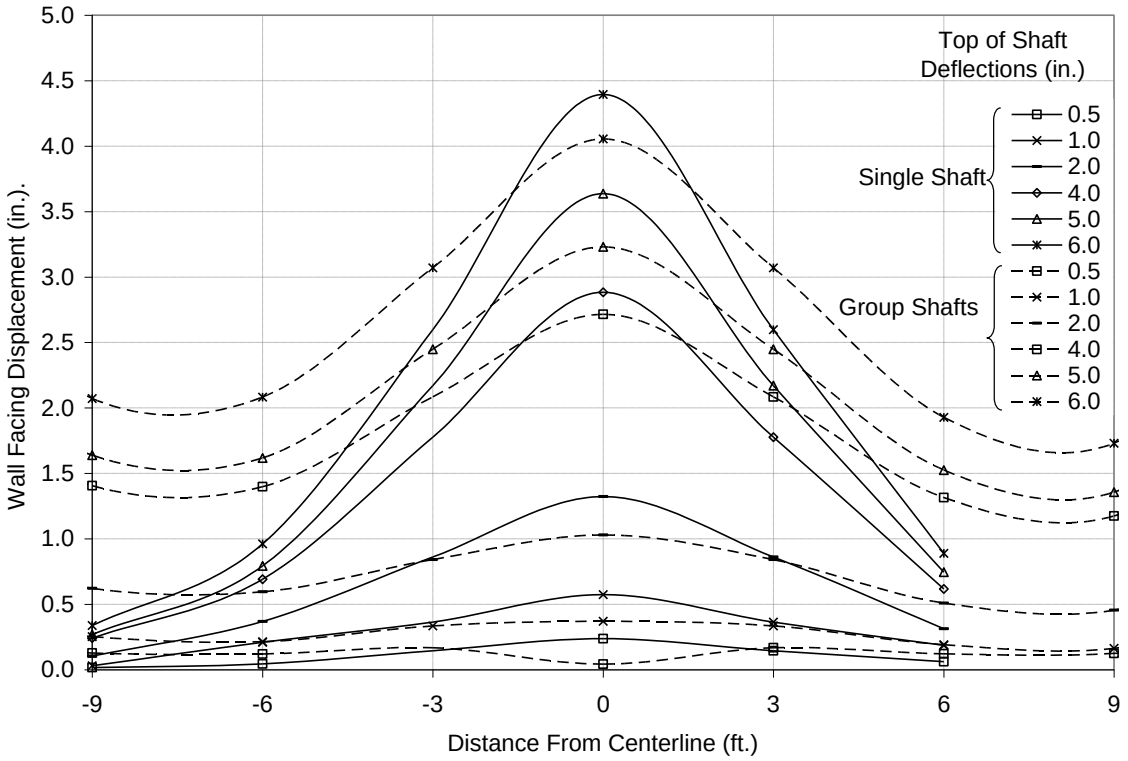

Figure 3.36 Plan view of wall facing deflection for a single shaft and a group shaft versus shaft displacement.

As Figure 3.36 shows, for the group the wall facing deflection decreases away from the center of BG2 until halfway between BG2 and the outside shafts, and then increases toward the outside shafts. Peak wall deflection for the group shafts was also slightly less than peak wall deflection for the individual shaft at the same shaft deflection. This is likely a result of the lower load on the group shafts for a given shaft deflection and the wider distribution of the load on the facing in front of the group as indicated by Figure 3.36.

As shafts are placed farther from the wall face, the lateral capacity increases and the width of influence also increases. For this research the extent of the width of influence of individual shafts (group effect) was defined as the distance along the wall face where deflection was larger than 10% of the maximum wall deflection for the single

shafts. Deflections of wall facing at the elevation of 5.4 m during single shaft testing are shown in Figure 3.37. Widths of influence were based on two inches of maximum wall facing deflection. The width of influence analysis was comparable at intermediate shaft deflections as can be seen in Figure 3.38. Equation 3.1 was developed using the two inches of maximum wall facing deflection criteria, and the relationship shown in Figure 3.38.

$W_{influence}$ (ft) = $1.47D_w + 6.23$ Equation 3.1

D_w = Distance from center of shaft to back of wall facing (ft).
$W_{influence}$ = Shaft spacing to avoid influence from neighboring shafts (ft).

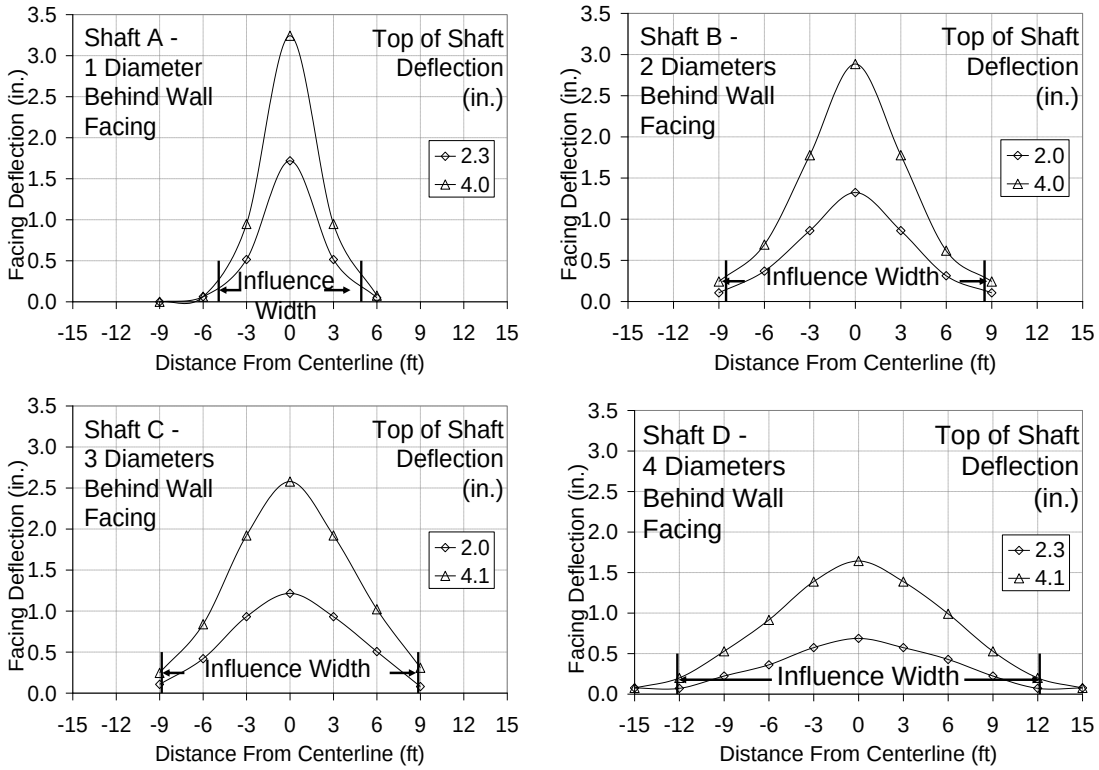

Figure 3.37 Plan view and influence width for single shafts for approximately equal shaft movements.

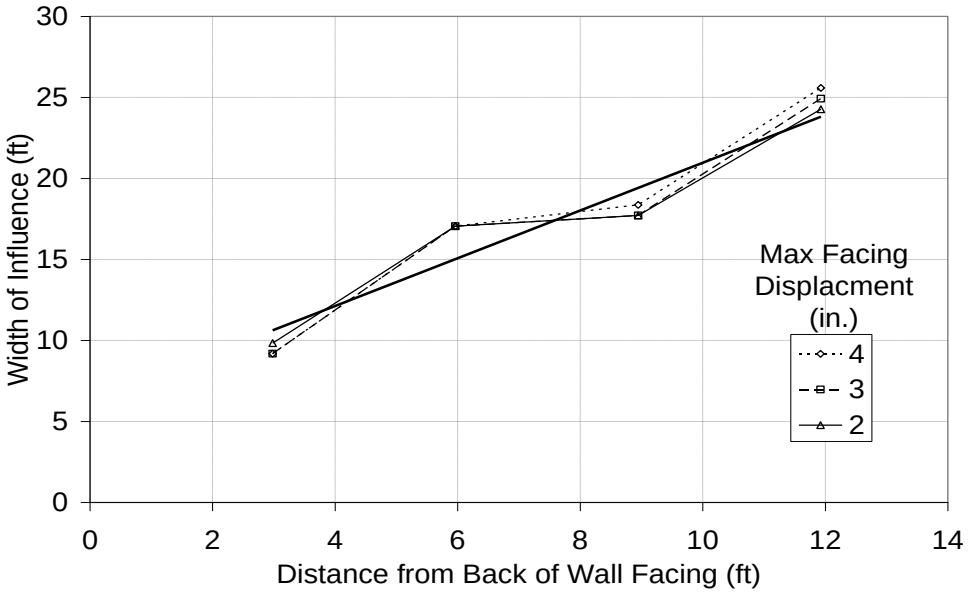

Figure 3.38 Plot of width of influence versus the center of shaft's distance from the back of the wall facing to avoid a group effect.

3.3.3 Estimation of Group Capacity

The capacity of a shaft in a group was estimated using the capacity for Shaft B from Figure 3.39 and the measured width of influence of Shaft B. A reduction factor of 0.88 was calculated by dividing the shaft spacing (15ft) by the measured width of influence (17ft). The reduced curve is plotted in Figure 3.39 and agrees well with the measured group data.

Since test shaft data for a specific configuration will often be unavailable, the group capacity was also estimated from the single shaft capacity for a shaft 6 ft from the wall facing from the equations in Figure 3.35 and reduced by the width of influence calculated from Equation 3.1. The reduced values developed using this method are also plotted in Figure 3.39 and agree well with the group data.

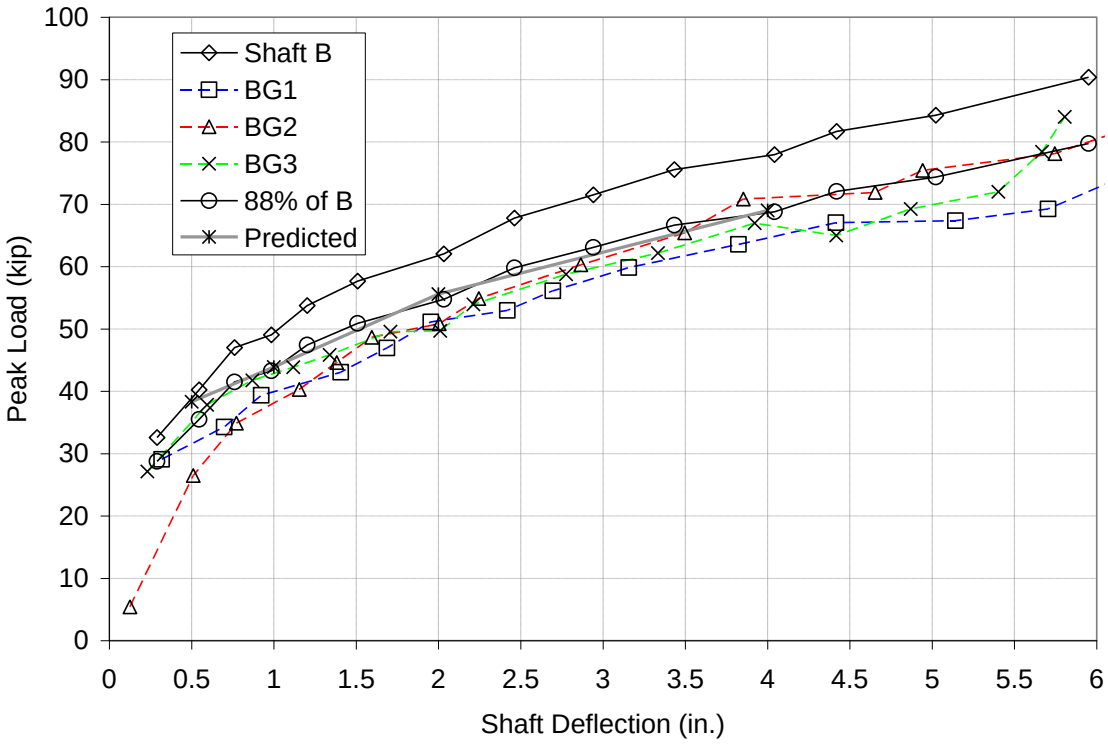

Figure 3.39 Peak load versus displacement for group shafts compared with a single shaft tested individually.

3.3.4 Load Response Prediction of Group Shafts

Preliminary design recommendations are presented using the unfactored load values presented in Tables 2.1 and 2.2.

- When designing for individual shaft capacity without site specific lateral load test information, capacities for shafts behind walls of similar geometry and backfill may be estimated from Table 2.1 or the equations presented in Figure 3.35.
- If the shaft to shaft spacing is less than the width of influence determined using Figure 3.37 or 3.38, then a group effect must be considered. If site specific lateral load data for an individual shaft exists, the capacity of a group shaft may be estimated by reducing the measured lateral capacity of a single shaft by the ratio

of the actual group spacing divided by the observed width of influence (Equation 3.2).

$P_{group} = P'_{single} * S_s' / W'_{influence}$ Equation 3.2

P_{group} = Reduced shaft capacity accounting for group loading (kip).
P'_{single} = Individual shaft lateral capacity measured at the site (kip).
S_s' = Actual shaft spacing (ft).
$W'_{influence}$ = Measured width of influence at the site (ft).

- Where no site specific data exist, the capacity of a group shaft may be estimated by reducing the lateral capacity calculated from the equations in Figure 5 by the ratio of the shaft spacing divided by the width of influence found using Figure 13 (Equation 3.3).

$$P_{group} = \frac{P_{single} * S_s'}{1.47 D_w + 6.23}$$ Equation 3.3

D_w = Distance from center of shaft to back of wall facing (ft).
P_{group} = Reduced shaft capacity accounting for group loading (kip).
P_{single} = Shaft capacity found in Figure 3.35 without group influence kip).
S_s' = Actual shaft spacing (ft).

- The results and recommendations presented in this section are based on a wall constructed with very high quality backfill. Caution should be exercised when using the results of this paper for projects where high quality backfill or similar wall/shaft geometry is not used.
- Shaft height and diameter, wall height, backfill and reinforcement materials are all important variables of system performance. They should be considered when designing without site specific data.

CHAPTER FOUR

Description of Modeling

Numerical modeling of the entire MSE wall – shaft system was conducted to expand on the physical results described in sections 2.1 and 3. The finite difference method was employed using the commercially available software FLAC3D v. 3.1. The following sections include a detailed description of the numerical modeling and calibration process, and a discussion of the relative importance of materials used in wall construction. Loads are reported as a percentage of the original value because other variables may have changed during the study. For this reason, load values from parameter to parameter are internally comparable, but not comparable to the load values of other parametric changes.

4.1 Description of the Modeling Approach and Parametric Study

Numerical modeling began before field testing with a predictive model (Huang et al. 2010). Huang developed a model using a solid continuous facing with a reduced stiffness, and predicted material properties (Figure 4.1). This model was able to accurately predict geogrid strain, system behavior, and was successful in characterizing the shaft top load response curve (Figure 2.26). Based on his success, modeling for this research was begun using a continuous facing. The post-field test model is shown in Figure 4.2. Only one-half of the shaft is required due to the plane of symmetry running from the facing through the center of the shaft. The general zones of material, geogrid reinforcement, and the boundary conditions are shown in Figure 4.2. All boundaries are a roller type with the exception of the plane opposite of the axis of symmetry. Boundary

conditions for this plane were fixed to stabilize the model and enable it to reach equilibrium. Due to the significant distance of this boundary from the plane of symmetry this will not have a significant impact on model results. In following figures the "Run ID" is listed. The "Run ID" describes the geometry and the sequence of the numerical model (i.e. B66 is Shaft B 66th run, TD2 is the Tall Wall Shaft D 2nd run).

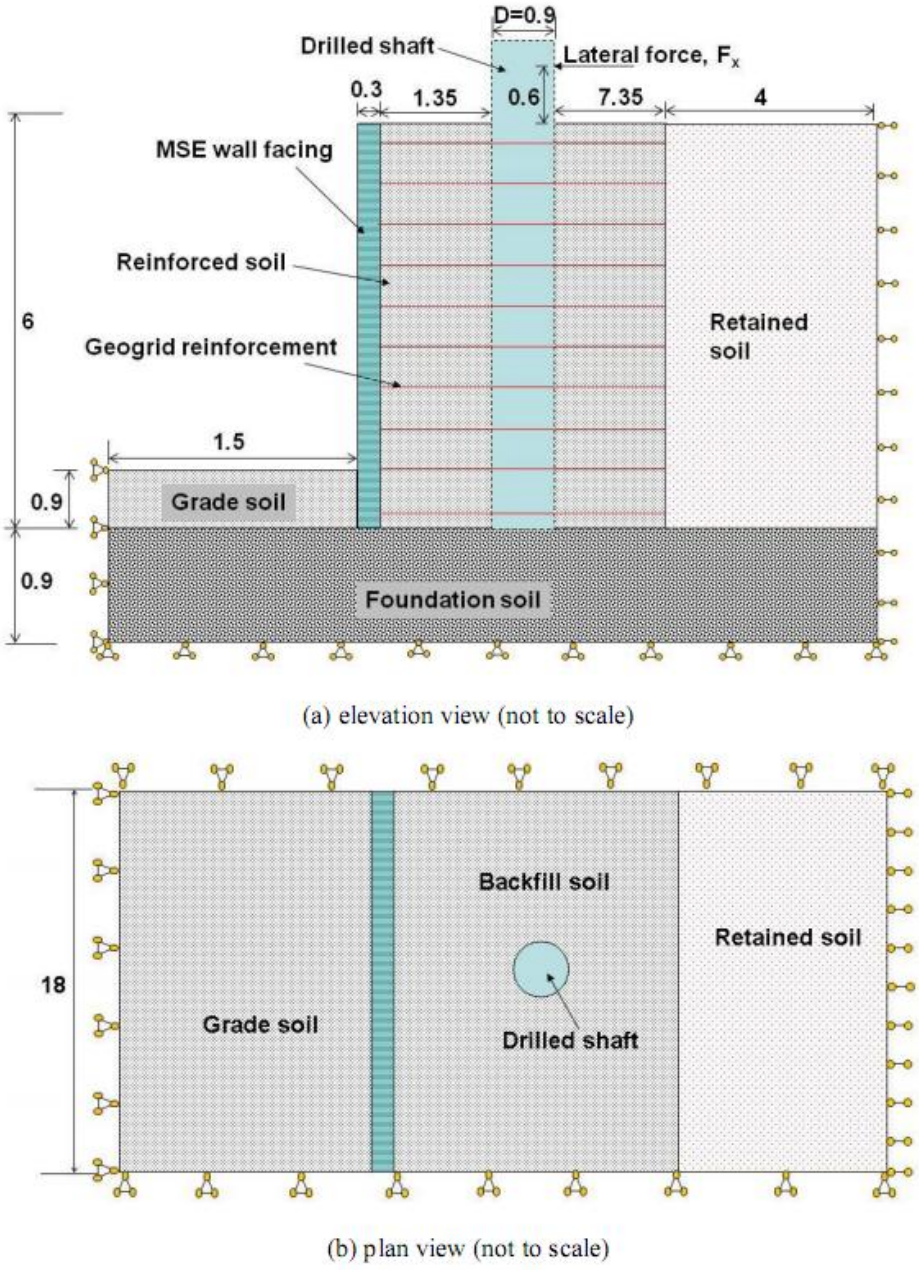

Figure 4.1 Schematic of predictive numerical model (Huang et al. 2010).

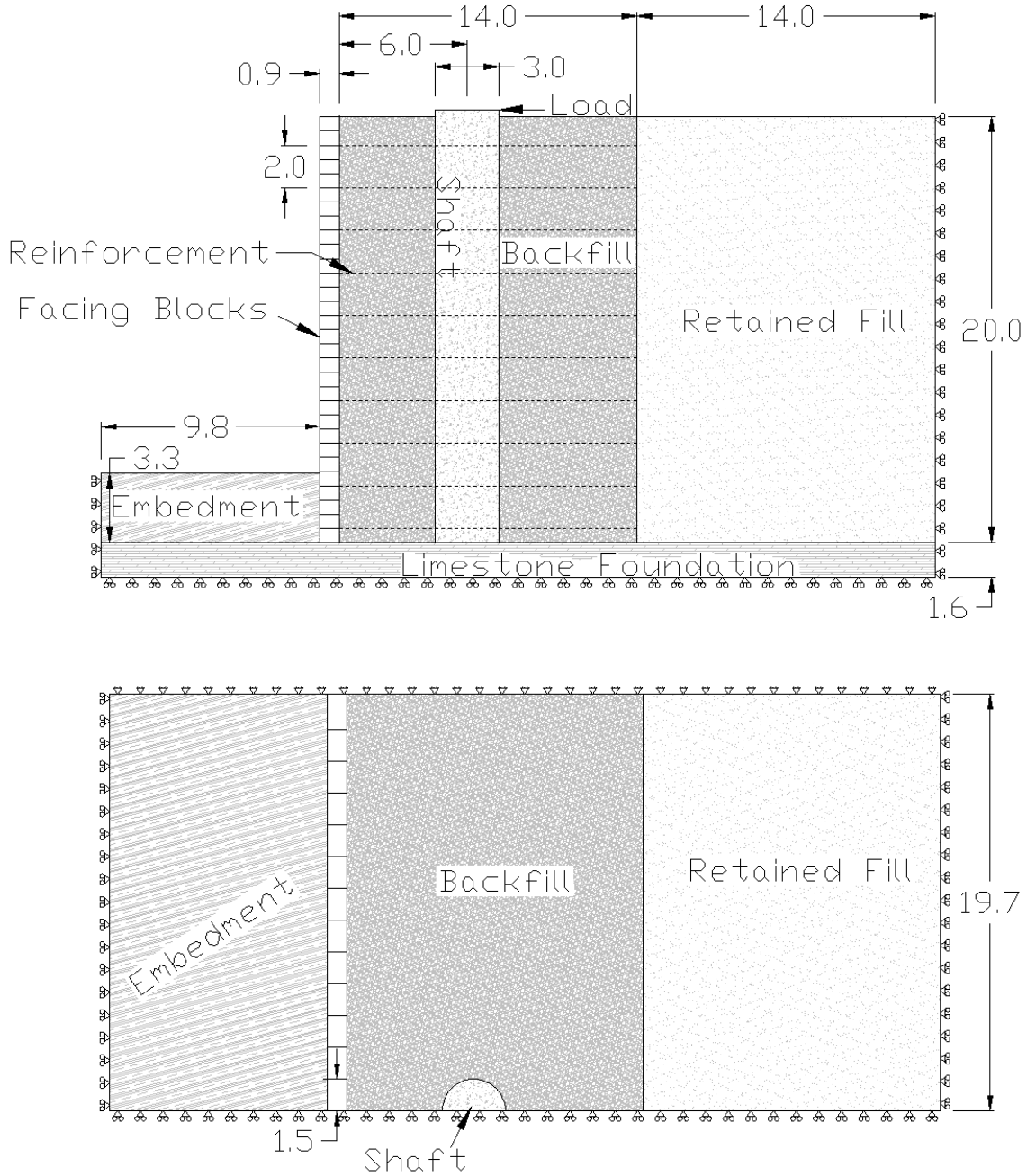

Figure 4.2 Schematic of numerical model. (All dimensions in feet)

4.2 Composite Facing

The initial models in this study used a continuous material as a composite facing to simulate the actual modular block wall of the physical test. To evaluate the behavior of

the composite facing, a parametric study was conducted by reducing the facing thickness (Pierson et al. 2009c). This reduction was done to simulate the low moment capacity of the modular block facing. The following is an excerpt from Pierson et al. 2009c.

> The first model was created used a solid concrete facing the same thickness as the original block facing (11 in). Use of a composite wall facing instead of individual blocks resulted in a wall that was much too stiff. If the facing stiffness is reduced the distribution of stress by the facing will be reduced. To reduce the stiffness the second model was constructed with a facing 2/3 as thick as the previous model, and the third model uses a facing one third as thick as the original block facing. All other properties of the model were the same as the full scale test. In the following figures showing model deflection movement with movements exaggerated by a factor of three. Contour colors indicate magnitude of movement.
>
> As expected the thick facing was too thick for the first model. When laterally loaded the entire solid concrete facing rotated outward. Some bowing of the facing was observed (Figure 4.3), but most of the facing movement was due to facing rotation. In Figure 4.3 this is indicated by the dark color of the motionless embedment and the light color of the moving fill at the top of the wall. This model shows all of the behaviors seen in the field test. A large separation between the back of the reinforced mass and the front of the unreinforced mass was observed due

to the entire wall facing rotating outward (Figure 4.4). Caving behind the shaft as well as shaft pinning was also observed.

The model with a facing thickness two thirds of the original block facing was also too stiff (Figure 4.5), but captured the shape of the block facing after the field test much better than the thickest facing. Material flow around the shaft as well as caving at the back of the shaft was more pronounced with this model than the previous thick facing. A gap at the back of the reinforced mass was also less pronounced with this model (Figure 4.6).

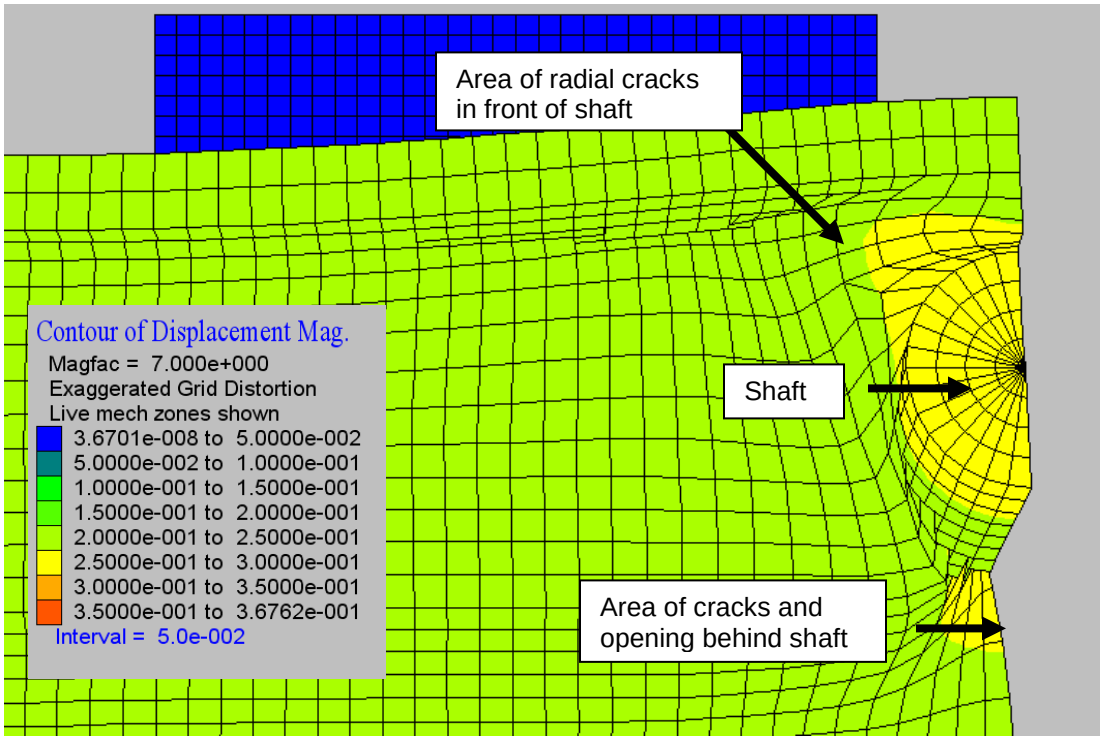

Figure 4.3 Plan view of movement of the model using a 12 in. thick composite facing (contour intervals in meters) (adapted from Pierson et al. 2009c).

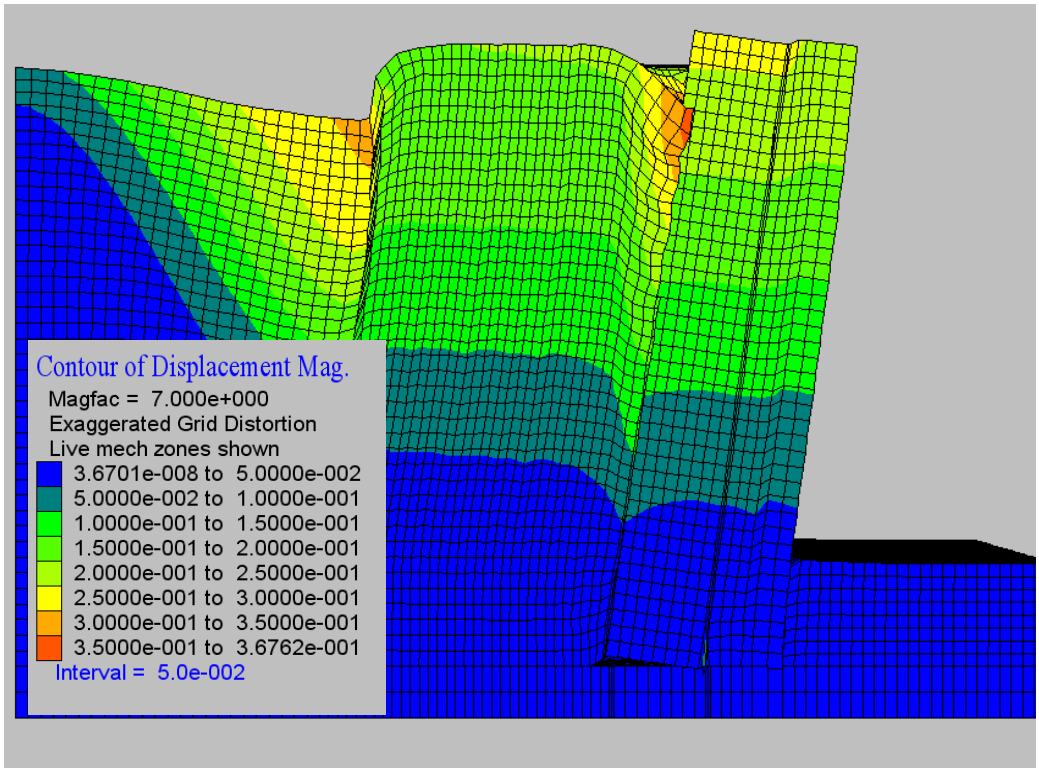

Figure 4.4 Cross-section showing movement of model using thick, 12 in., composite facing (contour intervals in meters) (adapted from Pierson et al. 2009c).

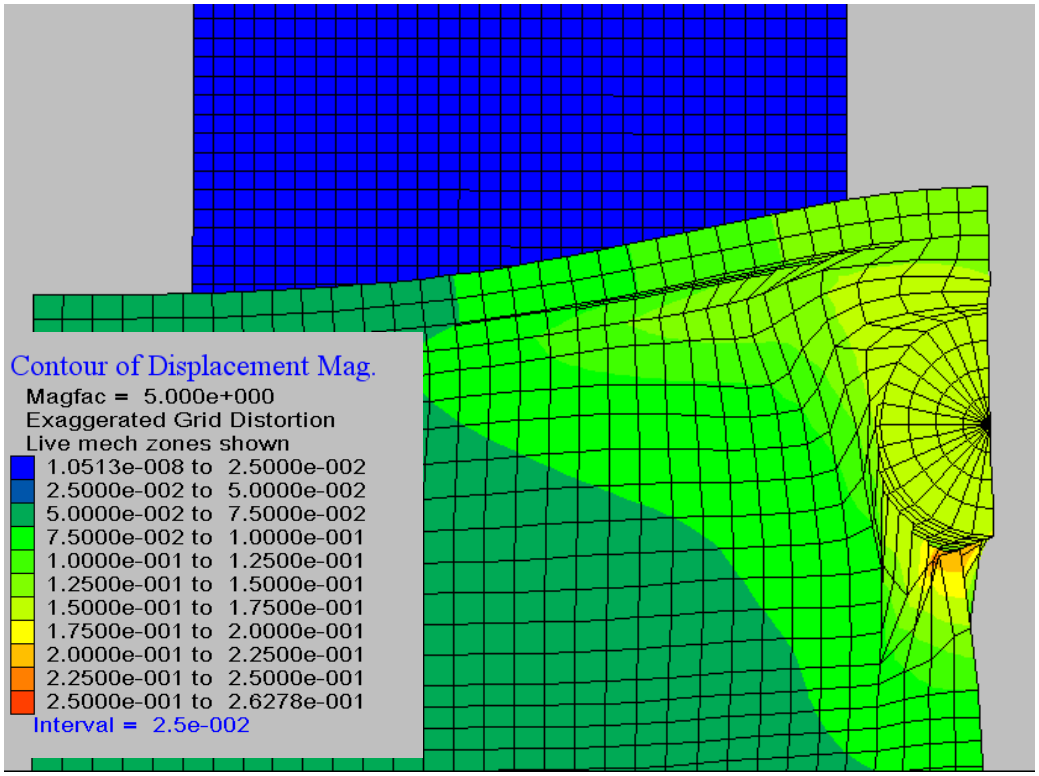

Figure 4.5 Plan view of movement of model using 2/3 thick solid concrete facing (contour intervals in meters) (adapted from Pierson et al. 2009c).

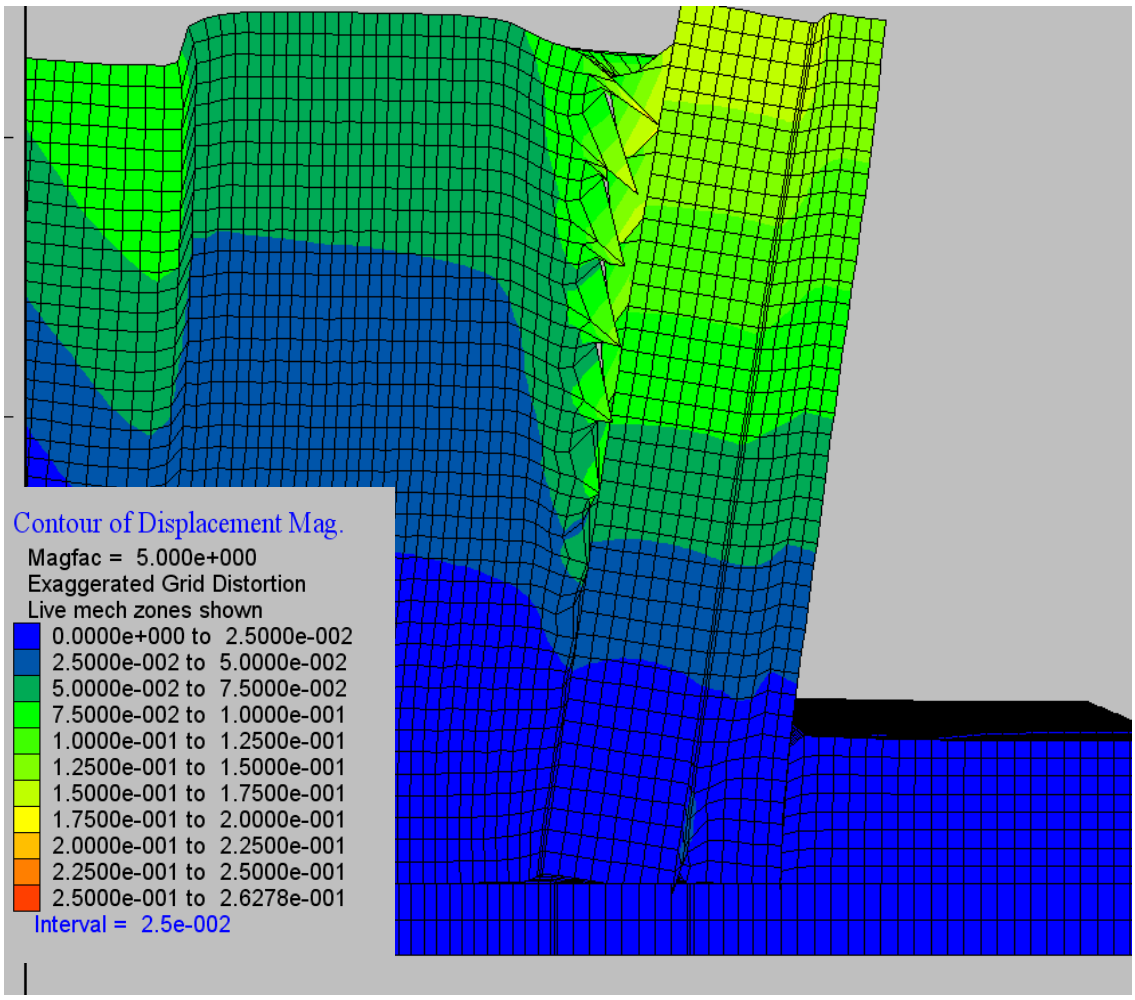

Figure 4.6 Cross-section showing movement of model using 2/3 thick concrete facing (contour intervals in meters) (adapted from Pierson et al. 2009c).

The final model with a facing one third as thick as the original block wall modeled facing deflection the best. Figure 4.7 shows this model's deflection as well as a dark line showing the field test results. This facing was also too stiff when compared with field test data. This model shows the smallest gap opening up at the back of the reinforced zone (Figure 4.8) due to increased local strain near the shaft. Caving and soil flow around the shaft and toward the back of the shaft were the most pronounced with this model.

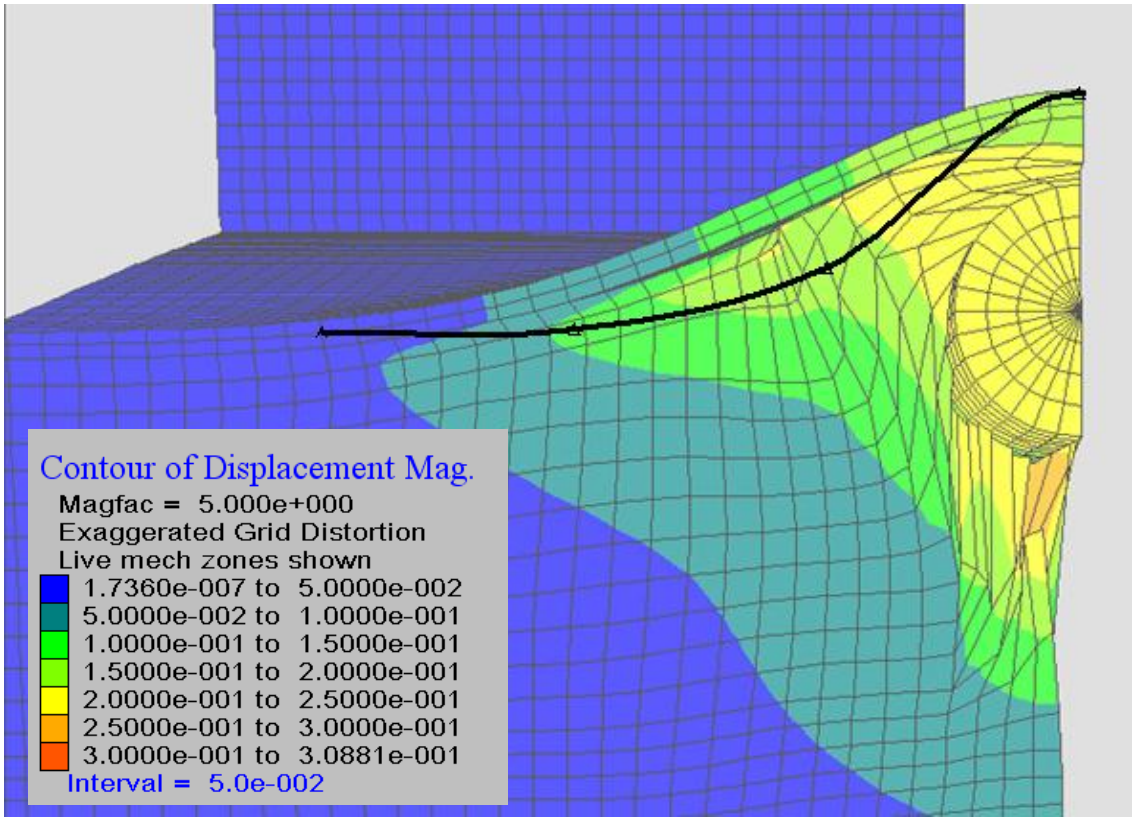

Figure 4.7 Plan view of movement of model using 1/3 thick solid concrete facing. Dark line indicates actual field performance (contour intervals in meters) (adapted from Pierson et al. 2009c).

4.2.1 Model Performance

Cracks opening up behind the reinforced zone, material caving behind the shaft, and diagonal cracks were found in the field during testing. These same behaviors can be found in the computer model.

During tests with significant shaft deflection, a crack opened up at the back of the reinforced zone on the surface within the cohesive top soil. In the model this behavior was most noticeable with the stiffest facing (Figures 4.4 and 4.9). Figure 4.9 shows a larger view of the area at the back of the reinforced zone as well as the location of reinforcement.

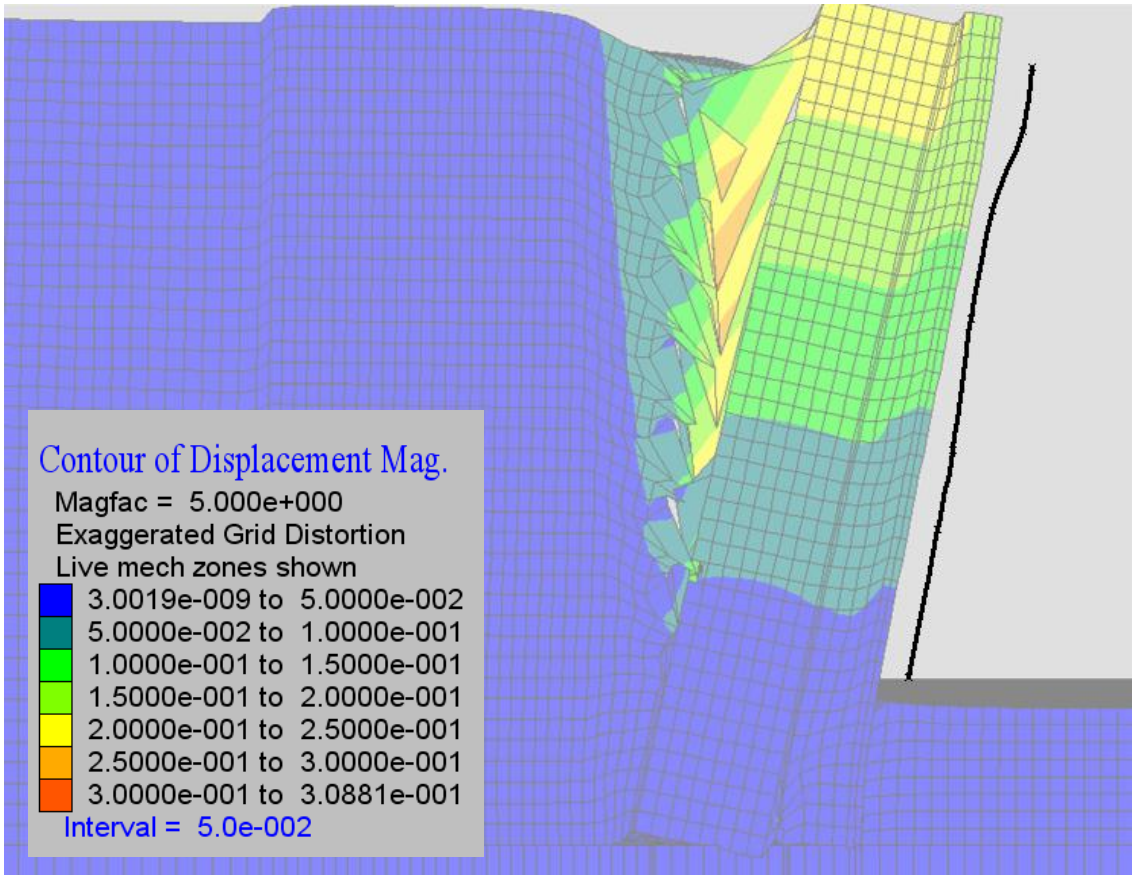

Figure 4.8 Cross-section showing movement of model using 1/3 thick concrete facing. Dark line indicates actual field performance (Line offset to allow comparison) (contour intervals in meters) (adapted from Pierson et al. 2009c).

Caving behind the shaft was also observed in both the field and model tests. Figure 4.9 also shows caving of material into the space left by the moving shaft. This behavior was most noticeable in model tests with the thinnest facing (Figure 4.7 and 4.8).

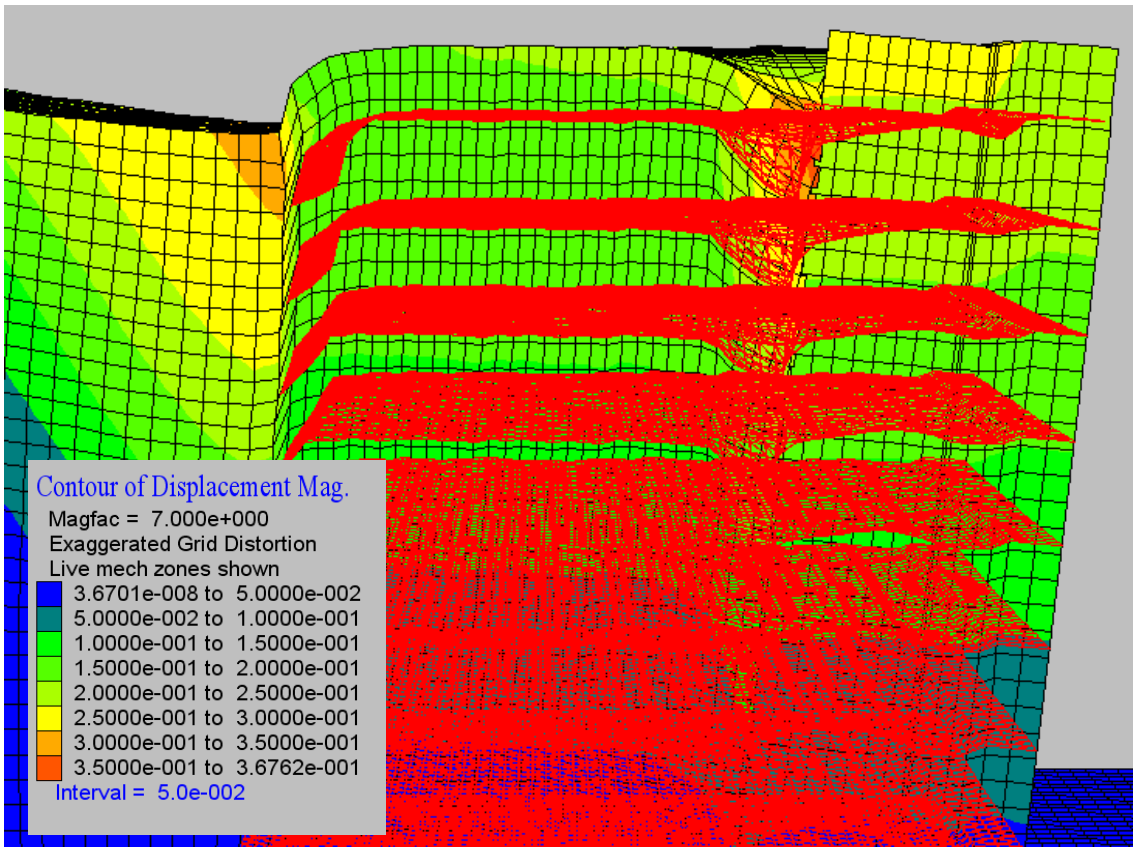

Figure 4.9 Close up of the crack at the back of the reinforced zone and caving at the back of the shaft. Red lines are geogrid (contour intervals in meters) (adapted from Pierson et al. 2009c).

Diagonal tension cracks radiating from the shaft toward the facing were found in the field and similar stress conditions developed in the model. This same pattern of lengthening in the direction of tension (σ_3), and shortening in the direction of compression (σ_1) was predicted by the modeling (Figure 4.10). The model with the thinnest facing (Figures 4.7, 4.8, and 4.10) showed this behavior most prominently.

Based on L-pile analysis shaft pinning is predicted to occur approximately 0.5 m above the base of the shaft. This behavior was also shown in each finite difference model (Figure 4.11).

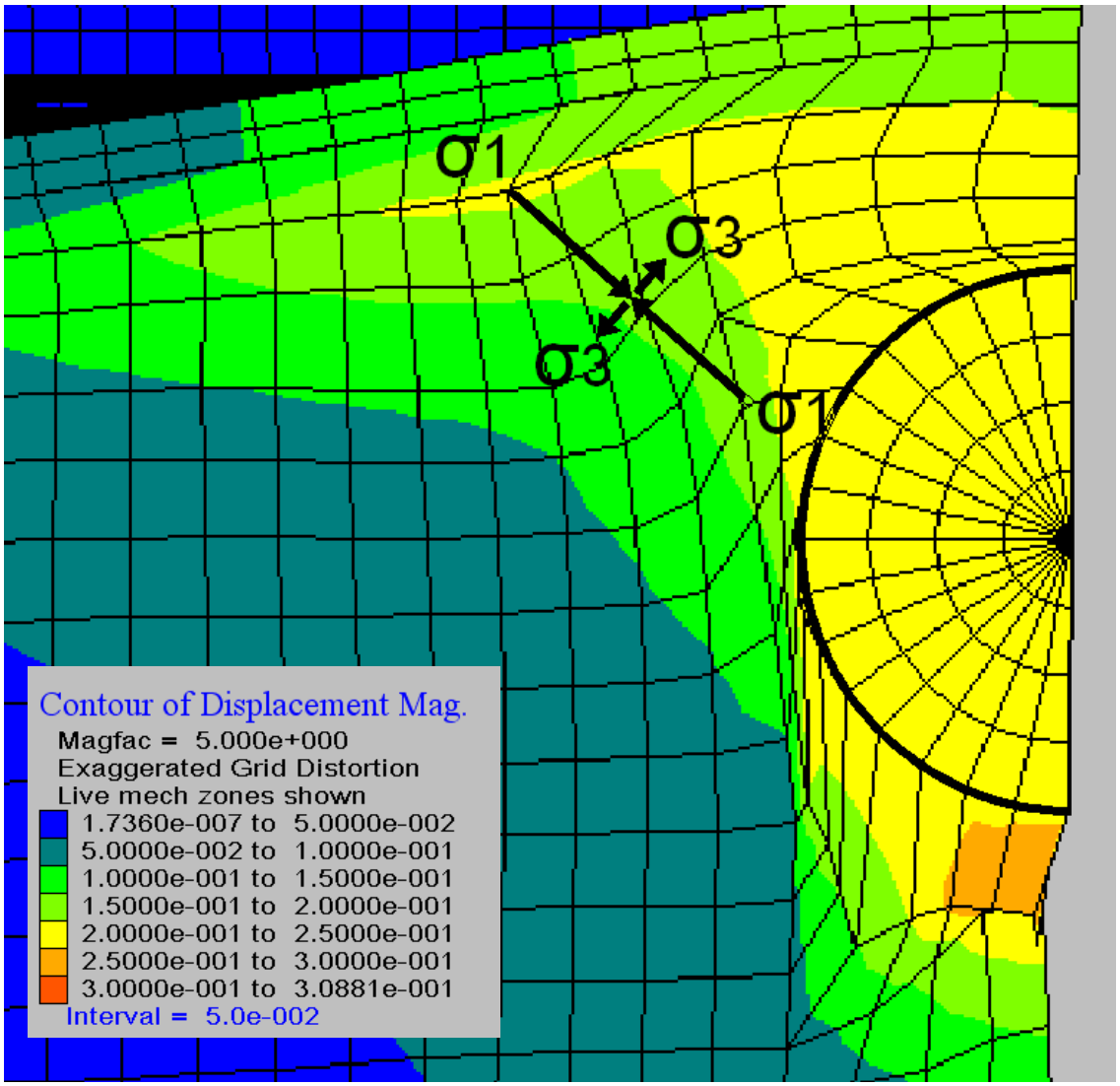

Figure 4.10 Plan view of model showing contours of movement, principal stress direction and distortion of mesh (contour intervals in meters) (adapted from Pierson et al. 2009c).

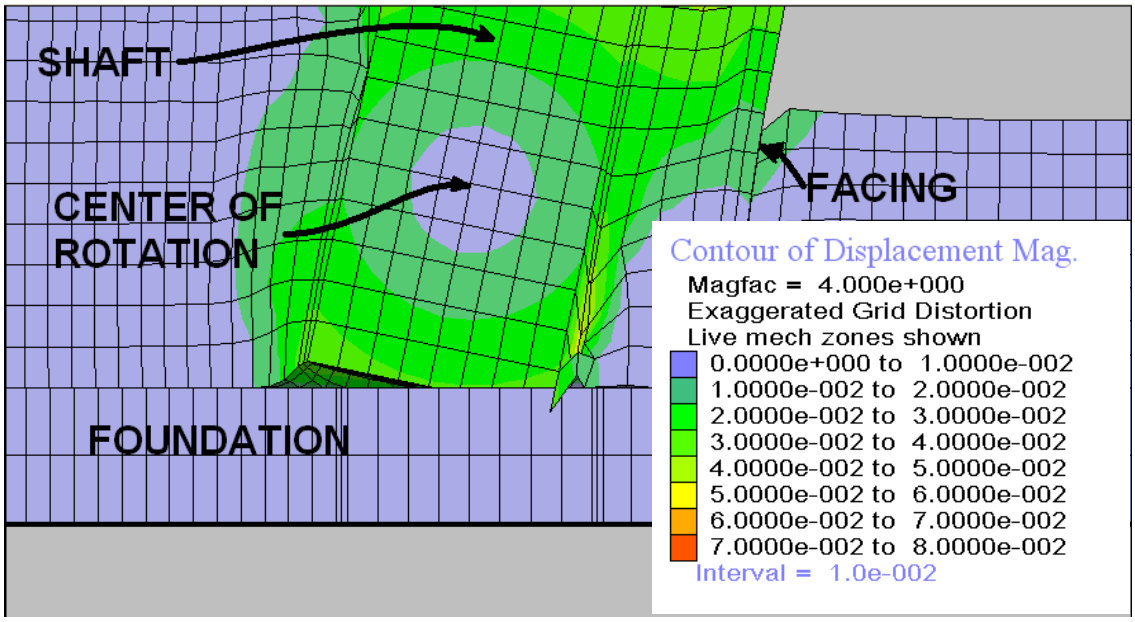

Figure 4.11 Cross section close-up showing pinning (contour intervals in meters) (adapted from Pierson et al. 2009c).

4.2.2 General Conclusions from the Use of a Composite Facing

Based on the results of the full scale testing and results from the models with composite wall facing several conclusions were drawn.

Three-dimensional finite difference modeling can be used to qualitatively model performance of MSE walls with laterally loaded shafts contained within the reinforcement. Details of wall/shaft movement characteristics observed during loading were also observed in the model output. These results showed great promise in developing quantitative models predicting performance of these structures for a wide variety of wall heights, backfill materials, and loading configurations.

Stiffness of the wall facing has an effect on system capacity and a significant influence on shaft capacity. As the stiffness of the wall facing is increased shaft resistance to lateral deflection will also increase and

more of the entire MSE mass will be will be stressed. This behavior is similar to that shown in field testing due to increasing spacing between the shaft and the wall facing. This indicates that to increase lateral foundation capacity one possible alternative to moving a shaft back from the facing is to use a stiffer facing than the modular block facing used in field tests. In the model with decreased facing thickness the strength of the shaft was also decreased, and local deformation was increased in areas near the shaft, and decreased in areas away from the shaft.

Based on the information learned in this study, additional efforts were put into using discrete modular blocks to model the facing.

4.3 Discrete Facing

Due to the sensitivity of the model with the composite facing to changes in wall facing stiffness and a desire for a more accurate representation of the physical test, a model was developed using discrete modular blocks for the facing. In this model each block has a rectangular shape with dimensions approximately equal to the concrete facing blocks used in the physical testing. The blocks were given the stiffness of concrete, and the interaction of each block with the adjacent blocks was governed by interface properties of interfaces applied to all appropriate sides of the facing blocks. Interaction with the blocks and the soil were also governed by interfaces and the geogrid was fixed to the facing blocks preventing a connection failure. No facing failures were observed in field testing, and the properties required to use the facing connection strength in the model were not well known.

The physical modular blocks have a frictional component, a shear pin used for alignment, and stiffness in the normal and sliding directions. In the numerical model each interface attached to the blocks is governed by the Coulomb shear-strength criterion. The properties used to define the interface include interface friction angle, cohesion, normal stiffness, and shear stiffness. These properties were examined in a parametric study to quantify their effect on model behavior. The exception was the normal stiffness of the interfaces, which were considered negligible. The normal stiffness on the block bottom and the block back needed to remain high enough to prevent intrusion from adjacent materials. On the block sides the interface normal stiffness was required to be relatively low to allow the blocks to rotate. The desired effect was to allow the possibility of a small amount of intrusion from one block into the next to simulate physical block rotation. This was deemed acceptable due to the shape of the physical block compared with the model block (Figure 4.12). A soft normal stiffness allows more rotation of the blocks in the model.

4.4 Parametric Study

A series of variables that contribute to the capacity of the system were varied individually to evaluate the relative importance of changes to those variables. When evaluating the effects of the parametric study, the primary items compared were the shaft response and the wall facing displacement for a specific shaft movement. In each of the following graphs only the property discussed has been changed. The analysis is done based on an individual shaft located six feet from the back of the wall facing as measured from the center of the shaft (Shaft B). Similar behavior was observed for other shaft spacings.

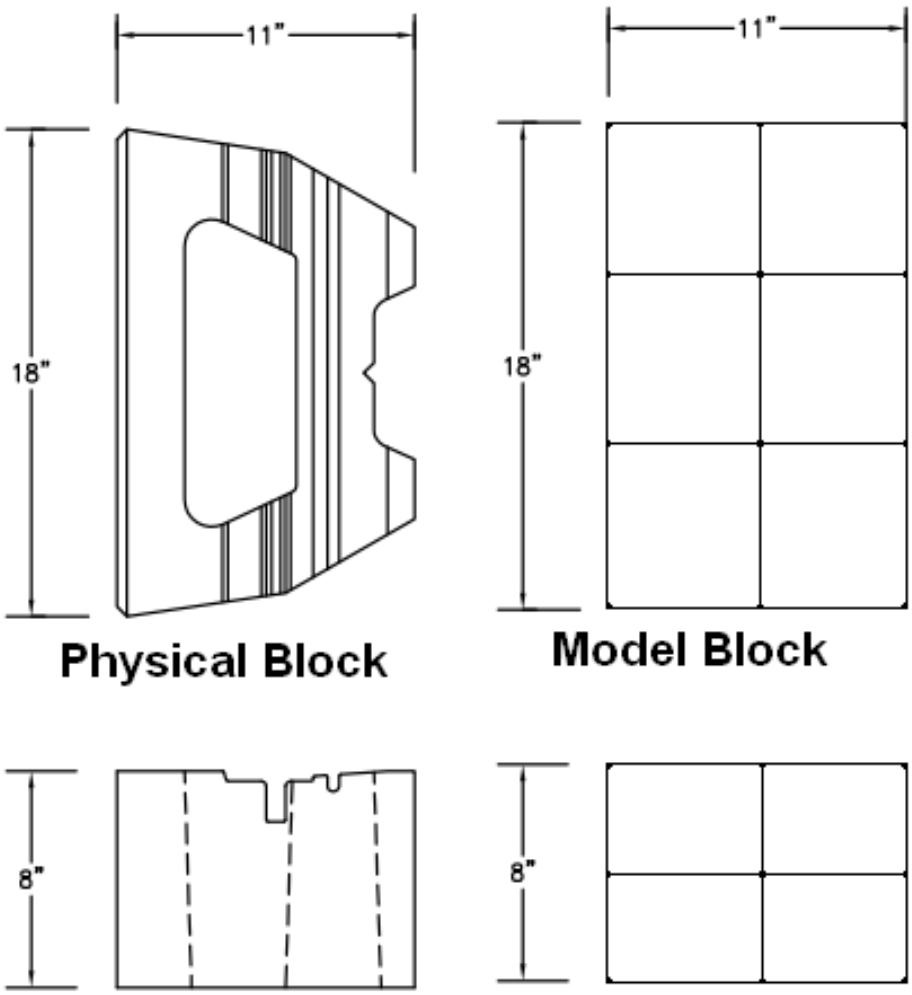

Figure 4.12 Comparison of physical and model block. Note: wedge shape of the physical block not present in the model block.

4.4.1 Bottom of Block Interface Friction Angle and Cohesion

The first parameters discussed are the interface friction angle and the interface cohesion at the base of the modular blocks (Figure 4.13, 4.14, and 4.15). The frictional resistance to sliding at the base of each block in the model was governed by Coulomb shear strength criteria for an interface. These parameters are friction angle and cohesion as seen in equation 4.1. The values of friction used in this study range from 30 degrees to 5 degrees, and the values of cohesion range from 144 to 0 psf. Based on research done by Tassios (Tassios and Vintzēleou, 1987) the coefficient of friction can vary greatly

depending on normal stress at the interface. Where specific testing information is not available, the appropriate range of friction angle is from 30 to 40 degrees (Concrete Construction Magazine, 1992). The interface cohesion term is used to simulate the shear connector between physical blocks. This physical connector does allow movement without failing (slop). Therefore, a reduced cohesion term was used to allow more movement of the facing. The reduced value of interface cohesion is 144 psf, which is about 45 percent of physical connector's shear strength. The influence of cohesion is negligible at the base of the wall due to the high normal force which causes the interface friction angle to dominate behavior.

Shear Strength = $c + \sigma' \tan\varphi'$ Equation 4.1

c = cohesion
σ' = effective normal stress
φ' = effective friction angle

Figure 4.13 shows the lateral resistance of the shaft was slightly reduced by reducing the block resistance to sliding. Figure 4.14 shows increased movement of the wall facing when the resistance of the blocks to sliding is decreased. Figure 4.15 shows increasing offset from block to block with decreasing frictional resistance to sliding on the base of the block. Based on this study the influence on shaft capacity and wall deformations from the interface friction angle in the appropriate range is very small. Using no cohesion reduced the lateral load measured at the shaft top (Figure 4.13), but caused substantial offset from block to block in the vertical direction (Figure 4.15). This was not observed in the test and does not represent a realistic situation due to the existence of the alignment pins between blocks in the vertical direction.

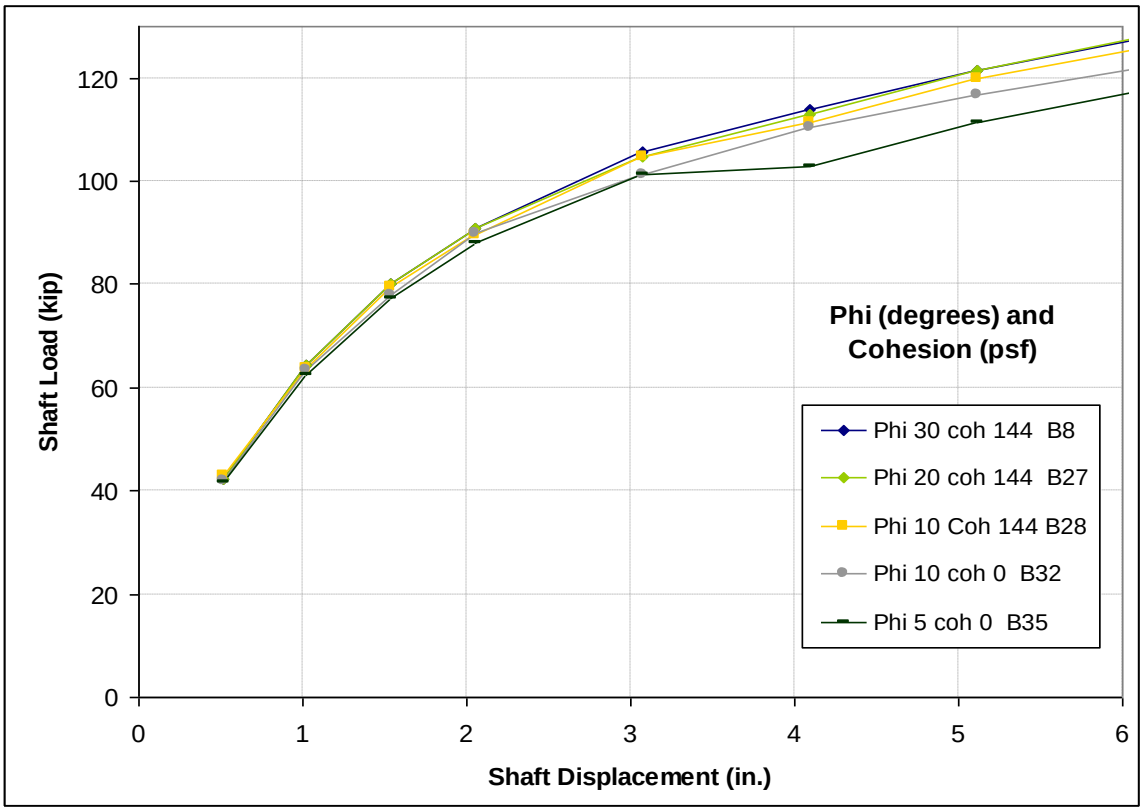

Figure 4.13 Shaft response with differing bottom of the block interface properties.

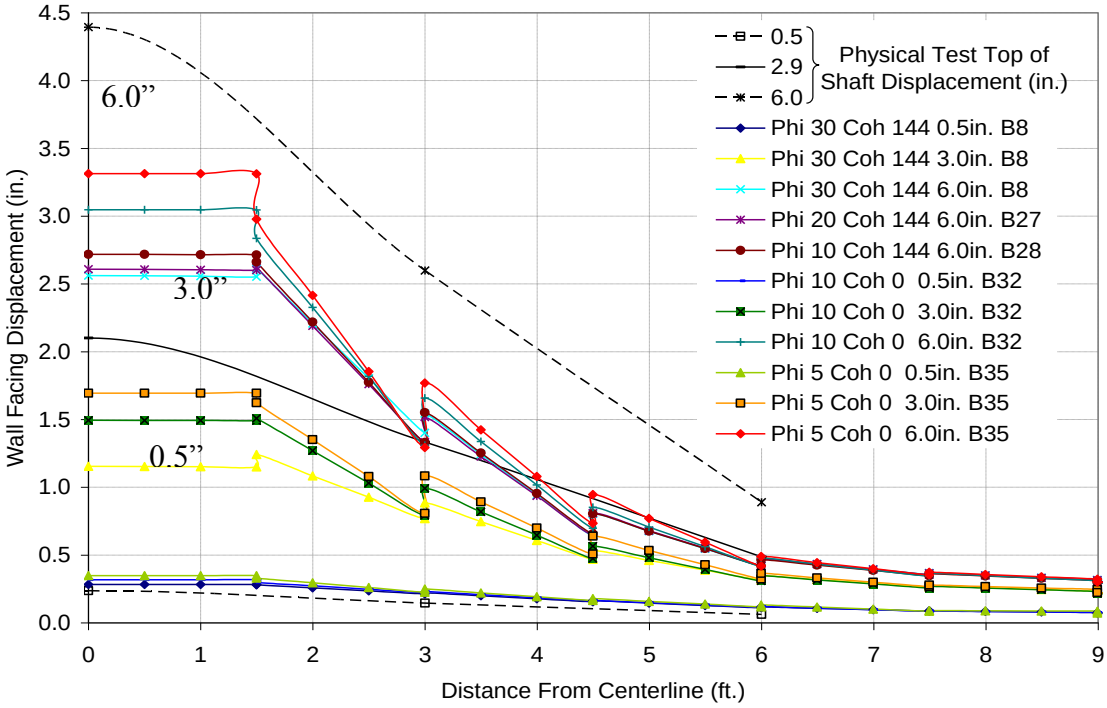

Figure 4.14 Plan view of wall facing displacement at 17.7 feet elevation. Physical test data compared with model results with differing bottom of the block interface properties for equal shaft top movements (0.5, 3.0, and 6.0 inches).

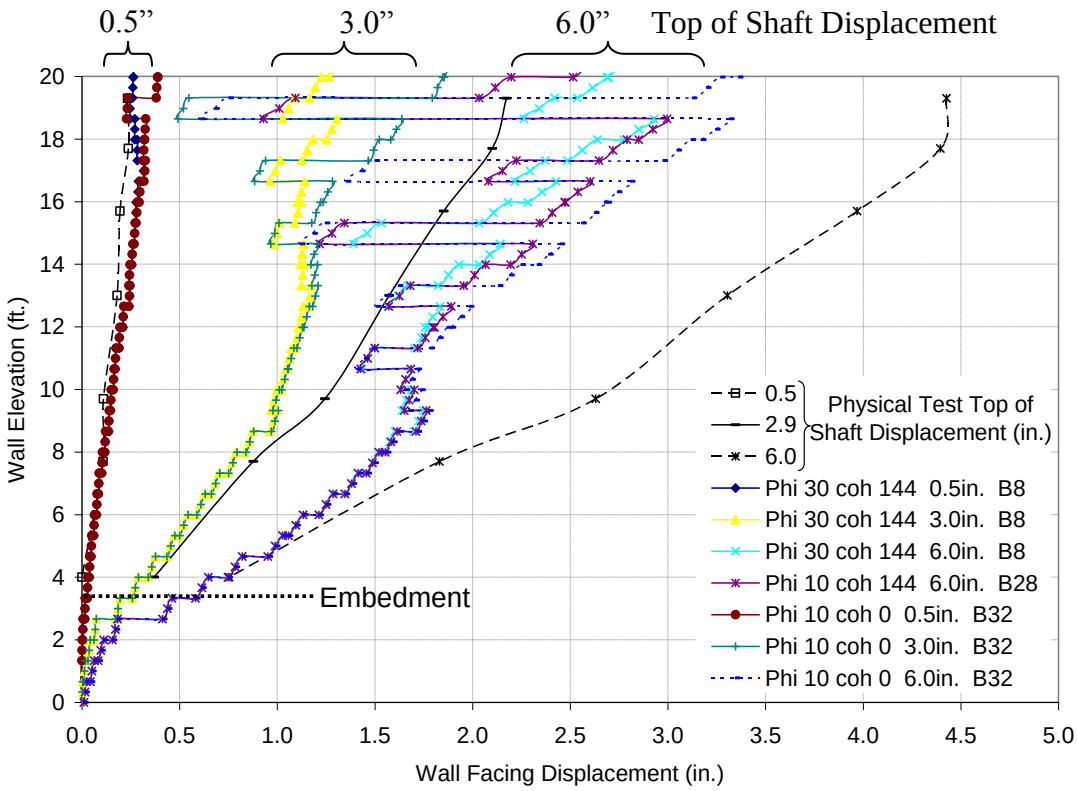

Figure 4.15 Cross section view of wall facing displacement directly in front of the shaft. Physical test data compared with model results with differing bottom of the block interface properties for equal shaft top movements (0.5, 3.0, and 6.0 inches).

4.4.2 Bottom of Block Interface Shear Stiffness

The facing interface shear stiffness was investigated to determine the impact of values in the reasonable range. Each interface also has a shear stiffness which controls the amount of shear movement if there is no slip along the interface as determined from equation 4.1. The shear stiffness of the blocks will be between the stiffness of concrete (2,550 ksi) and the stiffness of HDPE (116 ksi) which is sandwiched between blocks on courses with reinforcement. Due to the alignment pins discussed in the previous paragraphs, additional “slop” in the facing may be needed to simulate the physical blocks’ ability to rotate about the alignment pin.

Using a shear stiffness higher than concrete and lower than the HDPE reinforcement showed a slight influence on the shaft load at a given displacement (Figure

4.16) and significant influence on the behavior of the wall facing (Figure 4.17 and 4.18). The reduced block bottom interface shear stiffness reduced the top of shaft load at a given shaft displacement by 8% at ½ in. and 5% at 3 in. The impact to the response of the facing was more significant. With the reduced block bottom interface shear stiffness there was a much larger offset of blocks in the vertical direction at the location of reinforcement. This was not seen in the test and indicates a significant deviation in the behavior of the model when compared with the field test. The reduced shear stiffness also produced a much larger wall facing movement for a given shaft movement (Figure 4.17 and 4.18).

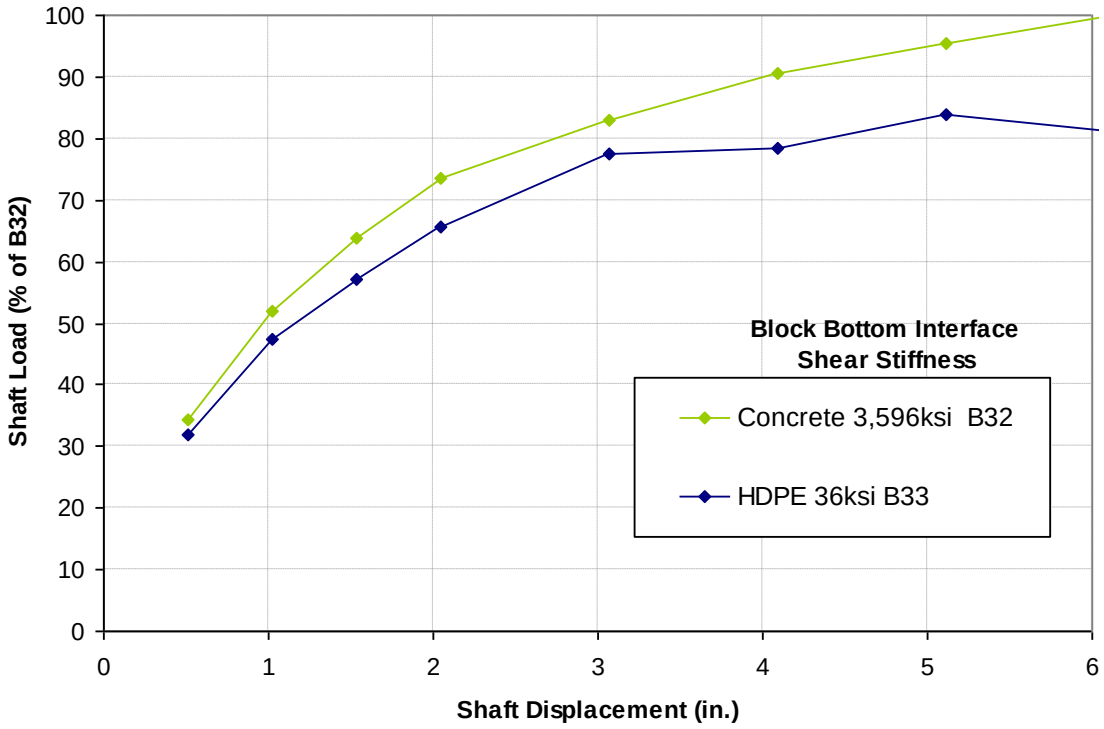

Figure 4.16 Shaft load response curves with a block bottom interface stiffness greater than concrete and less than HDPE.

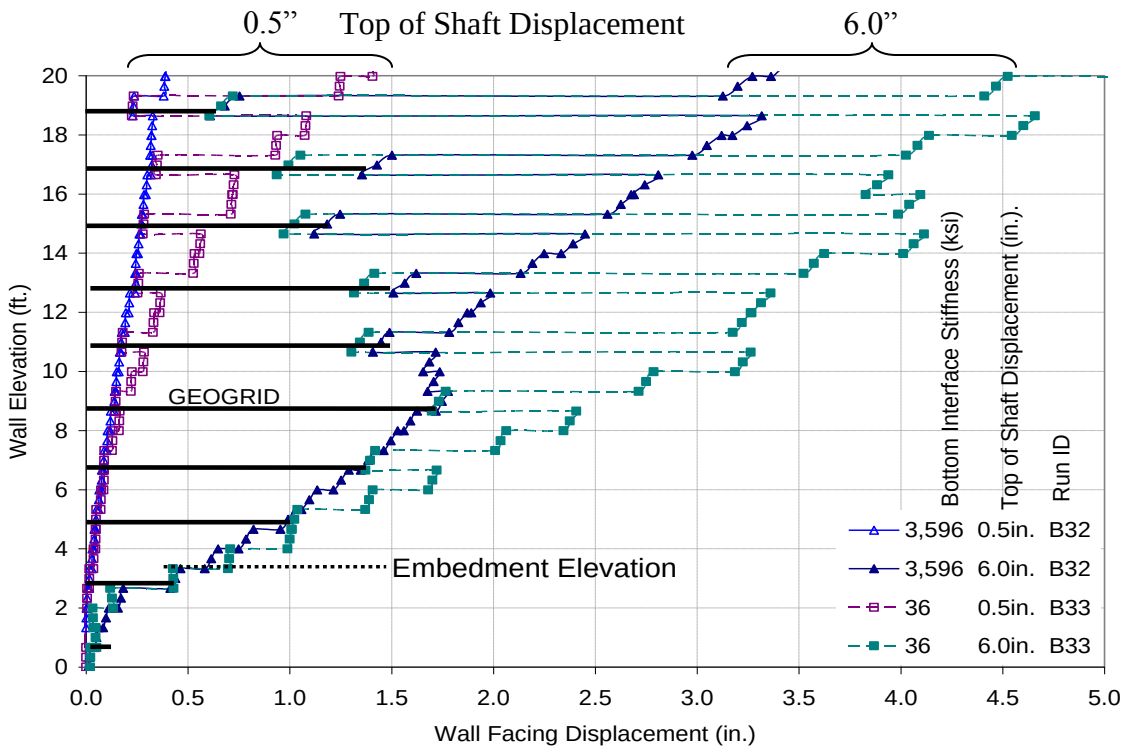

Figure 4.17 Profile view of wall facing displacement for two given shaft displacements using two different values of interface shear stiffness, one greater than concrete and one less than HDPE. (Black lines show geogrid locations)

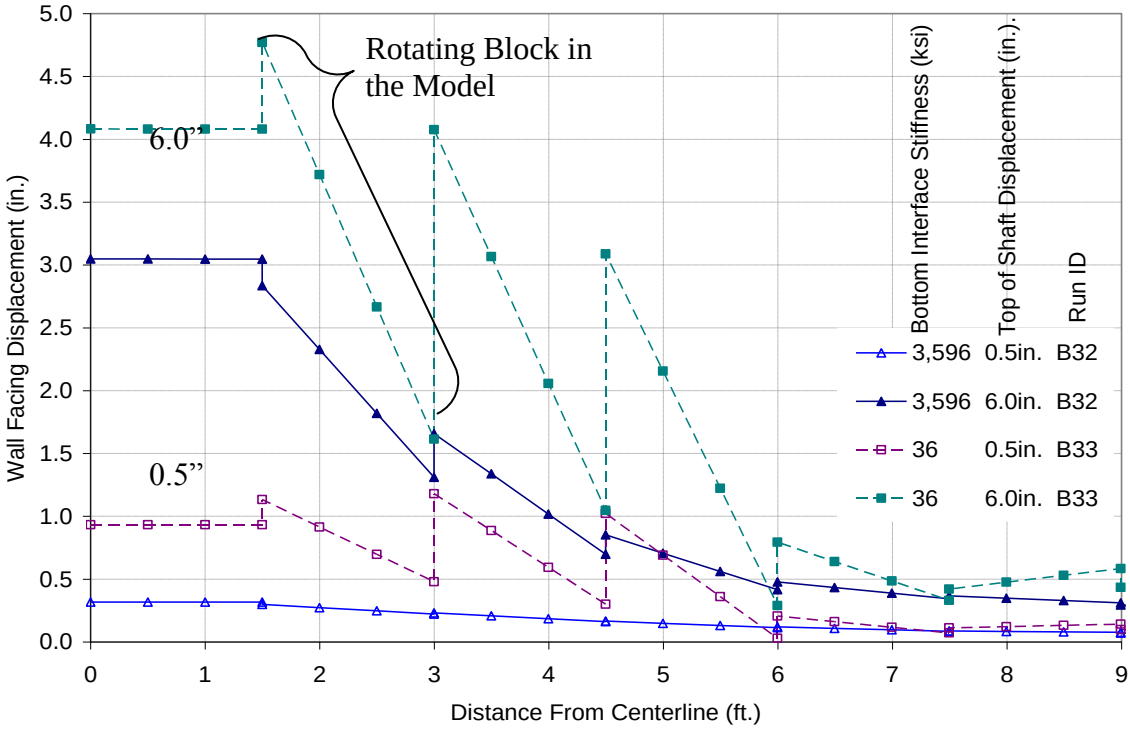

Figure 4.18 Plan view of wall facing displacement at 17.7 feet elevation for two given shaft displacements using two different values of interface shear stiffness, one greater than concrete and one less than HDPE.

4.4.3 Aggregate Properties

4.4.3.1 Aggregate Stiffness

The aggregate modulus found from triaxial testing was estimated to be 662 ksf. This is low for gravel which typically has a range from 2,000 to 4,000 ksf (Arora, 1987). Due to this the influence of aggregate modulus was investigated. The modulus found in triaxial testing was compared with the low end of the accepted range for gravel. With a 300% increase in modulus little change was found in the shaft load response (Figure 4.19) or the wall facing displacement (Figure 4.20 and 4.21).

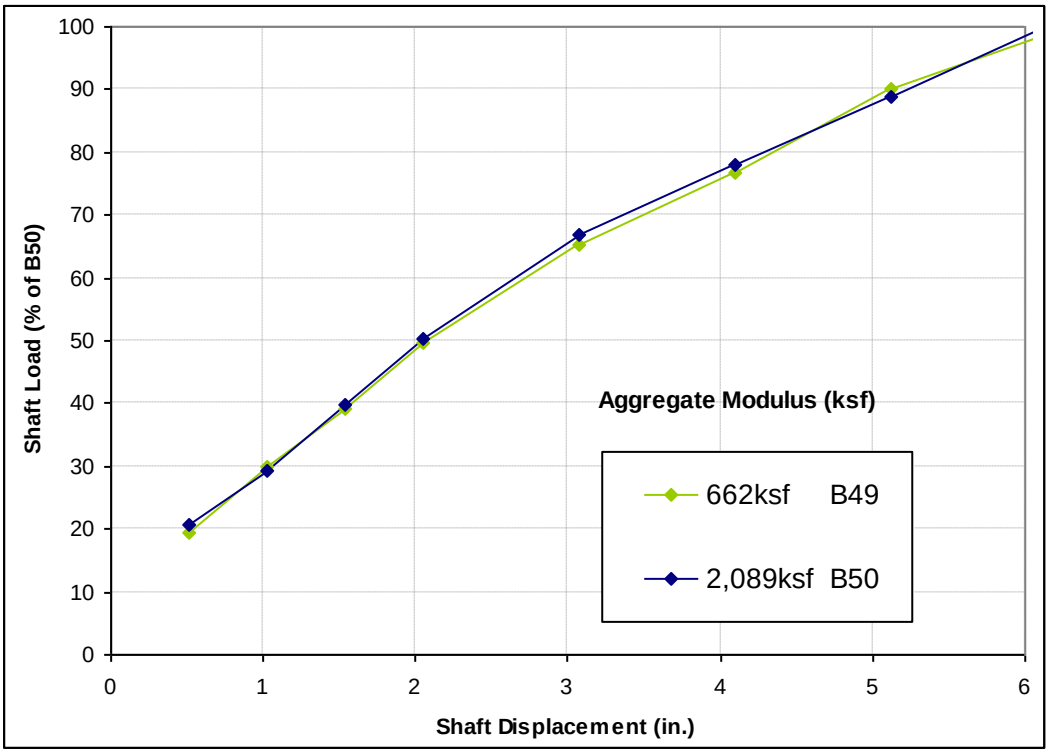

Figure 4.19 Shaft load response curves with two values of aggregate modulus.

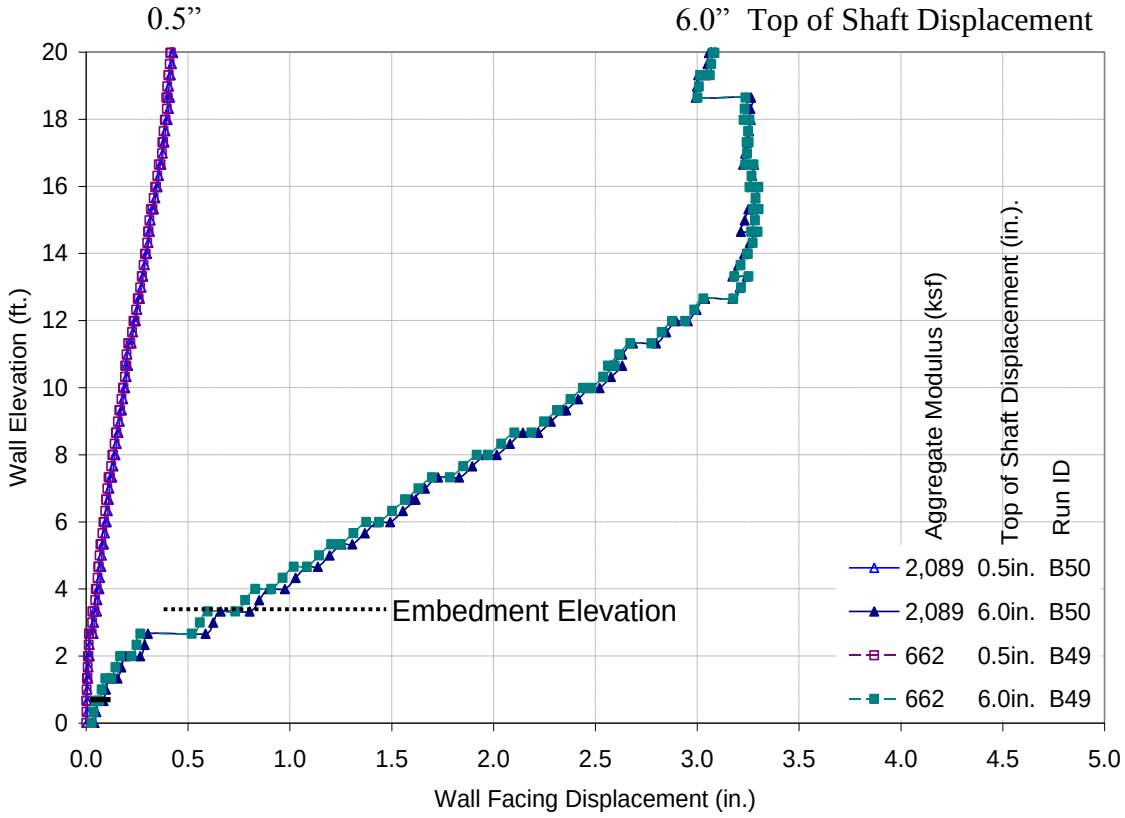

Figure 4.20 Profile view of wall facing displacement for two given shaft displacements using two values of aggregate modulus.

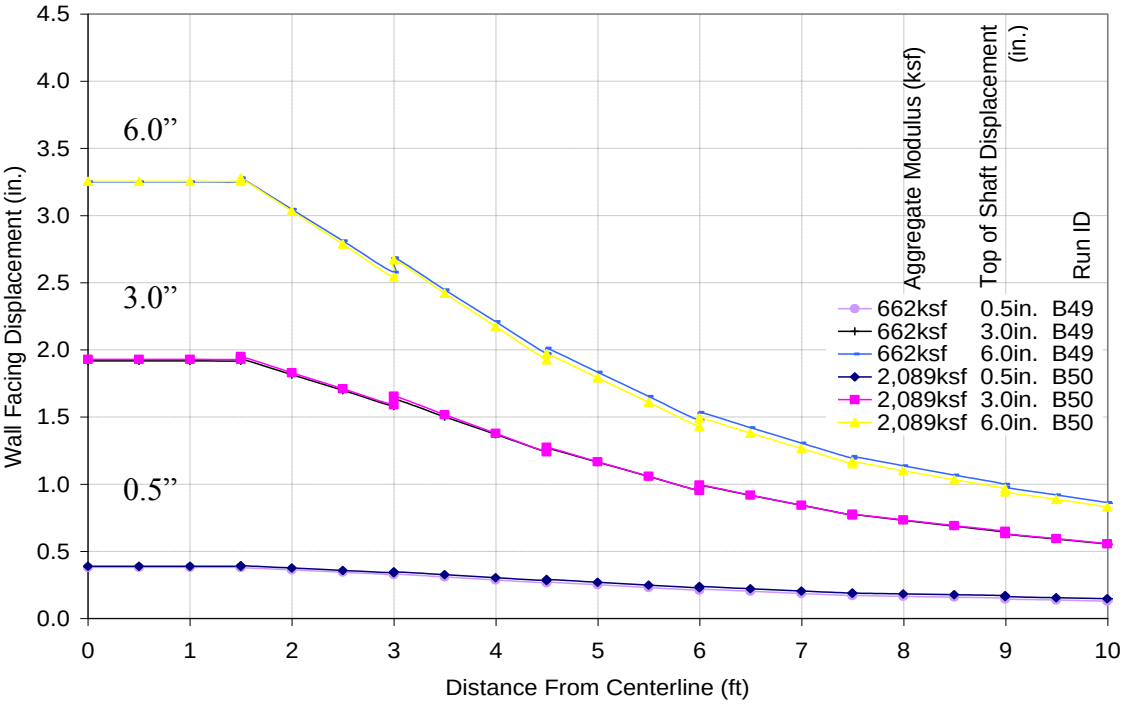

Figure 4.21 Plan view of wall facing displacement at 17.7 feet elevation for two given shaft displacements using two values of aggregate modulus.

4.4.3.2 Aggregate Friction Angle

The aggregate friction angle found in triaxial testing was 51°. This is higher than typical values used for design, so a slightly reduced value of 45° was evaluated. During this evaluation the geogrid on soil interface friction angle (δ) was left constant at 40°. Typically this value would change along with the friction angle of the soil (Φ). The relationship between the friction angle of the soil and the geogrid, the coefficient of interaction (C_i), is shown in equation 4.2. For gravels C_i is typically assumed to be 0.8 for design, but have been found to be as high as 1.07. In this case, the coefficient of interaction changed from 0.68 to 0.84 due to the decrease in soil friction angle and no decrease in geogrid on soil friction angle. A reduced soil friction angle reduced the load response curve by 11% at ½ in. of shaft movement and 2% at 3 in. of shaft movement (Figure 4.22). Little difference in wall facing movement was found when the aggregate friction angle was reduced (Figure 4.23 and 4.24).

$$C_i = \tan(\delta)/\tan(\Phi) \qquad \text{Equation 4.2}$$

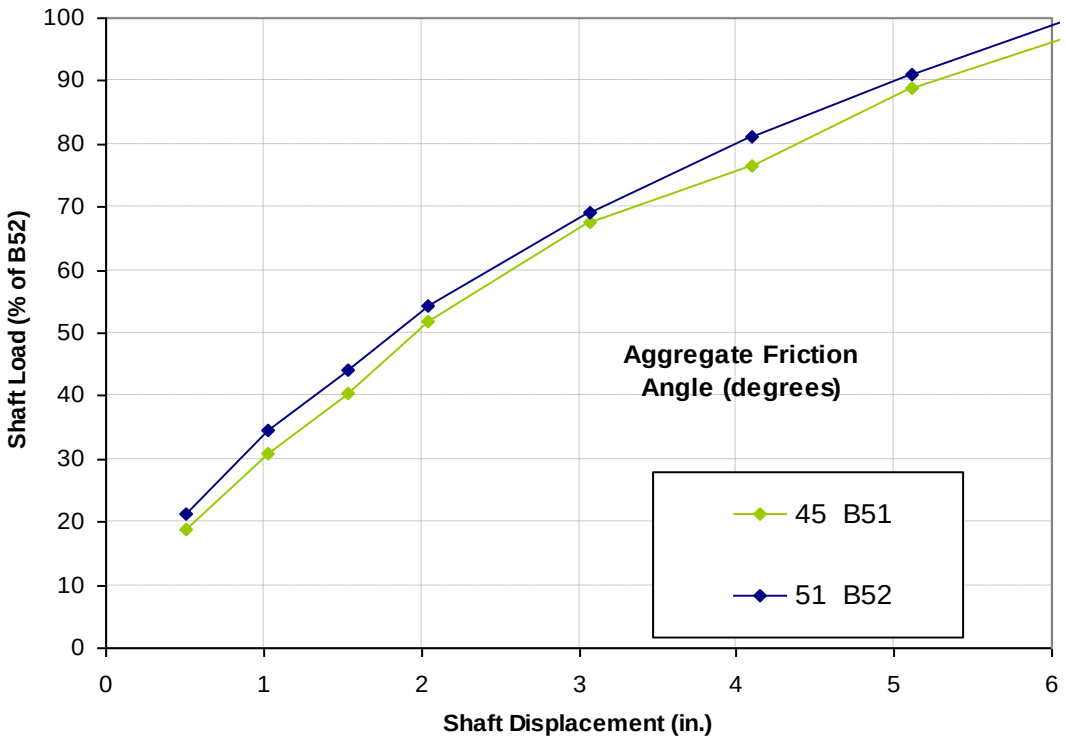

Figure 4.22 Shaft load response curves with two aggregate friction angles.

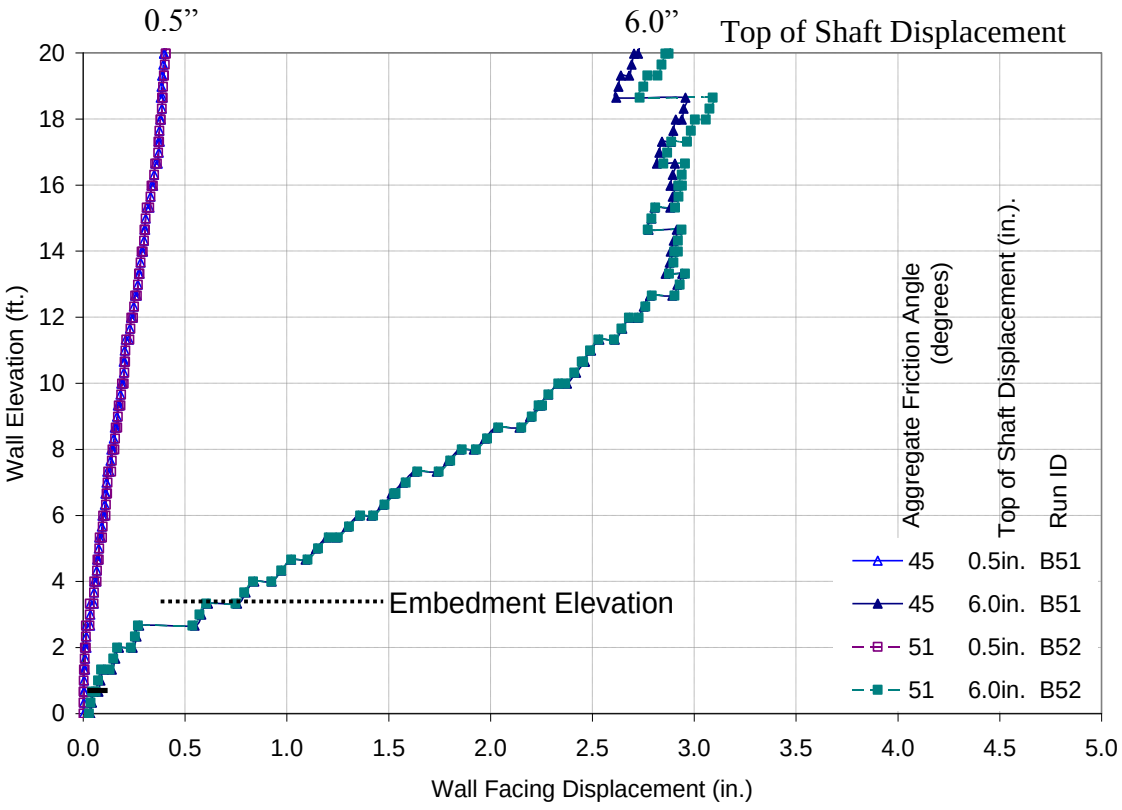

Figure 4.23 Profile view of wall facing displacement for two given shaft displacements using two different aggregate friction angles.

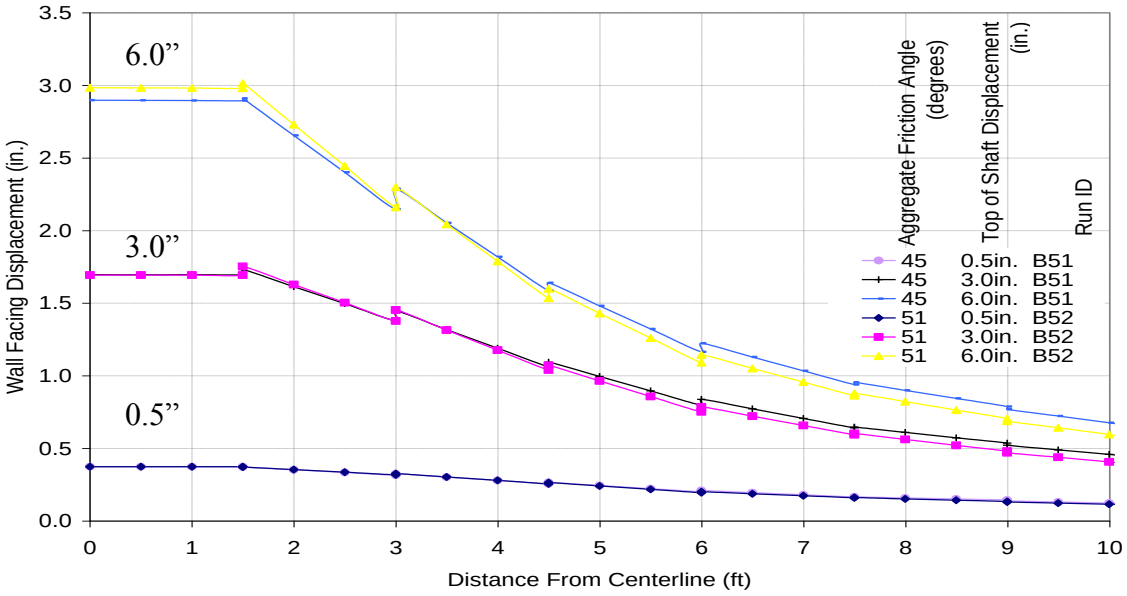

Figure 4.24 Plan view of wall facing displacement at 17.7 feet elevation for two given shaft displacements using two different aggregate friction angles.

4.4.4 Geogrid Properties

The properties associated with the uniaxial geogrid used in this study are not completely known. Values for stiffness at 5% strain and for strength are reported by the manufacturer in the strong direction. However the stiffness is not completely linear even at very low strains (5% or less). Testing at the University of Kansas indicates the stiffness at 1 percent strain to be at least twice the reported value at 5 percent as discussed in Section 3.2.3. Much less is known about stiffness in the weak direction, the in-plane shear stiffness, or other geogrid properties associated. The following section describes how the geogrid properties affect the model behavior.

4.4.4.1 Geogrid Interface Coefficient of Interaction

Values for the grid to soil interface friction angle (δ) were calculated using the coefficient of geogrid interaction (C_i) which is an estimated value (Equation 4.2). The range of C_i from 1.0 to 0.68 was evaluated to determine the sensitivity of the model to these parameters (Figures 4.25, 4.26, and 4.27). A reduced coefficient of geogrid

interaction reduces the lateral load measured at the shaft by 7% at ½ in. of shaft movement and 17% at 3 in. of shaft movement (Figure 4.25). The wall facing generally showed less movement for a given shaft displacement with a higher geogrid coefficient of interaction (Figure 4.26 and 4.27). The exception was the area directly in front of the shafts from 8 ft elevation to 14 ft elevation (Figure 4.26). The higher value of C_i produced more offset between blocks in the vertical direction (Figure 4.26) and more widely distributed the wall facing movement in the horizontal direction (Figure 4.27).

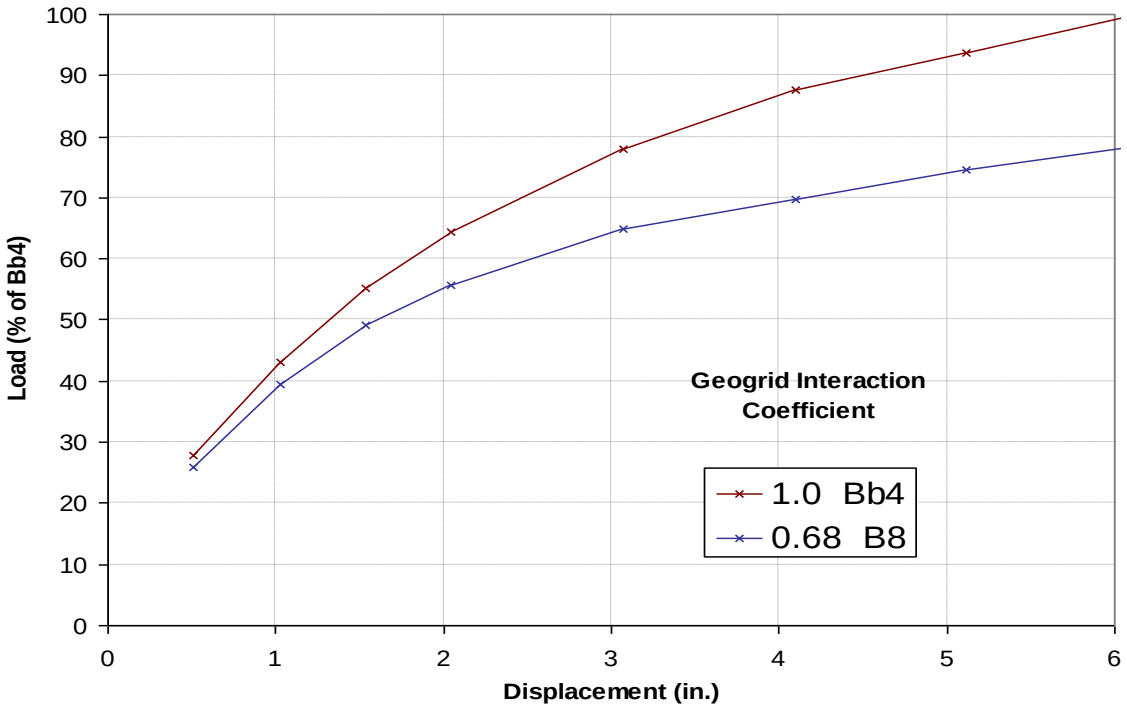

Figure 4.25 Shaft load response curves for two geogrid interaction coefficients.

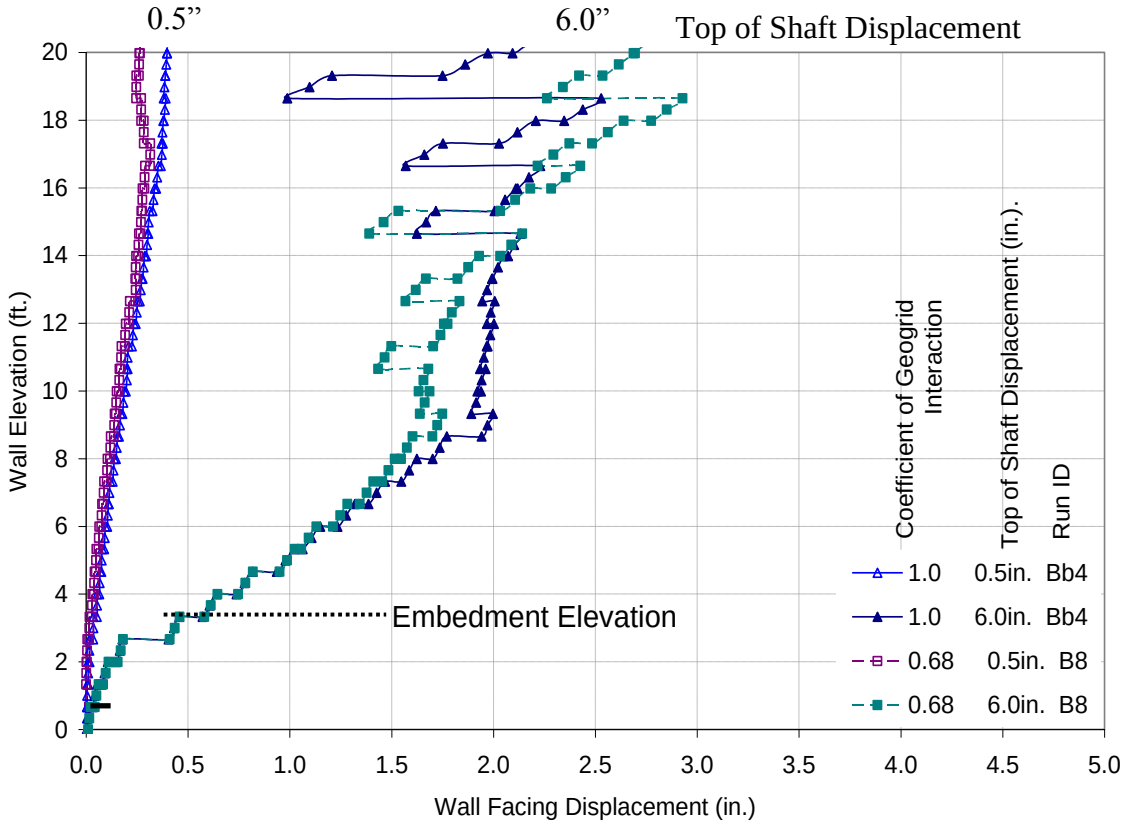

Figure 2.26 Profile view of wall facing displacement for two given shaft displacements using two different geogrid interaction coefficients.

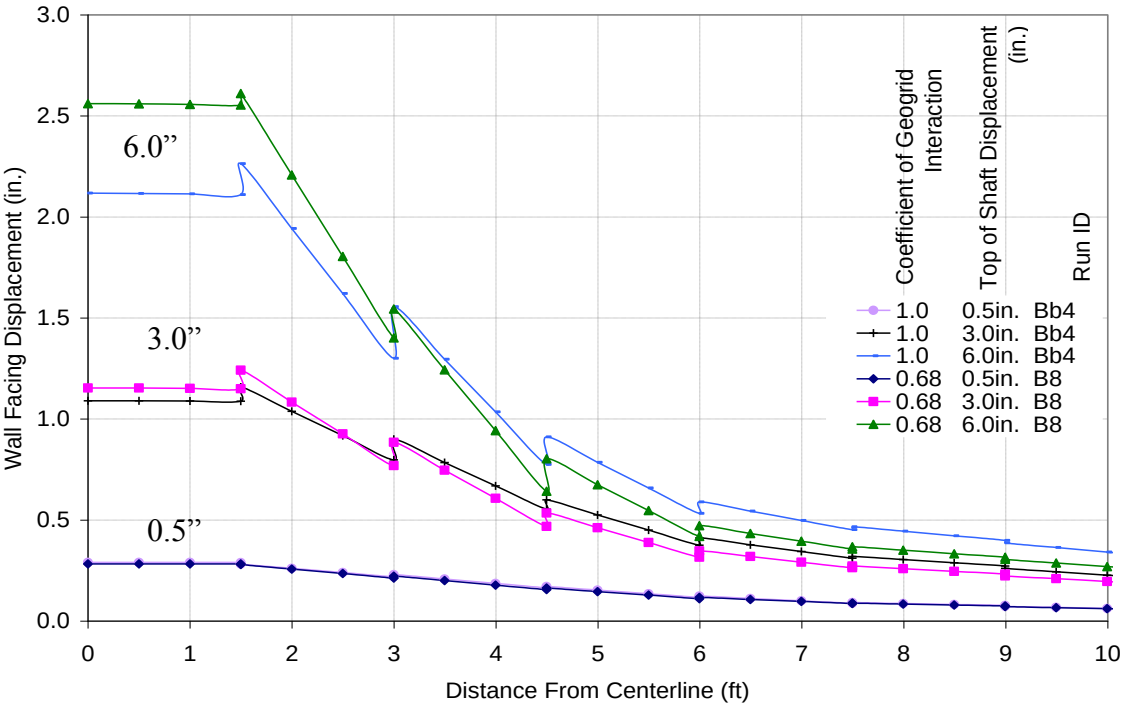

Figure 4.27 Plan view of wall facing displacement at 17.7 feet elevation for two given shaft displacements using two different geogrid interaction coefficients.

4.4.4.2 Geogrid Interface Shear Stiffness

The property that controls geogrid movement with respect to the soil before Coulomb sliding occurs is geogrid interface shear stiffness. The grid interface shear stiffness behaves in the same way as the interface shear stiffness at other interfaces. Several models were used to evaluate the magnitude of this effect. Accepted values for this parameter are not readily available in the literature. Estimates of this property were made based on qualitative observations of physical behavior and from several numerical models used to evaluate the geogrid interface shear stiffness. A change from 100ksi/in. to 1,000ksi/in. produced noticeable results, but a change from 1,000ksi/in. to 10,000ksi/in. showed no effect on the shaft top load response curve (Figure 4.28). For stiffness values above 1,000 ksi/in., the geogrid essentially does not move until the shear stress is greater than the shear resistance. Increasing the interface shear stiffness of the geogrid from 100ksi/in. to 1,000ksi/in. increased the shaft capacity 11% for ½ in. of shaft displacement and 6% at 3 in. of shaft displacement (Figure 4.28). The increased geogrid interface shear stiffness produced nearly the same wall facing movement directly in front of the shaft (Figure 4.29), and reduced wall facing displacement further away from the shaft centerline (Figure 4.30)

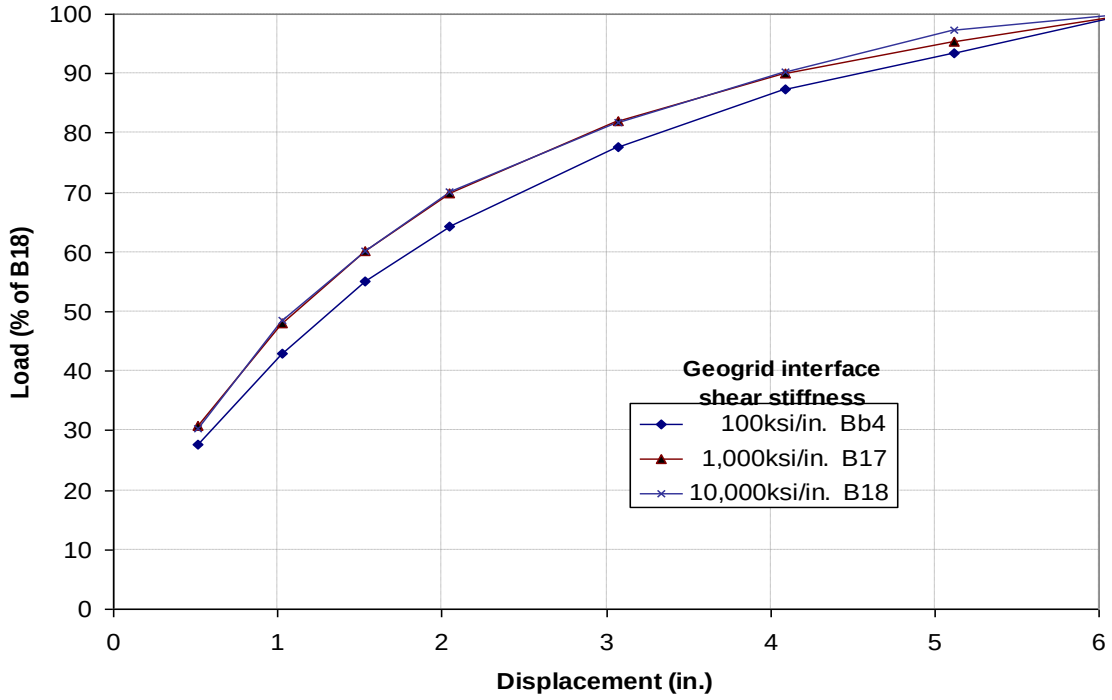

Figure 4.28 Shaft load response curves with a three geogrid interface shear stiffness values.

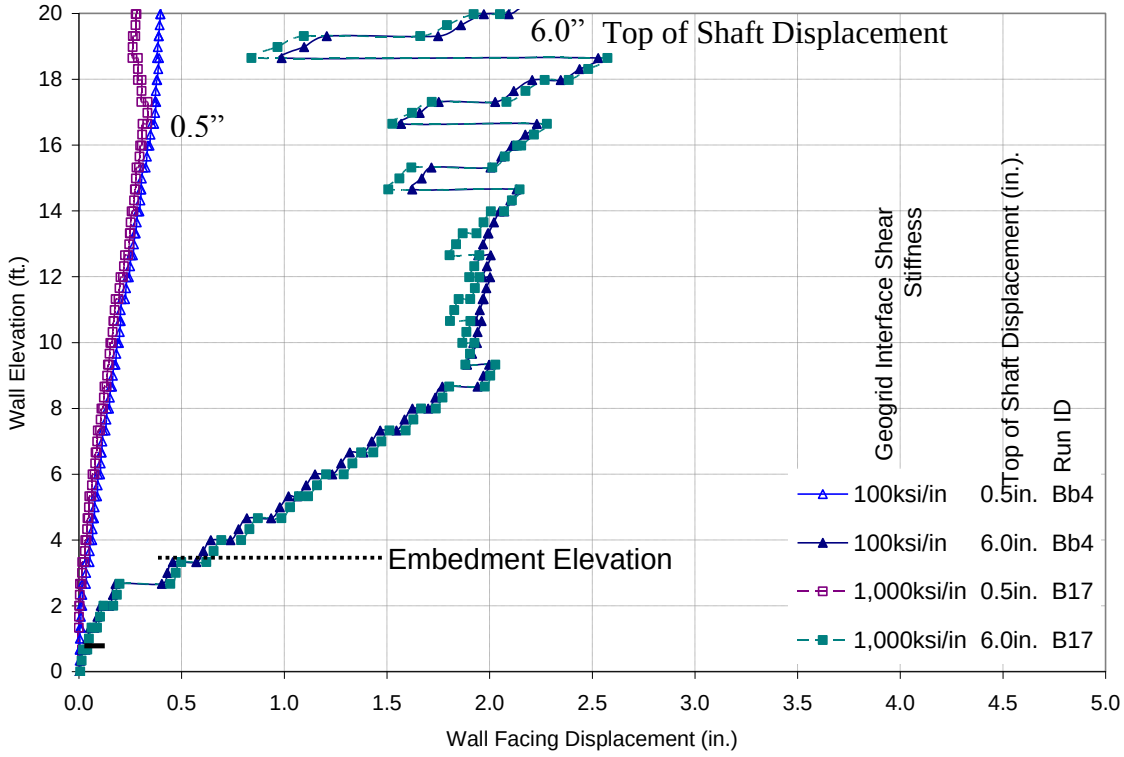

Figure 4.29 Profile view of wall facing displacement for two given shaft displacements using two different geogrid interface shear stiffness values.

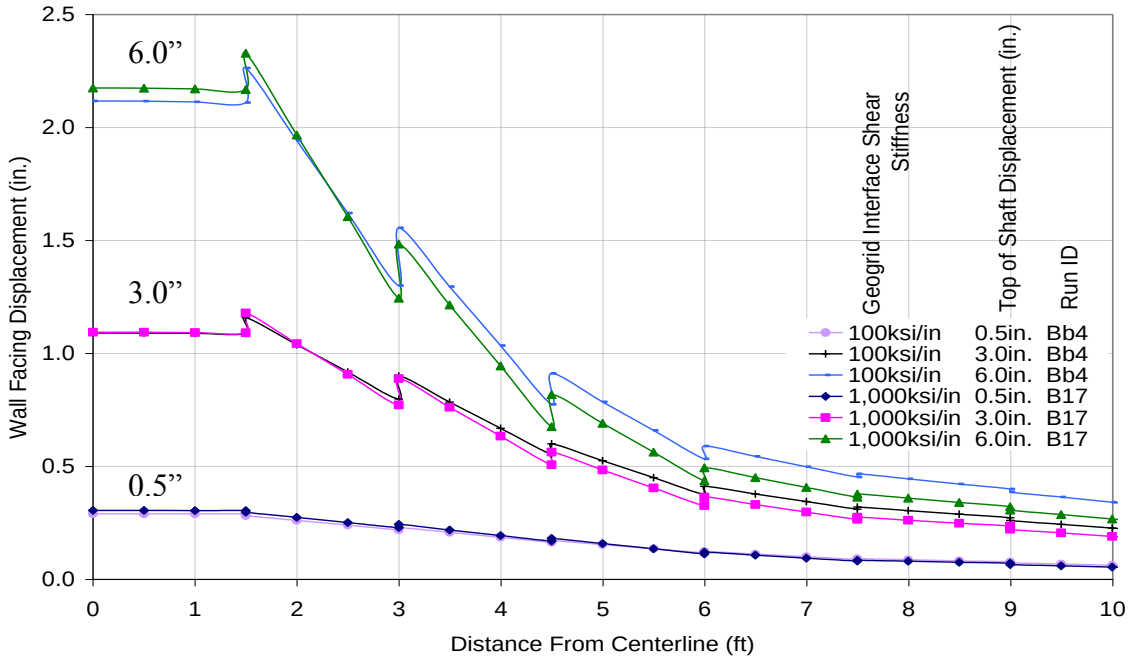

Figure 4.30 Plan view of wall facing displacement at 17.7 feet elevation for two given shaft displacements using two different geogrid interface shear stiffness values.

4.4.4.3 Geogrid Stiffness

The HDPE geogrid stiffness properties are described by the stiffness matrix in Equation 4.3. C11 and C12 control the stiffness in the x direction (the strong direction for the geogrid in the model), C12 and C22 control the stiffness in the y direction (the weak direction for the geogrid in the model), and C33 controls the stiffness of the geogrid for in-plane shear. All of these constants are determined from appropriate elastic modulus and Poisson’s ratios (Jones, 1998). The commonly used value for stiffness in the weak direction of uniaxial geogrid is 1/10th of the strong direction, and the accepted in-plane shear stiffness is the same or equal to the stiffness in the weak direction (Personal communication with Dr. Jie Han). However, the elastic modulus in the weak direction is not well known, and the shear modulus is even less well known. So these properties were examined to determine the influence they have on the system. For

several evaluations of the geogrid stiffness X is used as the baseline value. X is the reported value in the strong direction and other values of stiffness studied are a multiple of X. The reported stiffness value by Tensar Corporation International is based of the strength measured at 5% strain. The hyperbolic stress strain behavior of the HDPE (discussed in Sectin 2.2.4) required additional testing at The University of Kansas to determine the stiffness of the material at 1% strain, which is more representative of the strains measured during physical testing (Section 3.2.3). Testing of the HDPE indicates the stiffness of the HDPE in the strong direction at low strains is twice the value reported by Tensar. Additional testing indicates the stiffness in the weak direction is approximately 1/20th of the stiffness in the strong direction.

$$\sigma' = \begin{Bmatrix} \sigma_x' \\ \sigma_y' \\ \tau_{xy}' \end{Bmatrix} = [E'] \{\varepsilon'\} = \begin{bmatrix} c'_{11} & c'_{12} & 0 \\ & c'_{22} & 0 \\ sym. & & c'_{33} \end{bmatrix} \begin{Bmatrix} \varepsilon'_x \\ \varepsilon'_y \\ \gamma'_{xy} \end{Bmatrix} \quad \text{(orthotropic shell)}$$

Equation 4.3
(Itasca, 2006).

Geogrid Stiffness in the Weak Direction

The typical stiffness reduction for the weak direction of geogrid is 1/10th of the stiffness in the strong direction. This is for an intact sheet of geogrid. However, the reinforcement for physical wall had breaks in the weak direction every 4.3 ft. Also, due to the ten discrete reinforcement bars in the weak direction there could be localized regions which are more or less stiff than the average stiffness. Based on research by Tamura et al. (1993) the strength in the weak direction plays an important role, especially for larger shaft deformations. Stiffness in the weak direction was evaluated at 0.02 and 0.1 times the strength in the strong direction and is represented in the figures as a fraction

of X, where x is the strength reported in the strong direction (Figures 4.31, 4.32, and 4.33). Shaft load for a given shaft displacement was decreased by about 19% throughout the range of shaft movements with a reduction in the geogrid stiffness in the weak direction (Figure 4.31). The reduction in load was accompanied by an increase in wall facing movement, especially in the upper half of the wall (Figure 4.32 and 4.33).

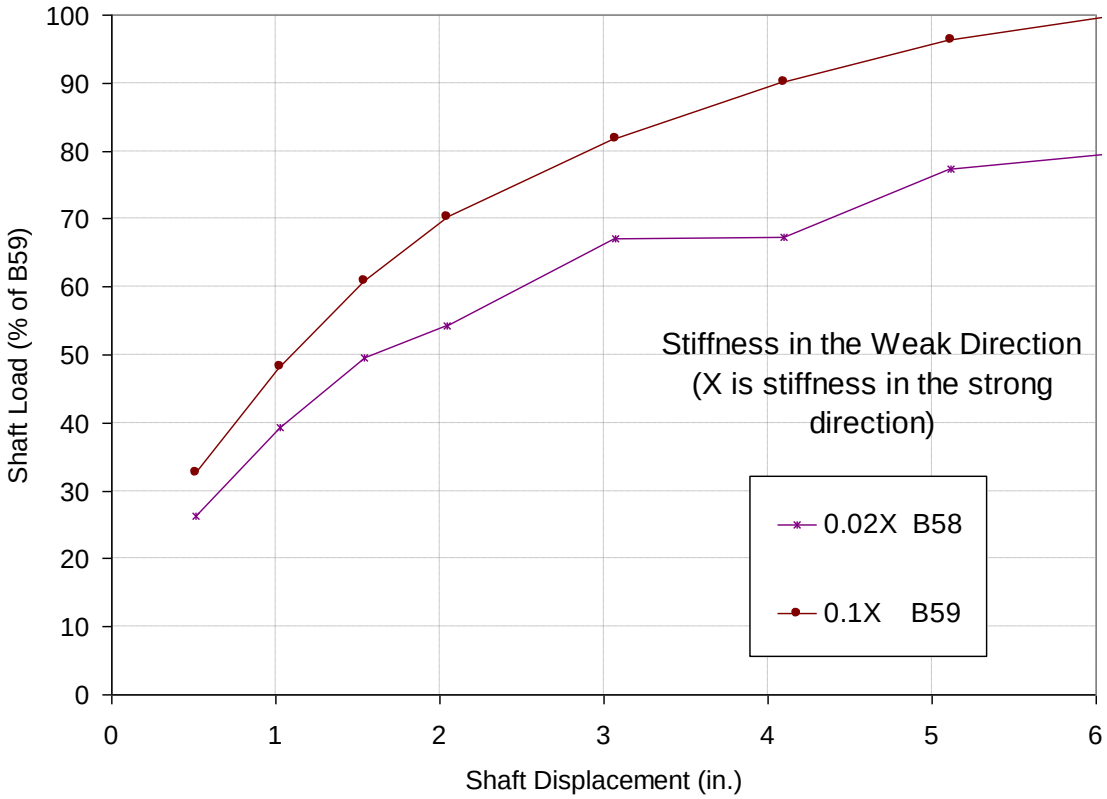

Figure 4.31 Shaft load response curves with changing geogrid stiffness in the weak direction.

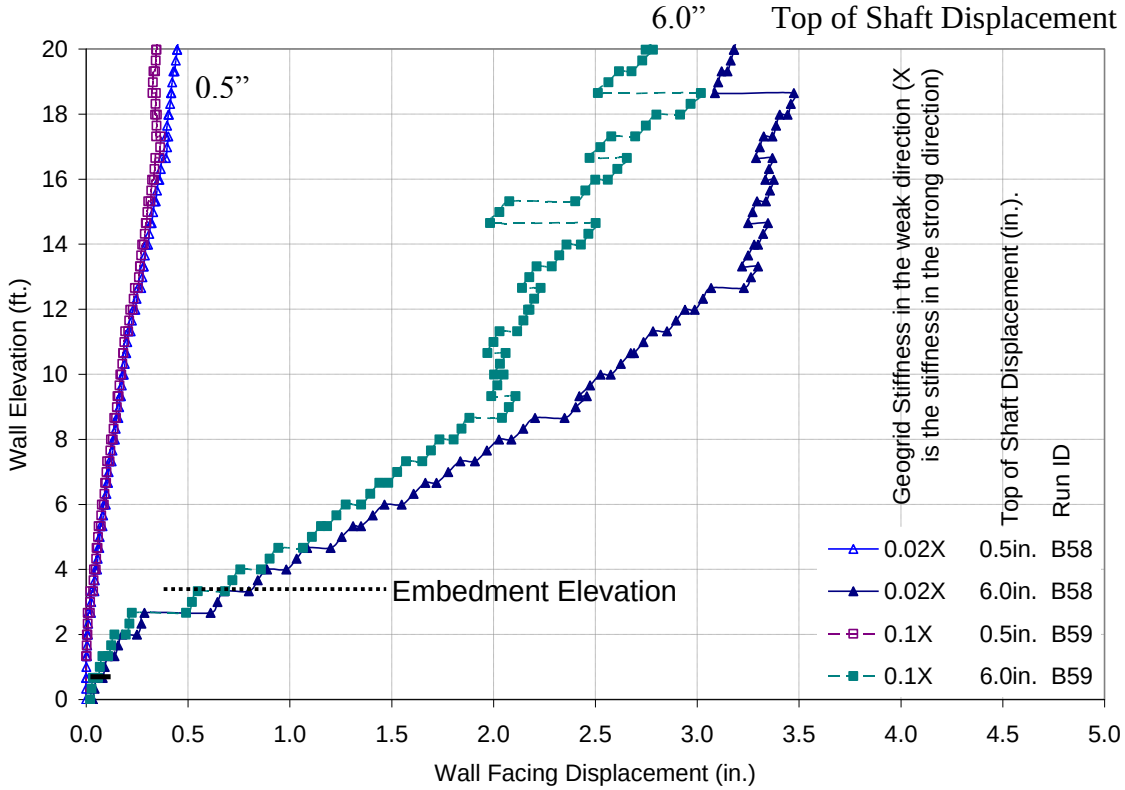

Figure 2.32 Profile view of wall facing displacement for two given shaft displacements using changing geogrid stiffness in the weak direction.

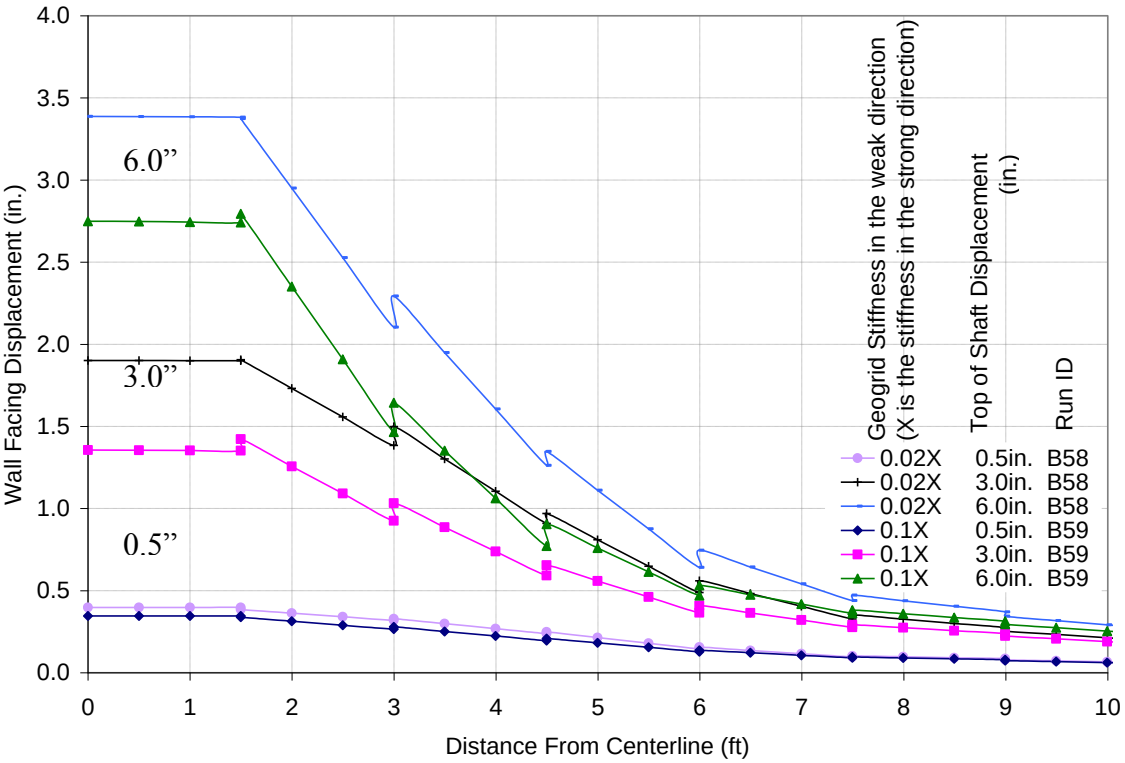

Figure 4.33 Plan view of wall facing displacement at 17.7 feet elevation for two given shaft displacements using changing geogrid stiffness in the weak direction.

Geogrid in-plane Shear Stiffness

The effect of the in-plane shear modulus was investigated because little is known about how the geogrid behaves within a soil mass. An accepted value for the shear modulus of the geogrid is equal to or slightly less than the modulus in the weak direction. To better understand the role the geogrid shear stiffness plays in the behavior of the system, a large range of shear modulus values were used. The increased shear stiffness increased shaft load 80% at ½ in. of shaft movement and 83% at 3 in. of shaft displacement (Figure 4.34). The increased shear stiffness produced decreased wall facing movement above elevation 14 ft (Figure 4.35). Wall facing displacement was more concentrated directly in front of the shaft by the increased shear stiffness (Figure 4.36).

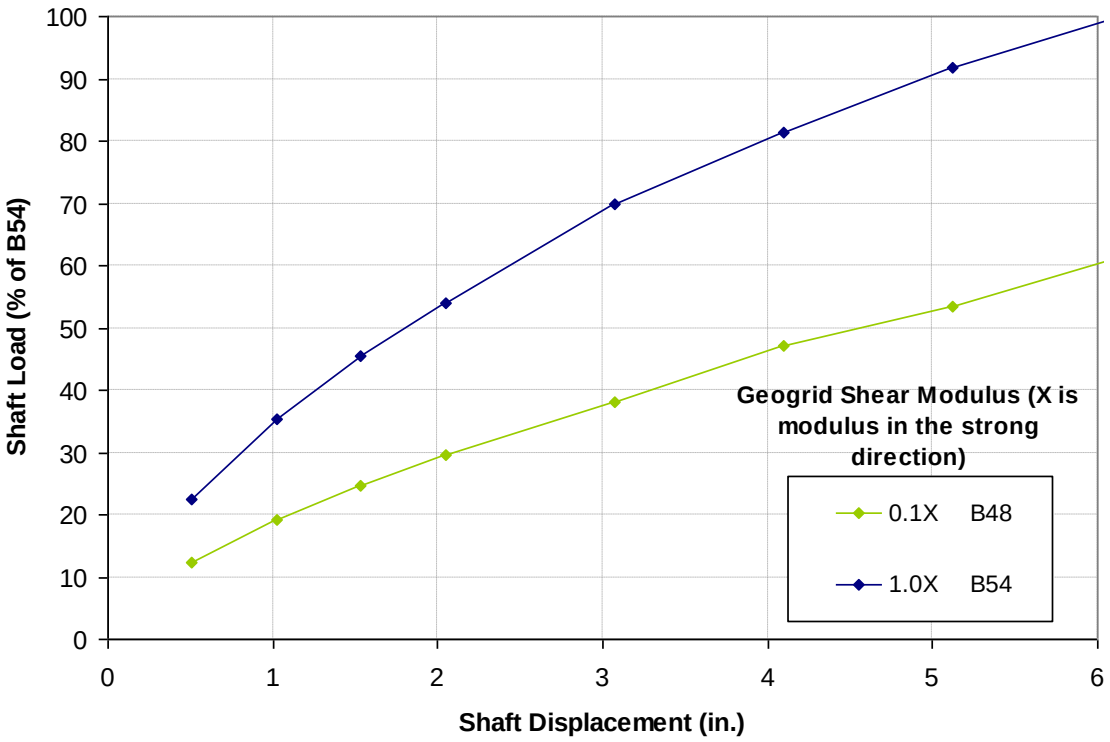

Figure 4.34 Shaft load response curves for two geogrid stiffness values in shear.

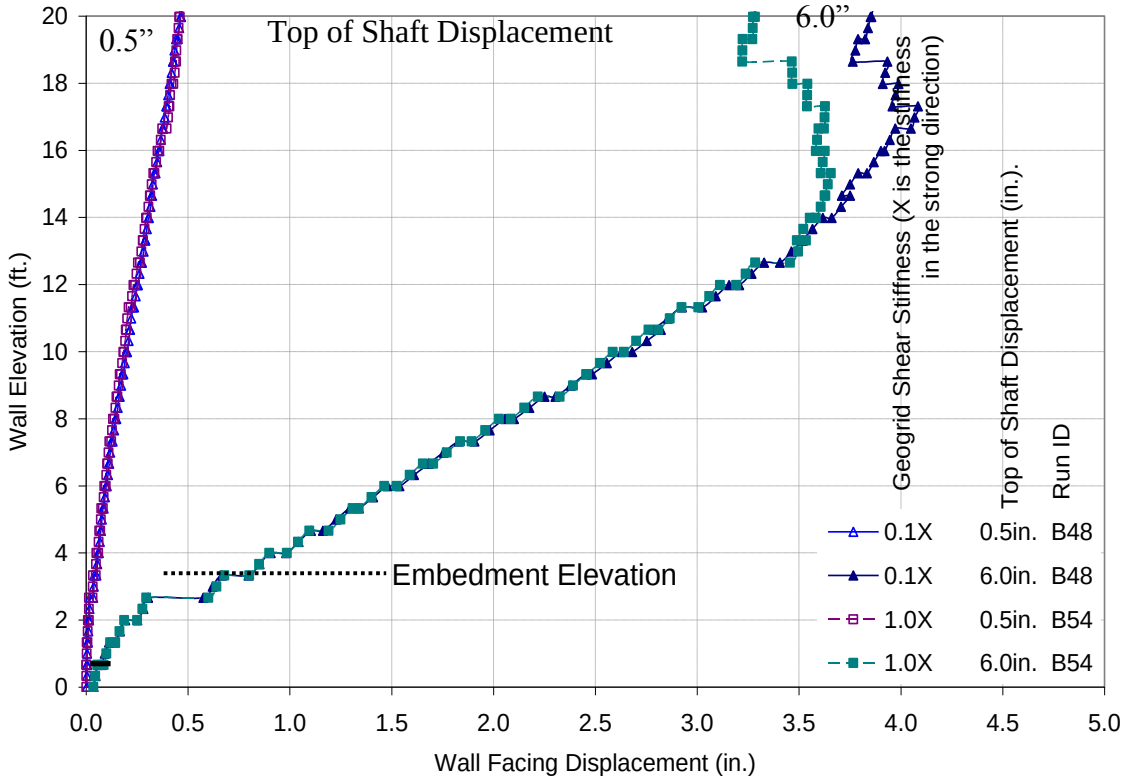

Figure 4.35 Profile view of wall facing displacement for two given shaft displacements using two different geogrid shear stiffness values.

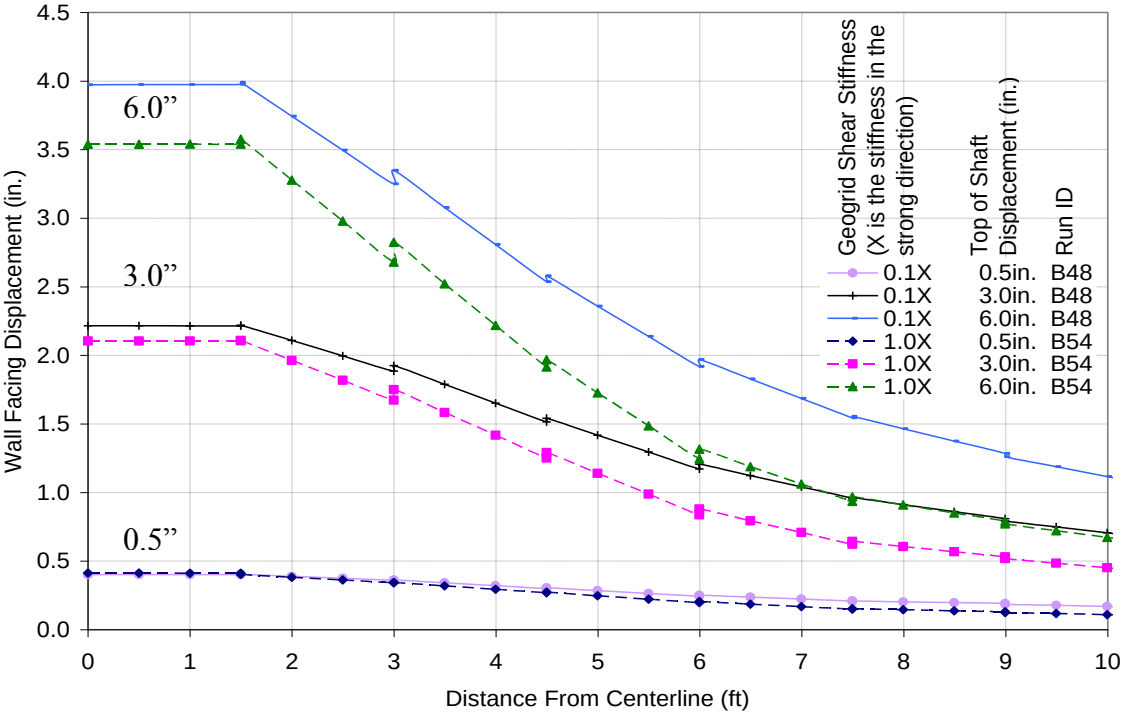

Figure 4.36 Plan view of wall facing displacement at 17.7 feet elevation for two given shaft displacements using two different geogrid shear stiffness values.

Geogrid Overall Stiffness

Several values of geogrid stiffness were compared to evaluate the influence of geogrid stiffness on model response (Figures 4.37, 4.38, 4.39, and 4.40). Increased shaft load at a given displacement occurs with increased geogrid stiffness (Figure 4.37 and 4.38). As geogrid stiffness increases the shaft load at a given displacement does not linearly increase (Figure 4.38). The wall facing movement is also reduced significantly using the increased geogrid stiffness (Figure 4.39 and 4.40). As geogrid stiffness increased, wall facing displacement directly in front of the shaft (Figure 4.39) has a change in displacement from a near linear tilt at 1x estimated stiffness to an inflection point at elevation 12 ft, and from elevation 16 ft to 20 ft a reduction in total movement at 12x estimated grid stiffness. The plan view of wall facing displacement at elevation 17.7 ft (Figure 4.40) shows decreased wall facing movement and a concentration of movement towards the shaft centerline with increasing geogrid stiffness.

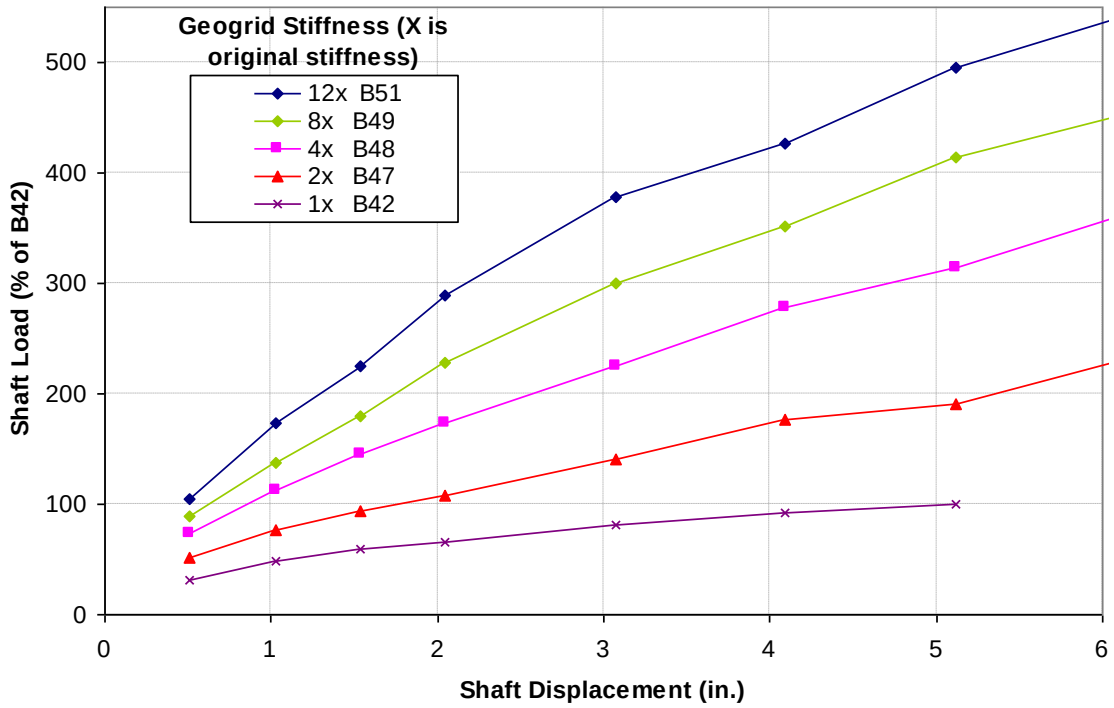

Figure 4.37 Shaft load response curves with a several geogrid stiffness values scaled from the original stiffness up to 12 times the original stiffness.

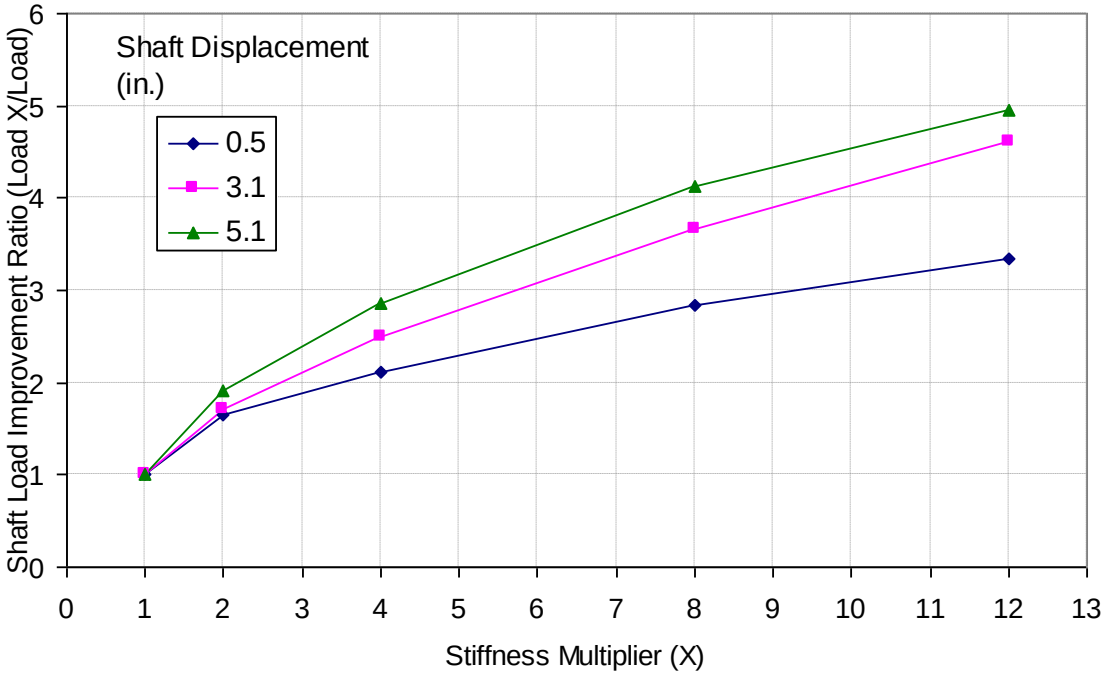

Figure 4.38 Plot showing the increase in shaft load improvement ratio (Increased load/original load) with increasing geogrid stiffness.

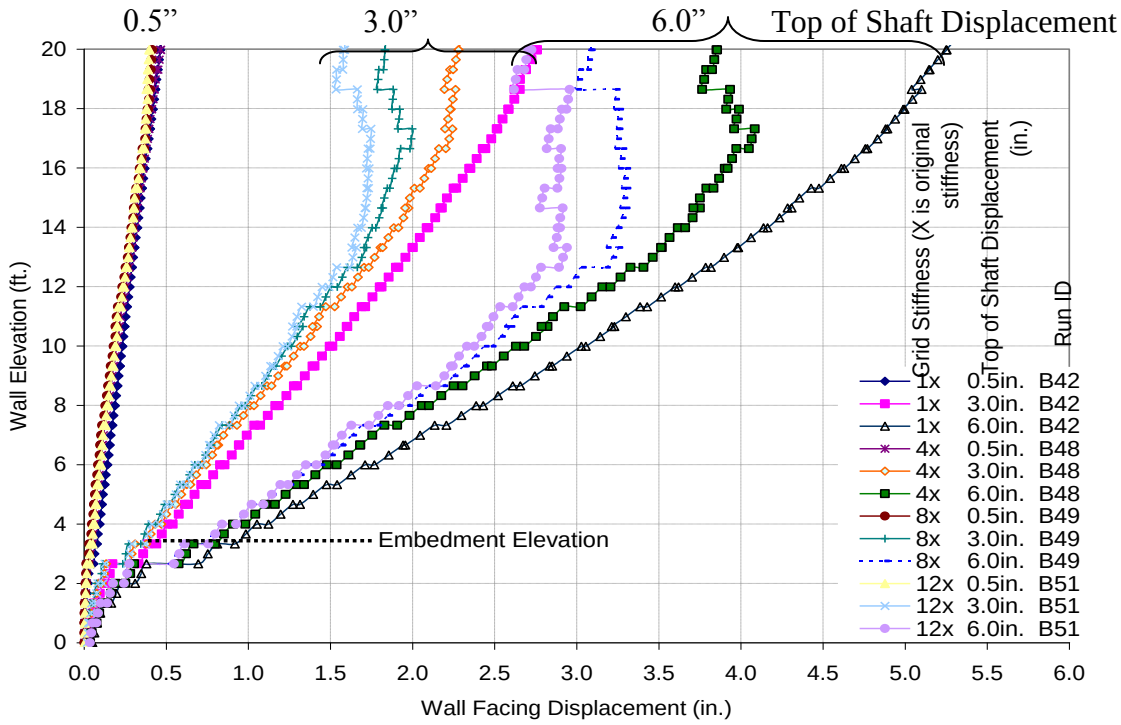

Figure 4.39 Profile view of wall facing displacement with several geogrid stiffness values scaled from the original stiffness up to 12 times the original stiffness.

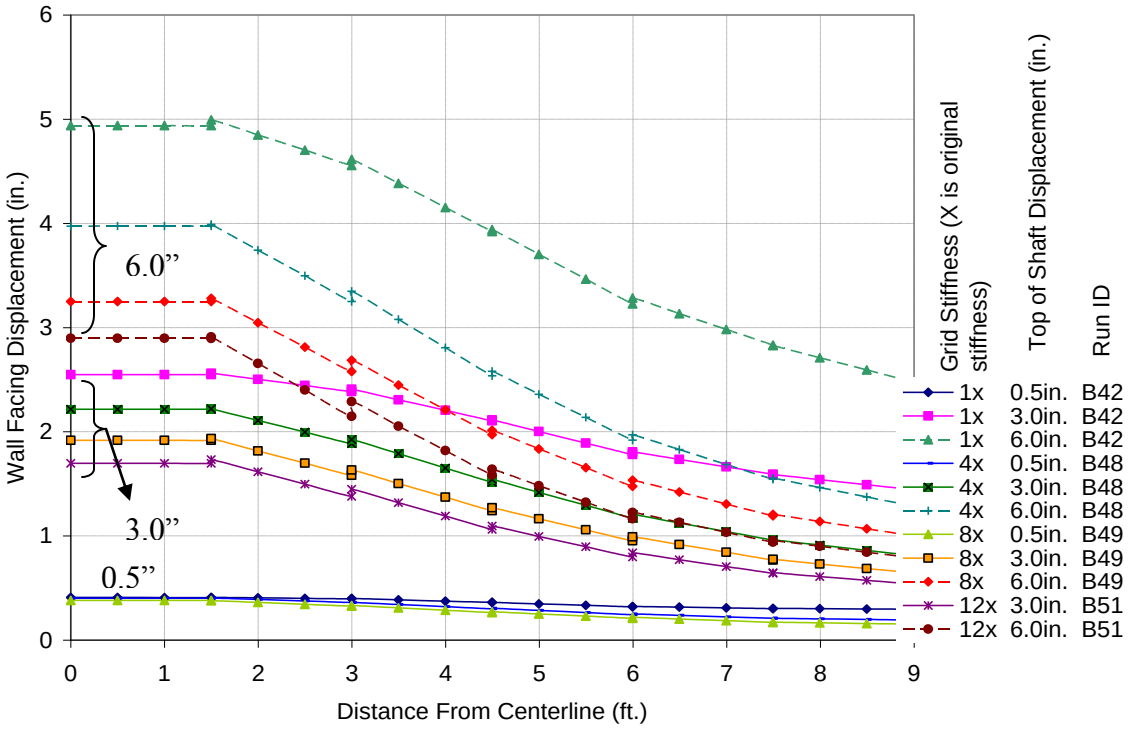

Figure 4.40 Plan view of wall facing displacement at 17.7 feet elevation for two given shaft displacements using several geogrid stiffness values scaled from the original stiffness up to 12 times the original stiffness. (Dashed lines are wall facing displacement at 6.0in. of shaft movement).

4.5 Wall Height

The developed numerical model (Figure 4.2) was modified to consider a taller and shorter wall height containing full length shafts to evaluate the influence of various geometries that may be needed in design. A ten foot tall and thirty foot tall wall with otherwise equal properties to the physical wall test were considered (Figure 4.41).

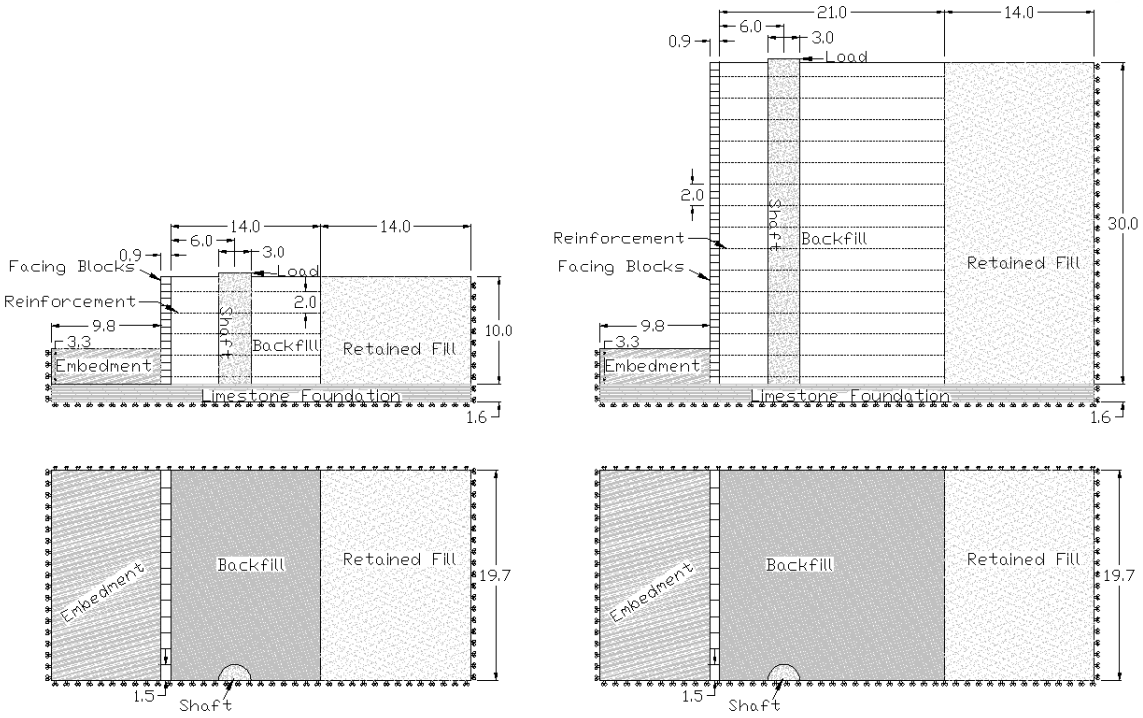

Figure 4.41 Schematic of ten and thirty foot tall model. (all dimensions are in feet)

For the ten foot wall the type of geogrid at a location was changed. The length of the geogrid was maintained at 14 ft (0.7 x 20 ft) from the physical test. The geogrid in the top 10 ft of the physical test was used for the top 10 ft of the short wall. This means there is only one type of geogrid used for the shorter wall, rather than two types as for the 20 ft tall wall.

The geogrid used in the thirty foot wall was lengthened to 70% of the wall height (21 ft). Six layers of a weaker geogrid were used at the top of the 30 ft wall which is

consistent with the 20 ft wall. The remainder of the 30 ft wall used the same stronger geogrid as the bottom 4 layers of the 20 ft wall. This design was verified with the Tensar specific software "Mesa Pro 2.3" (Tensar, 2007) which follows Demonstration Project 82 (FHWA 1997).

The influence of shaft distance from the wall facing at various wall heights was evaluated using a three foot diameter shaft spaced six feet and twelve feet from the back of the wall facing to the center of the shaft (Shaft B and Shaft D respectively).

Top of shaft load displacement curves for the two 30 foot tall, 20 foot tall, and 10 foot tall walls are compared in Figure 4.42. In this figure the values of load are reported as a percent of the 30 ft tall wall with a shaft spaced 12 ft from the wall facing (Shaft D). This was done to allow a qualitative comparison of the configurations since these models did not use the final baseline model parameters discussed in the next chapter. Wall facing displacements directly in front of the shafts are shown in Figures 4.43, 4.44, and 4.45 for the 10 ft, 20 ft, and 30 ft tall walls respectively. Wall facing displacements at elevation 7.3 ft, 17.7 ft, and 27 ft are shown in Figures 4.46, 4.47, and 4.48 for the 10 ft, 20 ft, and 30 ft tall walls respectively.

These results demonstrate that wall height doesn't significantly affect the initial portion of the top of shaft load response curve, for walls with reinforcement as described, but does have a significant effect on the ultimate capacity of the system (Figure 4.42). The wall facing displacement trends do not significantly change with varying wall height, but the width of influence grows larger at greater wall heights.

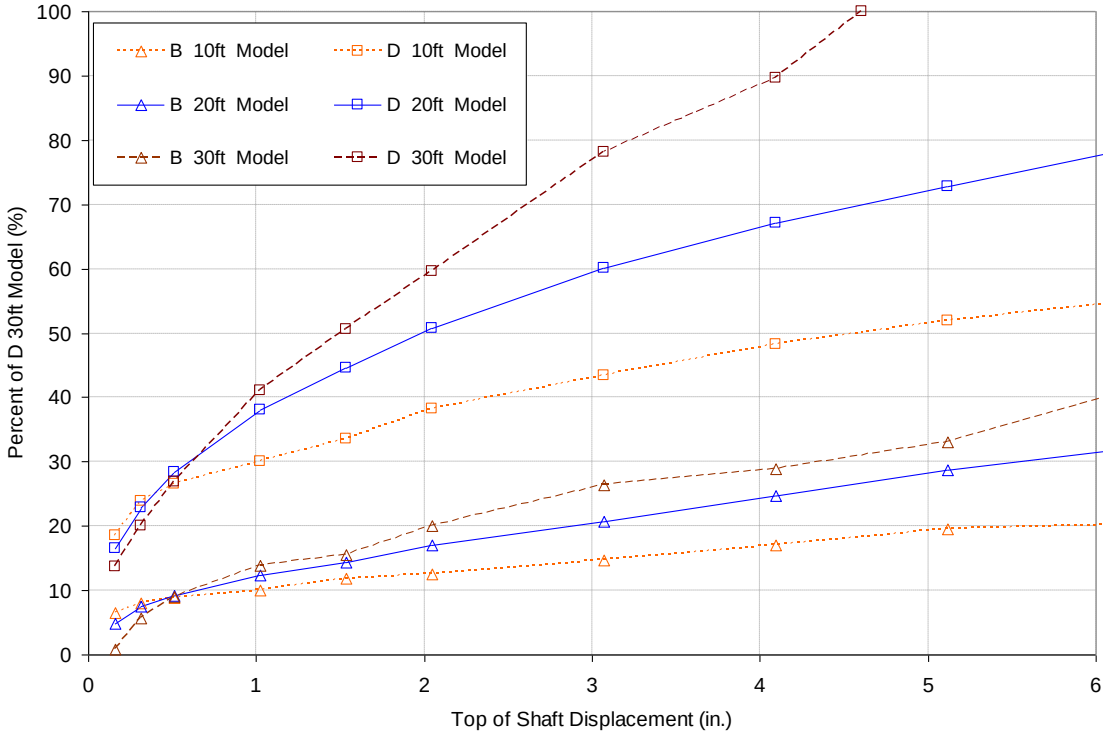

Figure 4.42 Top of shaft load versus displacement for the shafts of various wall heights, and spacing from the wall facing.

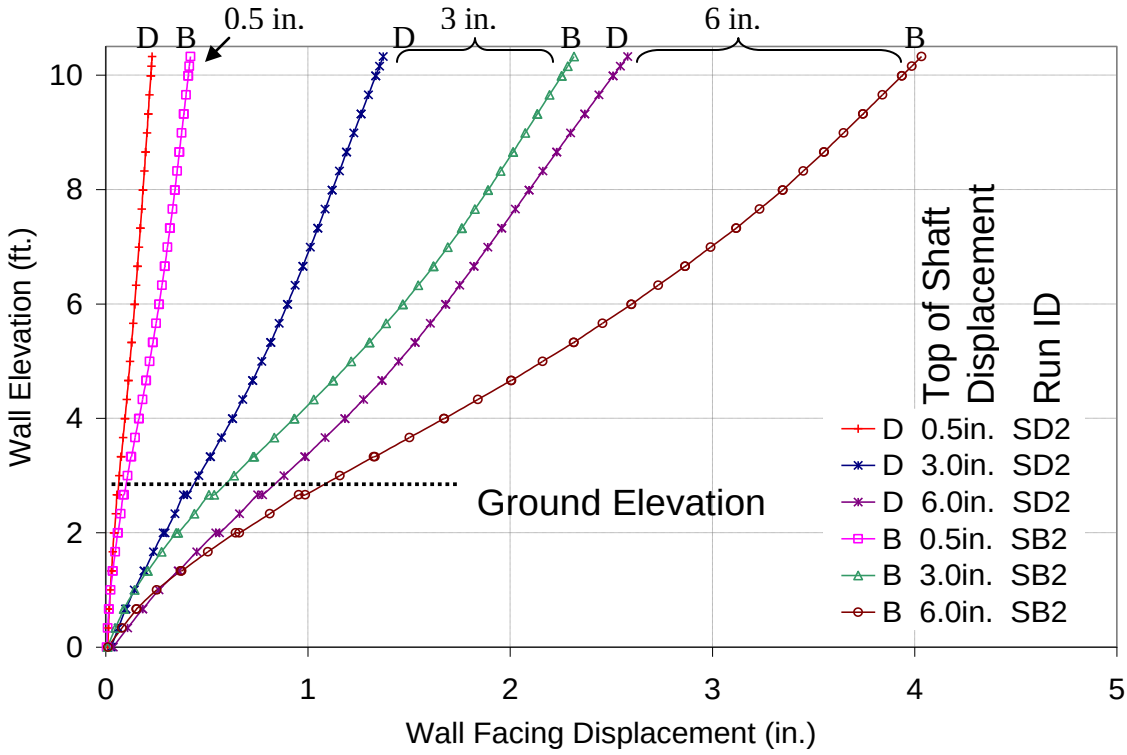

Figure 4.43 Wall facing displacement directly in front of the shafts for the 10 ft tall wall.

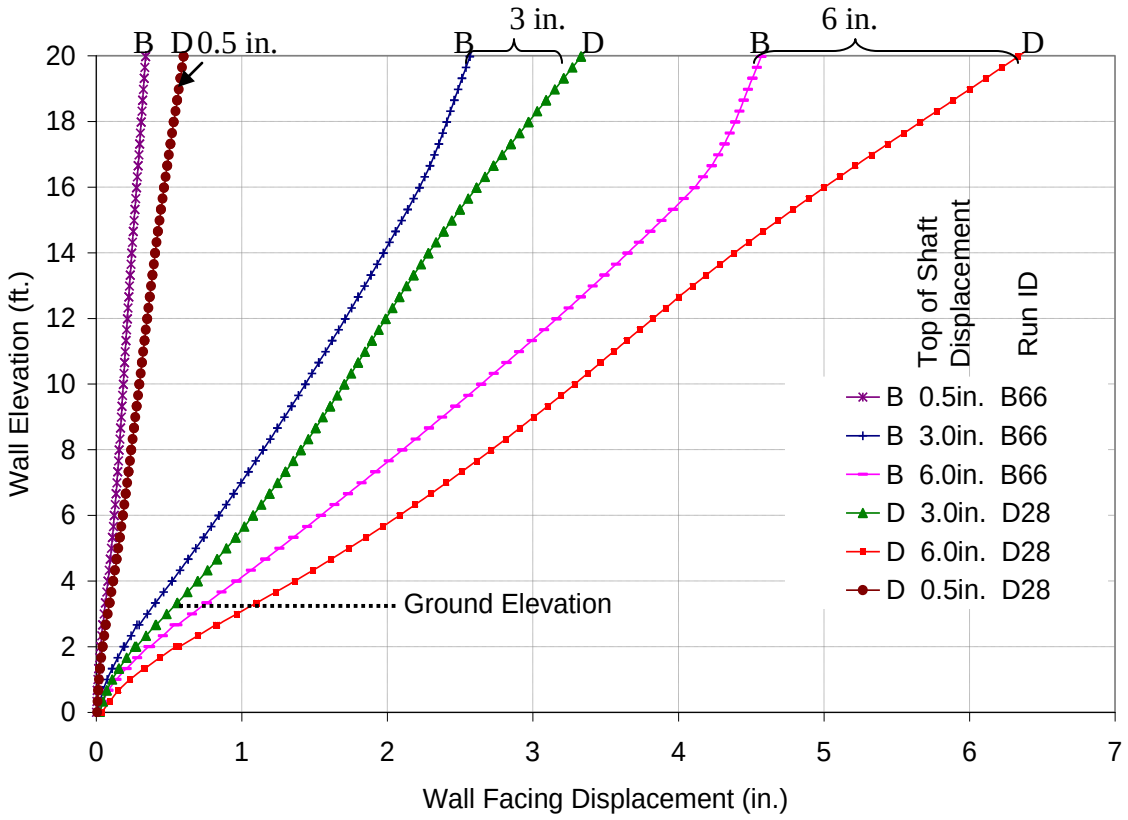

Figure 4.44 Wall facing displacement directly in front of the shafts for the 20 ft tall wall.

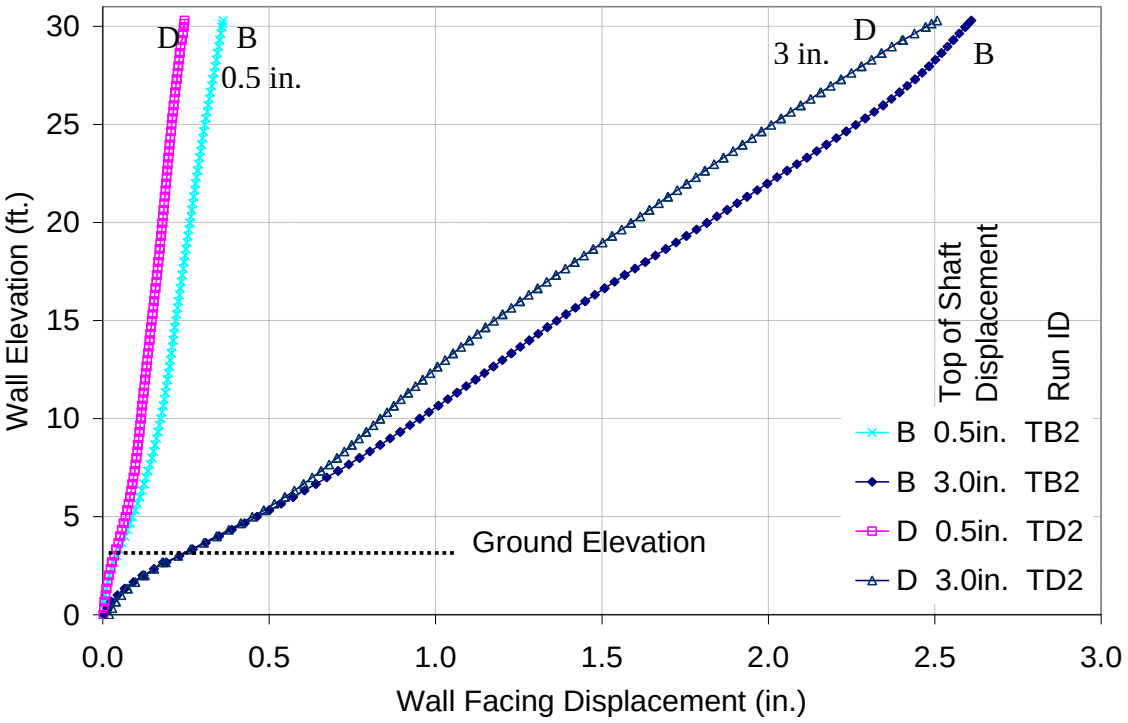

Figure 4.45 Wall facing displacement directly in front of the shafts for the 30 ft tall wall.

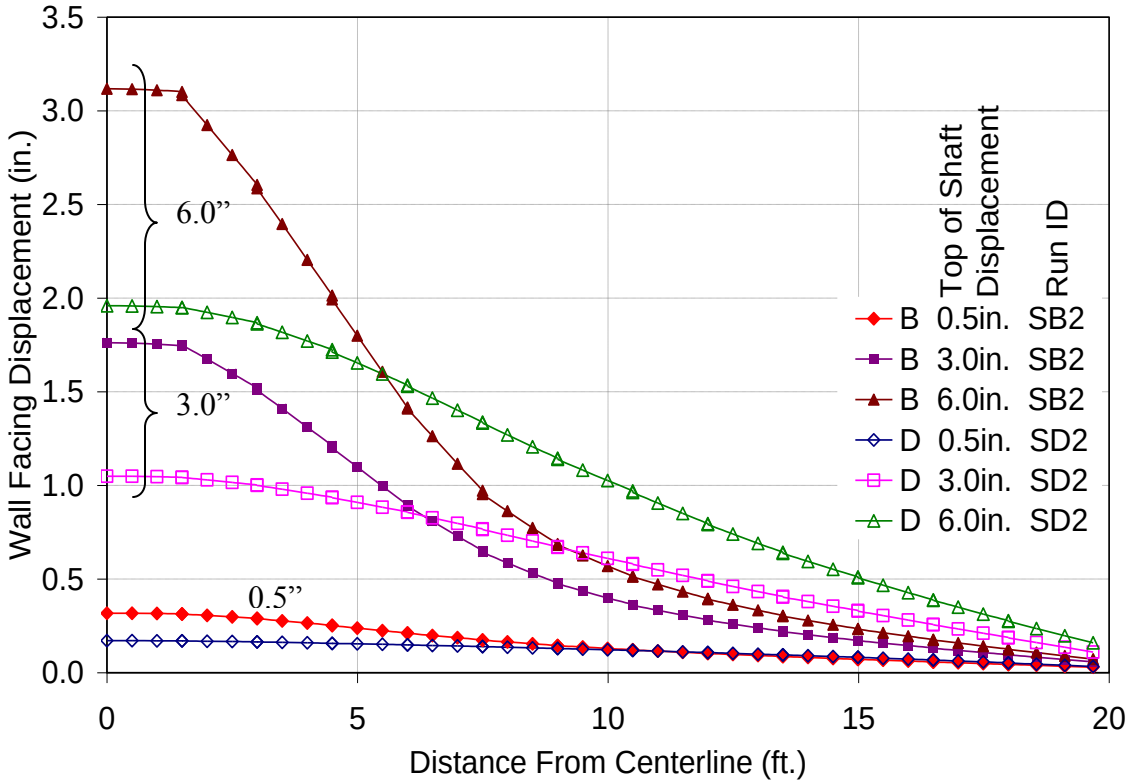

Figure 4.46 Wall facing displacement at elevation 7.3 ft for the 10 ft tall wall.

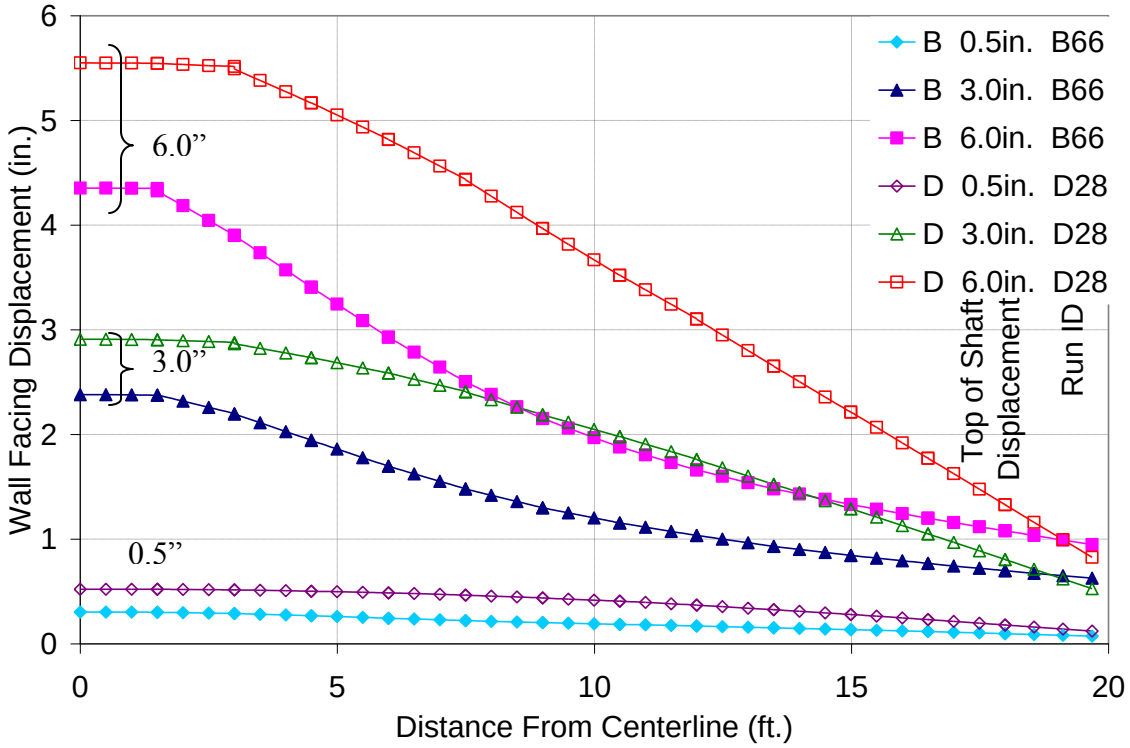

Figure 4.47 Wall facing displacement at elevation 17.7 ft for the 20 ft tall wall.

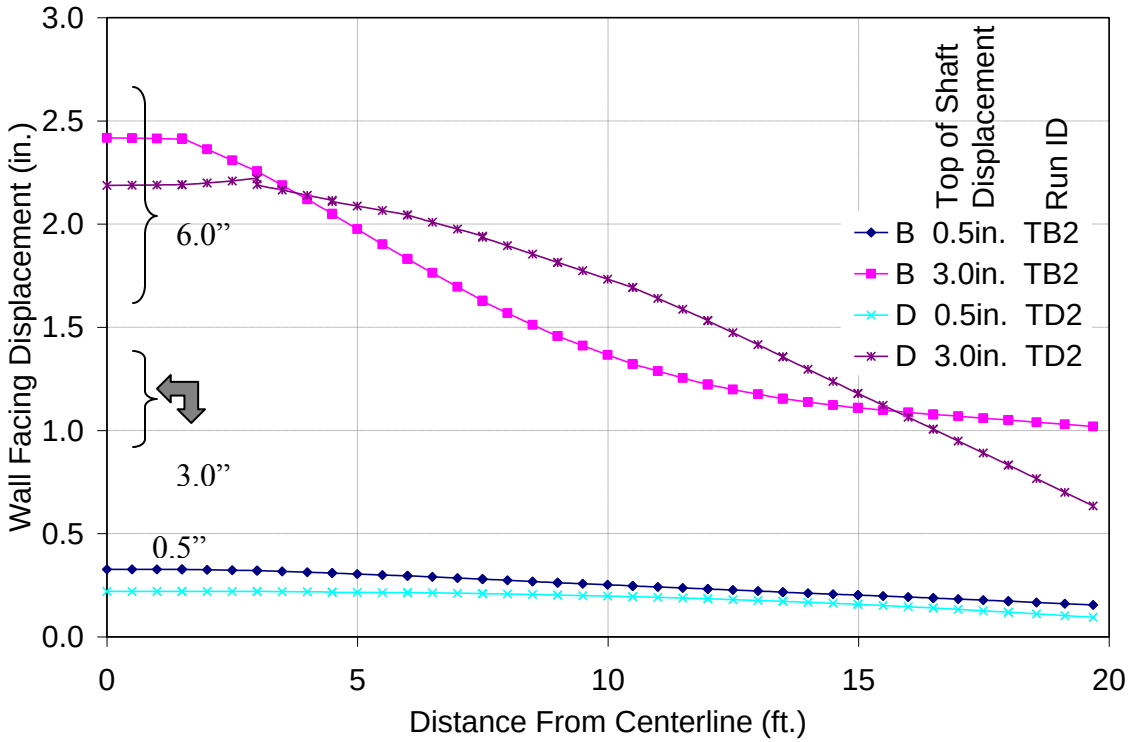

Figure 4.48 Wall facing displacement at elevation 27 ft for the 30 ft tall wall.

These results demonstrate that wall height doesn't significantly affect the initial portion of the top of shaft load response curve, but does have a significant effect on the ultimate capacity of the system (Figure 4.42). The wall facing displacement trends do not significantly change with varying wall height, but the width of influence grows larger at greater wall heights.

CHAPTER FIVE

Comparison of Field and Model Results

5.1 Introduction

Based on the parametric study, variables were adjusted to make the best possible match with field data (Section 5.2). These properties are shown in Table 5.1. Typically the highest values from the accepted ranges of values were used to achieve the best match between physical and model results. Additional model results are presented using a geogrid stiffness higher than accepted values to achieve the best possible match between field and model results (Section 5.3.

Table 5.1 Component Properties

Component	Properties
Aggregate	Φ' = 51° c = 41 psf E = 2,000 ksf v = 0.3 γ = 115 pcf
Embedment	Φ' = 34° E = 835 ksf v = 0.3 γ = 115 pcf
Foundation	E = 4,600 ksi v = 0.15
Shaft	E = 4,600 ksi v = 0.15
Shaft Interface	φ = 30° kn = 1,228 ksi/in. ks = .06 ksi/in.
Facing Blocks	E = 4,600 ksi v = 0.15
Block Bottom Interface	Φ' = 40° Cohesion = 500 psf ks = 1 ksi/in.
Geogrid 1	J_{md} = 42.8 kip/ft J_{tr} = 2.14 kip/ft J_{sh} = 2.14 kip/ft C_i = 1.0 ks = 18.4 ksi/in.
Geogrid 2	J_{md} = 71.3 kip/ft J_{tr} = 3.15 kip/ft J_{sh} = 3.15 kip/ft C_i = 1.0 ks = 33.2 ksi/in.

Φ' = Effective friction angle, E = elastic modulus, v = Poisson's ratio, γ = unit weight, kn = interface normal stiffness, ks = interface shear stiffness, J_{md} = tensile stiffness in the machine direction, J_{tr} = tensile stiffness in the weak direction, J_{sh} = in-plane shear stiffness, C_i = coefficient of geogrid reaction.

5.2 Comparison of Field and Model Results

Model results of top of shaft load versus displacement from all models using the previously specified parameters (Table 5.1) are discussed in this section. The first letter in each model indicates the configuration of the model and the number indicates the version of the model. Each model spaced from three to six feet (Shaft A and Shaft B, BS,

or BG2) from the wall facing is shown in Figure 5.1. As would be expected, shafts further from the wall facing were stiffer, and shafts which were longer had more stiffness than short shafts. The impact of a group effect can be seen as well. Figure 5.2 shows physical data from the four shafts spaced 3 or 6 ft from the wall facing compared with model test results. Model results of the shaft top load response curves are shown in Figure 5.3 for models spaced 9 and 12 feet from the wall facing, The physical behavior is matched well and the model results are conservative. A comparison of physical and model results of wall facing displacement directly in front of the shafts at three different top of shaft displacements is shown in Figure 5.4 for Shaft B and Figure 5.5 for Shaft D. Physical and model wall facing displacement at elevation 17.7 ft is compared in Figure 5.6 and 5.7 for Shaft B and D respectively. Shaft B model and physical data match well, while the Shaft D model deviates from the test data. Similar results were observed in other shaft configurations. Physical and model results of wall facing displacement agree well for configurations with a shaft near the wall facing. Figure 5.8 shows a comparison of wall facing displacement directly in front of the shafts loaded as a group. A comparison of the wall facing displacement at elevation 17.7 feet for the shafts loaded as a group is shown in Figure 5.9.

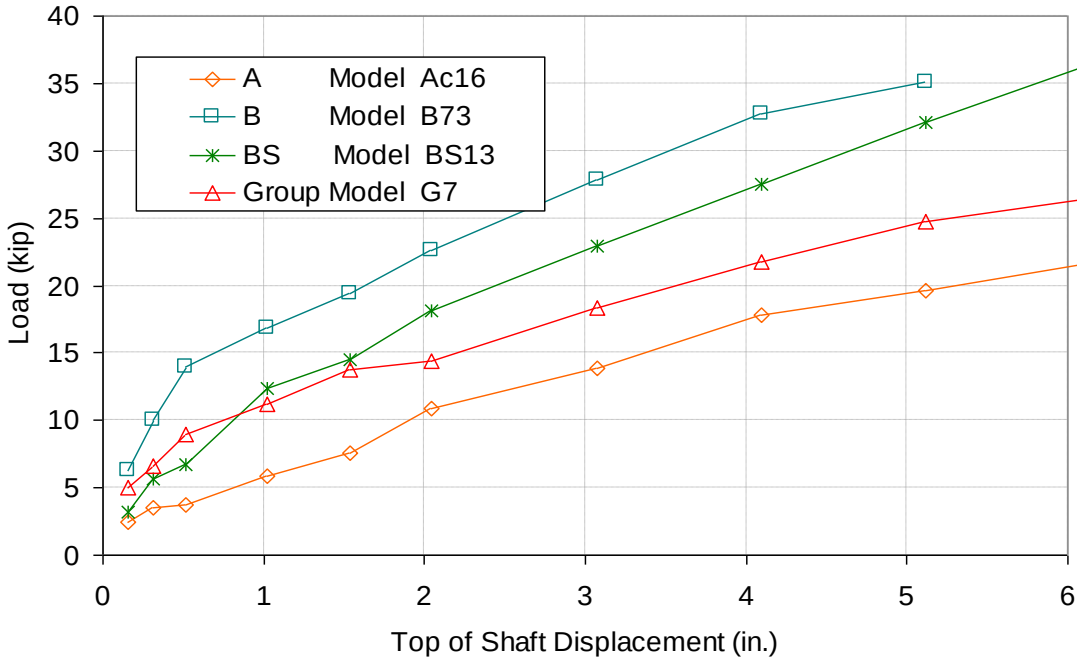

Figure 5.1 Shaft load response curves of models with shaft to wall facing spacing three of six feet.

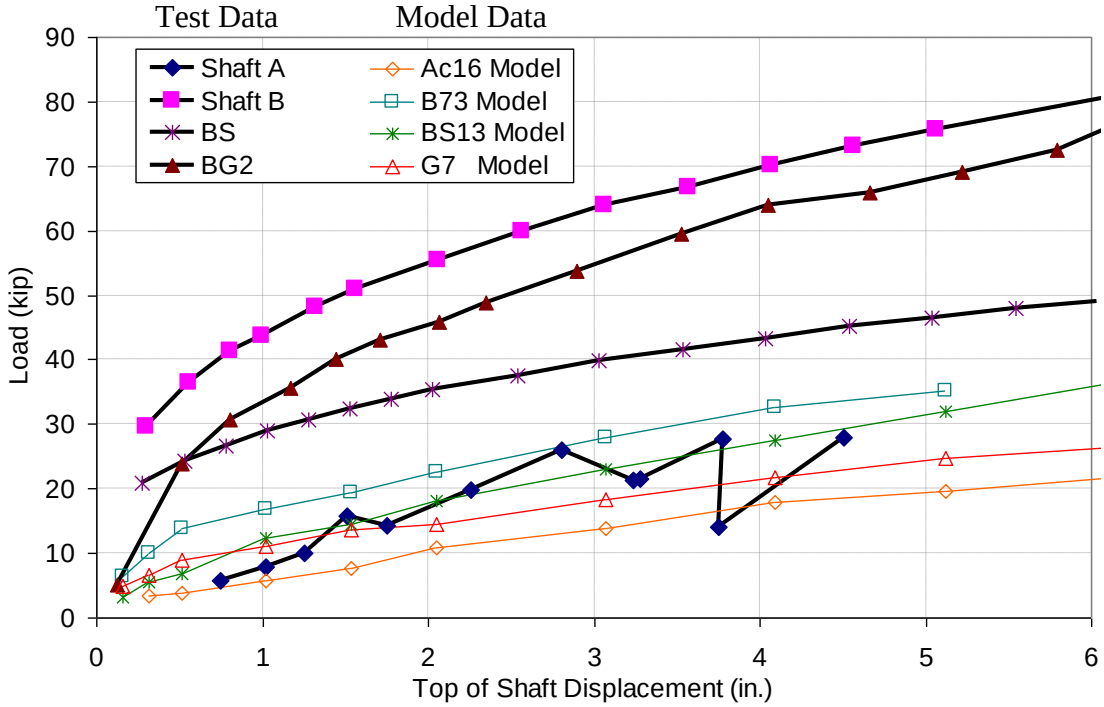

Figure 5.2 Shaft load response curves of shafts spaced within six feet or less of the wall facing compared with physical test results.

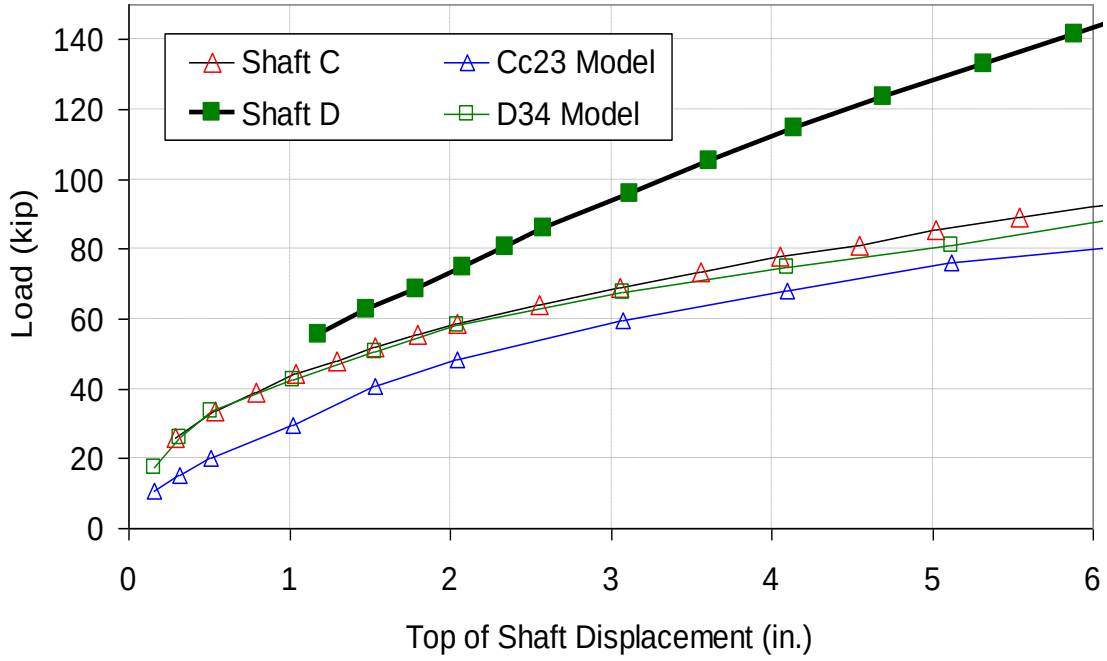

Figure 5.3 Shaft load response curves for shafts spaced greater than six feet from the wall facing compared with physical test results.

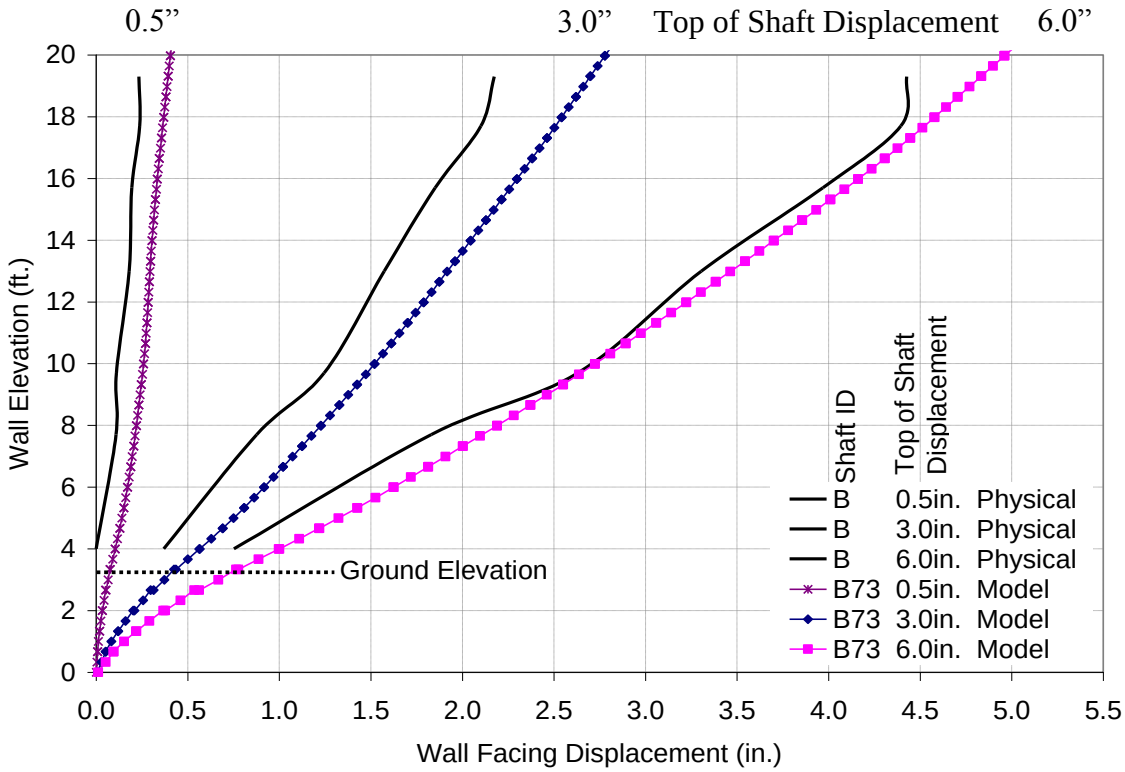

Figure 5.4 Profile view of wall facing displacement of physical and model results of single shafts spaced 6 ft (Shaft B) from the wall facing.

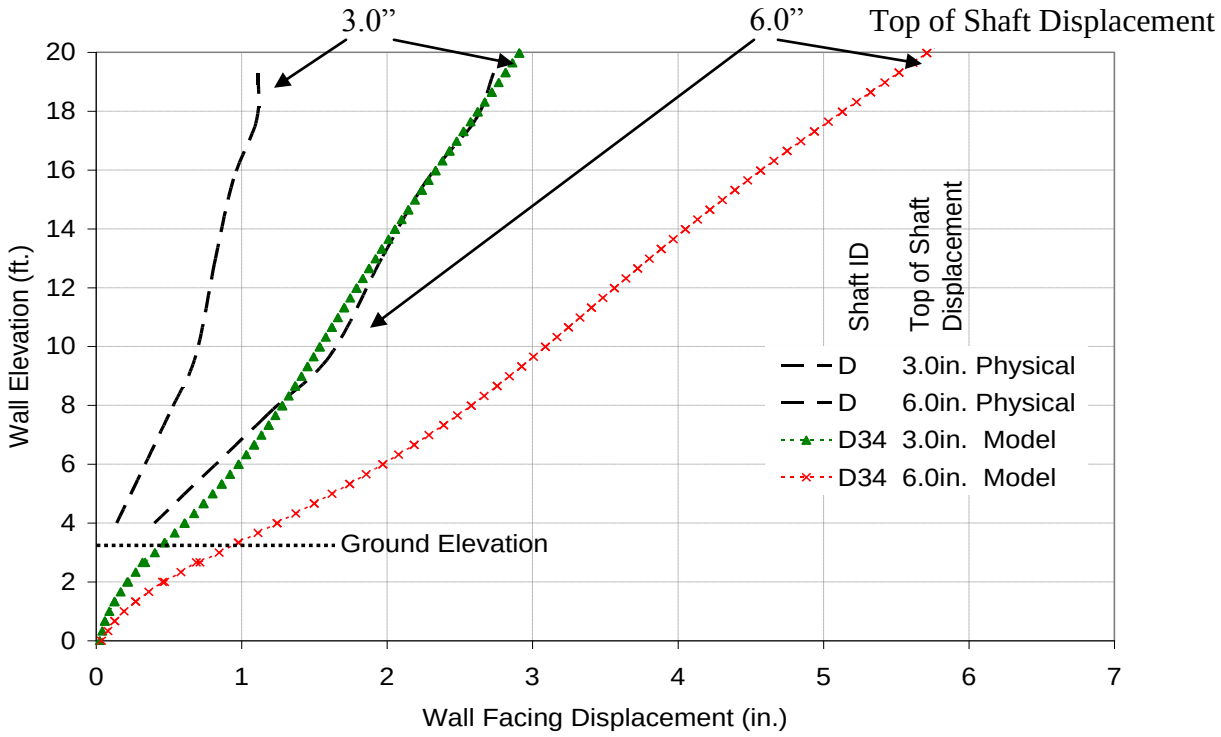

Figure 5.5 Profile view of wall facing displacement of physical and model results of single shafts spaced 12 ft (Shaft D) from the wall facing.

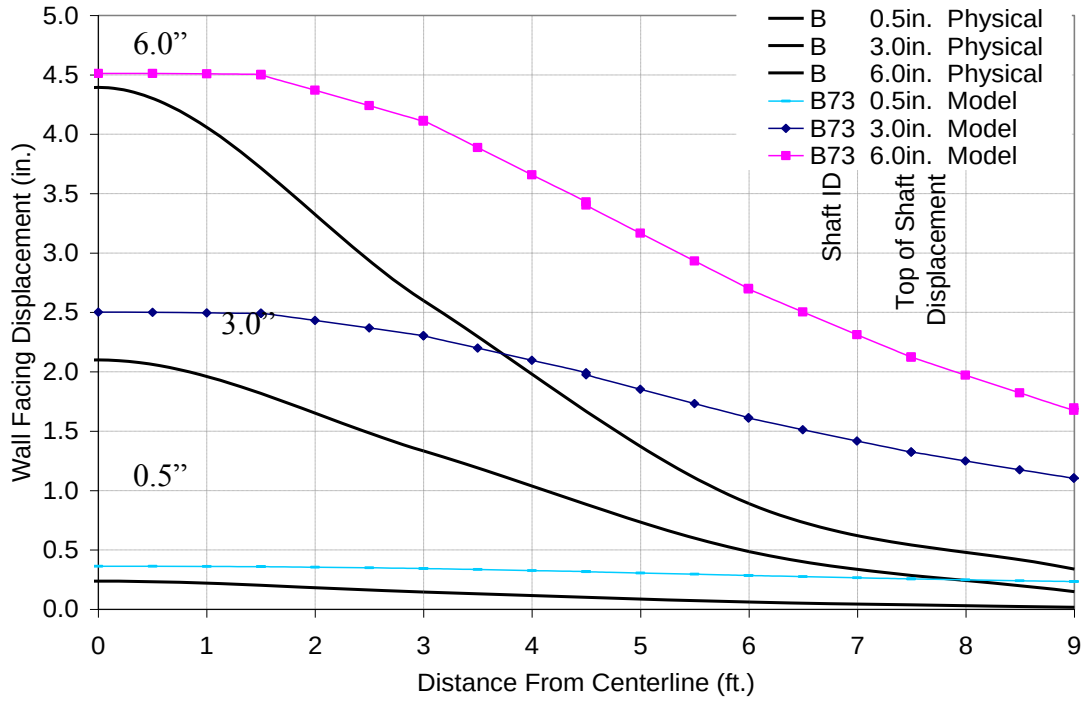

Figure 5.6 Plan view of wall facing displacement at 17.7 feet elevation of physical and model results of single shafts spaced 6 ft (Shaft B) from the wall facing.

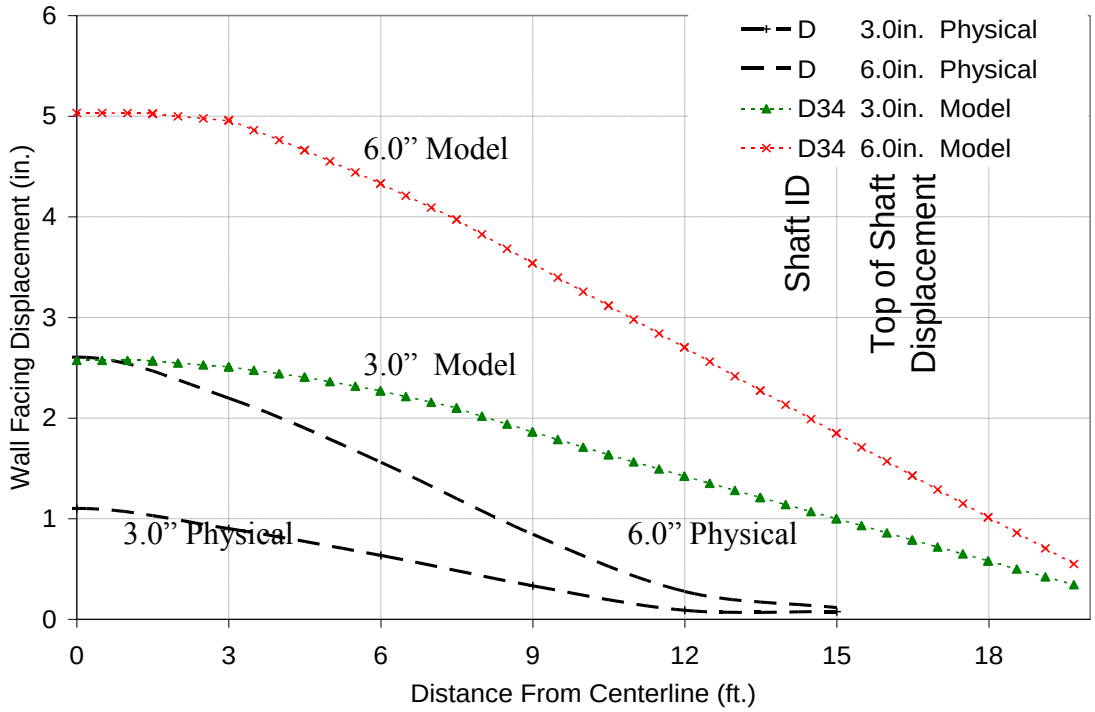

Figure 5.7 Plan view of wall facing displacement at 17.7 feet elevation of physical and model results of single shafts spaced 12 ft (Shaft D) from the wall facing.

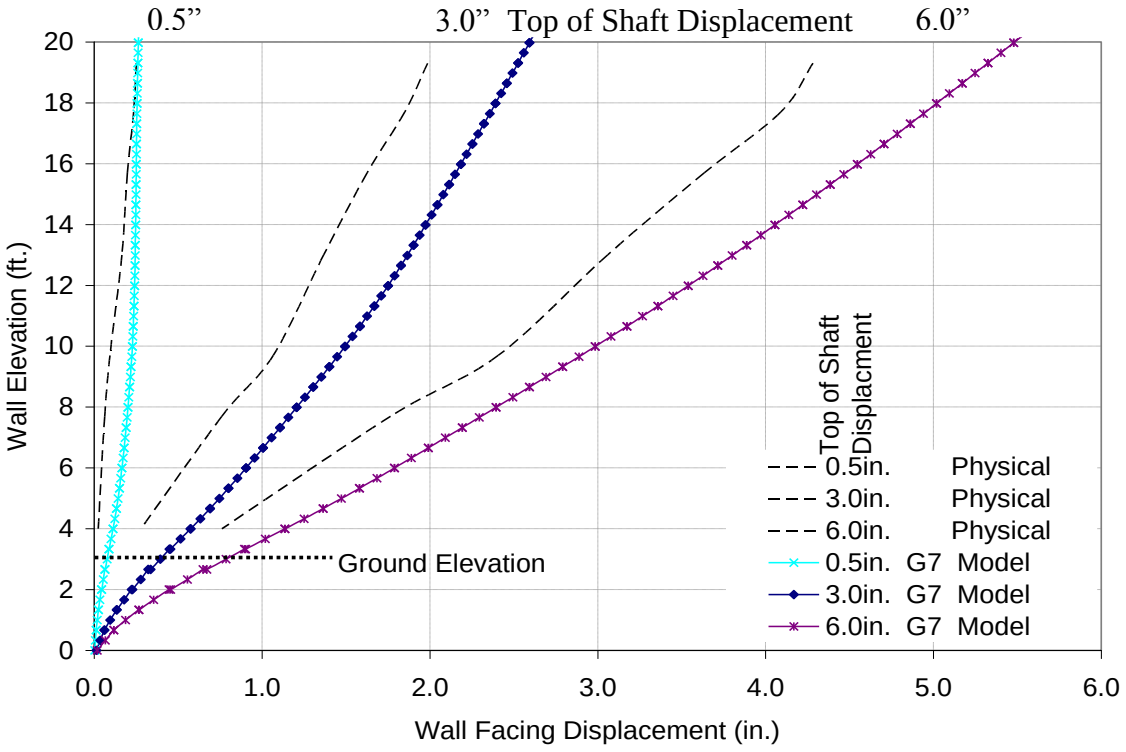

Figure 5.8 Profile view comparison of wall facing displacement from physical and model results in front of shafts loaded as a group spaced 6 ft from the wall facing (Shaft BG2).

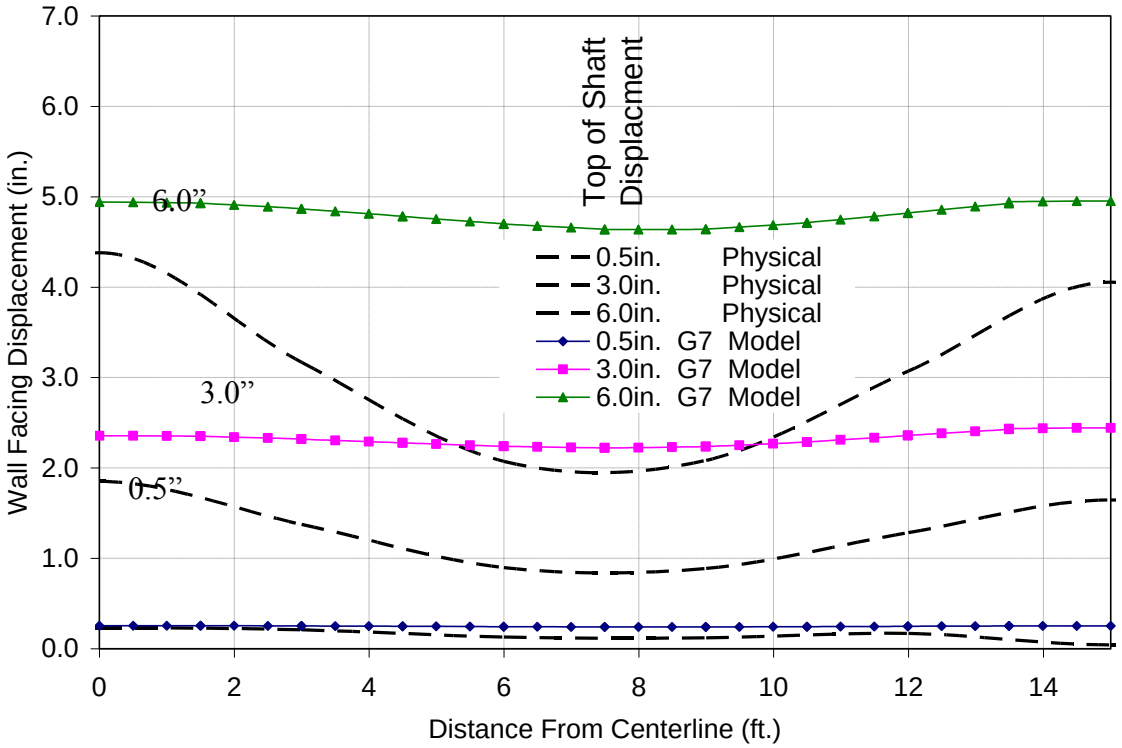

Figure 5.9 Plan view comparison of wall facing displacement from physical and model results at elevation 17.7 ft for the shafts loaded as a group spaced 6 ft from the wall facing (Shaft BG2).

Tell-tales were installed within the backfill material as well as attached to the geogrid at several points to compare with the numerical model (See Section 3.1 for more details). Selected tell-tales were compared with the numerical model to evaluate the accuracy of the numerical models. The location of the tell-tales is shown in figures taken from the main text, and placed after each comparison figure. Tell-tales attached to geogrid are located at elevation 14.7 ft and tell-tales located within the fill are at elevation 16 ft.

The first set of tell-tales to be compared the tell-tales installed near Shaft A. The magnitude of movement measured in the fill is very comparable with the movement measured in the field (Figure 5.10). The model shows the most movement near the

shaft and the field data shows the same thing. An additional point was examined half way between point 1 and 3 to examine any trends. Model data at this point agrees well with expected behavior. Model data for Shaft B (spaced 6 ft from the wall facing) shows excellent agreement with the model data (Figure 5.11). Figure 5.12 shows good agreement between model and field test data for Shaft C (spaced 9 ft from the wall facing). The model results for Shaft D show more displacement within the fill when compared with field results (Figure 5.13). Generally there is less agreement between the model and the field test when the shaft is farther from the wall facing. The same trend in behavior is observed in wall facing data. The magnitudes of movement for all measured locations in the model corresponded well with the magnitudes observed in the field.

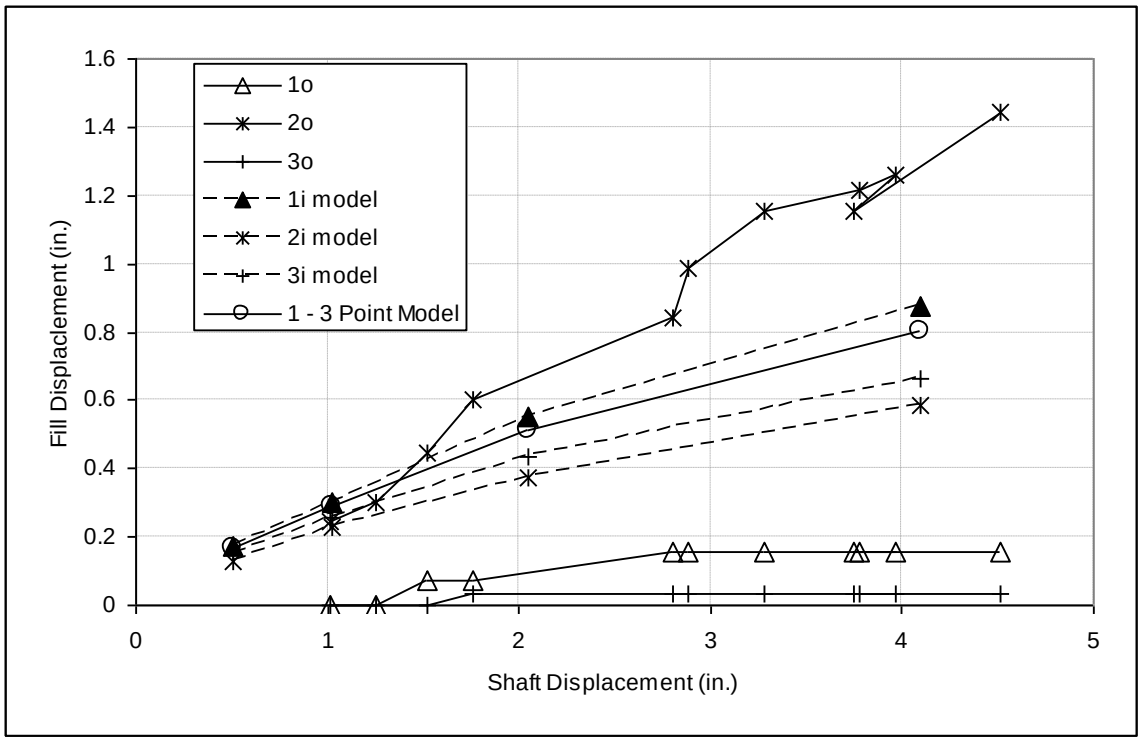

Figure 5.10 Comparison of model and field test tell-tale data for Shaft A.

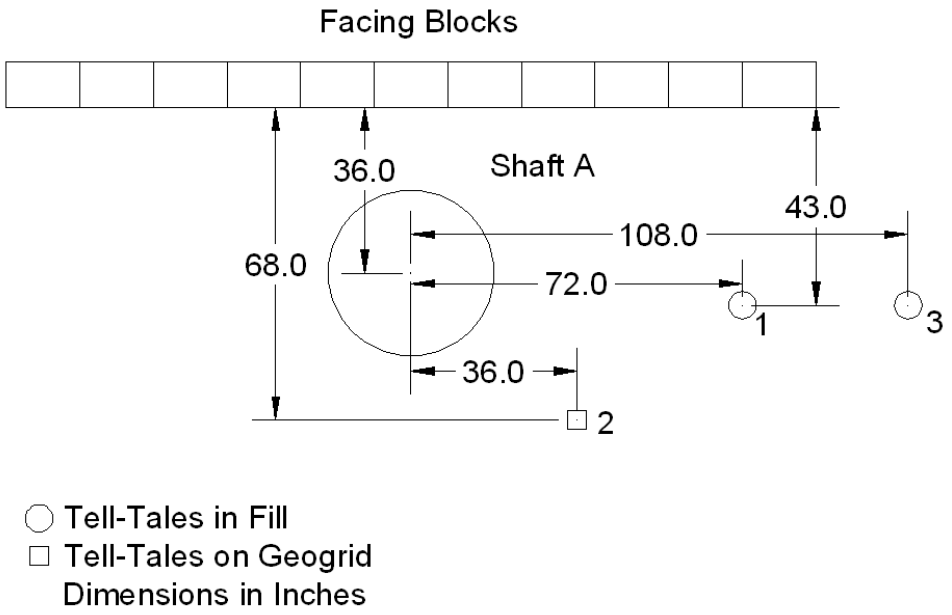

Figure 3.1 Location of tell-tales for Shaft A.

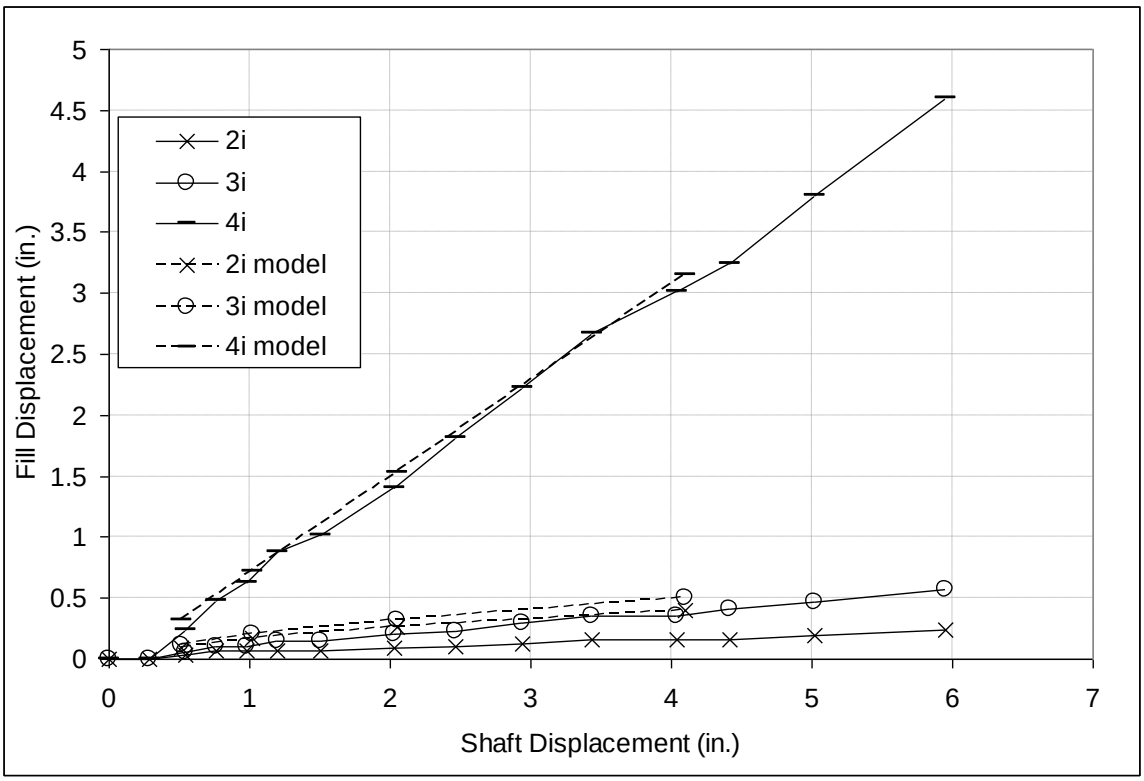

Figure 5.11 Comparison of model and field test tell-tale data for Shaft B.

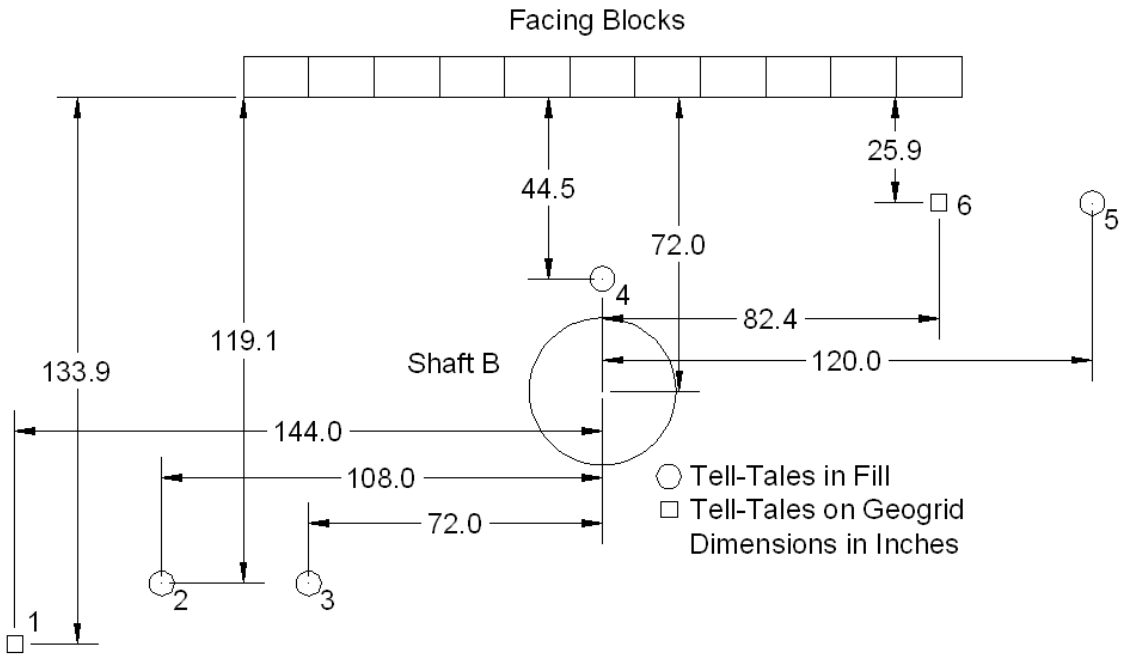

Figure 3.4 Location of tell-tales for Shaft B.

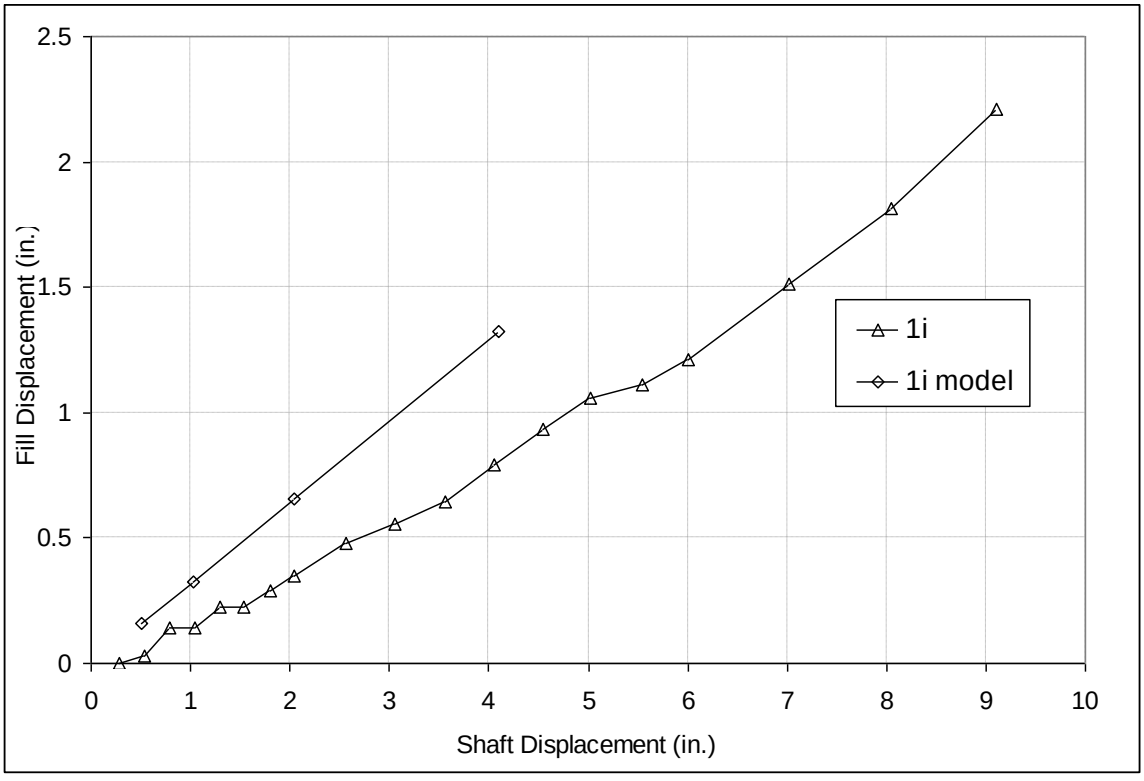

Figure 5.12 Comparison of model and field test tell-tale data for Shaft C.

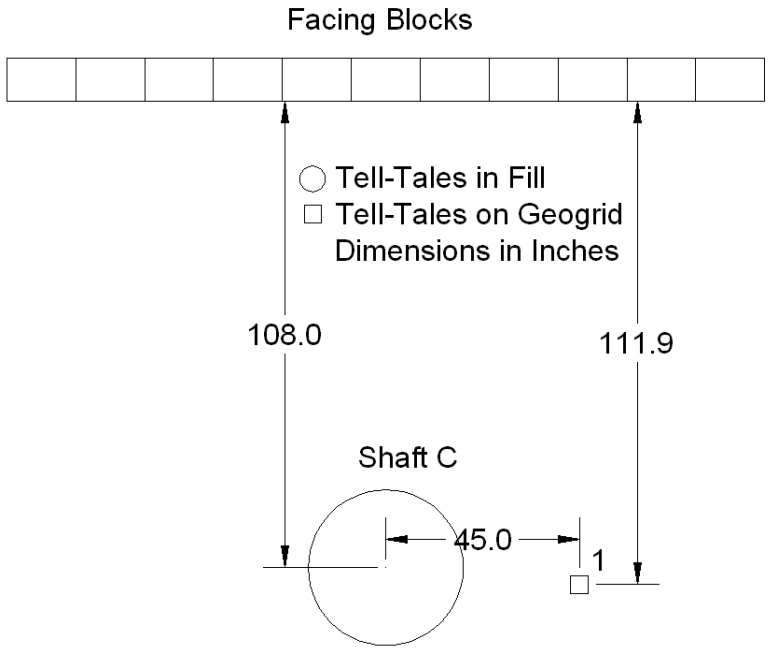

Figure 3.7 Location of tell-tales for Shaft C.

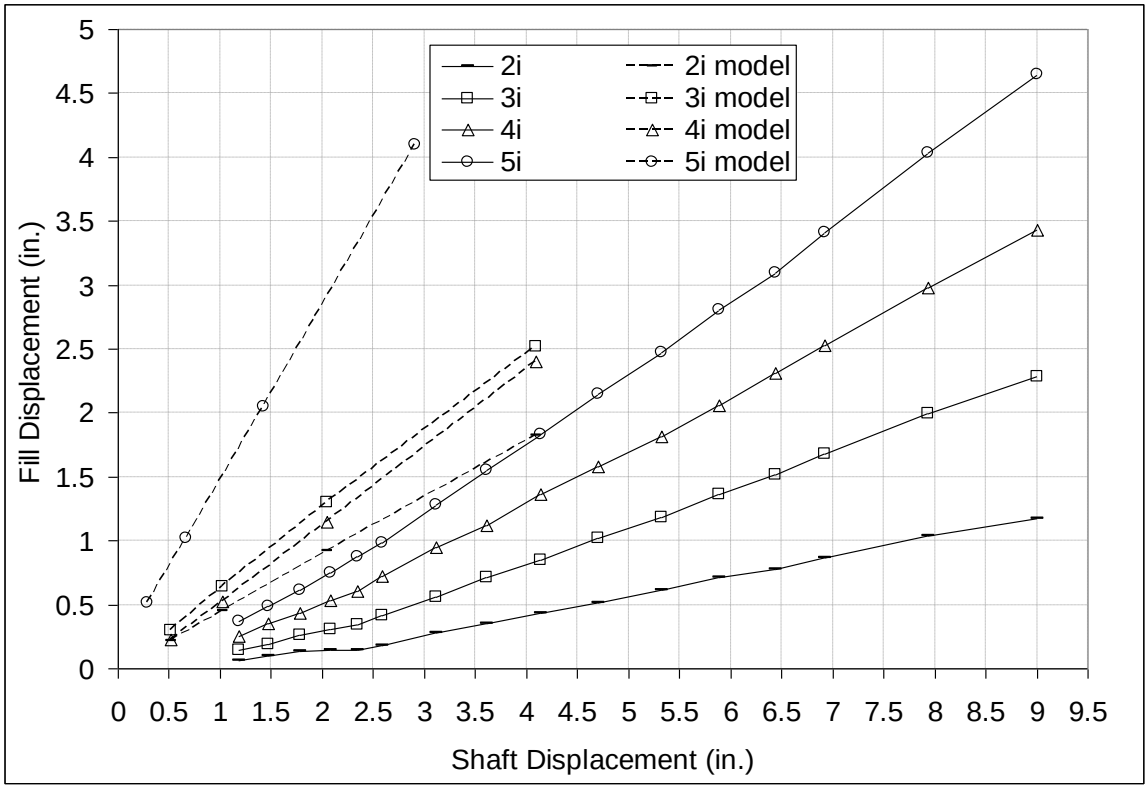

Figure 5.13 Comparison of model and field test tell-tale data for Shaft D.

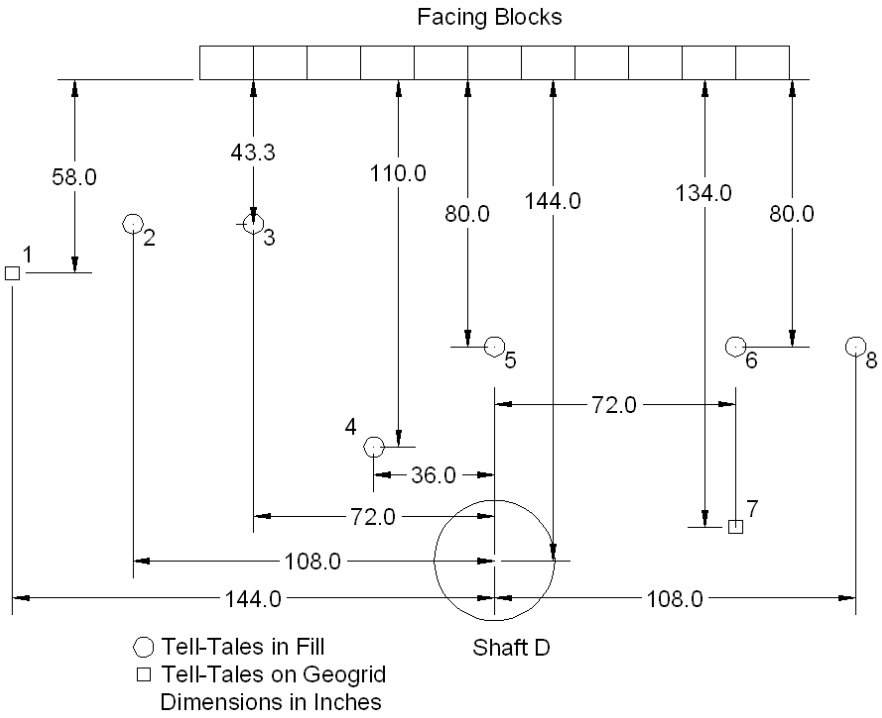

Figure 3.9 Location of tell-tales for Shaft D.

5.3 Alternative Geometries

Alternative geometries were modeled to increase the applicability of the system. The wall height was varied and the effect of changing the group spacing was evaluated. These results are discussed in the following sections.

5.3.1 Comparison of Wall Height

To evaluate the effect of wall height on the system, walls containing full length shafts were modeled at heights of 10, 20, and 30 feet. These results are compared in Figures 5.10 though 5.15. The effect of wall height on the top of shaft lateral load versus displacement curves is shown in Figure 5.10. The lower wall heights have a higher initial stiffness (the capacity is greater at very low shaft displacements), but the higher wall heights have more capacity at larger shaft displacements. The profile of wall facing displacement directly in front of the shaft for the 10 and 30 foot wall heights are shown in

Figures 5.11 and 5.12 respectively. The shafts spaced further from the wall facing produced less wall facing displacement. Figure 5.13 and shows the wall facing displacement in plan view at elevation 7.3 ft of the 10 ft tall wall. Figure 5.14 shows the same figure at elevation 27 ft of the 30 ft tall wall. The shafts spaced further from the wall facing produced less wall facing movement in front of the shaft and more facing movement away from the shaft than the shafts spaced nearer to the wall facing. The impact of this behavior is less dramatic for lower shaft movements. The taller wall shows more overall movement compared with the movement of the shorter wall approximately three feet below the top of each wall. This is partially caused by the larger amount of shaft rotation of the shorter wall.

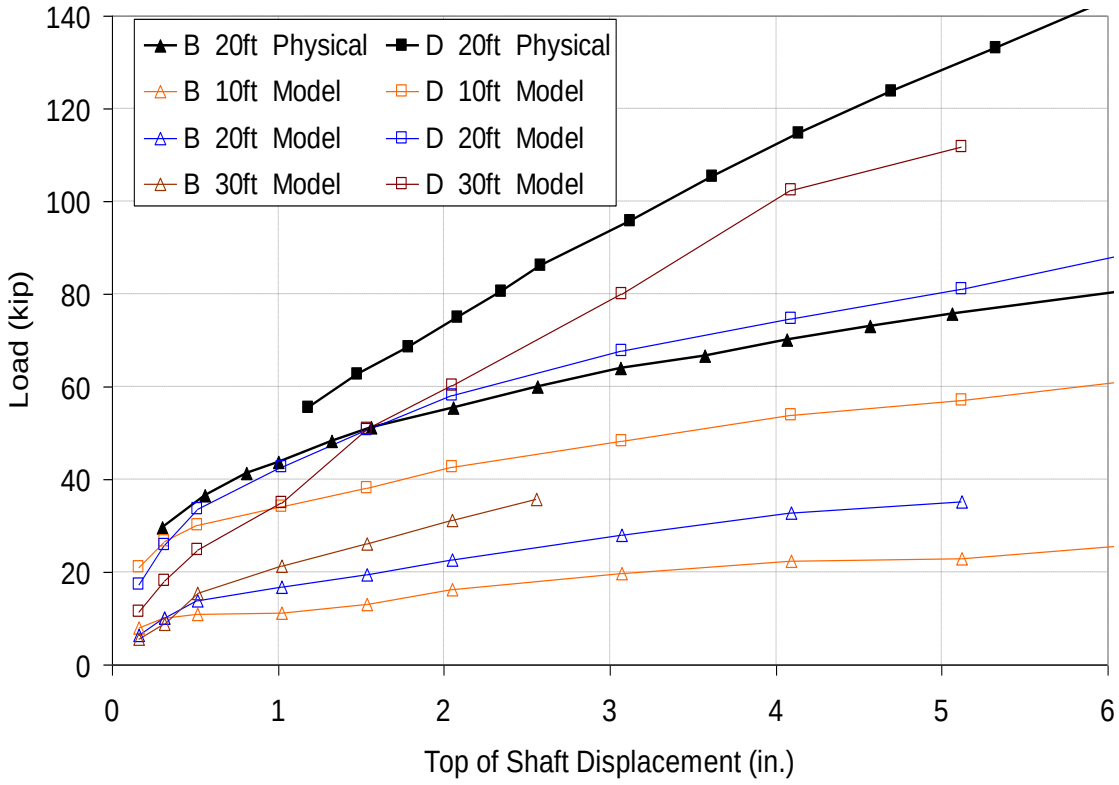

Figure 5.10 Load response curves for the wall heights of 10, 20, and 30 ft with shafts spaced either 6 or 12 feet from the wall facing (Shaft B or D configuration respectively).

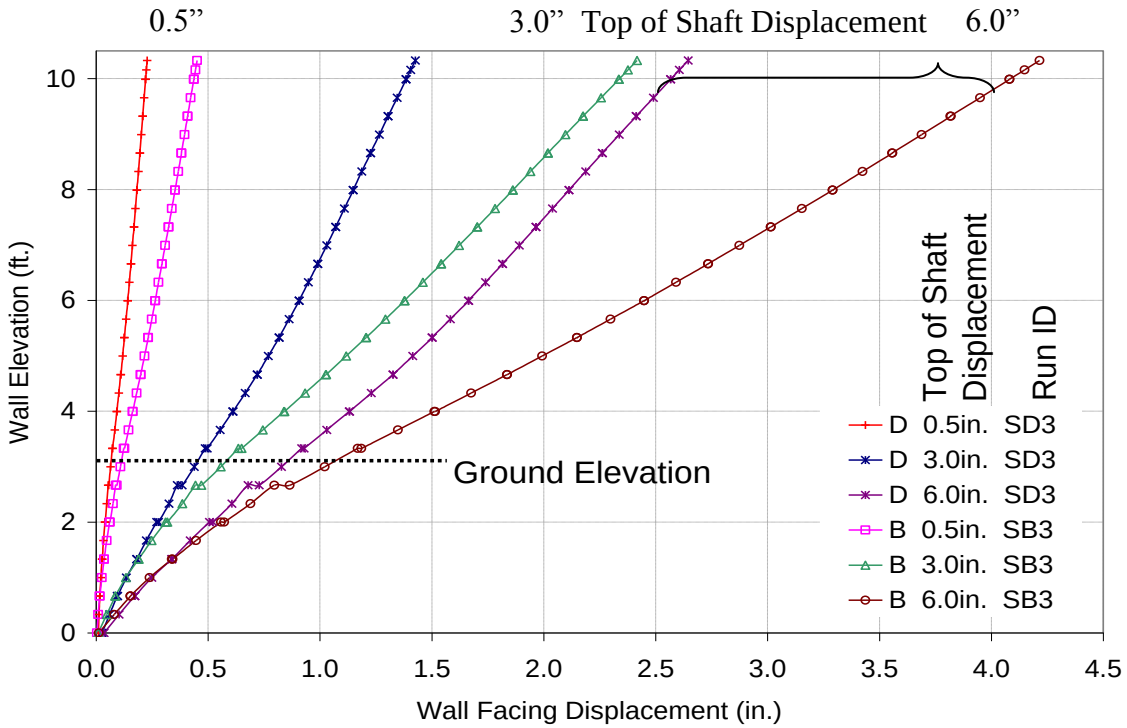

Figure 5.11 Profile view of wall facing displacement of 10 ft wall height with shafts spaced 6 and 12 ft from the wall facing (Shafts B and D).

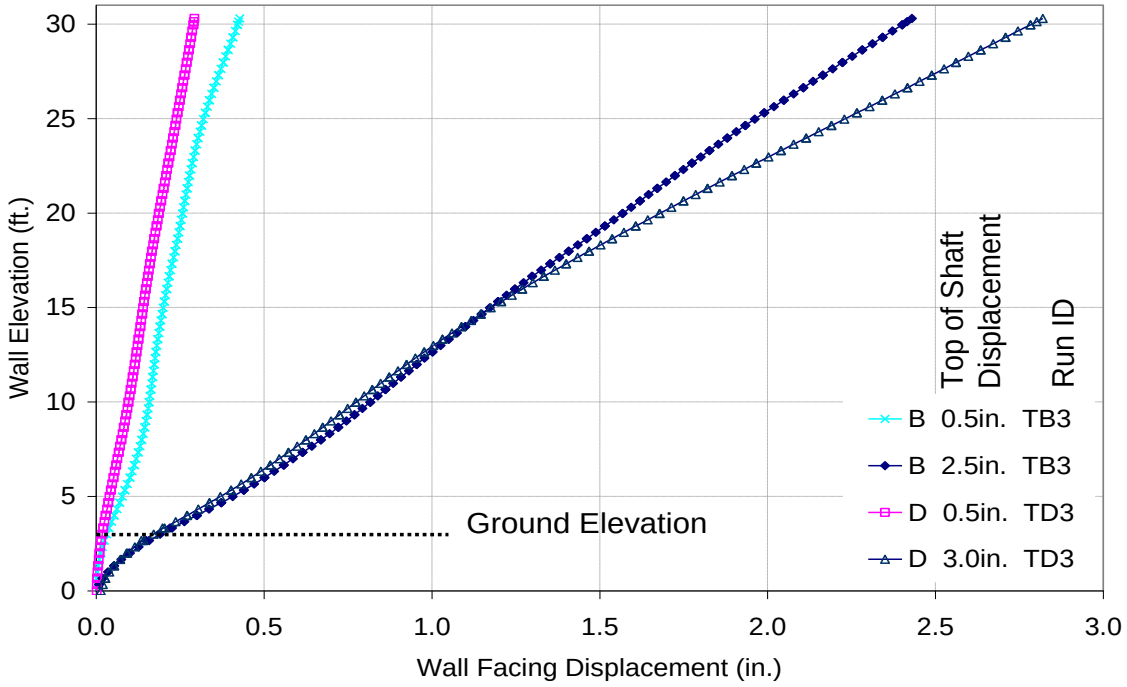

Figure 5.12 Profile view of wall facing displacement of 30 ft wall height with shafts spaced 6 and 12 ft from the wall facing (Shafts B and D).

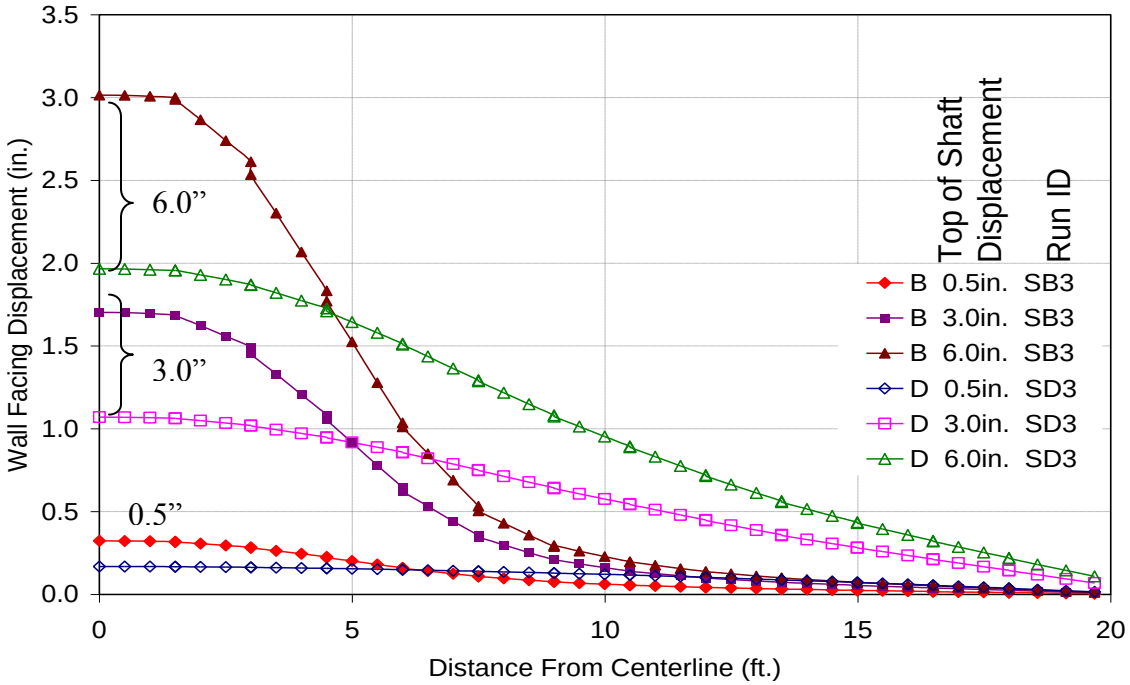

Figure 5.13 Wall facing displacement in plan view at elevation 7.3 ft of the 10 ft tall wall for shafts space either 6 or 12 feet from the wall facing (Shaft B or D).

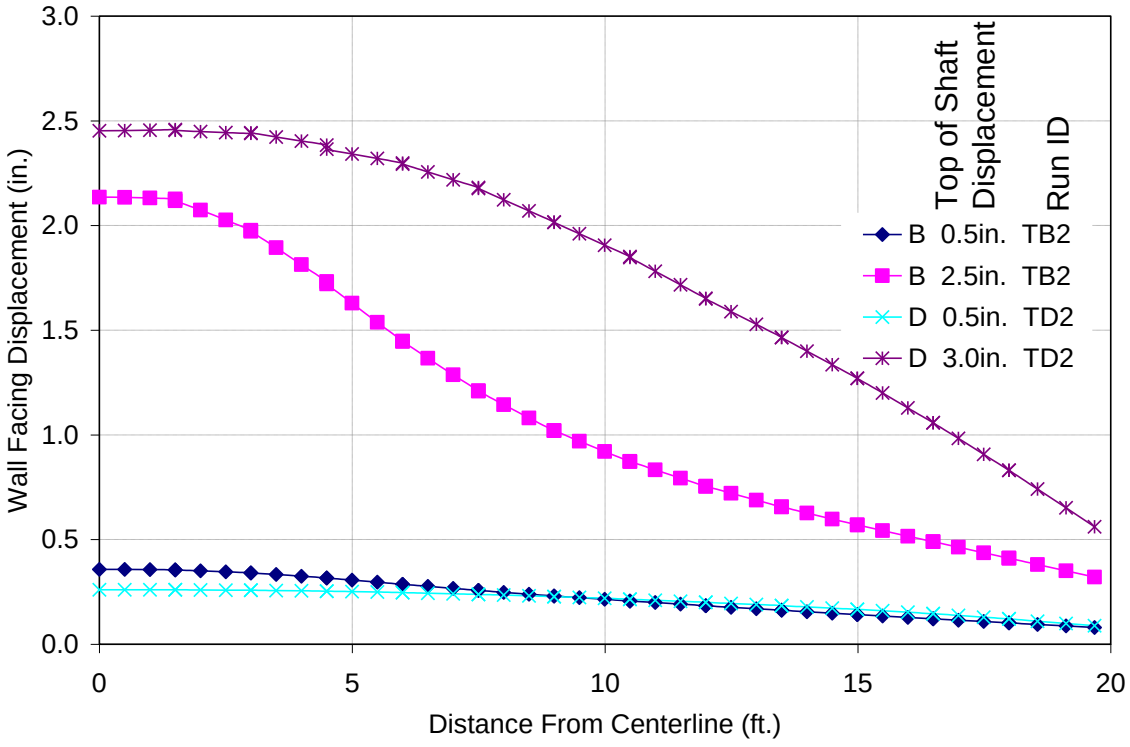

Figure 5.14 Wall facing displacement in plan view at elevation 27 ft of the 30 ft tall wall for shafts space either 6 or 12 feet from the wall facing (Shaft B or D).

5.3.2 Group Effect

The physical test contained a group test of shafts spaced 6 ft from the back of the wall facing to the center of the shafts to determine the influence of neighboring shafts on each other when spaced at 15 ft increments. To determine the group effect for shafts spaced 12 ft from the wall facing another model was constructed. The results of this test are compared with the results of the model with shafts spaced 6 ft from the wall facing loaded as a group. Figure 5.15 shows the top of shaft load response curve for each of these models loaded as a group as well the corresponding single shaft models. The percent reduction due to the group effect is smaller for the shafts spaced further from the wall facing. These results show the design method for estimating the reduction due to the group effect based on physical testing proposed in Section 3.3 is conservative. This design method specifies an increased reduction due to the group effect for shafts farther from the wall facing. The proposed method also calls for a linearly increasing reduction with greater shaft distances from the wall facing due to the group effect. The method proposed is limited due to the limited physical testing available. Modeling shows that increasing the shaft distance from the wall facing causes an increased role for passive soil resistance to shaft movement within the reinforced zone. The profile of wall facing movement in front of the group loading of shafts spaced 15 ft apart and 12 ft from the wall facing is shown in Figure 5.16. The plan view of wall facing displacement at elevation 17.7 ft under group loading with shafts spaced 15 ft apart and 12 ft from the wall facing is shown in Figure 5.17. These plots are shown for reference to estimate wall facing movement given similar geometry.

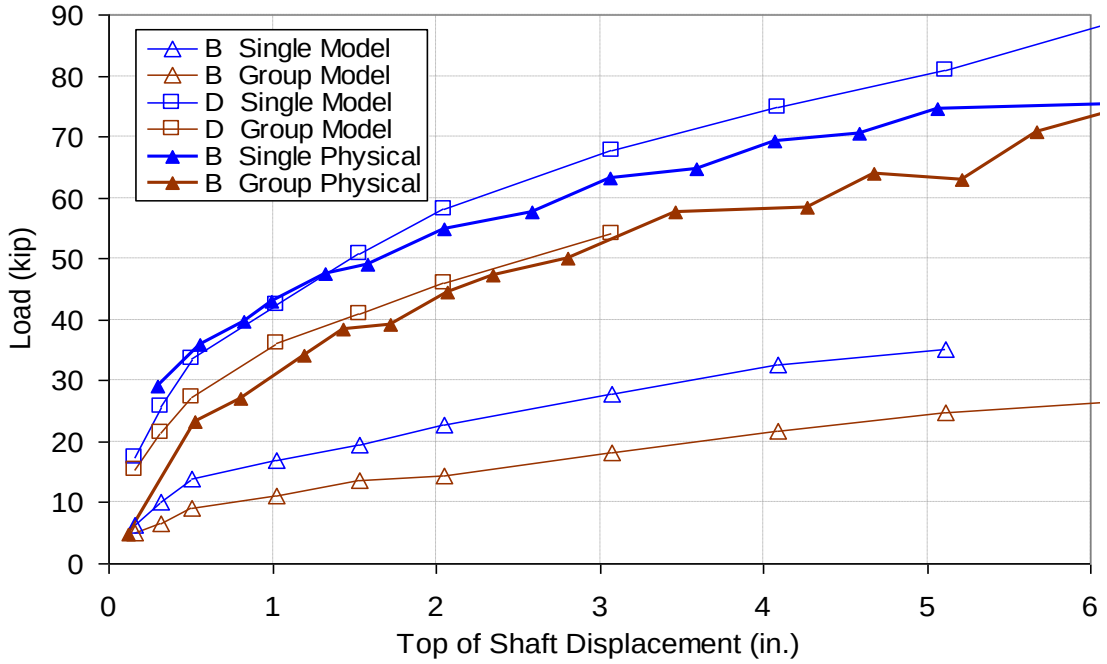

Figure 5.15 Load response curves for group and single models with shafts spaced 6 or 12 feet from the wall facing (Shaft B or D).

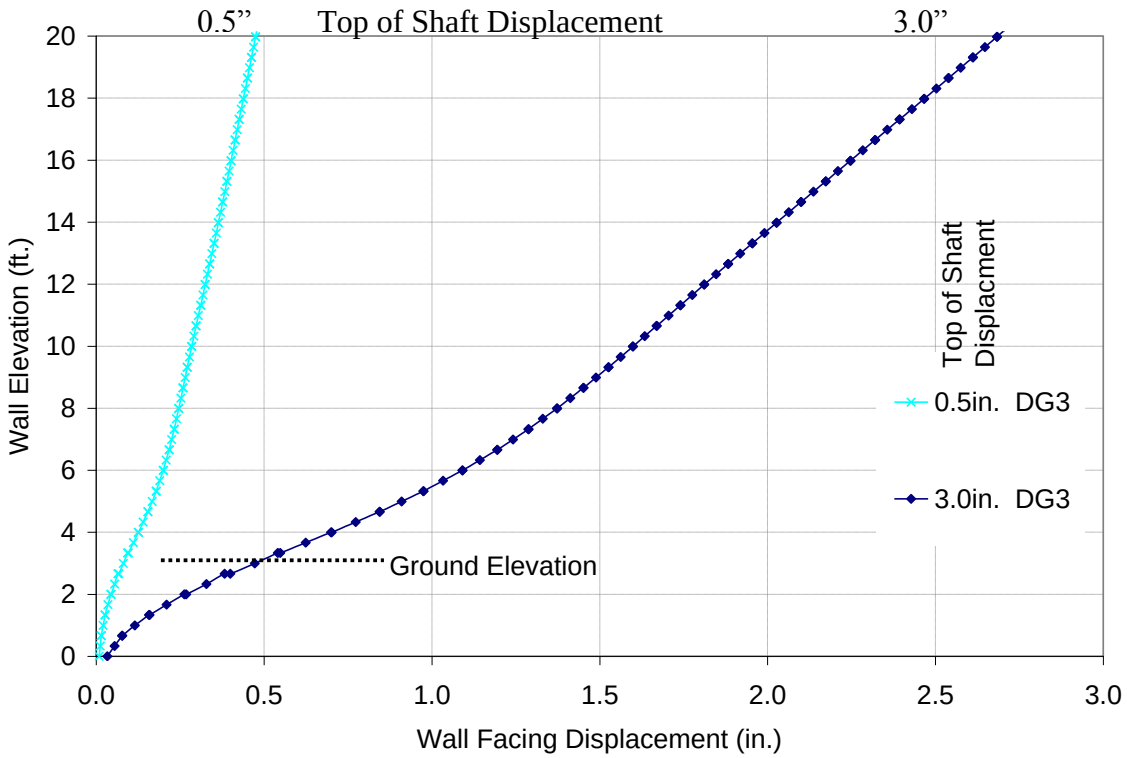

Figure 5.16 Profile view of wall facing displacement directly in front of the shaft under group loading with shafts spaced 15 ft apart and 12 ft from the wall facing.

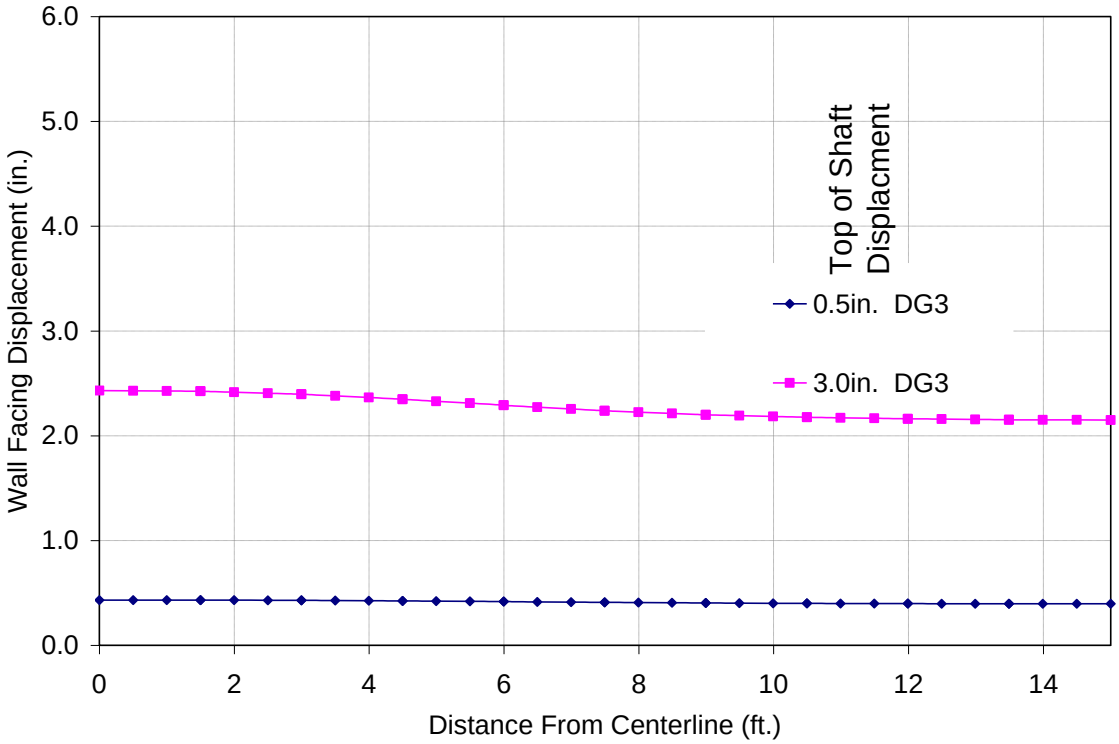

Figure 5.17 Plan view of wall facing displacement at elevation 17.7 ft under group loading with shafts spaced 15 ft apart and 12 ft from the wall facing.

CHAPTER SIX

Conclusions and Preliminary Recommendations for Design

A set of conclusions and recommendations was developed based on the numerical modeling study described in Chapters 4 and 5. Table 6.1 shows the variables examined in this study and their significance related to MSE wall – shaft systems. Each of these items is discussed and several preliminary design recommendations are made below.

Table 6.1 Conclusions Summary

Material and Property		Significance
Geogrid		
	Overall Stiffness	High
	Stiffness in the Weak Direction	High
	In-plane Shear Stiffness	High
	Coefficient of Interaction	High
	Lengthening Geogrid	Low
Aggregate		
	Friction Angle	Medium
	Young's Modulus	Low
Wall Facing		
	Bond From Block to Block	Low
	Friction from Block to Block	Low
Wall Height		Low

6.1 Conclusions from Parametric Study

Several conclusions can be made from the parametric study. All of the likely contributors to shaft response (wall facing, aggregate, and geogrid) contribute to the overall system response. The material most responsible for shaft lateral load capacity is the geogrid material followed by the facing and aggregate properties.

The interface properties at the bottom of the discrete blocks were the only properties changed in this study related to wall facing (Figure 4.12). Cohesion and block

friction played a small role in system behavior within the range of properties examined (Figures 4.13, 4.14, and 4.15). The interface shear stiffness, which controls the interface shear displacement before sliding occurs, plays a significant role only when the shear stiffness value is very low (Figures 4.16, 4.17, and 4.18). These findings indicate that increasing the cohesion and friction from block to block in the vertical direction would add significant capacity to the system. One option would be to backfill the blocks with aggregate, use increased capacity shear connectors, or use a high strength adhesive between blocks. Further research into this is needed to evaluate the magnitude of any improvement.

The role of aggregate properties was also found to have a significant effect on the system behavior. The friction angle of the gravel was found to have the largest impact on the system followed by the aggregate modulus. Aggregate friction angle showed a reduction in shaft load as high as 11% when changed from 51 to 45 degrees (Figure 4.22). The geogrid interface friction angle remained constant during this study. In reality the geogrid interface friction angle is related to the aggregate friction angle. This means a further reduction in shaft load would have occurred if the geogrid friction angle were allowed to change assuming a constant coefficient of interaction for the geogrid and soil. The aggregate modulus showed little impact for the accepted range of aggregate properties used in this study (Figures 4.19, 4.20, and 4.21). However, further investigation is needed to evaluate the effects caused by even lower values of aggregate modulus.

The geogrid properties had the greatest affect on modeling results. All of the geogrid related variables in this study affected the results. The geogrid coefficient of

interaction played a larger role for larger shaft displacements (Figure 4.25). Use of a higher geogrid coefficient of interaction resulted in less wall facing displacement and distributed the movement to a wider area in front of the shaft (Figure 4.26 and 4.27). This indicates increased geogrid friction would improve system behavior. This could be achieved by adding a texture to the geogrid surface or increasing the number of CMD bars (Figure 3.18). The geogrid interface shear stiffness, which controls displacement before sliding occurs, affected the results for low values only (Figures 4.28, 4.29, and 4.30).

The stiffness of the geogrid (Figure 4.31) was the greatest contributor to system behavior mainly due to the large range of the values used. The stiffness in the weak direction plays a significant role in system behavior (Figures 4.31, 4.32, and 4.33). The use of biaxial geogrid should provide a significant improvement in system response. The in-plane shear stiffness of the geogrid is the least known of all the geogrid properties. Its impact on behavior was very significant, increasing shaft response 80% with one order of magnitude increase in geogrid in-plane shear stiffness (Figures 4.34, 4.35, and 4.36). This indicates the use of triaxial, or even biaxial, geogrid would improve system response. The overall geogrid stiffness, which includes the stiffness in the strong, weak, and shear directions, was the largest contributor to system behavior (Figures 4.37, 4.38, 4.39, and 4.40). As the stiffness of the geogrid increases, the shaft load does not increase linearly (Figure 4.38). This indicates a condition of diminishing returns that is especially noticeable at lower shaft displacements. This is because as the geogrid stiffness increases the role of geogrid friction angle become more important. When using geogrids with

greater stiffness, it is possible that using twice as many reinforcement layers would give better results than increasing geogrid stiffness by a factor of two.

Geogrid strains measured in the numerical model, with low geogrid stiffness, at low shaft displacement are very low near the back of the reinforcement. However, at high shaft displacement more of the shaft load is being carried by the geogrid near the back of the reinforced zone. This indicates that lengthening the geogrid will increase the shaft capacity, but not its initial stiffness. Since most designs will not allow more than two inches of shaft displacement increasing the length of a weak geogrid will not increase shaft performance. If a very stiff geogrid is used the load will transfer to the back of the geogrid more quickly and shaft stiffness will increase. Further investigation is needed to verify this behavior and to evaluate the interplay of geogrid length, stiffness, and friction on shaft behavior.

6.2 Preliminary Design Recommendations Based on Modeling Results

For design purposes several recommendations can be made. Where possible, site specific physical load tests will provide the best possible results for design. The previous field tests (Section 3.3) may be used for design if a system is to be designed with the same geometry and material properties as previous field tests. The results from Chapters 4 and 5 were used to produce preliminary design recommendations for MSE walls with laterally loaded shafts contained within the reinforced zone which considers wall height, shaft spacing from the facing, and group effect. Table 6.2 contains a summary of all of the data from the shafts modeled in Chapter 5. This table shows the shaft distance from the facing, if a group effect is considered, wall height, shaft height, and the shaft load at a given top of shaft displacement. It is likely these values are conservative as the models

that correspond to the physical tests consistently under predicted the physical capacity of the shafts.

Table 6.2 Modeling Summary

Distance From Facing (Ft)	Group Effect?	Wall Height (ft)	Shaft Height(ft)	Shaft Load (kip)		
				0.5 in.	1.0 in.	2.0in.
3	No	20	20	3.7	5.8	11
6	No	20	20	14	17	23
9	No	20	20	19	25	37
12	No	20	20	34	43	58
6	No	20	15	6.7	12	18
6	Yes	20	20	9.0	11	14
12	Yes	20	20	27	36	46
6	No	10	10	11	11	16
12	No	10	10	30	34	43
6	No	30	30	16	21	31
12	No	30	30	25	35	60

note: Group effect was only considered given a 15 ft shaft to shaft spacing.

6.2.1 Changing Wall Height

If a wall height other than twenty feet (the height of the physical testing) is to be used the following preliminary recommendations are made. Wall heights less than 10 ft have not been considered and should not be used without special consideration.

- It is recommended that high quality aggregate be used for backfill unless substantial allowance is made for backfill materials with lower friction angles.
- If allowable displacement is one inch or less, it may be acceptable to use the previous field work for design. This is due to the insensitivity of shaft load to wall height for displacements of one inch or less.
- Wall heights shorter than twenty feet should maintain reinforcement lengths greater than or equal to the 14 foot reinforcement length used in the field test until further modeling or testing is complete.

- Wall heights greater than twenty feet must maintain reinforcement lengths greater than or equal to 70% of the wall height (AASHTO requirement).
- The top six courses of geogrid should be greater than or equal to the stiffness of the geogrid used in the field test. All geogrid below the top six courses should be greater than or equal to the lower four courses of geogrid used in the field test until further modeling or testing is complete.
- Wall heights greater than thirty feet must be designed to verify greater geogrid strength is not required in lower geogrid courses to prevent geogrid rupture.

6.2.2 Improving System Performance

The following section contains suggestions which will increase the performance of the MSE wall – shaft system. Many of these recommendations are taken from the parametric study conducted in Section 4.1. They will give design engineers options that will increase strength and stability and ensure greater performance over the life of the system.

- All materials including high quality aggregate backfill must be similar to the previous field tests until further testing or modeling is completed. Little benefit is gained from using aggregate with a greater friction angle or modulus than those used in this study.
- Geogrid is the greatest contributor to strength and stiffness.
    - Using bi-axial or triaxial geogrid will reduce wall facing displacements for a given load and increase shaft stiffness and strength.

    - Increasing the stiffness of the geogrid will increase the strength and stiffness of the wall system. (See next point)
    - As geogrid stiffness is increased, the geogrid length and interface friction angle play a larger role in determining the strength of the wall system.
- Wall facing stiffness is an important part of strength and stiffness.
    - Increasing the wall facing connector strength and stiffness increases shaft stiffness and strength.
    - Backfilling wall facing blocks will increase friction and stiffness of the wall facing which will increase shaft stiffness and strength.
    - The use of adhesive between blocks could be a means of increasing system stiffness and strength.

6.3 Conclusions

Shaft foundations within the reinforced mass behind an MSE wall are capable of resisting substantial lateral loads. MSE – shaft systems may be designed based on physical test data (Section 3.3), numerical modeling (Section 5.2 and 5.3), and improved with recommendations from Chapter 4. These systems are capable of supporting significant lateral loads at small shaft displacements and are able to tolerate large lateral loads due to the inherent system flexibility. Large savings may be gained when compared with the traditional system due to increased production time, decreased materials, and especially the lack of a socketed foundation which requires expensive drilling operations.

Future investments to improve the understanding of the system will increase the robustness and application of the system. Further numerical modeling should be done to determine the impact on system behavior from the following; backfill, geogrid length, shaft diameter, wall facing type, group behavior at multiple wall heights, shaft performance when placed behind the reinforced zone, impact loading, cyclic loading, and dynamic loading. Additional physical testing of geogrid type, wall height, group spacing, backfill type, and shaft diameter would increase the reliability of the numerical modeling and expand the range of potential uses of the system.

REFERENCES

Anderson, Peter L., "Increased Use of MSE Abutments," International Bridge Conference 2005 IBC-05-10. The Reinforced Earth Company, North Reading, MA, 2005.

Arora, K. R., "Soil mechanics and foundation engineering." Standard Publishers Distributors, Nai Sarak, Delhi, India p. 218 1987.

Bang, S., Shen, C.K., "Analytical study of laterally loaded cast-in-drilled-hole piles. Transportation Research Record No. 1219, p. 33-42, 1989.

Bay, J. A., Anderson, L.R., Budge, A. S., Eurfur, C., "Analytical modeling of MSE wall at 1-15 and 3600 south." Report No. UT-04.10, Utah Department of Transportation, 2004.

Boscardin, M. D., Selig, E. T., Lin, R. S., Yang, G. Y., "Hyperbolic parameters for compacted soils." ASCE Journal of Geotechnical Engineering, v 116, n 1, p. 88-104, January 1990.

Brinch Hansen, J., "The ultimate resistance of rigid piles against transversal forces." Geotecnisk Institute Bulletin, Copenhagen No. 12, 1961.

Broms, B.B., "Lateral resistance of piles in cohesive soils." ASCE Journal of the Soil Mechanics and Foundations Division, v 90, n SM2, p. 27-63, March 1964a.

Broms, B.B., "Lateral resistance of piles in cohesionless soils." ASCE Journal of the Soil Mechanics and Foundations Division v 90, n SM3, p. 123-156, May 1964b.

Budge, A. S., Bay, J. A., Anderson, L. R., "Calibrating vertical deformation in a finite element model of an MSE wall." GEOCongress 2006 geotechnical engineering in the information technology age; February 26 - March 1, 2006.

Davidson, J.L., Hays Jr., C.O., Hagan Jr., E.M., "Design of drilled shafts supporting highway signs." Transportation Research Record n 616, p. 62-66, 1976.

Ducan, J. M., Byrne, P., Wong, K. S., Mabry, P., "Strength, stress-strain and bulk modulus parameters for finite element analysis of stress and movements in soil masses." Report No. UCB/GT/80-1, Department of Civil Engineering University of California, Berkeley 1980.

Farouz, E., Esterhuizen, J., Landers, P., "Performance of MSE walls supporting bridge foundations." Proceedings of Geo-Trans 2004, p. 2231 – 2245, 2004.

FHWA, “Mechanically Stabilized Earth Walls and Reinforced Soil Slopes – Design and construction Guidelines,” FHWA-SA-96-071 August 1997.

Hatami, K. Bathurst, R. J., “Development and verification of a numerical model for the analysis of geosynthetic-reinforced soil segmental walls under working stress conditions.” Canadian Geotechnical Journal, v 42 n 4 p. 1066-1085, August 2005.

Helwany, S. M. B., Wu, J. T. H., Kitsabunnarat, A., “Simulating the behavior of GRS bridge abutments.” ASCE Journal of Geotechnical and Geoenvironmental Engineering, v 133, n 10, p. 1229-1240, October 2007.

Huang, J., Parsons, R. L., Han, J., Pierson, M. C., “Numerical analysis of a laterally-loaed shaft constructed within an MSE wall.” Geotextiles and Geomembranes (submitted Feb. 2010)

Itasca Consulting Group, FLAC – Fast Lagrangian Analysis of Continua. Version 4.00. Itasca Consulting Group Inc. Minneapolis, Minn., 2001.

Itasca Consulting Group, Inc. Fast Lagrangian Analysis of Continua in 3 Dimensions version 3.1 Itasca Consulting Group Inc. Minneapolis, Minn., 2006.

Johnson, Rebecca, “Soil Characterization and P-Y Curve Development for LOESS.” Master’s thesis, The University of Kansas 2006.

Jones, R. M., “Mechanics of composite materials.” Second Edition Bunner-Routledge, New York and London, p. 72, 1998.

Karpurapu, R., Bathurst, R. J., “Behaviour of geosynthetic reinforced soil retaining walls using the finite element method.” Computers and Geotechnics, v 17, n 3, p. 279 – 299, 1995.

Ling, H. I., Cardany, C. P., Sun, L-X., Hashimoto, H., “Finite element study of a geosynthetic - reinforced soil retaining wall with concrete – block facing.” Geosynthetics International, v 7, n 2, p. 137-162, 2000.

Ling, H. I., Liu, H., “Deformation analysis of reinforced soil retaing walls – simplistic versus sophisticated finite element analyses.” Acta Geotechnica, v 4, n 3, p. 203-213, September 2009.

Lopes, M. L., Cardoso, A. S., Yeo, K. C., “Modeling performance of a sloped reinforced soil wall using creep function.” Geotextiles and Geomembrains, v 13, n 3, p. 181 – 197, 1994.

NAVFAC DM-7. “Design manual – soil mechanics, foundations and earth structures.” Department of the Navy, Naval Facilities Engineering Command, 1971.

Parsons, R. L., Pierson, M. C., Han, J., Brennan, J. J., and Brown, D. A. "Lateral load capacity of cast-in-place shafts behind an MSE wall." ASCE Geotechnical Special Publication No. 186, p. 560-567, IFCEE 09' 2009a.

Parsons, R. L., Pierson, M. C., Han, J., Vulova, C., and Brennan, J. J. "Longer term monitoring of strains in MSE wall." Proceedings of Geosynthetics 2009, p. 300-308 2009b.

Pierson, M. C., Parsons, R. L., Han, J., and Brennan, J. J., "Laterally Loaded Shaft Group Capacities and Deflections Behind an MSE Wall". Submitted to the ASCE Journal of Geotechnical Engineering 2010.

Pierson, M. C., Parsons, R. L., Han, J., Brennan, J. J., and Vulova, C. "Instrumentation of MSE wall containing laterally loaded drilled shafts." ASCE Geotechnical Special Publication No. 187, p. 353-360, IFCEE 09' 2009a.

Pierson, M. C., Parsons, R. L., Han, J., and Brennan, J. J. "Capacities and deflections of laterally loaded shafts behind an MSE wall." Transportation Research Record, n 2116, p 62-69, 2009b.

Pierson, M. C., Parsons, R. L., and Han, J. "Modeling of MSE wall – drilled shaft systems." Proceedings of 34th Annual Conference on Deep Foundations, DFI, 2009c.

Pierson, M. C., Parsons, R. L., Han, J., Brown, D. A., and Thompson, R. W. "Capacity of Laterally Loaded Shafts Constructed behind the Face of a Mechanically Stabilized Earth Block Wall." Final Report, Kansas Department of Transportation, 81pages, http://www.ksdot.org/PublicLib/publicDoc.asp?ID=003782466 2008.

Rodriguez-Roa, Fernando. "Observed and calculated load-settlement relationship in a sandy gravel." Canadian Geotechnical Journal, v 37 n 2 p. 333-342, April 2000.

Shen, C-K., Romstad, K.M., Herriman, L.R., "Integrated study of reinforced earth.—II: behavior and design." ASCE Journal of the Geotechnical Engineering Division, v102, n 6, p. 577-590, June 1976.

Tamura, Y., Nakamura, K., Tateyama, M., Murata, O., Tatsuoka, F., "Full-scale lateral loading tests of column foundations in geosynthetic-reinforced soil retaining walls." Proceedings of International Symposium on Recent Cass Histories of Permanent Geosynthetic-Reinforced Soil Retaining Walls, Tokyo, Nov. 1992 (Tatsuoka and Leshchinsky, ed), Balkema, p. 277 – 284, 1993.

Tassios, Theodossius P., Vintzēleou, Elisabeth N., "Concrete-to-concrete friction" ASCE Journal of Structural Engineering Vol. 113, Issue 4, p. 832-849, April 1987.

Tateyama, M., Murata, O., Tamura, Y., Nakamura, K., Tatsuoka, F., and Nakaya, T., "Lateral loading tests on columns on the facing of geosynthetic-reinforced soil retaining

wall." Proceedings of International Symposium on Recent Cass Histories of Permanent Geosynthetic-Reinforced Soil Retaining Walls, Tokyo, Nov. 1992 (Tatsuoka and Leshchinsky, ed), Balkema, p. 287 – 294, 1993.

Tensar Earth Technologies, "Demonstration of pile driving through the HDPE geogrid reinforced soil fill of full-height precast concrete panel faced, mechanically stabilized earth wall," Report, Colorado E-470 Project, 2001.

Tensar Earth Techniologies, "Mechanically Stabilized Earth Walls: Program MesaPro Version 2.3" ADAMA Engineering and Tensar International Corporation Copyright 1998 – 2007.

Wang, S.T., Reese, L.C., "COM624P – laterally loaded pile analysis program fro the microcomputer." Version 2.0 Publication FHWA-SA-91-048, Federal Highway Administration, 1993.

Yang, K., Liang, R. Y., Nusairat, J., Abu-Hejleh, N., "Design of drilled shafts supporting sound walls." Deep Foundations Institute Journal, v1, n1, p. 28-36 November 2007.

Yang, X., Han, J., Parsons, R. L., Leshchinsky, D., "Three-dimensional numerical modeling of single geocell-reinforced sand." Accepted to Frontier of Architecture and Civil Engineering in China 2010.

Yoo, C., Jeon, Y-W., "Behavior of geosynthetic-reinforced segmental retaining walls in tiered arrangement." Geotechnical Engineering for Transportation Projects: Proceedings of Geo-Trans 2004, n 126 I, p. 647 – 656, 2004.

Yoo, C., Jung, H. Y., "Case history of geosynthetic reinforced segmental retaining wall failure." ASCE Journal of Geotechnical and Geoenvironmental Engineering, v 132, n 12, p. 1538-1548, December 2006.